School of Science
Department of Physics & Astronomy
International Centre of Radio Astronomy Research
Curtin Institute of Radio Astronomy

The connection between inflow and outflow around accreting stellar-mass black holes

Thomas David Russell

This thesis is presented for the Degree of
Doctor of Philosophy
of
Curtin University

May 2015

To the best of my knowledge and belief this thesis contains no material previously published by any other person except where due acknowledgement has been made. This thesis contains no material which has been accepted for the award of any other degree or diploma in any university.

.....
Thomas D. Russell
30 May 2015

Acknowledgements

The three year and two month journey to complete this research project has been exciting and demanding; I could not have done it without the help and support of many people.

First and foremost, I would like to thank my supervisors Drs. James Miller-Jones, Roberto Soria, Peter Curran and Professor Steven Tingay. I could not imagine a better group of supervisors. I will forever be indebted to you for setting high standards and goals, providing me with invaluable knowledge and time, and, most importantly, your friendship. Thank you for your constant support and guidance, both past and present.

Special thank you must go to Drs. Cormac Reynolds, Hayley Bignall, Andrew Walsh, Leith Godfrey and Brendan McGann, Pete Wheeler and Kirsten Gottschalk. I have really enjoyed working with you, but I have mostly enjoyed becoming friends. Thank you all for your reliable ability to provide relief from the seriousness and making the working week fun.

To all of the members of the CIRA and ICRAR staff, both past and present, thank you for your regular chats and tolerating my antics. The place would be a lot less interesting without you all. To the past and present ICRAR and non-ICRAR students, including Samuel Oronsaye, Hongquan Su, Dr. Hayden Rampadarath, Dr. Jun Yi 'Kevin' Koay, Vlad Tudor, Ryan Urquhart, Balwinder Arora Singh, Cdr. Chittawan Choeysakul, HaiHua Qiao, Rakesh Nath, Rebecca Lange, Angus Wright, Steven Murray, Scott Meyer, Sarah Bruzzese, Dr. Jacinta Delhaize, Dr. Laura Hoppmann, Jeremy Savage, Arwin Kahlon, Alex Tetarenko, Aina Musaeva, Laura Shishkovsky, Chris Jordan, Dr. Vanessa Moss and Claire Trenham, thanks for making it less about work.

Thank you to my international colleagues and friends, Professors Dave Russell, Sera Markoff, Elena Gallo and Rob Fender, Drs. Matt Middleton, Alexander van der Horst, Diego Altamirano, Rich Plotkin, Amy Reines and Jack Steiner for taking me under your wing, providing help and guidance, and for making every

trip an enjoyable experience. I would also like to thank Dr. Danny Price, Lindall Kidd, Andrew Han, Danny Pons, Kim Tran, Felix Prummel, Gareth Mohen and Zoe Bullock, as well as my Amsterdam family, Michiel, Elsje and Charlotte, for being friendly, familiar faces on the other side of the world.

I owe my friends a great deal of gratitude for remaining understanding and supportive of my regular absences over the past few years.

To my mum, dad, Bruno and Pam, thank you for always loving and supporting me, and shaping who I am today. To my grandparents, thank you for your support and for instilling in me the value of education. To my siblings, Sam, Leah, Leon, Rose, Louis, Sabrina and Marty, thank you for keeping me sane with your insane ways.

To Louisa, thank you for being there and for putting up with me unequivocally. Thank you for making things bright and for being five with me. I can't wait for the future.

Abstract

This thesis presents our multiwavelength monitoring of the Galactic black hole candidate X-ray binary MAXI J1836−194 during its 2011 outburst, in which the system underwent a dramatic brightening due to increased mass inflow (onto the black hole). The outburst peaked in the hard intermediate state before fading towards quiescence, and the compact jet remained on throughout. Quasi-simultaneous radio, sub-mm, infrared, optical, ultraviolet and X-ray observations have been used to probe the relationship between the inflow and outflow around this accreting stellar-mass black hole with unprecedented detail. The results of this study deliver new information on the evolution of the accretion and ejection processes and how they are coupled, providing insight into how accretion powered jets are launched on all physical scales, including those from active galactic nuclei (AGN).

Modelling the multiwavelength spectrum during the outburst cycle reveals the physical evolution of the compact jet and of the accretion flow. The broadband modelling shows that the jet spectral break, which is the transition between optically thick and optically thin synchrotron emission, shifted by 3 orders of magnitude in frequency during the outburst, and did not appear to be set by any one specific property of the accretion flow. In particular, the results show that the frequency of the break did not scale with the X-ray luminosity or with the inner radius of the accretion disk and instead was possibly set by the same accretion properties that drive the X-ray hardness. The evolution of the jet spectral break indicates that the size of the region where the electrons are first accelerated into a power-law at the base of the jet decreased by $\sim 10^3$ gravitational radii as the outburst decayed. The modelling also implies that the high-energy cooling break in the jet was located in the optical band early in the outburst (between $\approx 3.2 \times 10^{14}$ and 4.5×10^{14} Hz). This is the first detection of the cooling break in an X-ray binary, enabling an accurate measurement of the total radiative power of the jet.

Optical observations were used to constrain the physical parameters of the system, demonstrating that while MAXI J1836−194 is a typical black hole low-mass X-ray binary, it has the most face-on disk confirmed to date, with an inclination between ≈4° and 15° to the line of sight. Radio observations show linear polarisation from the compact jet at a level of a few percent and an agreement between the electric vector position angle ($-21 \pm 4°$) and the observed jet axis ($-21 \pm 2°$). This alignment implies that the magnetic field of the jet lies perpendicular to the observed compact jet axis. Astrometric observations taken during the outburst indicate that the black hole likely required an asymmetric natal kick from a supernova explosion during formation to account for its high space velocity, making this system a rare case in which the black hole formation mechanism can be constrained. During the decay phase of the outburst, MAXI J1836−194 displays an unusually steep hard-state radio/X-ray correlation of $L_{\rm R} \propto L_{\rm X}^{1.8\pm0.08}$, where $L_{\rm R}$ and $L_{\rm X}$ denote the radio and X-ray luminosities. This steep correlation cannot be explained by models of X-ray emission processes, but can be explained in principle by Doppler boosting steepening the observed correlation.

Abbreviations and acronyms

The page number indicated represents where the abbreviation or acronym is first introduced.

Abbreviations and acronyms

AAVSO	American Association of Variable Star Observers (p.74)
ADAF	Advection dominated accretion flow (p.13)
ADIOS	Advection dominated inflow-outflow solutions (p.14)
AGN	Active Galactic Nuclei (p.5)
AIPS	Astronomical Image Processing System (p.95)
APASS	AAVSO Photometric All-Sky Survey data release 7 (p.74)
ATCA	Australia Telescope Compact Array (p.98)
ATNF	Australia Telescope National Facility (p.98)
AU	Astronomical units (p.20)
BAT	Burst Alert Telescope on board *Swift* (p.120)
CASA	Common Astronomy Software Application (p.92)
CCD	Charge-coupled device (p.49)
CDAF	Convection dominated accretion flow (p.14)
CVN	Chinese VLBI Network (p.104)
DEC.	Declination (p.74)
DiFX	Distributed FX software correlator (p.95)
e-VLBI	Electronic very long baseline interferometry (p.61)
EFOSC2	ESO Faint Object Spectrograph and Camera (p.73)
ESO	European Southern Observatory (p.71)
EVPA	Electric vector position angle (p.104)
EVN	European VLBI Network (p.104)
EW	Equivalent line width (p.78)
FFT	Fast-Fourier transform (p.58)

FORS2	FOcal Reducer and low dispersion Spectrograph (p.72)
FWHM	Full width at half maximum (p.58)
FWZI	Full width at zero intensity (p.79)
GSC	Gas Slit Camera (p.29)
HEASARC	High Energy Astrophysics Science Archive Research Center (p.69)
HID	Hardness intensity diagram (p.24)
HIMS	Hard intermediate state (p.24)
HMXB	High-mass X-ray binary (p.4)
IC	Inverse Compton (p.39)
IMBH	Intermediate-mass black hole (p.3)
IMXB	Intermediate-mass X-ray binary (p.4)
IR	Infrared (p.5)
IRAF	Image Reduction and Analysis Facility (p.72)
ISCO	Innermost stable circular orbit (p.11)
LMXB	Low-mass X-ray binary (p.1)
mag	Magnitude (p.65)
MAXI	Monitor of All-sky X-ray Image (p.29)
MDAF	Magnetically dominated accretion flow (p.14)
MIDAS	Munich Image Data Analysis System (p.72)
MJD	Modified Julian Date (p.72)
NASA	National Aeronautics and Space Administration (p.69)
NIR	Near-Infrared (p.71)
NTT	New Technology Telescope (p.71)
PC	Photon-counting (p.119)
PCA	RXTE Proportional Counter Array (p.98)
PCU	RXTE Proportional Counter Units (p.100)
PSF	Point spread function (p.65)
R.A.	Right ascension (p.74)
RFI	Radio frequency interference (p.54)
RM	Rotation measure (p.104)
rms	Root mean square (p.24)
RXTE	Rossi X-ray Timing Explorer (p.98)
SDSS	Sloan Digital Sky Survey (p.119)
SIMS	Soft intermediate state (p.24)
SMA	Submillimeter Array (p.118)
SMBH	Super massive black hole (p.3)
SNR	Signal-to-noise ratio (p.61)

SSC	Synchrotron self-Compton (p.40)
2MASS	Two Micron All Sky Survey (p.119)
UCAC	U.S. Naval Observatory CCD Astrograph Catalogue (p.74)
UT	Universal time (p.93)
UV	Ultraviolet (p.7)
UVOT	ultraviolet/Optical Telescope on board *Swift* (p.71)
VCS	VLBA Calibrator Survey (p.95)
VISIR	VLT Imager and Spectrometer for the mid-Infrared (p.68)
VLA	Karl G. Jansky Very Large Array (p.17)
VLBA	Very Long Baseline Array (p.19)
VLBI	Very long baseline interferometry (p.7)
VLT	Very Large Telescope (p.68)
WT	Windowed-timing (p.119)
XRT	X-ray Telescope on board *Swift* (p.76)
XSPEC	X-Ray Spectral Fitting Package (p.79)

Contents

Acknowledgements **vii**

Abstract **xi**

Abbreviations and acronyms **xiii**

List of Tables **xxiii**

List of Figures **xxv**

1 Introduction **1**

1.1 Black holes 1

1.1.1 Observations of black holes 3

1.2 Structure of this thesis 6

2 Characteristics of X-ray binaries **9**

2.1 Accretion flows 9

2.1.1 Accretion disks 10

2.1.2 The corona 12

2.1.3 Advective accretion flows 13

2.2 Jets 15

2.2.1 Observations of jets in X-ray binaries 16

2.3 The disk-jet connection 23

2.3.1 Accretion states 23

2.3.2 VLBI observations 26

2.3.3 The radio/X-ray correlation 27

2.4 A case study of MAXI J1836−194 29

3 Radiation processes **31**

3.1 Synchrotron radiation 31

3.1.1 Synchrotron self-absorption 34

3.1.2 Synchrotron cooling break 35

3.1.3 Synchrotron radiation from a compact jet 36

3.1.4 Polarisation of synchrotron emission 37

3.1.5 Relativistic beaming and Doppler boosting 38

3.2 Inverse Compton scattering 39

3.2.1 Synchrotron self-Compton radiation 40

3.2.2 The inverse Compton catastrophe 41

3.3 Thermal bremsstrahlung emission 41

3.3.1 Thermal bremsstrahlung absorption 43

3.4 Blackbody radiation 43

3.4.1 Blackbody emission from an accretion disk 45

4 Instrumentation and calibration **49**

4.1 Radio observations and calibration 51

4.1.1 Interferometry and aperture synthesis 51

4.1.2 Reduction and calibration 54

4.1.3 Imaging and deconvolution 55

4.1.4 Self-calibration 60

4.1.5 VLBI data reduction and calibration 61

4.2 Optical/infrared observations and calibration 64

4.2.1 Photometry 65

4.2.2 Optical spectroscopy 67

4.2.3 Infrared image reduction 67

4.3 X-ray observations 69

4.3.1 Spectral analysis and modelling 69

5 Constraining the system parameters of MAXI J1836−194 **71**

5.1 Observations and data reduction 72

5.1.1 VLT . . . 72
5.1.2 *Swift*/UVOT . . . 73
5.1.3 NTT . . . 73
5.2 Results . . . 74
5.2.1 Optical photometry . . . 74
5.2.2 Optical spectroscopy . . . 78
5.3 Analysis and Discussion . . . 81
5.3.1 Emission lines . . . 82
5.3.2 Inclination angle of the disk . . . 83
5.3.3 Donor star size and orbital period . . . 86
5.3.4 Black hole mass . . . 88
5.4 Summary . . . 88

6 Radio monitoring of the compact jets of MAXI J1836−194 91
6.1 Observations . . . 92
6.1.1 Radio observations . . . 92
6.1.2 X-ray observations . . . 98
6.2 Results . . . 100
6.2.1 Source evolution . . . 100
6.2.2 Polarisation of the radio jet . . . 102
6.2.3 VLBA radio morphology . . . 104
6.2.4 Astrometry . . . 107
6.3 Discussion . . . 109
6.3.1 The evolving compact jet . . . 109
6.3.2 Jet axis alignment . . . 112
6.3.3 Proper motion . . . 113
6.4 Summary . . . 115

7 Accretion-ejection coupling in MAXI J1836−194 117
7.1 . . . 118
7.1.1 VLA . . . 118
7.1.2 Submillimeter Array . . . 118

7.1.3 IR/Optical/UV . . . 118
7.1.4 X-ray . . . 119
7.2 Spectral Modelling . . . 120
7.2.1 Simultaneous multiwavelength observations . . . 120
7.3 . . . 122
7.3.1 Light curves and spectral evolution . . . 122
7.3.2 Source evolution . . . 123
7.3.3 High-energy cooling break . . . 129
7.3.4 X-ray synchrotron model . . . 132
7.4 Discussion . . . 133
7.4.1 Break frequency . . . 133
7.4.2 First acceleration zone . . . 136
7.4.3 Radiative jet luminosity . . . 137
7.4.4 Distance to the source . . . 140
7.5 Summary . . . 142

8 The radio/X-ray correlation in MAXI J1836−194 143
8.1 . . . 143
8.1.1 VLA . . . 143
8.1.2 ATCA . . . 144
8.1.3 RXTE . . . 144
8.1.4 *Swift*/XRT . . . 145
8.2 Results and discussion . . . 146
8.3 Summary . . . 151

9 Conclusions 153
9.1 Observational results . . . 153
9.2 Future work . . . 155

Bibliography 159

A Interstellar extinction and reddening 193

B Parameters of the first acceleration zone **195**

B.0.1 Magnetic field $B_{\rm F}$ 195

B.0.2 Radius $R_{\rm F}$ 197

C VLA flux densities of MAXI J1836−194 **199**

D Publications **205**

E Copyright permission **209**

List of Tables

5.1 Quiescent magnitude limits of MAXI J1836−194 77
5.2 Line profiles for the Balmer emission and absorption components . 79
5.3 Line positions and the calculated systemic velocity 80
5.4 Calculated outer disk radii and inclination angles for MAXI J1836−194 85
5.5 Companion mass, size and orbital period estimates 87

6.1 Sample of the VLA flux densities of MAXI J1836−194 93
6.2 Fits to the VLBA images of MAXI J1836−194 97
6.3 ATCA flux densities of MAXI J1836−194 99
6.4 VLBA positions of MAXI J1836−194 at 8.4 GHz 107

7.1 Best fitting spectral parameters for the broadband observations . 125
7.2 Parameters for an unbroken optically-thin synchrotron power-law 132

8.1 ATCA flux densities of the 2012 reflare 144

C.1 Complete VLA flux densities of MAXI J1836−194 200

List of Figures

1.1 Roche lobe geometry of a binary system 4
1.2 Simplistic view of an accretion disk 5

2.1 Typical LMXB X-ray spectrum during outburst 12
2.2 The two-sided radio jet from 1E1740.7−2942 17
2.3 Discrete ejecta from GRS 1915+105 18
2.4 The compact jet of Cygnus X−1 19
2.5 Typical observed spectrum of a compact jet 20
2.6 Jet spectral break frequency versus X-ray luminosity 21
2.7 Typical hardness-intensity diagram 25
2.8 The radio/X-ray correlation 28

3.1 Synchrotron emission from an electron with a pitch angle a 32
3.2 The synchrotron spectrum of a single electron 33
3.3 Synchrotron spectrum from a power-law distribution of electrons . 36
3.4 Multi-temperature blackbody spectrum 44
3.5 Spectrum of an accretion disk radiating as a blackbody 47

4.1 Propagation of an electromagnetic wave from a source 52
4.2 The dirty image 56
4.3 The dirty beam 57
4.4 The residual image 59
4.5 The CLEAN image 60

5.1 Optical images of MAXI J1836−194 in outburst and quiescence . 75
5.2 *Swift*/UVOT lightcurve of MAXI J1836−194 76
5.3 Outburst VLT spectra of MAXI J1836−194 78
5.4 Determining the companion star with stellar evolutionary models 86

6.1 VLA spectrum of MAXI J1836−194 and a nearby unrelated source 94
6.2 Radio and X-ray lightcurves of MAXI J1836−194 101
6.3 Hardness-intensity diagram of MAXI J1836−194 102
6.4 Polarisation parameters during the outburst 103
6.5 VLBA images of MAXI J1836−194 at 8.4 GHz and 2.3 GHz 106
6.6 The measured position as a function of time 109
6.7 Evolution of the radio spectral index and X-ray hardness 111
6.8 Flux and polarisation from a compact, partially self-absorbed jet . 113
6.9 Peculiar velocity as a function of source distance 115

7.1 Multiwavelength epochs 121
7.2 Multiwavelength lightcurves of MAXI J1836−194 123
7.3 Broadband radio to X-ray spectra of MAXI J1836−194 126
7.4 Evolution of MAXI J1836−194 during its outburst 127
7.5 Detecting the synchrotron cooling break 130
7.6 Break frequency vs. X-ray luminosity, including MAXI J1836−194 134
7.7 Spectral break frequency versus X-ray hardness 136
7.8 Evolution of the jet acceleration region 138
7.9 The fading and recovery of the compact jet 139
7.10 Estimating the source distance 141

8.1 The hard-state radio/X-ray correlation of MAXI J1836−194 . . . 147
8.2 Variable Doppler boosting of MAXI J1836−194 149
8.3 Doppler boosting the full sample of LMXBs 150

9.1 Probing the jet break with ALMA 156

Chapter 1

Introduction

Astrophysical jets are ubiquitous across the visible universe. There is a fundamental connection between the accretion inflow and jet outflow around accreting black holes (and other compact objects) on all physical scales. Understanding the nature of this relationship is critical to improving our understanding of the processes that occur around a black hole. This thesis uses low-mass X-ray binaries (LMXBs) to study the accretion-ejection connection in a single source as the accretion rate evolves during outburst, attempting to identify the contemporaneous changes that are occurring within the accretion flow and the jets, having implications for all accreting sources.

1.1 Black holes

Black holes are regions in space where the pull of gravity is so strong that even light cannot escape. Predicted by general relativity, black holes cannot be directly observed, and instead are inferred from the effects that they have on the surrounding region, or the heating of matter as it falls in towards the black hole.

The concept of an object so massive that light could not escape was known as early as 1784, when John Michell, using Newtons corpuscular theory of light (Newton, 1704), first recognised that a star's gravitational pull might be such that the escape velocity would exceed the speed of light (Michell, 1784). In 1795, mathematician Pierre-Simon Laplace suggested a similar concept where light could be trapped by an object of sufficiently large mass and small radius (Laplace, 1795). Very shortly after Albert Einstein published the theory of general relativity in 1915 (Einstein, 1915), Schwarzschild (1916) proved theoretically that a black hole like object could exist with his solution of Einstein's field equations

to describe the gravitational field surrounding a spherical mass. However, at the time it was not known that Schwarzschild's solutions contained a complete description of a spherical, non-rotating black hole of neutral charge. In the early 1930's, Chandrasekhar (1931) argued that special relativity demonstrates that a non-radiating body over a certain mass would collapse because there is nothing stopping it. Arthur Eddington disagreed with this concept, because it implied that the formation of black holes would be the inevitable fate of the evolution of massive stars (Eddington, 1935a,b). Eddington insisted that there should be a law of nature opposing a star collapsing in such a way. Then, in the late 1930's Robert Oppenheimer and Hartland Snyder calculated the collapse of a homogeneous sphere of pressure-less gas (Oppenheimer and Snyder, 1939), finding that the sphere would eventually be unable to communicate with the rest of the Universe. This was the first rigorous calculation of the formation of a black hole. Despite this, the concept of black holes was then largely ignored until the 1960's when the discovery of compact X-ray sources (Giacconi et al., 1962), quasars (Schmidt, 1963) and pulsars (Hewish et al., 1968) motivated an intensive theoretical study of black holes (Shapiro and Teukolsky, 1983). They were initially referred to as frozen stars since an outside observer would see the collapse rapidly slow down and become heavily redshifted near the Schwarzschild radius (r_s ; the radius around the black hole in which the escape velocity equals the speed of light) before freezing in time the instant that the star's surface crosses this radius. The term black hole was not used until 1964 by journalist Ann Ewing in an article reporting on a meeting of the American Association for the Advancement of Science. The term then became widely adopted in the late 1960's following a description by Wheeler (1968).

Defined as a region of spacetime that cannot communicate with the external universe, black holes are predicted to form in nature if a sufficient amount of mass accumulates in a region of space. As the mass grows, gravity will increasingly deform the space around it until the escape velocity equals the speed of light and nothing can escape. At this point, an event horizon is formed within which matter and energy must inevitably collapse on to a singularity. Having only three properties, mass, charge and spin, a black hole will continually accrete mass, in the form of gas and dust, from its surroundings.

In theory, black holes of any mass may exist and it is by this characteristic that they are categorised. *Stellar-mass black holes* are of order $10\,\mathrm{M}_\odot$ (typically 4–$15\,\mathrm{M}_\odot$, where $\mathrm{M}_\odot$ is the mass of the Sun; Kreidberg et al. 2012) and are thought to be formed by the gravitational collapse of an evolved, massive star, either

through a direct collapse or in a delayed formation when matter accretes onto a pre-existing neutron star (Fryer and Kalogera, 2001; Heger et al., 2003). Theoretically, black holes of mass less than a few solar masses may also exist, however, they can only be created if the matter is subjected to enormous pressures and temperatures from some source other than self-gravitation. The enormous pressures and temperatures required are thought to have existed in the moments after the Big Bang, and primordial black holes with masses smaller than that of the Sun may have been created (Shapiro and Teukolsky, 1985), but have never been observed. *Supermassive black holes* (SMBHs) reside at the centres of most large galaxies, including our own, and have masses of 10^5–$10^9\,M_\odot$. There are several theories describing the formation of a SMBH (e.g. Shapiro and Teukolsky, 1985; Lee, 1987; Haehnelt and Rees, 1993; Adams et al., 2001; Shibata and Shapiro, 2002; Volonteri et al., 2003; Begelman et al., 2006; Li et al., 2007) that include direct gravitational collapse of a dense cluster of stars, accretion of large amounts of mass onto a stellar-mass 'seed' black hole, or the merger of numerous stellar-mass black holes. Stellar-mass black holes and SMBHs have been observationally confirmed by their interaction with matter and space around them. Black holes in the mass range 10^2–$10^5\,M_\odot$ are called *Intermediate-mass black holes* (IMBHs): their existence has been predicted based on theoretical argument, but not observationally confirmed yet and there are very few candidate black holes of this class. It is proposed that IMBHs may form by the gravitational collapse of a superstar (e.g. Baumgarte and Shapiro, 1999; Shibata and Shapiro, 2002), the collapse of dense star clusters (e.g. Begelman and Rees, 1978; Shapiro and Teukolsky, 1985; Quinlan and Shapiro, 1990; Portegies Zwart et al., 2004), accretion onto a stellar-mass black hole (Li et al., 2007; Alvarez et al., 2009), or by the merger of many stellar-mass black holes (Lee, 1995; Taniguchi et al., 2000; Mouri and Taniguchi, 2002).

1.1.1 Observations of black holes

Due to their extreme gravity, black holes cannot be directly observed and their presence must be inferred by the effect that they have on their surroundings. One of the most notable effects is accretion, where gravitational potential energy is extracted from infalling material. The importance of accretion as a power source in astrophysical objects was first recognised in quasars by Salpeter (1964) and its importance in Galactic X-ray binary systems was first recognised in the mid-1960's (Shklovsky, 1967).

X-ray binaries are a class of double star system that comprise a compact object, either a stellar-mass black hole or neutron star, that is in orbit with a less-evolved companion star. At some stage in their binary stellar evolution, binary systems in a sufficiently close orbit may start to transfer matter. In X-ray binaries, this generally occurs in one of two ways that is dependent on the companion star. The companion can be any stellar object, from a brown dwarf to a main sequence star to a degenerate white dwarf, and X-ray binaries can be divided into classes based on the mass of the companion star: high-mass X-ray binaries (HMXBs), intermediate-mass X-ray binaries (IMXBs) and LMXBs. HMXBs generally contain a type O, B, or Wolf Rayet star, which typically belong to young stellar populations, have masses greater than $10\,M_\odot$ and lose mass through strong winds, some of which will then be gravitationally captured by the compact object. IMXBs have 2–$10\,M_\odot$ late B and A-type companion stars that are rarely observed due to short-lived high mass transfer rates and weak outflowing winds (Podsiadlowski and Rappaport, 2000). It is thought that many of the current LMXBs may have descended from systems with intermediate-mass donor stars (Podsiadlowski et al., 2002). The companion star in a LMXB system is usually a F-type or later star, which is usually less than $2\,M_\odot$; belongs to older stellar populations, and transfers mass primarily via Roche-lobe overflow.

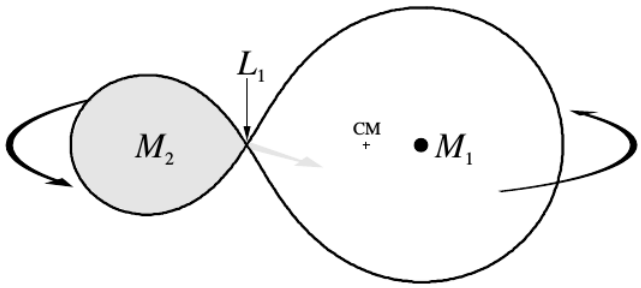

Figure 1.1: Roche lobe geometry of a binary system where a secondary star of mass M_2 is filling its Roche lobe and transferring mass through the inner Lagrangian point L_1 to the compact primary of mass M_1. CM is the centre of mass of the system. Figure from (Frank et al., 2002).

The Roche lobe is the region surrounding an object in a binary system within which orbiting matter is gravitationally bound. In a binary system the two lobes form an equipotential surface that joins at the inner Lagrangian point L_1 (see Figure 1.1). Mass transfer through this point occurs when the companion star fills its Roche lobe by either expanding due to stellar evolution, or a decrease in

the binary separation of the two objects (Shakura and Sunyaev, 1973). Matter reaching L_1 can then flow into the Roche lobe of the compact object (Pringle and Rees, 1972). The matter that passes through L_1 settles into a circular orbit around the black hole, at a radius determined by the conservation of angular momentum of the incoming gas (at L_1). Then, viscous friction causes this initial ring to spread into an accretion disk (Frank et al., 2002). As angular momentum is transported outwards, the gas inside the accretion disk spirals inwards towards the black hole in a succession of circular orbits (Figure 1.2), radiating away part of its gravitational energy. The accretion disk produces a multi-temperature thermal spectrum (Section 3.4) that peaks in the X-ray band (Frank et al., 2002). Non-thermal X-ray emission (Section 3.2) may also arise from a corona of highly-energetic plasma that surrounds the compact object (Bisnovatyi-Kogan and Blinnikov, 1977; Galeev et al., 1979; White and Holt, 1982).

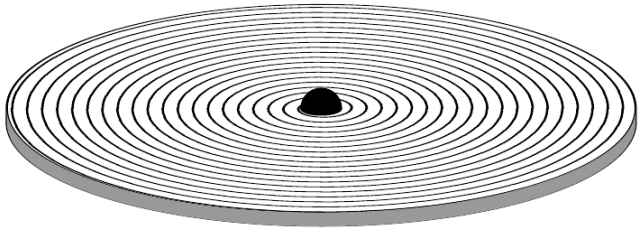

Figure 1.2: Simplistic view of an accretion disk with the in-falling matter spiralling inwards in a succession of circular orbits. Figure taken from Frank et al. (2002).

X-ray binary systems may occasionally go into outburst, where their observed properties change drastically. The outburst phase is due to an increased rate of accretion onto the compact object thought to be the consequence of either thermal disk instabilities changing the disk viscosity, allowing matter to move inwards, or increased mass transfer from the companion star (Frank et al., 2002).

Astrophysical jets are powerful, collimated outflows that may be accelerated from the inner regions of the inflow and are an ubiquitous feature of accretion onto black holes on all scales, from stellar-mass black holes in X-ray binaries to supermassive black holes in active galactic nuclei (AGN). Jets carry energy away from the system (Fender et al., 2003; Gallo et al., 2005) and emit non-thermal synchrotron emission (Section 3.1) that is observable in the radio to infrared (IR) band (Section 3.1.3), and (in some cases) up to the X-ray band (Pe'er and Markoff, 2012; Russell et al., 2013; Shahbaz et al., 2013). In X-ray binaries, jets

are observed in two distinct forms: a steady, compact jet, and a brighter, transient jet (e.g. Dhawan et al., 2000; Fender, 2006). During an outburst the jet properties change dramatically and it is thought that changes within the accretion flow are responsible for the contemporaneous changes in the jet behaviour (e.g. Fender et al., 2004).

While there is a clear relationship between the morphology and spectrum of the jets and the structure of the accretion flow, at present the causal sequence of events leading to the changes is poorly understood. However, X-ray binaries provide an ideal observational laboratory to study this relationship as they evolve through their distinct modes of accretion on timescales of weeks and months as opposed to the millions of years in AGN. This rapid evolution allows us to study the full range of accretion states in the same object on human timescales to investigate how jets are launched in accreting systems on all physical scales. This relationship has broader implications as well; quantifying the proportion of energy that the jets carry away from the accretion flow may be used to determine the rate at which black holes are able to grow and the roles that mass and spin play in jet launching. The feedback effect of jets from AGN is thought to heat the surrounding intracluster medium, counteracting cooling flows and affecting the evolution of galaxies and galaxy clusters, either triggering or suppressing star formation (e.g. Churazov et al., 2002; McNamara and Nulsen, 2007; Fabian, 2012). Findings from this project can also be used to test universal scaling relations between the accretion inflow and jet outflow (Heinz and Sunyaev, 2003; Merloni et al., 2003; Falcke et al., 2004; Plotkin et al., 2012), determining the applicability of the accretion-ejection relationship to the more massive black holes in AGN.

1.2 Structure of this thesis

In this thesis, results from a detailed study of the Galactic black hole candidate low mass X-ray binary MAXI J1836−194 are presented and analysed, coupling the process of accretion to the observed changes in the radio jet. High-cadence, simultaneous multiwavelength observations of the source during outburst are used to monitor the entire evolution of the system during its outburst in 2011. Chapter 2 provides a brief review of the accretion processes and jets from X-ray binaries. Chapter 3 describes the radiative processes at work in X-ray binaries. Chapter 4 gives a brief overview of the multiwavelength observing techniques used, including the theory of interferometry, as well as the fundamental principles of optical/IR

and X-ray calibration and data reduction. In Chapter 5, optical observations of the system during outburst and in quiescence are used to constrain the system parameters of MAXI J1836−194, estimating the size and mass of the companion star and the compact object, as well as a determining a number of the orbital parameters (such as the inclination and orbital period). Chapter 6 details intensive radio monitoring of the system during its 2011 outburst, revealing the evolution of the polarised radio jets and determining the alignment of the magnetic fields within the jet. High-resolution very long baseline interferometry (VLBI) observations are also used to directly resolve the compact jet and determine the motion of the system across the sky, from which the formation mechanism of the black hole can be constrained. Chapter 7 examines the complete multiwavelength radio, sub-millimetre, infrared, optical, ultraviolet (UV) and X-ray observations of the 2011 outburst. These simultaneous, broadband observations are modelled, tracking the physical changes in the jet and accretion flow to determine the interplay between the inflow and outflow. Chapter 8 examines the radio/X-ray correlation of MAXI J1836−194 during its 2011 outburst and 2012 reflare, presenting a model to describe the observed relationship. Conclusions and future work are presented in Chapter 9.

Chapter 2

Characteristics of X-ray binaries

2.1 Accretion flows

Despite the majority of stars being in binary systems, population synthesis models only predict of order a few thousand X-ray binary systems in the Milky Way (Dalton and Sarazin, 1995; Iben et al., 1995a,b); this number is relatively low due to the particular conditions required for accretion to occur (Illarionov and Sunyaev, 1975). For stable mass transfer, the two objects must be separate enough to not merge in a common envelope, yet close enough to allow mass to transfer between them. Since these parameters depend on many factors (Frank et al., 2002) including the mass of the objects, the orbital parameters of the system, as well as the evolutionary phase of the companion star, these conditions occur in relatively few systems. For systems in which it does occur, the gravitationally captured matter may flow onto the compact object in a number of ways. When radiative dissipation is efficient, matter forms a geometrically thin, Keplerian accretion disk. When it is inefficient, it forms a geometrically thick, hotter, advection-dominated flow.

There is a theoretical limit to the luminosity, referred to as the Eddington luminosity, $L_{\rm Edd}$. An object may only accrete matter as long as the inwards gravitational attraction is stronger than the outward radiation pressure produced by photons from the closer-in regions of the accretion flow. If the radiation pressure exceeds the inward gravitational attraction, then accretion would be halted as the infalling matter is dispersed. Considering a steady, spherically-

symmetric accretion flow the maximum luminosity, $L_{\rm Edd}$, is given by

$$L_{\rm Edd} = 4\pi G M m_{\rm p} {\rm c}/\sigma_{\rm T} \tag{2.1}$$

$$\cong 1.3 \times 10^{38} (M/{\rm M}_{\odot}) \ {\rm erg \ s^{-1}}, \tag{2.2}$$

where G is Newton's gravitational constant, M is the mass of the accreting object, $m_{\rm p}$ is the mass of the accelerating particle, c is the speed of light and $\sigma_{\rm T}$ is the Thomson cross-section of the photon-particle interaction. In the case of non-spherical accretion a source may appear super-Eddington.

For accretion onto a black hole, with no hard surface, much of the accretion energy could disappear into the hole and simply increase the mass, rather than be radiated. Therefore, the accretion luminosity needs to be parameterised by an efficiency, η, such that the accretion luminosity of an accretion disk $L_{\rm disk}$ around a black hole can be expressed as $L_{\rm disk} = \eta \dot{m} {\rm c}^2$, where $\dot{m}$ is the mass accretion rate. Correspondingly, the Eddington mass accretion rate can be defined as $\dot{m}_{\rm Edd} = L_{\rm Edd}/\eta {\rm c}^2$.

In X-ray binaries, the accretion of matter by the compact object from the companion star generally occurs in two different ways: Roche-lobe overflow (Section 1.1.1) or wind accretion. In the case of black hole LMXBs the accretion process is dominated by Roche-lobe overflow. However, wind accretion can play a significant role in some binaries (such as HMXBs where the donor is a massive early-type star e.g. Cyg X−1; Gies and Bolton e.g. 1986; Orosz et al. e.g. 2011), and a combination of the two accreting mechanisms may also occur.

2.1.1 Accretion disks

Provided that the separation between the two objects is sufficiently large, accreted matter is likely to have sufficient angular momentum that it is unable to fall directly onto the compact source and instead forms a differentially rotating disk (Pringle and Rees, 1972), the structure and radiation spectrum of which depends on the mass and size of the binary objects, as well as the rate of inflow at the external boundary (Shakura and Sunyaev, 1973). It is best described as a geometrically thin (where the local disk height H is much less than its radius R), optically thick disk of gas (Pringle and Rees, 1972; Shakura and Sunyaev, 1973; Novikov and Thorne, 1973; Lynden-Bell and Pringle, 1974) that is dominated by gas pressure or, in the inner regions, radiation pressure (recent work also suggests that magnetic pressure may also be important; e.g. Begelman et al. 2015). In the thin disk model, the angular velocity will have the Keplerian form

($\Omega_v(R) = (GM/R^3)^{1/2}$, where R is the radius) so that the circular velocity will be $u_\phi = R\Omega_v(R) \propto R^{-1/2}$ (Frank et al., 2002). Viscous torques between neighbouring annuli of matter slowly tap energy from the bulk orbital motion, transporting angular momentum outward (Pringle and Rees, 1972). This transport of angular momentum allows matter to slowly spiral inwards towards the compact source, releasing gravitational energy locally at a rate determined by the rate of viscous dissipation. Some of the liberated gravitational energy $E_{\rm g}$ increases the kinetic energy of rotation, with the rest being converted to thermal energy $E_{\rm th}$ that is radiated from the surface of the disk (virial theorem; $E_{\rm th} = -E_{\rm g}/2$). Due to the temperature of the disk, which can reach $\sim 10^7$ K near the black hole, the matter is radiating as a black body (see Section 3.4 for a description of black body radiation) and in a plasma state.

The main sources of energy in the disk are viscous heating and the interception and thermalisation of X-ray photons from regions close to the compact object (Shakura and Sunyaev, 1973; van Paradijs and McClintock, 1995; Frank et al., 2002). The latter generally dominates at large disk radii, where most of the optical/UV emission comes from. In the viscous-dominated part of the disk, the emitted spectrum is a multicolour blackbody with an effective temperature, $T_{\rm eff}$, scaling with radius, as, $T_{\rm eff}(R) \sim R^{-3/4}$ (Shakura and Sunyaev, 1973), while in the irradiation-dominated outer disk, $T_{\rm eff}(R) \sim R^{-1/2}$ (Frank et al., 2002), see Section 3.4.1 for further description of the blackbody spectrum. Typically, the external X-ray irradiation in the outer disk will form a temperature-inversion layer in the disk chromosphere; as a result emission and absorption lines can be observed from the accretion disk. For example, He II λ4686 and Hα are detected in emission, and higher lines of the Balmer series generally have narrow emission cores superposed on broader absorption formed in deeper layers (van Paradijs and McClintock, 1995).

In a black hole system during outburst, the inner edge of the accretion disk is thought to extend inwards, towards the black hole and towards the position of the most tightly bound stable orbit, referred to as the innermost stable circular orbit (ISCO; McClintock and Remillard, 2006). Once the inward spiralling matter reaches the ISCO, it plunges into the black hole without radiating a significant amount of energy between the ISCO and the event horizon.

This standard model of a geometrically thin, optically-thick accretion disk successfully reproduces the soft X-ray emission that is observed in accreting binaries (Figure 2.1). However, it cannot account for the non-thermal, hard X-rays that are observed from these systems.

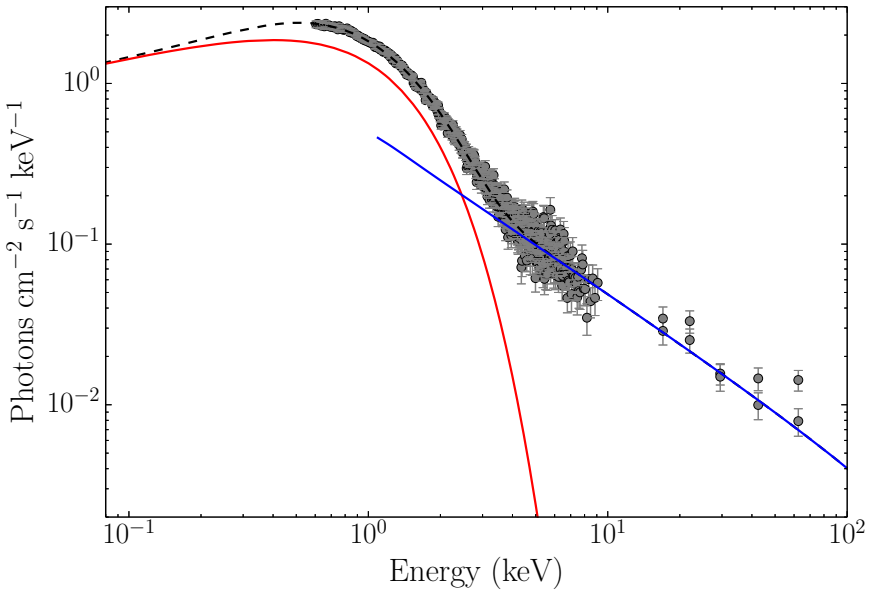

Figure 2.1: Typical LMXB X-ray spectrum during outburst. The data (grey points) are represented by a black body component from the soft X-ray emission (solid red line) and the non-thermal power-law component from the hard X-rays (solid blue line). While the soft X-rays are well described by the accretion disk model, there is a clear need for a power-law component to account for the hard X-rays.

2.1.2 The corona

It has been proposed that the high-energy X-ray emission in X-ray binaries can be explained by the inverse Compton scattering of soft photons by a corona of hot electrons (e.g. Shapiro and Lightman, 1976; Sunyaev and Titarchuk, 1980). This corona is thought to be made up of (quasi-)thermal electrons that have a mean energy of $kT_{\rm e} \sim 50 - 100\,{\rm keV}$ and is located close to the compact object, where most of the accretion energy is released. While not producing many photons themselves, coronal electrons will instead interact with a fraction of the photons emitted from the disk (e.g. Haardt and Maraschi, 1991, 1993), which will then gain energy through inverse Compton scattering and produce non-thermal, power-law emission (e.g. Walter and Courvoisier, 1992). See Section 3.2 for further details of inverse Compton scattering.

Following Poutanen (1998), there are a number of models commonly considered to describe the corona. Here, I will mention two physically motivated models. In the *sombrero* configuration, the accretion disk is truncated at a cer-

tain inner radius and the corona fills the regions closer to the compact object (Bisnovatyi-Kogan and Blinnikov, 1977; Poutanen et al., 1997). The outer radius of the corona is larger than the inner radius of the disk. It is thought that the mechanism in which the inner disk is truncated and the corona is formed could be due to the central regions of the X-ray binary system evaporating material from the inner accretion disk. In a *patchy* corona, magnetic fields in the inner disk may be amplified by turbulence and differential rotation such that they may emerge from the disk in the form of magnetic loop-like structures (Galeev et al., 1979; Haardt et al., 1994). These structures could lead to the formation of a hot, magnetically-confined corona, producing hard X-ray emission via inverse Compton or bremsstrahlung mechanisms (Gilfanov, 2010). It has also been proposed that the corona could be the base of the outflowing jet (e.g. Markoff et al., 2005).

While there is currently no consensus on the detailed geometry of this region, the typical size of the corona may be estimated from the variability timescale of the hard X-ray emission. If $t_{\rm min}$ is the shortest variability timescale, then the radius of the emitting region (i.e. the corona) cannot be larger than $R_{\rm corona} \lesssim ct_{\rm min}$. For Galactic black hole X-ray binaries, $t_{\rm min} \sim 1\,{\rm ms}$, corresponding to an emitting region of radius $\lesssim$300 km, which is $10r_{\rm s}$ for a $10\,{\rm M}_{\odot}$ black hole.

2.1.3 Advective accretion flows

At low accretion rates

When the accretion rate is $\sim$0.01–1 $\dot{m}_{\rm Edd}$, it is thought that the gas density is high enough that it can radiate efficiently and the thin disk model is a good approximation. However, at lower accretion rates the gas density may be sufficiently low that it is unable radiate energy efficiently. In this case, the energy generated by the viscosity will be advected inwards with the accretion flow and the disk will become hot, geometrically thick and radiatively inefficient. In an accreting black hole system, the in-falling matter will reach the inner disk boundary and fall into the black hole before all of its thermal energy has been radiated.

Initially proposed by Ichimaru (1977) and later developed by Narayan and Yi (1994) and Abramowicz et al. (1995), advection dominated accretion flows or ADAFs occur because the accretion rate is so much lower than the Eddington critical rate ($\dot{m}_{\rm crit}$) that the gas cannot cool (Frank et al., 2002). In this low density state, the Coulomb transfer (between the ions and electrons) is inefficient and the gas becomes a two temperature plasma. The ions are now at virial temperature and contain most of the viscous energy. By contrast the electrons

are able to radiate efficiently and, as a result, are much cooler than the ions. The accretion flow will then become a nearly spherical flow with sub-Keplerian rotation. ADAFs are therefore spherical, not disk-like at all, with part of the viscously-released energy being advected with the accreting gas.

It has been suggested that accretion onto a black hole may actually consist of two zones: an outer thin disk and an inner ADAF (Narayan et al., 1996, 1997; Esin et al., 1997). At the lowest accretion rates the thin accretion disk is truncated at a relatively large transition radius and the accretion flow has switched to an ADAF. The radius of the transition from the disk to ADAF is likely to be related to the angular momentum of the material flowing from the companion star (Esin et al., 1997). For $\dot{m}$ up to $\dot{m}_{\rm crit}$ the geometry of this flow remains similar, although as the radiative efficiency of the flow increases it will become quite luminous (Esin et al., 1997). When $\dot{m} \geq \dot{m}_{\rm crit}$, the hot ADAF zone radiates too efficiently to remain advection dominated, resulting in a shrinking ADAF size and the inner edge of the thin accretion disk moving to smaller radii. As this continues, the central ADAF zone almost entirely disappears with the remnants being confined to a low-density corona above the thin disk, while the inner edge of the thin disk moves down to the ISCO.

In the ADAF model, a significant fraction of the accretion energy is advected through the event horizon of the black hole. However, alternative models where the accretion flow is under-luminous due to very low net accretion rates exist, such as the advection dominated inflow-outflow solutions (ADIOS; Blandford and Begelman 1999), convection dominated accretion flows (CDAFs; Quataert and Gruzinov 2000) and magnetically dominated accretion flows (MDAFs; Meier 2005), in which this may not be the case. Proposed by Blandford and Begelman (1999), in the ADIOS scenario only a small fraction of the gas actually accretes onto the black hole and the binding energy it releases is transported radially outward, which may drive away the remainder in the form of a wind. This mass loss implies that the accretion rate onto the black hole is much lower than the rate at which matter is supplied, leading to a much lower luminosity than a standard accretion flow. In CDAFs, it is proposed that a significant fraction of the energy is transported outwards by convection. In the MDAF model, the outer region of the disk is geometrically thin and optically thick, while in the inner regions the inflow is extremely inefficient as magnetic forces dominate over thermal and radiation forces.

At high accretion rates

It is possible to have gas accreting at super-Eddington accretion rates, i.e. when $\dot{m} > \dot{m}_{\rm Edd}$, that may still radiate with low efficiency, such that luminosity $L \lesssim L_{\rm Edd}$. In this class of radiatively inefficient accretion flows, the radiation produced is thought to be trapped by the optically thick flow and pulled into the black hole with the gas as the accretion timescales are much shorter than the radiation timescales.

Abramowicz et al. (1988) propose a *slim disk* model for radiatively inefficient flows with moderately super-Eddington accretion rates. In this model, the accretion disk is optically thick and geometrically slim (with a disk height comparable to the radius). The accretion flow is stabilised by advection of heat into the black hole (Abramowicz et al., 1988). The slim disk model accounts for advective cooling and does not impose Keplerian angular momentum; therefore, it can be applied to disks at any accretion rate. At high accretion rates a large fraction of the viscosity-generated heat is advected inward and released closer to the black hole or not released at all, and radiation may even be emitted from within the ISCO. As the advection rate increases, the radiative efficiency decreases with increasing accretion rate.

2.2 Jets

Jets, or collimated outflows, that are accelerated from the inner regions of the accretion flow are amongst the most energetic phenomena in the universe. They can carry away a significant fraction of the available accretion power in collimated flows, eventually heating the surrounding medium. The launching and collimation mechanisms behind relativistic jets remain an unsolved astrophysical problem. Observable at radio to infrared frequencies, as well as (in a few cases) optical (Han and Hjellming, 1992; Kanbach et al., 2001; Fender, 2001; Corbel et al., 2001; Uemura et al., 2004; Russell and Fender, 2010), ultraviolet (Curran et al., 2010) and even X-ray wavelengths (Pe'er and Markoff, 2012; Russell et al., 2013; Shahbaz et al., 2013), jets emit energy primarily via synchrotron radiation, where relativistic electrons spiral around magnetic field lines, or via inverse Compton processes (see Sections 3.1 and 3.2 for further details of synchrotron and inverse Compton emission, respectively). While it is believed that the formation and collimation of jets involves magnetic fields, it is not well understood how they are launched and collimated. Also, while it is clear that electrons or positrons

are responsible for most of the observed jet emission, the overall composition (baryonic or leptonic) of the jets is unclear. Several mechanisms (as outlined below) have been proposed for the launching of outflows from around accreting black holes.

Blandford and Znajek (1977) proposed a model where the jets are powered by the rotation of the ergosphere as the black hole spins. An accretion disk will carry matter towards the black hole so that the density of the accreting matter will rise sharply close to the event horizon, and matter that has magnetised over time will create strong magnetic field lines in this region. As the accreted material is swallowed by the black hole the magnetic field lines remain, threaded through the event horizon. The rotation of space-time will twist the field lines in this region, accelerating charged plasma along the axis of rotation, giving rise to a Poynting flux jet that dissipates at large distances. However, this model requires the presence of a black hole, and cannot be applied to other accreting objects (such as neutron stars).

Blandford and Payne (1982) instead proposed that jets may be accelerated by strong magnetic fields held in a differentially rotating accretion disk. Energy and angular momentum are removed magnetically from the accretion disk by field lines that leave the disk and extend to large distances. Due to the magnetic energy density being larger than the thermal and kinetic energies above the disk, disk coronal material is accelerated upward and outward along the co-rotating field lines as they try to uncoil. Acceleration stops at the point where the kinetic energy density becomes comparable to the magnetic energy density but collimation will continue (Livio et al., 1999). The tension in the field lines allows the toroidal component of the field to collimate the flow into a pair of anti-parallel jets that point perpendicular to the plane of the disk (Blandford and Payne, 1982). This model launches the jet from the accretion disk and, therefore, does not require a black hole and can be valid for any disk system.

2.2.1 Observations of jets in X-ray binaries

Galactic X-ray binaries were among the first objects detected when the first space-based X-ray missions were launched (e.g. Sco X−1; Giacconi et al. 1962). While they were known to be strong non-thermal emitters, it wasn't until Margon et al. (1979) detected large periodic Doppler shifts in the optical spectrum of SS 433 that a Galactic jet source was first discovered. The observed Doppler shifts were interpreted as two oppositely-directed precessing jets of collimated matter moving

with a velocity of 0.26c (Fabian and Rees, 1979; Abell and Margon, 1979; Milgrom, 1979), which was later confirmed (Spencer, 1979) and subsequently resolved (Hjellming and Johnston, 1981) with high angular resolution radio observations.

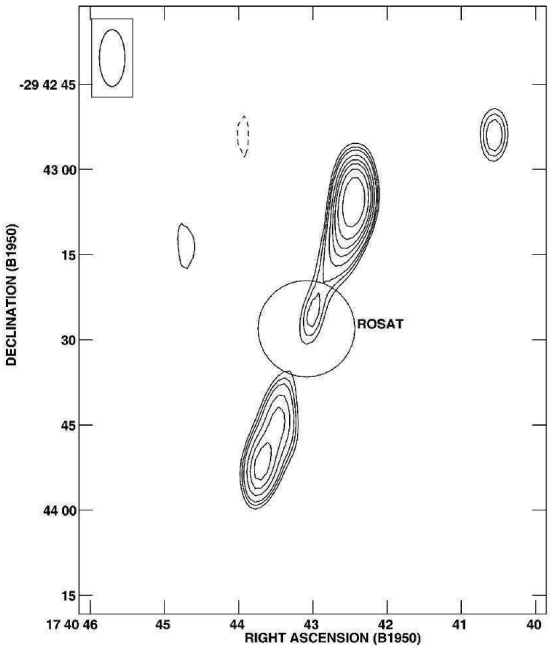

Figure 2.2: Very Large Array (VLA) radio contour map of the radio counterpart of 1E1740.7−2942 at 5 GHz (Mirabel et al., 1992; Mirabel and Rodríguez, 1999). The beamsize is shown in the top left corner. Contours are -4, 4, 5, 6, 8, 10, 12, 15, and 20 times 28 μJy beam^{-1}. The X-ray position and error circle from Heindl et al. (1994), is shown.

Although radio emission from outbursts of X-ray transients had previously been observed (e.g. A0620−00; Owen et al. 1976), due to its resolved radio jet SS 433 was thought to be a rare object within the Milky Way for more than a decade and, with its relatively low jet speed, its relation to quasars was not clear. It wasn't until radio observations of X-ray and gamma-ray sources in the region of the Galactic centre in the early 1990's that the relation between Galactic jet sources and quasars was proposed. Radio and X-ray observations of 1E 1740.7−2942 (Figure 2.2; Mirabel et al. 1992) and GRS 1758−258 (Rodriguez et al., 1992) showed these two objects both consist of a compact X-ray component located at the centre of a bright two-sided jet that terminates with extended lobes that showed no significant radio flux variation, strikingly similar to distant radio galaxies. Shortly after, it was shown that jets from X-ray binaries can be significantly relativistic when apparent superluminal motions were detected

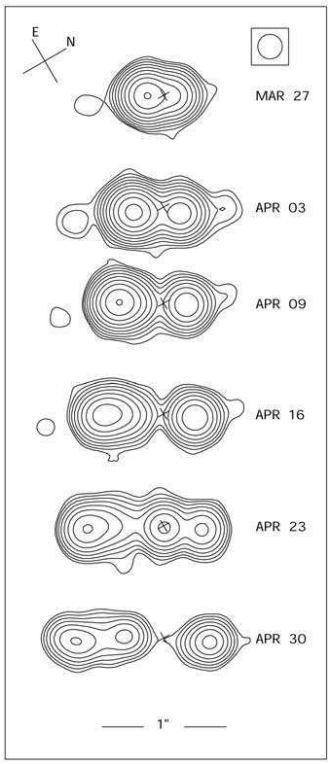

Figure 2.3: 8.4 GHz VLA image of discrete ejecta moving away with time from the core of GRS 1915+105, showing apparent superluminal motion. The beamsize is in the top right. Contours are 1, 2, 4, 8, 16, 32, 64, 128, 256, 512, and 1024 times 0.2 mJy beam^{-1} for all epochs shown, except 27 March, where contour levels are multiples of 0.6 mJy beam^{-1}. Figure from Mirabel and Rodríguez (1994).

in the outflows of the Galactic sources GRS 1915+105 (Figure 2.3; Mirabel and Rodríguez 1994) and GRO J1655−40 (Tingay et al., 1995; Hjellming and Rupen, 1995) with high-resolution VLBI images, confirming the analogy between these Galactic objects and quasars. Termed microquasars[1] (Mirabel et al., 1992; Mirabel and Rodríguez, 1998), these objects are Galactic stellar-mass black holes that mimic many of the phenomena observed in quasars, just on much smaller scales; phenomena that include synchrotron emission from highly energetic jets of collimated material and thermal X-ray emission from an accretion disk heated by viscous dissipation that surrounds a black hole. Since then, extensive monitoring of X-ray binaries has been conducted over the last two decades and more than

[1]The term 'microquasar' was first used to describe a Galactic source by Fomalont and Geldzahler (1991), describing the possible radio lobes of Scorpius X−1 (which were in fact background sources).

300 X-ray binaries have been observed. Through multiwavelength monitoring, jets have been detected in many of these systems.

Despite the extensive monitoring of jet sources, it still remains unclear whether the jets are composed of electron/positron pairs or an electron/proton mix (but see Margon et al., 1979; Kotani et al., 1994; Díaz Trigo et al., 2013, for evidence favouring baryonic jets in SS 433 and 4U 1630−47). However, electrons are responsible for most of the observed jet radiation through either synchrotron or inverse Compton processes. The non-thermal emission from the jets is characterised by high ($> 10^7$ K) brightness temperatures. Jets can carry away a significant fraction of the available accretion power in collimated flows (Fender et al., 2003), eventually heating the surrounding medium (Corbel et al., 2002; Heinz et al., 2008).

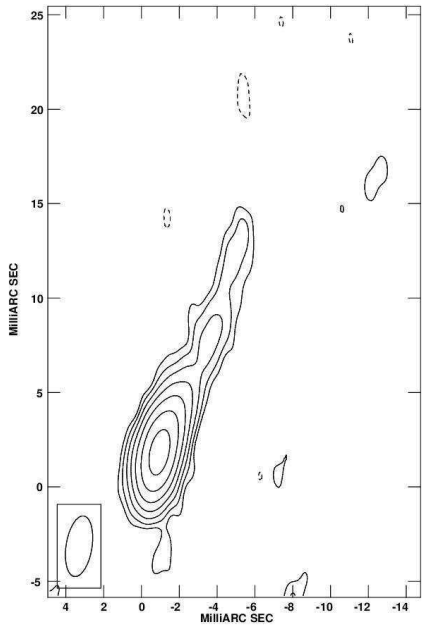

Figure 2.4: Very Long Baseline Array (VLBA) and phased VLA image of the compact jet of Cygnus X−1 at 8.4 GHz, showing the ∼20 AU extension of the compact jet (Stirling et al., 2001). This system is located 1.86 kpc from Earth (Reid et al., 2011). The beamsize is shown in the bottom left corner. The peak flux density is 9.0 mJy beam^{-1} and the lowest contour is 0.1 mJy (contour lines represent a factor of 2).

Jet morphology

X-ray binaries generally produce a persistent, compact jet that becomes progressively more transparent at lower frequencies as the particles travel away from the jet base. Compact jets are thought to be mildly relativistic, with bulk Lorentz factors of $\Gamma \leq 2$ (Fender et al., 2004). They have only been spatially resolved in two black hole LMXBs, GRS 1915+105 (Dhawan et al., 2000) and Cygnus X−1 (Stirling et al., 2001, see Figure 2.4), showing characteristic sizes of order a few tens of astronomical units (AU). At times of increased accretion, a brighter transient jet may be observed, characterised by rapidly varying flux from discrete ejections of synchrotron emitting plasma travelling with bulk velocities close to the speed of light. The ejecta may travel several thousand AU away from the radio core (e.g. as shown by the radio image of the transient jet of GRS 1915+105, Figure 2.3).

The jet spectrum

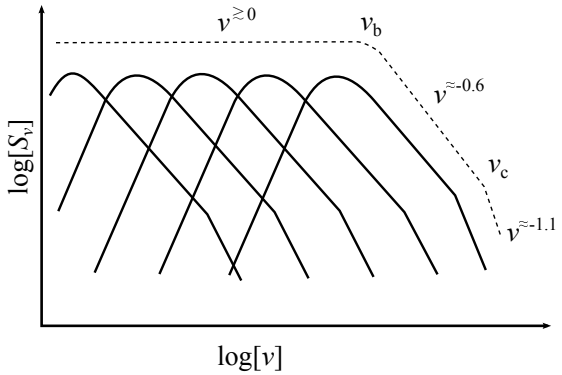

Figure 2.5: Typical spectrum of a compact jet, resulting from overlapping self-absorbed synchrotron contributions. ν_b is the break from optically-thick to optically-thin synchrotron emission and ν_c is the synchrotron cooling break. Also shown are typical spectral index values for each region. See Section 3.1.3 for full details.

While the transient jet shows a rapid evolution to an optically-thin radio spectrum ($\alpha \sim -0.6$, where α is the spectral index, derived from the observed flux density S_ν and observing frequency ν such that $S_\nu \propto \nu^\alpha$; Fender 2001), the steady compact jet produces a flat or inverted radio spectrum ($\alpha \gtrsim 0$). This spectrum is explained by partially self-absorbed synchrotron emission (Figure 2.5 and Section 3.1.3) from electron populations at different distances along the jet

and extends up to a frequency above which the jet is no longer self-absorbed. At this frequency the optically-thick synchrotron jet spectrum breaks to an optically-thin spectrum, where $\alpha \approx -0.6$ (e.g. Russell et al., 2013). The spectral break (Figure 2.5) corresponds to the most compact region in the jet where the electrons are first accelerated from a thermal to a power-law distribution (Markoff et al., 2001, 2005), potentially via diffusive shock acceleration (e.g. Bell, 1978; Drury, 1983) though the exact mechanism is not yet known. Typically seen at GHz frequencies in AGN (e.g. Ho, 1999) and the IR band in LMXBs (e.g. Corbel and Fender, 2002; Gandhi et al., 2011; Russell et al., 2013), the frequency at which the break occurs, $\nu_{\rm b}$, is related to the offset distance from the central black hole at which the acceleration occurs and has been found to lie in the range of 10–1000 $r_{\rm g}$ (where $r_{\rm g} = GM/c^2$ is the gravitational radius) from the central black hole for brighter hard states (Markoff et al., 2001, 2003, 2005; Migliari et al., 2007; Gallo et al., 2007; Markoff et al., 2008; Maitra et al., 2009).

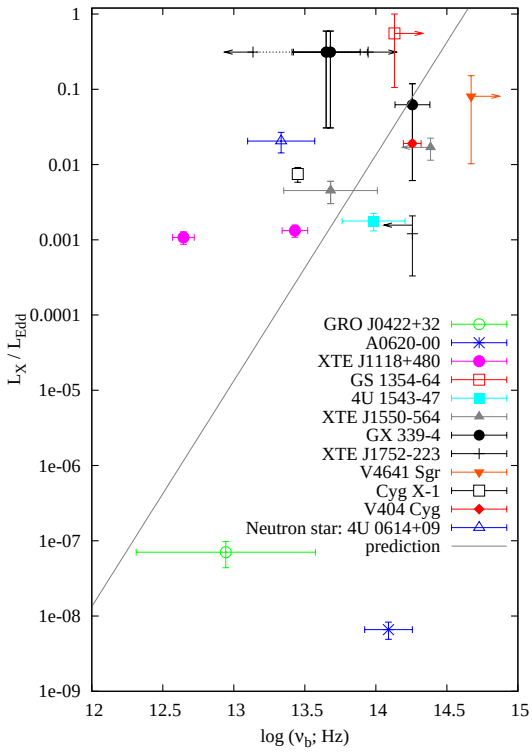

Figure 2.6: Jet break frequency versus X-ray luminosity as a fraction of Eddington luminosity. Shown are the measured break frequencies for both black holes and neutron stars. The grey line represents the predicted $\nu_{\rm b} \propto L_{\rm X}^{1/3}$ relationship. Figure from Russell et al. (2013).

The break frequency has been seen to vary between sources (Figure 2.6; Russell et al. 2013) and observations of GX 339−4 during outburst in 2012 suggest that the spectral break also varies with time (Gandhi et al., 2011). Standard jet theory predicts, in all steady jets from LMXB or AGN, a positive correlation between $\nu_{\rm b}$ and the source luminosity, if the break is associated with the same scale (i.e. distance normalised to $r_{\rm g}$) of the jet at all times (Falcke and Biermann, 1995; Markoff et al., 2003; Heinz and Sunyaev, 2003; Falcke et al., 2004). Assuming that a constant fraction of the accretion power is channelled into the jets (Falcke and Biermann, 1995), the frequency of the spectral break is expected to scale with the mass accretion rate as $\nu_{\rm b} \propto \dot{m}^{2/3}$. For the radiatively inefficient hard state (Heinz and Sunyaev, 2003) the X-ray luminosity $L_{\rm X} \propto \dot{m}^2$, thus predicting a relation $\nu_{\rm b} \propto L_{\rm X}^{1/3}$ (Figure 2.6; Russell et al. 2013). While it is unknown how the jet break frequency varies during outburst, constraining if and how it changes can provide essential constraints on jet parameters, such as the cross-sectional radius $R_{\rm F}$ and magnetic field $B_{\rm F}$ of the region where the electrons are first accelerated up into a power-law (Rybicki and Lightman, 1979; Casella and Pe'er, 2009; Chaty et al., 2011). Despite its importance, $\nu_{\rm b}$ has been observed in relatively few systems due to the lack of simultaneous multiwavelength monitoring at frequencies close to $\nu_{\rm b}$, specifically in the sub-mm and mid-IR parts of the spectrum, and because the companion star or accretion disk may dominate the jet emission at the expected break frequency (Gallo et al., 2007; Migliari et al., 2007; Rahoui et al., 2011; Russell et al., 2013). Therefore, multiwavelength observations of X-ray binaries during outburst are essential to monitor the evolution of $\nu_{\rm b}$ to understand and model how jets are produced and how they may evolve with the accretion flow.

At higher frequencies (above $\nu_{\rm b}$) a further break can occur in the jet spectrum (Figure 2.5; to a slope steeper by $\Delta\alpha = 0.5$ than the optically-thin synchrotron emission) due to the highest-energy electrons losing a significant fraction of their energy through radiation on timescales that are faster than the dynamical time scale of the source (Sari et al., 1998), see Section 3.1.2. This cooling break ($\nu_{\rm c}$; observed to evolve with time from the X-ray to the optical band in Gamma ray bursts, Sari et al. 1998; Galama et al. 1998), has been suggested to shift from UV energies during low accretion states in LMXBs to X-ray energies during high accretion states (Pe'er and Markoff, 2012; Russell et al., 2013). However, the evolution of $\nu_{\rm c}$ may also be dependent on other factors, such as the magnetic field (Plotkin et al., 2013), and is generally thought to be buried beneath emission from the accretion disk or companion star.

Polarisation

Synchrotron theory predicts linear polarisation (LP) at levels of up to ∼10% for optically-thick synchrotron emission and up to ∼72% for optically-thin synchrotron emission in the presence of an ordered magnetic field (Pacholczyk and Swihart, 1967; Scheuer and Williams, 1968; Rybicki and Lightman, 1979; Longair, 2011), see Section 3.1.4 for further details. However, these levels are rarely observed in LMXBs (e.g. Fender, 2003), because the magnetic field may not necessarily be ordered, there may be multiple polarised components with different polarisation angles within the jet (Stirling et al. 2004), or there could be spatially dependent Faraday rotation (see Brocksopp et al. 2013 for further discussion). However, fractional polarisations of $\sim$ 50% have been seen in a few cases (see Brocksopp et al., 2013; Curran et al., 2014). When detected, linear polarisation can be used to infer properties of the magnetic fields within the jet and surrounding medium. However, Linear polarisation is often not reported, even as upper limits, so the majority of LMXBs have no constraints.

2.3 The disk-jet connection

X-ray binaries provide unique insights into the behaviour of accretion flows and jets. However, while clear patterns of behaviour have been observed, the detailed interplay between the changes in the inflow during an outburst and the outflow remains unclear. Therefore, studying the accretion and the ejection, as well as the connection between the two, is of paramount importance to both our understanding of these systems and our understanding of jet launching from accretion flows on all physical scales. This section provides a brief summary of LMXB outbursts and spectral states (see e.g. Fender et al., 2004; Belloni et al., 2005; Homan and Belloni, 2005; Remillard and McClintock, 2006; Fender, 2006; Fender et al., 2009; Belloni et al., 2011, for a full review of outburst phenomenology and X-ray spectral states).

2.3.1 Accretion states

X-ray binaries display various modes of accretion that can be categorised into canonical states according to their spectral hardness (defined as a ratio of observed counts in two X-ray energy bands, which can be a crude measure of the dominant X-ray emitting mechanism, the accretion disk or corona). Transitions

between these accretion modes are associated with dramatic changes in the structure and power of the jets. Accretion states are best studied in the X-ray band and exhibit reproducible behaviour that traces out a characteristic locus in a hardness intensity diagram (HID; Figure 2.7). Observing LMXBs as they evolve through the various modes of accretion provides an unprecedented insight into the processes responsible for the jet launching.

X-ray binaries spend the majority of their life times in a low-luminosity hard or quiescent state (shown in Figure 2.7 as the bottom right corner of the q-shaped path). In the canonical model, in this state the X-ray spectrum is dominated by a hard, non-thermal, broadband power-law component, with an X-ray photon index of $\gtrsim$1.5 (Plotkin et al., 2013), plus a weak thermal blackbody component originating from a truncated accretion disk, with the central regions of the inflow being composed of a geometrically-thick, optically-thin, radiatively-inefficient accretion flow (Narayan and Yi, 1995), see Section 2.1.3. This X-ray state is associated with a steady, self-absorbed, compact jet (Dhawan et al., 2000; Corbel et al., 2000; Stirling et al., 2001), and optical emission that is dominated by the companion star (White et al., 1995).

During the initial rise of a typical outburst, while remaining the hard state, both the radio and X-ray luminosities increase considerably, meaning the source will trace a path upwards along the right hand vertical line in Figure 2.7. This canonical hard state is characterised by an X-ray photon index of $\sim$1.5 (e.g. Remillard and McClintock, 2006) and the continued presence of the compact jet. The source may then enter, and transit through the hard intermediate state (HIMS) and soft intermediate state (SIMS), distinguished by the increasing photon index and a decreasing fractional root mean square (rms) X-ray variability. As the source softens during this transition (moving left in Figure 2.7), the compact radio jet persists. As this evolution progresses, the accretion rate increases and a geometrically-thin disk extends further in towards the central compact object. Soft X-rays from the inner accretion disk begin to dominate as the source approaches a full soft state, where the jet properties change drastically. The transition to the full soft state yields dramatic changes to the jet emission with the launching of discrete, bright, relativistically-moving knots of emission (Corbel et al., 2004; Fender et al., 2004). The compact jet switches off and radio flaring occurs, which is thought to be the result of the faster, more recently ejected jet colliding with the pre-existing, slower-moving flow, giving rise to internal shocks within the jet (Jamil et al., 2010). The X-ray spectrum is now dominated by soft, thermal, blackbody radiation with temperature $kT \lesssim 1\,\mathrm{keV}$ originating from a

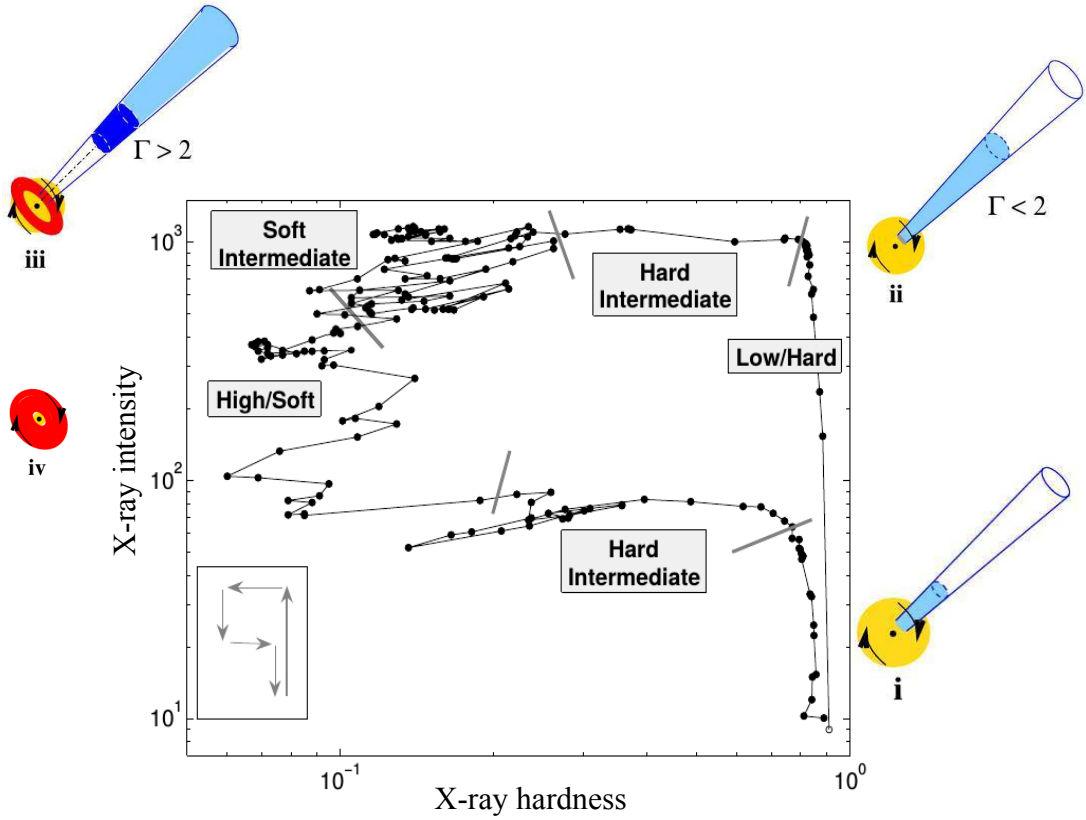

Figure 2.7: A typical hardness-intensity diagram, which is a plot of total X-ray intensity versus X-ray hardness (where the hardness is a proxy for the dominant X-ray emission component). The central box is the HID of the 2002/2003 outburst of GX 339−4 (Belloni et al., 2005), the grey lines mark the transitions between the states described in the grey boxes (Belloni, 2005). The inset on the lower left shows the idealised 'q-shaped' nature of the evolution. X-ray hardness increases to the right(i.e. the power law dominates over the disc emission) and intensity increases upwards. The outer images illustrate the relative contributions of the jet (blue), corona (yellow) and the accretion disk (red) at the stages of (i) quiescence, (ii) increased luminosity while still remaining in the hard state, (iii) internal shock in the jet due to discrete ejecta and (iv) the quenching of the jet in the disk-dominated soft state (Fender et al., 2004). Figure adapted from Fender et al. (2004), Belloni et al. (2005) and Belloni (2005).

geometrically thin, optically thick accretion disk that extends down to the ISCO, as well as a weak, steep power-law component (Fender et al., 2004), with an X-ray photon index of ∼2.5 (Remillard and McClintock, 2006). The source may then enter the high/soft state where the radio emission is quenched by at least

2.5 orders of magnitude (Fender et al., 1999; Coriat et al., 2011; Russell et al., 2011), implying that the jets are prevented from being launched in this state. The quenching of the radio emission could be due to the spectral break moving through the radio band from higher to lower frequencies before returning in the reverse transition. In such a high accretion rate regime the central X-ray source may illuminate the outer disk, heating it and increasing thermal pressure that may drive a wind capable of reducing the local accretion rate and carrying away enough mass and energy to quench the compact jet (Neilsen and Lee, 2009; Ponti et al., 2012). X-ray binaries may oscillate back and forth between the soft state and the very high/intermediate states producing flares at each hard-to-soft transition and re-forming the compact jet at each soft-to-hard transition (Fender et al., 2004).

At the end of the outburst, the X-ray luminosity decreases significantly and the source makes a reverse transition back through the intermediate states into the hard state. During the transition the compact jet is gradually re-established, being detected first in the radio and then in the optical/IR band (Miller-Jones et al., 2012; Corbel et al., 2013; Kalemci et al., 2013). The gradual jet recovery may be due to an evolution of the jet power over the course of the outburst, as shown by the movement of the jet spectral break to higher frequencies during the outburst decay (Corbel et al., 2013).

During an outburst, it is thought that most of the optical and UV light arises in the outer accretion disk as a result of X-ray reprocessing (Cunningham, 1976; Vrtilek et al., 1990; van Paradijs and McClintock, 1995, see Section 3.4.1). However, from spectral (Han and Hjellming, 1992; Fender, 2001; Corbel et al., 2001; Brocksopp et al., 2002; Markoff et al., 2003; Russell and Fender, 2010; Curran et al., 2010) and timing (Kanbach et al., 2001; Uemura et al., 2004) studies, it has been shown that in some cases this light may contain significant (or even dominant) contributions from other processes, such as the jet, which may extend into the optical/UV band and beyond.

2.3.2 VLBI observations

High resolution, VLBI observations (see Section 4.1.1, for an overview of interferometry and VLBI) can reveal information about the properties of the system. These observations can constrain key source parameters and probe a range of fundamental physics including the driving mechanism responsible for jet launching, as well as black hole formation and the existence of event horizons. Directly

imaging the jet can determine the orientation of the jet axis, and the bulk motion and structure of the jet, which can then be coupled to the changing accretion flow. High-cadence observations of the discrete ejecta as the system moves into the soft state can determine the proper motions of the ejected material. Extrapolating backwards in time, the moment of launching may then be coupled to changes within the accretion flow to identify the mechanisms responsible for the launching of the ejecta (Miller-Jones et al., 2012). While discrete ejecta have been observed in a number of systems in outburst (e.g. Mirabel and Rodríguez, 1994; Tingay et al., 1995; Hjellming and Rupen, 1995; Fender et al., 1999), the hard state compact jet has only been spatially resolved in two systems, GRS 1915+105 (Dhawan et al., 2000) and Cygnus X−1 (Stirling et al., 2001), both of which are not typical LMXBs (i.e. GRS 1915+105 has remained in a persistent state of outburst since its discovery in 1992 and Cygnus X−1 is partially wind-fed). Accurate source distances D are crucial to constrain the physical parameters of the binary system, such as the luminosity of the hotspot (in quiescence; Froning et al. 2011), disk inclination, donor star size (and type), binary orbital period, and mass of the compact object (see Chapter 5.3.4). With accurate source parameters, the spin of the black hole can be well constrained by fitting relativistic accretion disk models to the X-ray spectra (McClintock et al., 2014), providing information on whether the jets are powered by the spin of the black hole. Astrometric observations of a system over time may also allow for the proper motion of the system to be calculated, which, in conjunction with multiwavelength observations, can then be used to constrain the formation mechanism of black holes (Miller-Jones, 2014). Accurate distance measurements are required to precisely determine the source luminosity, which in quiescence can be used to probe the existence of black hole event horizons (Garcia et al., 2001). Supported by the under-luminous nature of black hole X-ray binaries (when compared to their neutron star counterparts with similar orbital periods (e.g. Narayan et al., 1997; Menou et al., 1999), it is thought that a significant fraction of the accretion energy is directly advected through the event horizon (however, alternative scenarios such as emission from the corona; Bildsten and Rutledge 2000, or energy being channelled into the jets; Fender et al. 2003, are possible).

2.3.3 The radio/X-ray correlation

While the processes that are responsible for launching the jets are poorly understood, there exists a well-studied relationship between the radio $L_{\rm R}$ and X-ray

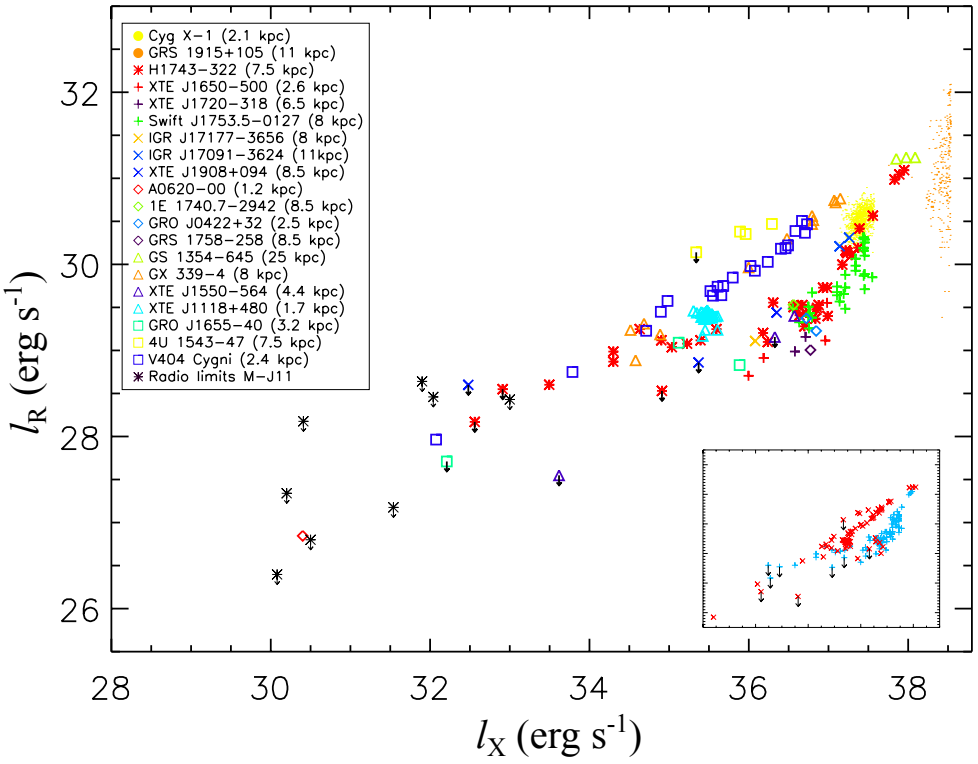

Figure 2.8: The observed radio/X-ray correlation of 18 different X-ray binaries. l_R and l_X denote the log of the radio and X-ray luminosities, respectively. The inset differentiates between sources with accurate distance measurements (red points) and uncertain distance measurements (blue points). Figure from Gallo et al. (2012).

luminosities in hard state LMXBs (Figure 2.8). Despite the jet contributing a small fraction of the overall radiative output of the system, it is closely coupled with the X-ray luminosity, which is responsible for the bulk of the radiative output. This relationship has been observed for both individual sources (e.g. GX 339−4; Hannikainen et al. 1998; Corbel et al. 2003, 2013) and the entire sample of black hole X-ray binaries (e.g. Gallo et al. 2003, 2012). The correlation extends over more than three orders of magnitude in X-ray luminosity, from quiescence (below a few $10^{-5}\,L_{\rm Edd}$) up to $\sim$2% $L_{\rm Edd}$, above which the source transitions into a soft state and the radio emission from the core is quenched. Although recent work has cast some doubt over the universality of the relation (Gallo et al., 2014), it is generally described by two distinct power-law tracks in the radio/X-ray luminosity plane; an upper track with a best fitting slope of 0.63±0.03 and a lower, steeper, 'radio-quiet' track with a best fitting slope of

0.98±0.08 (Gallo et al., 2012), which are not consistent with each other or the widely adopted value of ∼1.4 for neutron stars (Migliari and Fender, 2006). The track followed by a given source does not appear to be connected to any property of the object (such as spin; Soleri and Fender 2011) and there is evidence for some individual sources transitioning between the two tracks as their X-ray luminosity fades (Coriat et al., 2011; Jonker et al., 2012; Ratti et al., 2012). It has also been suggested that this bimodal relationship may also exist in AGN, supporting the theory that the mechanisms responsible for extracting energy from the accretion flow are similar across the mass scale (King et al., 2013).

2.4 A case study of MAXI J1836−194

MAXI J1836−194 was discovered at the onset of its outburst on 2011 August 2011 with the Monitor of All-sky X-ray Image (MAXI)/Gas Slit Camera (GSC; Matsuoka et al. 2009) on the International Space Station (Negoro et al., 2011). The detection triggered an intensive multiwavelength observing campaign including radio, sub-mm, IR, optical, UV and X-ray observations. This source was classified as a black hole candidate due to its X-ray spectral and timing properties (Strohmayer and Smith, 2011; Nakahira et al., 2011; Del Santo et al., 2011; Reis et al., 2012), as well as its bright radio emission (Miller-Jones et al., 2011). MAXI J1836−194 transitioned from the hard state (spectral states are defined by X-ray spectral and timing properties; Ferrigno et al., 2012) to the HIMS on 2011 September 11. The outburst 'failed' to enter the full soft state, remaining in the HIMS, reaching its softest spectral state on September 16, following which it transitioned back to the hard state on September 28 and faded towards quiescence. In 2012 March, the system underwent a period of renewed activity but remained in the hard state (Krimm et al., 2012; Yang et al., 2012; Grebenev et al., 2013) before returning to quiescence by 2012 July 05 (Yang et al., 2012).

This thesis presents results from an intensive multiwavelength observing campaign of the black hole LMXB MAXI J1836−194 during its 2011 outburst and 2012 reflare. Using high cadence, quasi-simultaneous, broadband observations this research project attempts to constrain the parameters of the system and how they evolved over time. By investigating the evolution of the disk and jets, this project explores the causal relationship between the accretion inflow and jet outflow, providing insights into the processes that occur around an accreting black hole.

Chapter 3

Radiation processes

The purpose of this Chapter is to outline the radiation processes relevant to the multiwavelength study of black hole LMXBs.

3.1 Synchrotron radiation

Synchrotron emission is produced when relativistic electrons spiral around magnetic field lines, and is the process responsible for the diffuse background emission from our Galaxy (Haslam et al., 1981, 1982). Following Rybicki and Lightman (1979) and Longair (2011), the accelerating particles emit a narrow cone of highly beamed and polarised emission, concentrated in the direction of motion of the particle primarily due to relativistic aberration (Figure 3.1). The emission cone has a half angle opening of γ^{-1}, where γ is the Lorentz factor of the electron, and significant radiation is only observed by a distant observer when the electron's velocity vector is within an angle of $1/\gamma$ radians to the line of sight of the observer. For a single electron, the spectrum of the radiation peaks at the critical angular frequency, $\omega_{\rm crit}$, given by

$$\omega_{\rm crit} = \frac{3}{2}\frac{c}{v}\gamma^3\omega_r \sin a \tag{3.1}$$

where v is the speed of the electron, a is the pitch angle of the electron and $\omega_r = eB/\gamma m_e c$, which is frequency of the rotation in the magnetic field where B is the magnetic field strength and e and m_e are the charge and mass of an electron, respectively.

In the case of a single electron, the spectral emissivity from synchrotron ra-

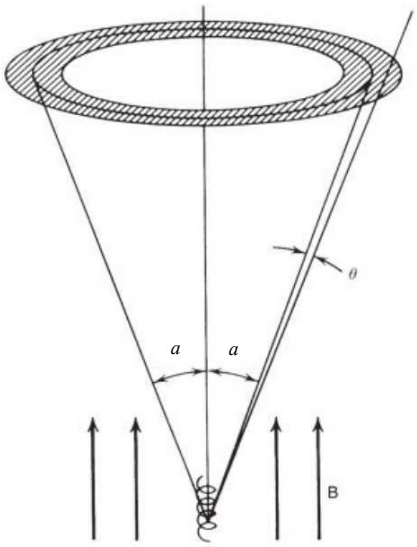

Figure 3.1: Synchrotron emission from an electron with a pitch angle a. The emission is confined to the shaded region, where $\theta = \gamma^{-1}$. Figure from Rybicki and Lightman (1979).

diation in the relativistic limit is (Longair, 2011, equation 8.58)

$$j(\omega) = \frac{\sqrt{3}e^3 B \sin a}{8\pi^2 \epsilon_0 c m_e} F(x), \tag{3.2}$$

where

$$F(x) = x \int_x^\infty K_{5/3}(z) dz, \tag{3.3}$$

$x = \omega/\omega_{\rm crit} = \nu/\nu_{\rm crit}$, $\nu_{\rm crit} = \omega_{\rm crit}/2\pi$, $K_{5/3}(z)$ is a modified Bessel function of order 5/3 and ϵ_0 is the permittivity of free space. In the high and low frequency limits, $F(x)$ can be expressed by (for e.g. Rybicki and Lightman, 1979, equation 6.34a and b)

$$F(x) = \frac{4\pi}{\sqrt{3}\Gamma_f(1/3)} \left(\frac{x}{2}\right)^{1/3} \qquad \text{when } x \ll 1, \tag{3.4}$$

$$F(x) = \left(\frac{\pi}{2}\right)^{1/2} x^{1/2} \exp(-x) \qquad \text{when } x \gg 1, \tag{3.5}$$

Where Γ_f is the Gamma function. Substituting these expressions, the high frequency emissivity of the electron becomes (Figure 3.2)

$$j(\nu) \propto \nu^{1/2} \exp(-\nu/\nu_{\rm crit}). \tag{3.6}$$

This solution is dominated by the exponential cut-off at frequencies $\nu \gg \nu_{\rm crit}$.

At low frequencies, $\nu \ll \nu_{\rm crit}$ and the synchrotron spectrum becomes

$$j(\omega) = \frac{\sqrt{3}e^3 B \sin a}{8\pi^2 \epsilon_0 c m_e} \frac{4\pi}{\sqrt{3}\Gamma_f(1/3)} \left(\frac{\nu}{2\nu_c}\right)^{1/3}. \tag{3.7}$$

In the low frequency regime the spectral emissivity of a single electron is therefore proportional to $\nu^{1/3}$ (Figure 3.2).

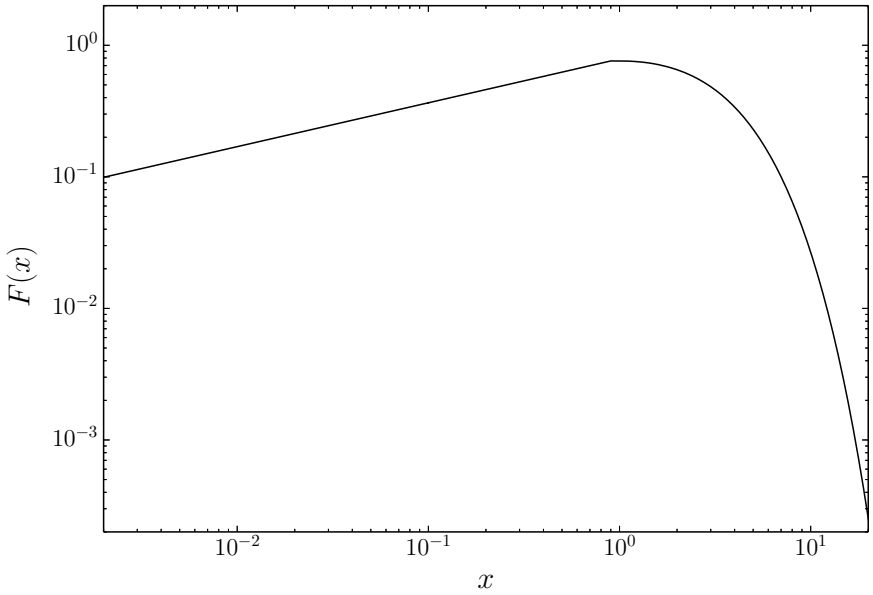

Figure 3.2: The synchrotron spectrum of a single electron is proportional to $F(x)$. Here $x = \omega/\omega_{\rm crit} = \nu/\nu_{\rm crit}$ and $F(x)$ is given by Equations 3.4 and 3.5.

For a synchrotron-emitting source, particles will have a distribution of energies that are typically modelled as a power-law distribution, with an energy spectrum given by $N(E)\,dE = \kappa E^{-p}\,dE$, where $N(E)\,dE$ is the number density of electrons per unit volume (with energies between E and $E + dE$), p is the spectral index of the particle energies and κ is the normalisation. In this case, the contributions of electrons of different energies to the intensity at angular frequency ω, or equivalently, at $x = \omega/\omega_{\rm crit}$ must be integrated over, such that the emissivity per unit volume for an emitting source is (Longair, 2011, equation 8.83)

$$J(\omega) = \int_0^\infty j(x)\kappa E^{-p} dE. \tag{3.8}$$

Evaluating this integral

$$J(\omega) = \frac{\sqrt{3}e^3 B \kappa \sin a}{8\pi^2 \epsilon_0 c m_e (p+1)} \left(\frac{\omega m_e^3 c^4}{3eB\sin a}\right)^{-(p-1)/2} \Gamma_f\left(\frac{p}{4} + \frac{19}{12}\right) \Gamma_f\left(\frac{p}{4} - \frac{1}{12}\right). \tag{3.9}$$

Therefore, the emissivity of the electron at a particular frequency, ω, depends strongly on the pitch angle, a. For an isotropic distribution of pitch angles that have a probability distribution of $P(a) = \frac{1}{2}\sin(a)da$, the emission per unit volume becomes

$$J(\omega) = \frac{\sqrt{3}e^3 B\kappa}{16\pi^2\epsilon_0 c m_e(p+1)}\left(\frac{\omega m_e^3 c^4}{3eB}\right)^{\frac{-(p-1)}{2}} \sqrt{\pi}\frac{\Gamma\left(\frac{p}{4}+\frac{19}{12}\right)\Gamma_f\left(\frac{p}{4}-\frac{1}{12}\right)\Gamma_f\left(\frac{p}{4}+\frac{5}{4}\right)}{\Gamma_f\left(\frac{p}{4}+\frac{7}{4}\right)}. \tag{3.10}$$

Therefore, the emissivity is expressed in terms of κ, B, ν such that

$$J(\nu) \propto \kappa B^{(p+1)/2}\nu^{-(p-1)/2}. \tag{3.11}$$

The emitted spectrum, $J(\nu) \propto \nu^{-(p-1)/2}$, is a power-law, which is determined by the slope of the electron energy spectrum rather than by the shape of the emission spectrum of a single electron.

3.1.1 Synchrotron self-absorption

For a population of electrons, the synchrotron-emitting electrons will also absorb a fraction of the emitted radiation in a process known as synchrotron self-absorption. These absorption effects increase with decreasing frequency, which causes the emission spectrum to turn over at low frequencies.

Synchrotron emission is non-thermal, however, an equivalent brightness temperature, T_b, is often used to characterise the intensity of the emission. T_b is defined as the temperature that would be required of a black body (the most efficient absorber and emitter) to produce the observed intensity if the emission is thermal. Following Longair (2011), if a source has the same physical size at all frequencies,

$$T_b = \frac{c^2}{2\nu^2 k_\mathrm{B}}\frac{S_\nu}{\Omega}, \tag{3.12}$$

where k_B is Boltzmann's constant and Ω is the solid angle the source subtends at the observer. When the brightness temperature of the radiation approaches the thermal temperature of the emitting electrons, absorption processes are expected to be significant.

For a power-law distribution of electron energies, the absorption coefficient is (Longair, 2011, equation 8.112)

$$\chi_\nu = \frac{\sqrt{3}e^3\kappa c}{32\pi^2\epsilon_0 m_e}\left(\frac{3e}{2\pi m_e^3 c^4}\right)^{p/2}\Gamma_f\left(\frac{3p+22}{12}\right)\Gamma_f\left(\frac{3p+2}{12}\right)(B\sin a)^{(p+2)/2}\nu^{-(p+4)/2}. \tag{3.13}$$

Averaging over an isotropic distribution of pitch angles with a probability distribution $P(a) = \frac{1}{2}\sin(a)da$, Equation 3.13 becomes

$$\chi_\nu = \frac{\sqrt{3\pi}e^3\kappa B^{(p+2)/2}c}{64\pi^2\epsilon_0 m_e}\left(\frac{3e}{2\pi m_e^3 c^4}\right)^{p/2}\frac{\Gamma\left(\frac{3p+22}{12}\right)\Gamma\left(\frac{3p+2}{12}\right)\Gamma\left(\frac{p+6}{4}\right)}{\Gamma\left(\frac{p+8}{4}\right)}\nu^{-(p+4)/2}. \tag{3.14}$$

Applying this function to the emission spectrum of a region of thickness l_{thick}, if the source is optically thin, $\chi(\nu)l_{\text{thick}} \ll 1$, the intensity becomes

$$I_\nu = \frac{J(\nu)l_{\text{thick}}}{4\pi} \tag{3.15}$$

and the absorption does not affect the observed spectrum. However, if the source is optically thick, $\chi(\nu)l_{\text{thick}} \gg 1$,

$$I_\nu = \frac{J(\nu)}{4\pi\chi_\nu} \tag{3.16}$$

and the absorption effects become important. Substituting Equation 3.14 and Equation 3.10 into Equation 3.16 gives

$$I_\nu \propto \frac{m_e\nu^{5/2}}{B^{1/2}}, \tag{3.17}$$

and the self absorbed spectrum scales as $S_\nu \propto \nu^{5/2}$.

3.1.2 Synchrotron cooling break

At high frequencies, the highest energy synchrotron electrons are depleted by radiative losses on shorter timescales than the dynamical timescale of the source (i.e. the radiation losses become so large that the emitting particles lose energy to any radiation). The total energy loss rate by synchrotron radiation in the ultra-relativistic limit (when $v \to c$) is (Longair, 2011, equation 16.17)

$$-\left(\frac{\mathrm{d}E}{\mathrm{d}t}\right)_{\text{synch}} = 2\sigma_{\text{T}}c\gamma^2 U_B \sin^2 a, \tag{3.18}$$

where $U_B = B^2/2\mu_0$ is the magnetic energy density and μ_0 is the permeability of free space. Averaging over the isotropic pitch angle distribution gives

$$-\left(\frac{\mathrm{d}E}{\mathrm{d}t}\right)_{\text{synch}} = \frac{4}{3}\sigma_{\text{T}}c\gamma^2 U_B, \tag{3.19}$$

and the total energy loss rate is proportional to E^2.

High energy charged particles diffuse, where they are subject to energy gains and losses. For relativistic electrons with energy losses $b(E)$, assuming there is an infinite, uniform distribution of sources, each injecting high energy electrons with an injection spectrum $Q(E) = \kappa E^{-p}$, and that $N(E) \to 0$ as $E \to \infty$, the diffusion-loss becomes

$$N(E) = \frac{\kappa E^{-(p-1)}}{(p-1)b(E)}. \tag{3.20}$$

If synchrotron losses dominate, $b(E)$ will scale as E^2 (Equation 3.19) and the spectrum will steepen by one power of E. Consequently, the spectral index of optically thin synchrotron radiation breaks from $\alpha = -(p-1)/2$ to $\alpha = -p/2$.

3.1.3 Synchrotron radiation from a compact jet

For a self-absorbed source, at low frequencies where absorption processes dominate, the emission spectrum scales as $S_\nu \propto \nu^{5/2}$. At higher frequencies the emission is optically thin, the absorption effects are not important, and the spectrum scales as $S_\nu \propto \nu^{-(p-1)/2}$. The highest energy electrons may cool due to radiation losses and the spectrum is proportional to $\nu^{-p/2}$ (Figure 3.3, left panel).

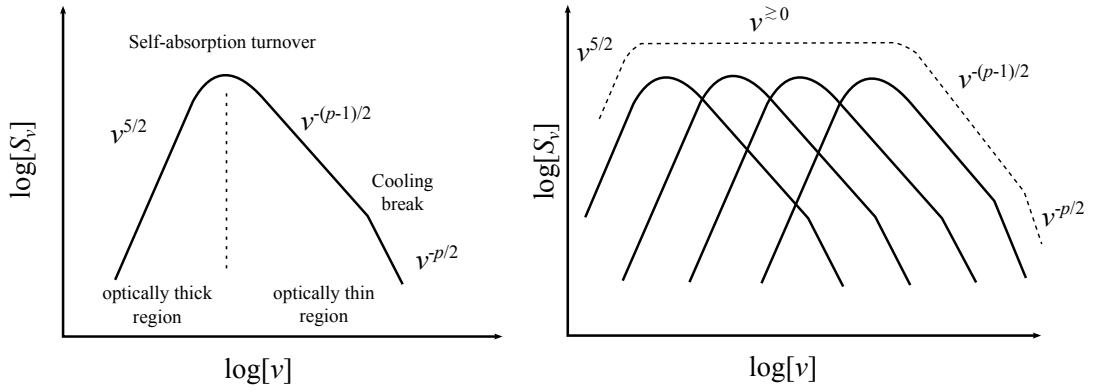

Figure 3.3: Synchrotron spectrum from a power-law distribution of electrons of energies $N(E)\,dE = \kappa E^{-p}\,dE$. Left panel: a single synchrotron component, displaying the effects of synchrotron self-absorption and synchrotron cooling. Right panel: the superposition of many single components to produce the observed synchrotron spectrum from a compact jet (dashed line).

Compact astrophysical jets are observed to have a flat or inverted radio spectrum (i.e. $\alpha \gtrsim 0$) in the GHz regime, which is explained by the superposition of many partially self-absorbed synchrotron components (Figure 3.3, right panel)

from electron populations at different distances along the jet (Blandford and Königl, 1979).

3.1.4 Polarisation of synchrotron emission

The radiation from a single electron is elliptically polarised (Longair, 2011). For a population of particles with a uniform distribution of pitch angles, the components of elliptical polarisation that are parallel to the projection of B will cancel out, due to the emission cones contributing equally from both sides of the line of sight and the resultant observed polarisation is linear. Integrating over a power-law distribution of electron energies, the fractional polarisation, FP, is given by (Longair, 2011, equation 8.95)

$$FP = \frac{\int_0^\infty G(x)x^{(p-3/2)}dx}{\int_0^\infty F(x)x^{(p-3/2)}dx}, \tag{3.21}$$

$F(x)$ is defined in Equation 3.3 and $G(x) = xK_{2/3}(x)$, where $K_{2/3}(z)$ is a modified Bessel function of order 2/3. Evaluating this integral gives

$$FP = \frac{p+1}{p+\frac{7}{3}}. \tag{3.22}$$

Assuming a typical energy spectrum ($p = 2.5$; Longair 2011), the fractional polarisation from ultra-relativistic electrons in a uniform magnetic field is expected to be ≈72%.

In the optically thick region of the spectrum (due to self-absorption), the electric vector of the emitted radiation is parallel to the magnetic field (rather than perpendicular). Hence the degree of polarisation for a uniform magnetic field is (Longair, 2011, equation 8.120)

$$FP = \frac{3}{6p+13}. \tag{3.23}$$

Therefore, assuming a typical energy spectrum of $p = 2.5$ (Longair, 2011), the expected fractional polarisation for a uniformly magnetic field in the optically-thick region is ≈ 11%.

If the electrons do not have sufficiently high Lorentz factors, some circular polarisation may be expected, due to the elliptically polarised components not cancelling each other exactly. However, this effect is minimal and the fractional circular polarisation will be of order γ^{-1} of the linear polarisation (Longair, 2011).

3.1.5 Relativistic beaming and Doppler boosting

Due to the relativistic bulk flow of particles in jets, emission is beamed in a forward emission cone in the observer's frame of reference. This beaming results in emission pointing away from the observer to appear faint, and those pointing towards the observer to appear much brighter. In the rest frame of the observer, the jet emission from a source is boosted by the relativistic Doppler factor δ where

$$\delta = \Gamma^{-1}(1 - \beta\cos\theta)^{-1}, \tag{3.24}$$

the jet bulk velocity $\beta = v/c$ and θ is the angle of the jets relative to the line of sight of the observer. A source that emits in its rest frame F' and is observed in the observer's rest frame F, will have an observed flux density S_ν such that

$$S_\nu = S'_\nu \delta^{n-\alpha}, \tag{3.25}$$

where S'_ν is the flux density in the rest frame of the source, n=2 for a continuous stream of emission and n=3 for a discrete components (i.e. transient ejecta). Therefore, the flux ratio of approaching and receding jet knots (assuming a symmetric bipolar outflow) in the frame of the compact object is

$$\frac{S_{\rm app}}{S_{\rm rec}} = \left(\frac{\delta_{\rm app}}{\delta_{\rm rec}}\right)^{n-\alpha} = \left(\frac{1+\beta\cos i}{1-\beta\cos i}\right)^{n-\alpha}, \tag{3.26}$$

where the subscripts app and rec denote the approaching and receding jets, respectively.

The appearance of the components will also differ due to the relativistic effects. For symmetric jets travelling at a significant fraction of the speed of light, observations will show the receding jet as it was at an earlier time than the approaching jet due to light travel time. Therefore, the approaching jet will appear to moved have further from the core than the receding jet at the time of the observation. The ratio of the distance travelled $l_{\rm D}$ for each side of the jet due to this effect is

$$\frac{l_{\rm D,app}}{l_{\rm D,rec}} = \frac{1+\beta\cos i}{1-\beta\cos i}. \tag{3.27}$$

For knots moving with a velocity βc at a distance D (from the observer), the observed proper motions of the approaching $\mu_{\rm app}$ and receding $\mu_{\rm rec}$ components are

$$\mu_{\rm app} = \frac{\beta\sin i}{1-\beta\cos i}\frac{c}{D}, \tag{3.28}$$

and

$$\mu_{\rm rec} = \frac{\beta\sin i}{1+\beta\cos i}\frac{c}{D}, \tag{3.29}$$

which, given a sufficiently low inclination angle, can produce apparent superluminal motion of the knots.

3.2 Inverse Compton scattering

Inverse Compton (IC) scattering is the scattering of low energy photons to higher energies by relativistic electrons. In this process energy is gained by the photons at the expense of the kinetic energy of the electrons. This is an inevitable drain of energy for high-energy electrons that pass through a region in which there is a large energy density of radiation. Following Longair (2011), considering a collision between a photon and a relativistic electron as seen in both the laboratory frame of reference F and the rest frame of the electron F', if $\gamma\hbar\omega \ll m_e c^2$ (where $\hbar$ equals Planck's constant h divided by 2π), the centre of momentum frame is very closely that of the relativistic electron. Given that the energy of the photon is $\hbar\omega$, for an angle of incidence θ_i in F the photon energy in F' is $\hbar\omega' = \gamma\hbar\omega[1 + (v/c)\cos\theta_i]$.

Provided $\gamma\hbar\omega \ll m_e c^2$, the Compton interaction in the electron rest frame F' is Thomson scattering and hence the energy loss rate in F' is the rate at which energy is re-radiated by the electron such that (Longair, 2011, equation 9.33)

$$-\left(\frac{dE}{dt}\right) = \sigma_{\rm T} c u'_{\rm rad}, \tag{3.30}$$

where $u'_{\rm rad}$ is the energy density of the radiation in the rest frame of the electron. The time interval between the arrival of photons from the direction θ'_i is shorter by $[\gamma(1 + (v/c)\cos\theta_i)]$ in the rest frame F' than in F. Correspondingly, the number density of photons in F' when compared to F is greater by this factor $[\gamma(1 + (v/c)\cos\theta_i)]$. Thus, $u'_{\rm rad} = [\gamma(1 + (v/c)\cos i)]^2 u_{\rm rad}$. Assuming that the radiation field is isotropic and the contribution to $u'_{\rm rad}$ from the solid angle $\mathrm{d}\Omega$ in F is

$$\mathrm{d}u'_{\rm rad} = u_{\rm rad}\gamma^2(1 + (v/c)\cos\theta_i)]^2 \frac{1}{2}\sin\theta_i \mathrm{d}\theta_i. \tag{3.31}$$

Integrating over the solid angle gives

$$u'_{\rm rad} = \frac{4}{3} u_{\rm rad}\left(\gamma^2 - \frac{1}{4}\right). \tag{3.32}$$

Given that $(\mathrm{d}E/\mathrm{d}t) = (\mathrm{d}E/\mathrm{d}t)'$, Equation 3.30 becomes

$$-\left(\frac{dE}{dt}\right) = \frac{4}{3}\sigma_{\rm T} c u_{\rm rad}\left(\gamma^2 - \frac{1}{4}\right). \tag{3.33}$$

With the identity $(\gamma^2 - 1) = (v^2/c^2)\gamma^2$, the energy loss rate in the laboratory rest frame F is (Longair, 2011, equation 9.41)

$$\left(\frac{dE}{dt}\right)_{\rm IC} = \frac{4}{3}\sigma_{\rm T} c u_{\rm rad} \left(\frac{v^2}{c^2}\right) \gamma^2. \tag{3.34}$$

For an incident isotropic photon field at a single frequency, ν_0, the spectral emissivity, I_ν, may be written (Longair, 2011, equation 9.43)

$$I(\nu)\, d\nu = \frac{3\sigma_{\rm T} c}{16\gamma^4} \frac{N(\nu_0)}{\nu_0^2} \nu \left[2\nu \ln\left(\frac{\nu}{4\gamma^2\nu_0}\right) + \nu + 4\gamma^2\nu_0 - \frac{\nu^2}{2\gamma^2\nu_0} \right] d\nu, \tag{3.35}$$

where the isotropic radiation field in the laboratory frame of reference F is assumed to be monochromatic with frequency ν_0 and $N(\nu_0)$ is the number density of photons. At low frequencies the term in square brackets is a constant and the radiation spectrum is of the form $I(\nu) \propto \nu$.

3.2.1 Synchrotron self-Compton radiation

Photons produced by synchrotron emission in an astrophysical source may be inverse Compton scattered by the same population of electrons responsible for their emission. This process is called Synchrotron self-Compton (SSC) radiation.

Following Rybicki and Lightman (1979), the power emitted by each electron in synchrotron emission may be written

$$P_{\rm Synch} = \frac{4}{3}\sigma_{\rm T} c \gamma^2 \beta^2 U_B. \tag{3.36}$$

Combining Equation 3.34 and Equation 3.36, the ratio of power from synchrotron emission compared to that of inverse Compton processes ($P_{\rm Compt}$) is the ratio of the magnetic field energy density and photon energy density $U_{\rm ph}$, such that

$$\frac{P_{\rm Synch}}{P_{\rm Compt}} = \frac{U_B}{U_{\rm ph}}. \tag{3.37}$$

The total power radiated per electron is

$$P_{\rm total} = \frac{4}{3}\sigma_{\rm T} c \gamma^2 \beta^2 (U_B + U_{\rm ph}). \tag{3.38}$$

The electron cooling timescale due to energy losses by these two processes is

$$t_{\rm cool} = \frac{\gamma m_e c^2}{P_{\rm total}}. \tag{3.39}$$

3.2.2 The inverse Compton catastrophe

The brightness temperature of a synchrotron emitting source is limited by the inverse Compton scattering, because the synchrotron photons may be scattered multiple times, resulting in what is called the inverse Compton catastrophe. The density of the synchrotron photons may reach a level where they induce a higher loss rate through Compton scattering than the synchrotron rate itself. Following Longair (2011), re-writing Equation 3.37, the ratio ζ of the rates of energy loss of an ultra-relativistic electron by inverse Compton and synchrotron radiation in the presence of a photon energy density $U_{\rm ph}$ and magnetic flux density B is

$$\zeta = \frac{(dE/dt)_{\rm IC}}{(dE/dt)_{\rm synch}} = \frac{U_{\rm ph}}{B^2/2\mu_0}. \tag{3.40}$$

If this ratio is greater than one, then the energy density of the X-rays is greater than that of the radio photons and the electrons will suffer even greater energy loss by scattering these X-rays to γ-ray energies and so on (catastrophic electron cooling).

For a self-absorbed source, the electron temperature of the relativistic electrons is equal to the brightness temperature $T_{\rm b}$ of the source, i.e. $T_{\rm e} = T_{\rm b}$. Therefore, the energy density of radiation $U_{\rm ph}$ is

$$U_{\rm ph} \sim \frac{2k_{\rm B}T_{\rm b}\nu}{\lambda^2 c}. \tag{3.41}$$

For a self-absorbed source

$$B = \frac{2\pi m_e}{e}\left(\frac{m_e c^2}{3k_{\rm B}T_{\rm b}}\right)^2 \nu, \tag{3.42}$$

and ζ becomes

$$\zeta = \frac{(dE/dt)_{\rm IC}}{(dE/dt)_{\rm synch}} = \frac{81e^2\mu_0 k_{\rm B}^5}{\pi^2 m_e^6 c^1 1}\nu T_{\rm b}^5. \tag{3.43}$$

When $\zeta = 1$, $T_{\rm b} \approx 10^{12}\nu_{\rm GHz}^{-1/5}$ K, where $\nu_{\rm GHz}$ is the frequency (in GHz) at which the brightness temperature is measured. Therefore, no compact radio source should have brightness temperatures that exceed $\approx 10^{12}$ K.

3.3 Thermal bremsstrahlung emission

Radiation may also arise due to the acceleration of a charge in the Coulomb field of another charge. This process is called bremsstrahlung or free-free emission.

From Longair (2011), the radiation spectrum of an electron in an encounter with a charged nucleus with a collision parameter b_c is (Longair, 2011, equation 6.34)

$$I(\omega) = \frac{Z^2 e^6}{24\pi^4 \epsilon_0^3 c^3 m_e^2 v^2} \frac{\omega^2}{\gamma^2 v^2} \left[\frac{1}{\gamma^2} K_0^2 \left(\frac{\omega b_c}{\gamma v} \right) + K_1^2 \left(\frac{\omega b_c}{\gamma v} \right) \right], \tag{3.44}$$

where Z is the atomic charge, v is the velocity of the electron relative to the nucleus, and K_0 and K_1 are modified Bessel functions of order 0 and 1. K_0 and K_1 have asymptotic limits where if

$$y \ll 1 \qquad K_0(y) = -\ln y \quad \text{and} \quad K_1(y) = 1/y \tag{3.45}$$

$$y \gg 1 \qquad K_0(y) = K_1(y) = \left(\frac{\pi}{2y} \right)^{1/2} \exp(-y). \tag{3.46}$$

At high frequencies, there is an exponential cut-off in the radiation spectrum where little power is emitted at frequencies greater than $\omega \approx \gamma v / b_c$. The high frequency spectrum has the form

$$I(\omega) = \frac{Z^2 e^6}{48\pi^3 \epsilon_0^3 c^3 m_e^2 v^2} \frac{\omega}{\gamma v b_c} \left[\frac{1}{\gamma^2} + 1 \right] \exp\left(-\frac{2\omega b_c}{\gamma v} \right). \tag{3.47}$$

At low frequencies, the spectrum is described as

$$I(\omega) = \frac{Z^2 e^6}{24\pi^2 \epsilon_0^3 c^3 m_e^2 v^2} \frac{1}{b_c} \left[1 + \frac{1}{\gamma^2} \left(\frac{\omega b_c}{\gamma v} \right)^2 \ln^2 \left(\frac{\omega b_c}{\gamma v} \right) \right]. \tag{3.48}$$

When $\omega b_c / \gamma v \ll 1$, Equation 3.48 becomes

$$I(\omega) = \frac{Z^2 e^6}{24\pi^2 \epsilon_0^3 c^3 m_e^2 v^2 b_c^2} = \text{constant}. \tag{3.49}$$

The radiation spectrum arises from accelerations parallel and perpendicular to the direction of motion of the electron. The perpendicular impulse contributes the majority of the intensity, and results in significant radiation at low frequencies. For a relativistic particle, the intensity due to the parallel impulse is decreased by a factor of γ^{-2} with respect to the non-relativistic scenario. Therefore, at low frequencies the dominant contribution to the intensity results from the momentum impulse perpendicular to the direction of travel of the electron. To a good approximation the low frequency spectrum is flat up to $\omega \approx \gamma v / b_c$, above which it cuts off exponentially.

For a thermal plasma of temperature T, the bremsstrahlung emission spectrum is found by integrating over the collision parameters and electron velocities, which have a Maxwellian distribution such that (Longair, 2011, equation 6.44)

$$N_e(v)\, dv = 4\pi N_e \left(\frac{m_e}{2\pi k_\mathrm{B} T} \right)^{3/2} v^2 \exp\left(-\frac{m_e v^2}{2 k_\mathrm{B} t} \right) dv, \tag{3.50}$$

where N_e is the number density of electrons. In this case, the spectral emissivity of the plasma is (Longair, 2011, equation 6.47)

$$\kappa_\nu = \frac{1}{3\pi^2}\left(\frac{\pi}{6}\right)^{1/2}\frac{Z^2e^6}{\epsilon_0^3c^3m_e^2}\left(\frac{m_e}{k_\mathrm{B}T}\right)^{1/2}N_nN_e\exp\left(-\frac{h\nu}{k_\mathrm{B}T}\right)g(\nu,T), \tag{3.51}$$

where N_n is the number density of nuclei and $g(\nu,T)$ the Gaunt factor; which is a slowly varying function that can be expressed as

$$g(\nu,T) = \frac{\sqrt{3}}{2\pi}\left[\ln\left(\frac{128\epsilon_0^2k_\mathrm{B}^3T^3}{m_ee^4\nu^2Z^2}\right) - \gamma^{1/2}\right] \tag{3.52}$$

in the radio band, and

$$g(\nu,T) = \frac{\sqrt{3}}{2\pi}\ln\left(\frac{k_\mathrm{B}T}{h\nu}\right) \tag{3.53}$$

in the X-ray band. At these higher frequencies, the emitting region is transparent, such that the optical depth $\tau \ll 1$, and $S_\nu \propto \nu^{-0.1}$.

3.3.1 Thermal bremsstrahlung absorption

The absorption coefficient for thermal bremsstrahlung has the form (Longair, 2011, equation 6.53)

$$\chi_\nu \propto \frac{NN_e}{\nu^3T^{1/2}}g(\nu,T)\left[1-\exp\left(-\frac{h\nu}{k_\mathrm{B}T}\right)\right]. \tag{3.54}$$

At high frequencies $h\nu \gg k_\mathrm{B}T$ and the absorption coefficient is

$$\chi_\nu \propto \frac{NN_e}{\nu^3T^{1/2}}g(\nu,T). \tag{3.55}$$

At low frequencies $h\nu \ll k_\mathrm{B}T$ and $1-\exp(-h\nu/k_\mathrm{B}T) = h\nu/k_\mathrm{B}T$. Therefore, the absorption coefficient becomes

$$\chi_\nu \propto \frac{NN_e}{\nu^2T^{3/2}}g(\nu,T). \tag{3.56}$$

At frequencies low enough that $\tau \gg 1$ and the emitting region becomes opaque, the spectrum approaches that of a blackbody and $S_\nu \propto \nu^2$.

3.4 Blackbody radiation

Blackbody radiation is the radiation emitted by optically thick media in thermal equilibrium. Following Rybicki and Lightman (1979), the spectrum of blackbody radiation at a temperature T can be expressed by Planck's law:

$$B_\nu(T) = \frac{2h\nu^3}{c^2}\left[\exp\left(\frac{h\nu}{k_\mathrm{B}T}\right)-1\right]^{-1}. \tag{3.57}$$

Expressed in terms of wavelength, Equation 3.57 is given by (see Figure 3.4)

$$B_\lambda(T) = \frac{2hc^2}{\lambda^5}\left[\exp\left(\frac{hc}{\lambda k_\mathrm{B}T}\right) - 1\right]^{-1}. \tag{3.58}$$

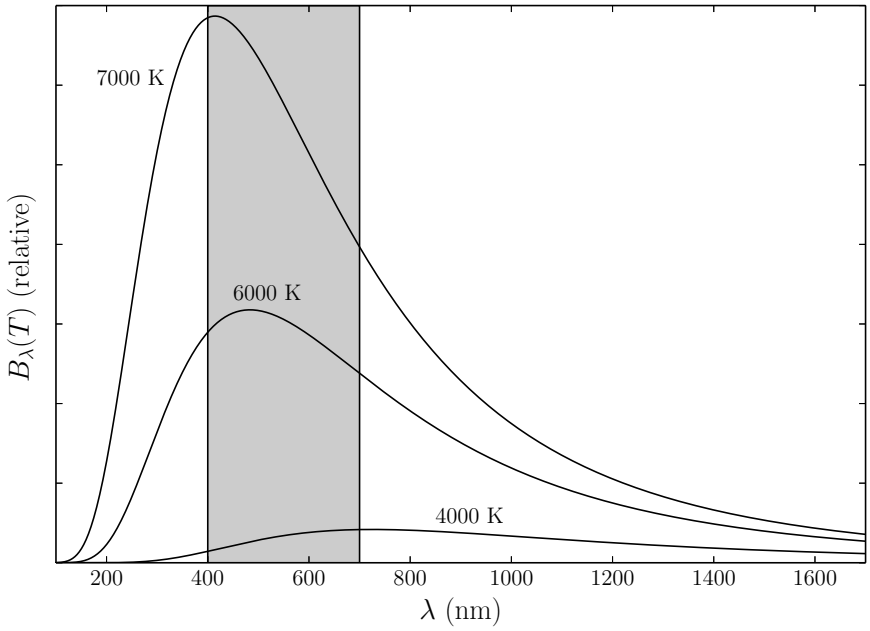

Figure 3.4: Spectrum of blackbody radiation at various temperatures, from Equation 3.58. The grey shaded region represents visible light.

Rayleigh-Jeans limit: $h\nu \ll k_\mathrm{B}T$

At sufficiently low frequencies the energy of each photon is much smaller than the average kinetic energy of the particles radiating inside the blackbody. In this scenario, the exponential in Equation 3.57 is expanded for $h\nu/k_\mathrm{B}T \ll 1$, giving the specific intensity in the Rayleigh-Jeans part of the spectrum

$$I_\nu(T) = \frac{2\nu^3}{c^2}k_\mathrm{B}T. \tag{3.59}$$

The Rayleigh-Jeans law applies at low frequencies, and in the radio band it almost always applies.

Wien limit: $h\nu \gg k_\mathrm{B}T$

For $h\nu \gg k_\mathrm{B}T$, the discrete quantum nature of photons must be applied, giving rise to the Wien limit. If the energy of the photon exceeds the typical energy of

the radiating particles Equation 3.57 becomes

$$I_\nu(T) = \frac{2\nu^2}{c^2} \exp\left(-\frac{h\nu}{k_\mathrm{B}T}\right) \tag{3.60}$$

and the specific intensity has an exponential cut-off.

3.4.1 Blackbody emission from an accretion disk

For a thin disk, we assume that the disk is axisymmetric and that the matter lies close to the plane z=0, where z is the plane of the disk. Letting R and ϕ be the radial and angular cylindrical coordinates, respectively, the matter moves in circles about the accreting object of mass M, with angular velocity Ω_v. Following Frank et al. (2002, chapter 5), it is assumed that the angular velocity is Keplerian, such that

$$\Omega_v = \Omega_{v\mathrm{K}}(R) = \left(\frac{GM}{R^3}\right)^{1/2}, \tag{3.61}$$

and the circular velocity is $u_\phi = R\Omega_{v\mathrm{K}}(R)$. The matter also has a small radial velocity v_R, which is negative near the accreting object such that matter will be accreted. $v_R \sim \nu_\mathrm{k}/R$, where ν_k is the constant kinematic viscosity. The viscous or radial drift timescale can then be expressed as $t_\mathrm{visc} = R/v_R$, which is an estimate of the timescale for the material in the disk to move a radial distance R.

If the rotation of the disk is assumed to be Keplerian then the viscous dissipation per unit area per unit time at radius R_* can be given by (Pringle, 1981, equation)

$$D(R) = \frac{3GM\dot{m}}{4\pi R^3}\left[1 - \left(\frac{R_*}{R}\right)^{1/2}\right]. \tag{3.62}$$

Integrating $D(R)$ from the inner most stable circular orbit of the disk, R_in, to ∞ gives the total radiated power

$$L_\mathrm{disk} = \int_{R_\mathrm{in}}^{\infty} D(R) 2\pi R dR \tag{3.63}$$

$$= \frac{GM\dot{m}}{2R_\mathrm{in}}. \tag{3.64}$$

For a black hole,

$$L_\mathrm{disk} = \eta\dot{m}\mathrm{c}^2 \tag{3.65}$$

where η measures how efficiently the rest mass energy of the accreted material is converted into radiation. In the case of a non-rotating black hole, $R_\mathrm{in} = 6GM/c^2$, therefore, with Equations 3.64 and 3.65, $\eta = 1/12$. For a maximally rotating black

hole $R_{\rm in} = GM/c^2$ and $\eta = 1/2$, however, including relativistic effects $\eta \approx 0.42$ (e.g. Bardeen et al., 1972; Page and Thorne, 1974). Therefore, only a fraction of the gravitational energy of the accretion flow is radiated from the surface of the disk (independent of the viscosity). The rest is radiated at smaller radii than the inner radius of the accretion disk or advected into the black hole.

If the disk is optically thick in the disk plane, each element at radius R of the disk face radiates approximately as a blackbody with temperature (Frank et al., 2002, equation 5.43)

$$T(R) = \left[\frac{3GM\dot{M}}{8\pi R^3\sigma}\left(1 - \left[\frac{R_*}{R}\right]^{1/2}\right)\right]^{1/4}, \tag{3.66}$$

where M is the mass of the accreting object and R_* is the radius where angular momentum stops being transported outwards (the innermost radius where the inflow is affected by viscous torques).

The spectrum emitted by each element of area of the disk may be approximated by Equation 3.57. This approximation neglects the effects of the atmosphere of the disk. Following Frank et al. (2002), for an observer at distance D whose line of sight makes an angle i from the normal of the disk plane the flux of the disk is given as

$$S_\nu = \frac{4\pi h\cos(i)\nu^3}{c^2 D^2}\int_{R_*}^{R_{\rm out}} \frac{R\,dR}{\exp(h\nu/k_{\rm B}T(R)) - 1}, \tag{3.67}$$

where $R_{\rm out}$ is the outer disk radius. Notably, this is independent of the disk viscosity. The shape of the spectrum for disks with different ratios $R_{\rm out}/R_{\rm in}$ is shown in Figure 3.5. For frequencies where $\nu \ll k_{\rm B}T(R_{\rm out})/h$ the spectrum takes the Rayleigh-Jeans form where $S_\nu \propto \nu^2$. When $\nu \gg k_{\rm B}T(R_{\rm out})/h$ the function assumes the Wien form, and is dominated by the hottest parts of the disk. For intermediate frequencies, the spectrum takes the form $S_\nu \propto \nu^{1/3}$ and is the characteristic disk spectrum.

Disks in LMXBs are thought to be heated by irradiation from the central compact source, modifying the structure and spectrum of the disk. The effective temperature $T_{\rm eff,i}$ due to the irradiation is described as

$$T^4_{\rm eff,i} = \frac{L_{\rm pt}}{4\pi R^2\sigma}\left(\frac{H}{R}\right)\left[\frac{d\ln H}{d\ln R} - 1\right](1 - A), \tag{3.68}$$

where $L_{\rm pt}$ is the luminosity of the central point source, H is the local scale height of the disk and A_s is the albedo, which is the effective fraction of incident

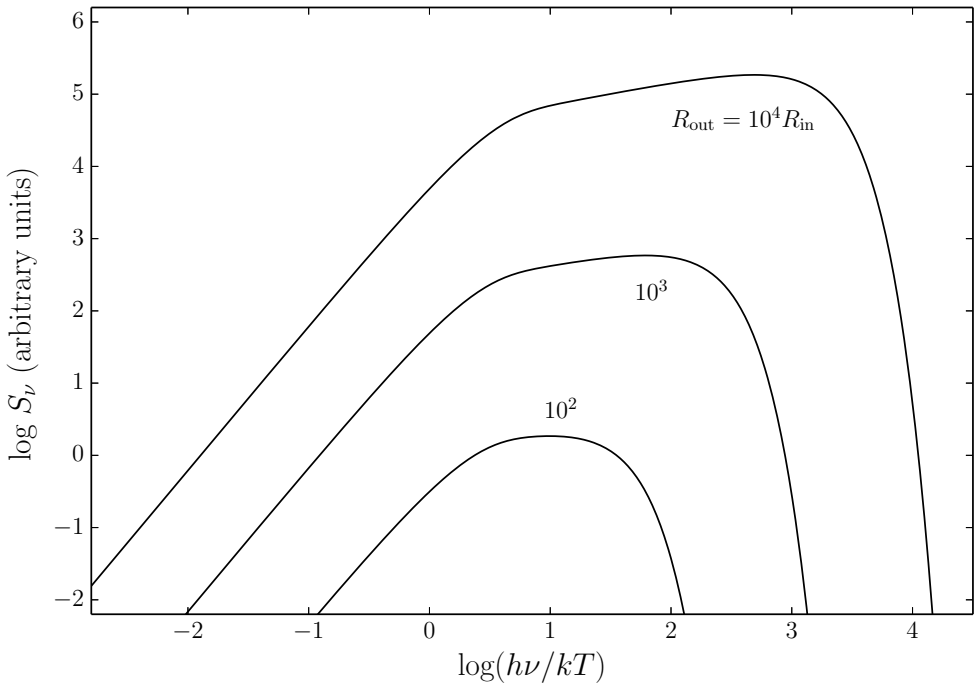

Figure 3.5: Continuum spectrum S_ν of a steady optically thick accretion disk radiating locally as a blackbody, for disks with different ratios $R_{\rm out}/R_{\rm in}$. The frequency is normalised to $k_{\rm B}T_{\rm out}/h$, where $T_{\rm out} = T(R_{\rm out})$.

radiation scattered from the surface without absorption. In a disk, the ratio H/R is approximately constant, therefore in the irradiation-dominated part of the disk the effective temperature scales as $T_{\rm eff} \propto R^{-1/2}$ and in the viscous dominated part of the disk $T_{\rm eff} \propto R^{-3/4}$ (from Equation 3.66). For a complete analysis of the disk spectrum, see Frank et al. (2002), chapter 5.

Chapter 4

Instrumentation and calibration

Due to the nature of the radiation, there is a difference in how radio, IR, optical, and X-ray telescopes measure incoming radiation and how the observations are calibrated. This research project has made use of astronomical data taken in each of these regimes and this section outlines the basic principles of observation and data reduction at these wavelengths, outlining the basic techniques used to observe astronomical objects and remove any atmospheric, instrumental and observational effects.

Optical and infrared telescopes work in much the same way as each other; they both use lenses and mirrors to focus the observed radiation onto a detector, such as a charge-coupled device (CCD), which measures the number of photons that strike its surface per unit time interval. The intercepted light produces a response in the detector that is proportional to the number of photons striking it over the observation time. The result of this is a measure of the intensity of the emitting source.

X-ray observations require techniques that differ considerably from observations at longer wavelengths. X-ray radiation is unable to penetrate the Earth's atmosphere and therefore telescopes must be space-based. X-rays are so energetic that simple glass mirrors cannot be used to focus the incoming radiation; instead, grazing-incidence mirrors made of gold or iridium are used to focus soft X-rays ($\lesssim$20 keV), while coded masks are typically used for hard X-rays ($\gtrsim$20 keV). Similar to the optical/IR regime, X-ray detectors measure incoming photons. However, due to the low X-ray count rate from X-ray emitting sources, detection is done on a photon-by-photon basis. X-ray detectors absorb the energy of an incoming photon, producing a measurable response (such as an electric charge, light or heat, depending on the detector) which is recorded as a count.

Over time, enough measurements can be accumulated to produce an image of the source. Unlike optical and IR observations, X-ray telescopes record information on the location, the time of arrival and energy of each photon such that an image, a lightcurve, or a spectrum can be created from a single observation.

Radio telescopes are fundamentally different to optical and X-ray telescopes in that they exploit the wave nature of the incoming emission, gathering information about the phase and amplitude of the radio wave. The waves are collected with the use of an antenna and receiver. Radio astronomy signals are in general extremely weak, necessitating large amounts of collecting area and the most sensitive receivers, and the signal is amplified to a usable level (keeping the signal directly proportional to the incoming radiation). Due to their long wavelengths, radio waves are able to propagate through dust and gas that obscures other wavelengths, and some parts of the radio band (5–15 GHz) are not strongly affected by the atmosphere[1]. Also, radio emission from the Sun is not as scattered as at higher wavelengths allowing for observations at both night and day, making radio telescopes a unique tool to observe astronomical sources. The strength of an observed radio source is generally represented as a spectral flux density $S(\nu)$, which is the amount of energy per second, per unit frequency interval striking unit area of the telescope. Radio measurements are usually expressed in units of Jansky (Jy), where $1\,\mathrm{Jy} = 10^{-26}\,\mathrm{W\,m^{-2}\,Hz^{-1}}$.

Sensitivity and angular resolution are the two main parameters that determine the performance of a telescope. They determine the minimum signal that a telescope can distinguish above the background noise, and the telescope's ability to differentiate closely-separated objects, respectively. In soft X-rays, grazing incidence telescopes provide spatial resolution of a few arcseconds, but in hard X-rays, use of coded mask results in much poorer angular resolution (arcminutes) and typically poorer sensitivity. The sensitivity of radio and optical/IR[2] telescopes relates to the total collecting area; in terms of angular resolution, these telescopes are diffraction-limited, such that the angular resolution of the telescope θ_A (in radians) is related to the observing wavelength λ and the aperture size A such that

$$\theta_{\mathrm{A}} \approx \frac{\lambda}{A}. \tag{4.1}$$

Due to this wavelength dependence, single-dish radio telescopes generally have

[1] Incoming radiation above 15 GHz is affected by the troposphere, while the light below 5 GHz is affected by the ionosphere.

[2] Although the resolution of ground based optical/IR telescopes can be seeing-limited, as opposed to diffraction-limited.

poor angular resolution. For example, to produce an angular resolution equivalent to a 1 m optical telescope (around 1 arcsecond), a single radio dish observing at 5 GHz ($\lambda = 6$ cm) would have to be approximately 12.4 km in diameter, which is not practical to build[3]. Therefore, radio telescopes generally have poor angular resolution and special techniques must be used to observe at high spatial resolution.

The technique of radio interferometry (also known as synthesis imaging) allows high-resolution observations at radio wavelengths. Here, an array of smaller radio telescopes are used together, producing a final resolution that is not defined by the diameter of the single components, but the distance between the two most widely-separated antennas, $b_{\rm max}$, such that

$$\theta_{\rm A} \approx \frac{\lambda}{b_{\rm max}}. \tag{4.2}$$

4.1 Radio observations and calibration

This section provides a brief introduction to the fundamentals of interferometry and aperture synthesis, as well as data reduction techniques. A full treatment of these principles can be found in Taylor et al. (1999) and Thompson et al. (2001).

4.1.1 Interferometry and aperture synthesis

Radio interferometry is the process in which two or more radio antennas, that are separated by some distance, are used to collect and combine the electromagnetic radiation from a radio source. Synthesis arrays are simply ensembles of two-element interferometers, where the number of independent pairs from N elements is $N(N-1)/2$, with elements that are separated by the baseline distance b.

Following Clark (1999), consider a quasi-monochromatic component $\mathbf{E}_\nu(\mathbf{R})$ of a time-varying electric field $\mathbf{E}_\nu(\mathbf{R},t)$ emitted from an astrophysical source at location $\mathbf{R}$ and observed at $\mathbf{r}$ (Figure 4.1). The linearity of Maxwell's equations allows the electric fields from all sources to be superposed at the observer,

$$\mathrm{E}_\nu(\mathbf{r}) = \iiint P_\nu(\mathbf{R},\mathbf{r})\ \mathbf{E}_\nu(\mathbf{R})\ dx\ dy\ dz. \tag{4.3}$$

[3]The largest steerable single-dish radio telescope in the world is the Robert C. Byrd Green Bank Telescope (GBT), with an elliptical 100 by 110 m active surface area, while the largest non-steerable telescope is currently the Arecibo radio telescope (305 m). The Five hundred meter Aperture Spherical Telescope (FAST) will be a 500 m diameter non-steerable radio telescope, which is currently under construction in China and expected to be finished in 2016 September.

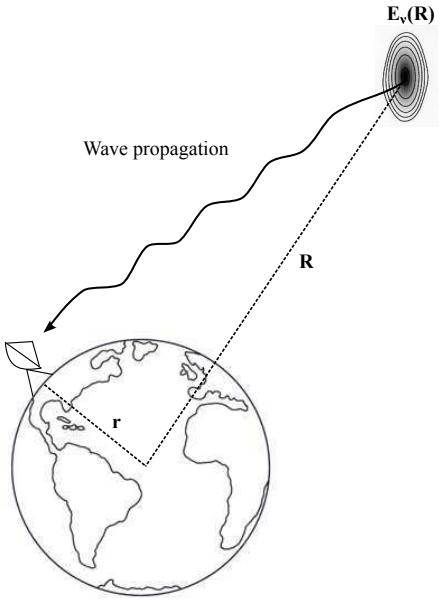

Figure 4.1: Propagation of an electromagnetic wave $\mathbf{E}_\nu(\mathbf{R})$ from an astrophysical source at location $\mathbf{R}$, observed by a radio telescope at $\mathbf{r}$.

Here, $P_\nu(\mathbf{R}, \mathbf{r})$ is the propagator, which describes how the electric field at $\mathbf{R}$ affects the electric field at $\mathbf{r}$.

For simplicity, for the moment the electromagnetic radiation can be considered to be a scalar field, thus ignoring all polarisation phenomena. In the case of astronomical observations, it is also assumed that sources of interest lie at great distances and we only need to consider the surface brightness $\mathcal{E}_\nu(\mathbf{R})$ of the source. Furthermore, we also assume that there are no additional sources of radiation between the observer and the celestial sphere, and the electromagnetic wave propagates through empty space, thus the propagator is simplified and the quantity observed by the radio telescope $E_\nu(\mathbf{r})$ becomes

$$E_\nu(\mathbf{r}) = \int \mathcal{E}_\nu(\mathbf{R}) \frac{e^{2\pi i \nu |\mathbf{R}-\mathbf{r}|/c}}{|\mathbf{R}-\mathbf{r}|}\, dS, \tag{4.4}$$

where dS is the element of surface area on the celestial sphere.

An interferometer measures the spatial coherence function (visibility), V_ν, of the electric fields radiating from a source, which is the correlation of the electric fields at the locations of the two antenna $\mathbf{r}_1$ and $\mathbf{r}_2$. The correlation of the electric field is described as (Clark, 1999)

$$V_\nu(\mathbf{r_1}, \mathbf{r_2}) = \langle \mathbf{E}_\nu(\mathbf{r_1})\, \mathbf{E}^*_\nu(\mathbf{r_2}) \rangle. \tag{4.5}$$

With the previous assumptions, the visibility becomes a function of the separation vector $\mathbf{r}_1 - \mathbf{r}_2$ such that

$$V_\nu(\mathbf{r_1}, \mathbf{r_2}) \approx \int I_\nu(\mathbf{s}) e^{-2\pi i \nu \mathbf{s}\cdot(\mathbf{r_1}-\mathbf{r_2})/c}\, d\Omega, \tag{4.6}$$

where $I_\nu(\mathbf{s})$ is the observed brightness or intensity of an element of solid angle $d\Omega$ in the direction of the unit vector $\mathbf{s}$. When tracking a source, the mapped field is centred at a reference position referred to as the phase tracking centre. This position is typically offset (by 2–3 synthesised beams) from the centre of the source that is under observation, to avoid correlator artefacts at the phase centre.

Timing delays are introduced into various elements of the interferometer to compensate for the geometric delay between antennas (where the radiation will arrive at each antenna at different times). Now, all interferometric visibilities can be placed on a single plane with axes u and v (referred to as the uv-plane) that is perpendicular to the line of sight, with a third w axis along the line of sight. Projecting the baseline $\mathbf{b} = \mathbf{r}_1 - \mathbf{r}_2$ onto the uv-plane, defines the quantities of u and v, which are the projected components of the antenna spacings measured in units of wavelength λ such that $\mathbf{r}_1 - \mathbf{r}_2 = \lambda(u, v, w \equiv 0)$. Here, the assumption $w = 0$ requires that the radiation come from a small region on the celestial sphere around the phase tracking centre, or that the observations are all made in a two-dimensional plane. In this coordinate system, the components of the unit vector $\mathbf{s}$ are (l, m, $n = \sqrt{1 - l^2 - m^2}$). Equation 4.6 becomes

$$V_\nu(u, v, w \equiv 0) = \iint I_\nu(l, m) \frac{e^{-2\pi i(ul+vm)}}{\sqrt{1 - l^2 - m^2}}\, dl\, dm. \tag{4.7}$$

With the assumptions that the radiation comes from a small region on the celestial sphere at the phase tracking centre, l and m will be small, and $\sqrt{1 - l^2 - m^2}$ approaches unity. Also, antennas are not point probes, they have a finite size and are directionally sensitive. Thus, the observed visibility is modified by the primary beam or normalised reception pattern, $\mathcal{A}_\nu(\mathbf{s})$, of the interferometer elements, and is now written

$$V_\nu(u, v) = \iint \mathcal{A}_\nu(l, m) I_\nu(l, m) e^{-2\pi i(ul+vm)}\, dl\, dm. \tag{4.8}$$

$\mathcal{A}_\nu(\mathbf{s})$ is the sensitivity of the interferometric antennas as a function of direction and rapidly falls to zero away from the pointing centre, limiting the field of view of a single pointing to a small region of sky. $\mathcal{A}_\nu(\mathbf{s})$ is generally well-determined and allows the assumption that the radiation comes from only a small region of

the celestial sphere (and hence $w = 0$). $V_\nu(u, v)$ is often referred to as the complex visibility.

The true intensity of the source can then be determined by taking the inversion of the Fourier transform relationship (Equation 4.8) to determine $\mathcal{A}_\nu(l, m)I_\nu(l, m)$, which is then divided by $\mathcal{A}_\nu(l, m)$, the result of which is the convolution of the true sky brightness with the Fourier transform of the sampling function. To image the source, a deconvolution must be performed (Section 4.1.3).

4.1.2 Reduction and calibration

During an observation, elements of the interferometer sample the electric field at set times. Following which, the signals are amplified, converted, correlated and averaged before a data point for each antenna pair is recorded. These are the observed visibilities. These raw data must then be calibrated, where the data are corrected for the effects of the atmosphere and instrument and the true sky brightness determined. This section briefly summarises the discussions of Fomalont and Perley (1999).

Editing

The raw data must first be edited, which is the process of identifying and discarding corrupted or discordant measurements. This is an important step in the data reduction process, where the data are carefully inspected and any discrepant data identified and removed ('flagged'). These corrupted data may be antenna, time, frequency, or baseline dependent and can result from radio frequency interference (RFI), poor weather conditions, recording errors, and hardware or software failures. These data will be flagged to avoid incorrect calibration.

Amplitude and phase calibration

In practice, the measured visibilities $\tilde{V}_{ij}(t)$ observed at time t by a pair of antennas forming the baseline ij often deviate from the true visibilities $V_{ij}(t)$. Such deviations may arise from the antenna gains being dependent on source elevation, time-varying atmospheric effects, pointing and tracking errors, as well as random stochastic noise. For a well-designed instrument, the relation between $\tilde{V}_{ij}(t)$ and $V_{ij}(t)$ can be considered as linear and the individual measurements are well isolated, such that the response associated with one antenna pair does not depend on the response of any other pair. The observed visibilities can be related to the

true visibilities as

$$\tilde{V}_{ij}(t) = \mathcal{G}_{ij}(t)V_{ij}(t) + \epsilon_{ij}(t) + \eta_{ij}(t), \tag{4.9}$$

where $\mathcal{G}_{ij}(t)$ is the baseline-based complex gain, $\epsilon_{ij}(t)$ is the baseline-based complex offset, and $\eta_{ij}(t)$ is stochastic noise. $\mathcal{G}_{ij}(t)$ can be approximated by the product of the two antenna-based complex gains $g_i(t)$ and $g_j(t)$ such that

$$\mathcal{G}_{ij}(t) = g_i(t)g_j^*(t)g_{ij}(t) = a_i(t)a_j(t)a_{ij}(t)e^{i(\phi_i(t)-\phi_j(t)+\phi_{ij}(t))}, \tag{4.10}$$

where $a(t)$ is an antenna-based amplitude correction, $\phi(t)$ is the antenna-based phase correction, and $g_{ij}(t)$, $a_{ij}(t)$ and $\phi_{ij}(t)$ are residual baseline-based gains. In a well designed array, these residual baseline-based effects should be less than 1%.

Observations of a calibrator source can determine g_i and g_j for each of the interferometer pairs. The primary (or flux) calibrator is a source whose flux density is well known and does not vary with time, while the secondary (or phase) calibrator should be a nearby ($\lesssim 5°$), bright and unresolved source with high positional accuracy. Observations of the secondary calibrator are used to determine amplitude and phase corrections as a function of time. The complex gains as a function of time are recorded, where gains between successive calibrator observations are estimated via interpolation. However, due to temporal and spatial variations between scans on the calibrator source and target source, some small residual errors may remain, leading to imperfect measurements of the true target flux density.

4.1.3 Imaging and deconvolution

Taking the inverse Fourier transform of the sampled (and calibrated) visibility function recovers the sky brightness:

$$\mathcal{A}_\nu(l,m)I_\nu(l,m) = \iint V_\nu(u,v)e^{2\pi i(ul+vm)}\,du\,dv. \tag{4.11}$$

Here, the sky brightness is modified by the primary beam of the interferometer elements. In the final step of deriving the sky intensity this modification is corrected for by simply dividing the derived intensities by $\mathcal{A}_\nu(l,m)$, hence, it will be ignored in the following descriptions.

The spatial coherence function V_ν is not known everywhere, it is sampled only at particular points on the uv-plane. Therefore, it is not possible to directly use

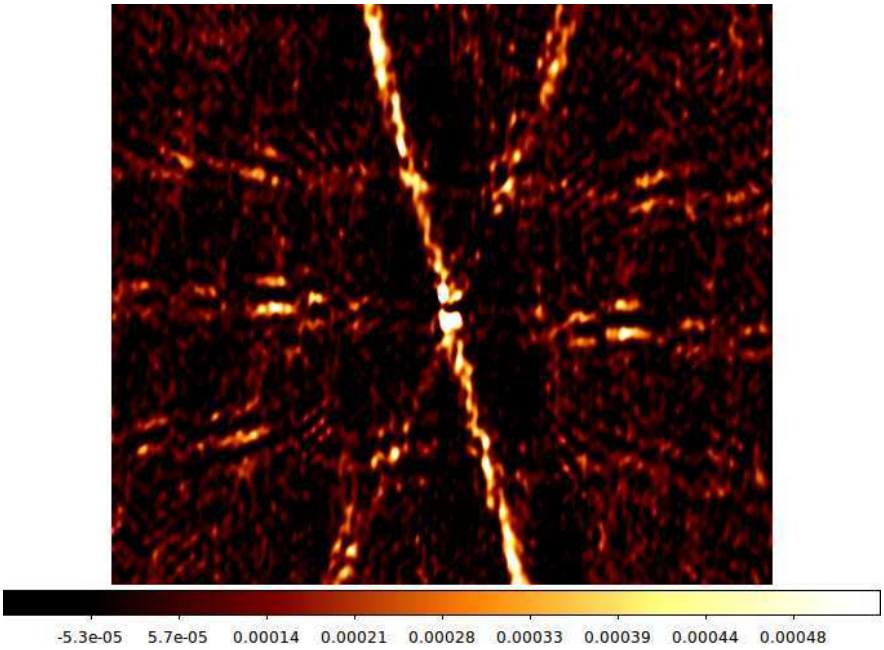

Figure 4.2: Dirty image $I_\nu^D(l,m)$, which is the image that is recovered from the sampled visibility function. This is the convolution of the true source brightness distribution I_ν with the point spread function B. The colour bar indicates the flux density in units of Jy beam^{-1}.

the inverse Fourier transform. The sampling function $S(u,v)$ gives the values for u and v for which the visibility function is sampled and is zero where no data have been taken (Briggs et al., 1999). $S(u,v)$ can be expressed in terms of a two-dimensional Dirac delta function:

$$S(u,v) = \sum_k w_k \delta(u-u_k, v-v_k), \tag{4.12}$$

where (u_k, v_k) are the points where the visibility measurements are recorded and w_k is a weighting function that may be introduced to modify the shape of the sampling function to favour certain aspects of the data (Cornwell et al., 1999). The image that is recovered from the sampled visibility function is called the *dirty image* (Figure 4.2), which is described as

$$I_\nu^D(l,m) = \iint S(u,v) V_\nu(u,v) e^{2\pi i(ul+vm)}\, du\, dv. \tag{4.13}$$

$I_\nu^D(l,m)$ is therefore the convolution of the true source brightness I_ν distribution with the synthesised beam or point spread function B, such that

$$I_\nu^D(l,m) = I_\nu * B, \tag{4.14}$$

where B is known as the *dirty beam* (Figure 4.3) and is the Fourier transform of the (known) sampling function:

$$B(l,m) = \iint S(u,v)e^{2\pi i(ul+vm)}\,du\,dv. \tag{4.15}$$

Hence, the dirty beam B must be deconvolved from the dirty image I^D to recover the real image intensity distribution.

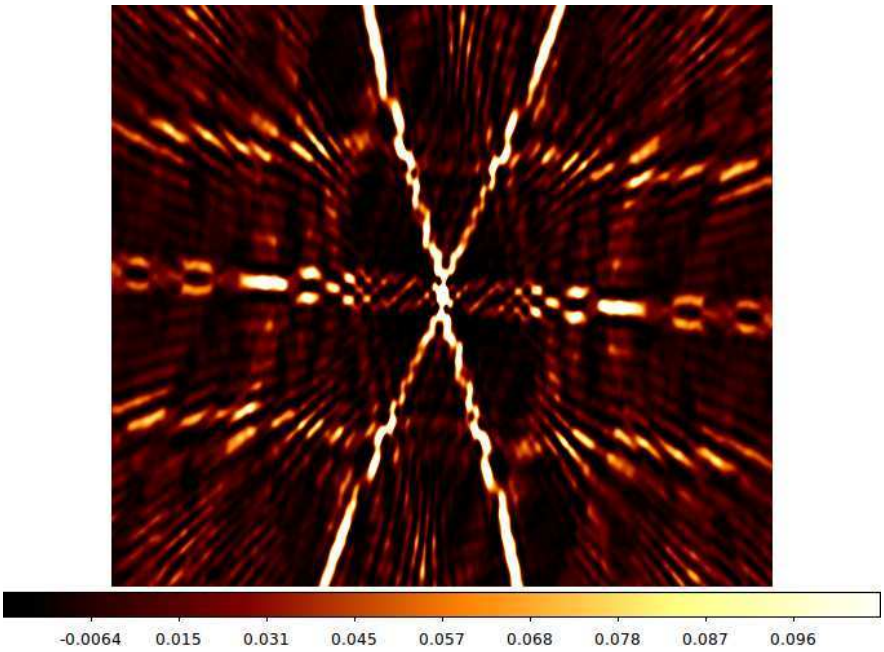

Figure 4.3: The dirty beam B, which is the Fourier transform of the sampling function. The colour bar represents the normalised (to one) intensity of the dirty beam.

The weighting function (Equation 4.12) $w_k = R_k T_k W_k$ is non-zero where visibility points have been measured. R_k accounts for the reliability of each data point, T_k is a smooth tapering function, usually Gaussian, that can be used to down-weight data at higher spatial frequencies, i.e. the poorly-sampled outer regions of the uv-plane, and W_k describes a density weighting function that can be used to compensate for the non-uniform sampling of the uv-plane. *Natural weighting* optimises the signal-to-noise ratio by setting the weights W_k to the reciprocal of their variance, giving higher weighting to the lower spatial frequencies (which tend to be better sampled in a real interferometer). *Uniform weighting* optimises the resolution by setting the weights W_k as the inverse of the density of the visibility points within a region of the uv-plane, attempting

to provide a uniform weighting to each cell in the uv-plane. The *Briggs robust weighting* scheme (Briggs, 1995) is an intermediate approach, in which either uniform or natural weighting may be chosen, or a combination of the two.

Following the Fourier transform into the image plane, the true sky brightness distribution $I_\nu(l, m)$, can be obtained by deconvolving the point spread function B from the dirty image $I^D_\nu(l, m)$. However, since the uv-plane is discretely sampled, the beam contains regions where $S(u, v) = 0$. Letting Z be an intensity distribution that corresponds to the unmeasured spatial frequencies, then $B * Z = 0$. Therefore, any $I + aZ$, where a is any number, is a solution to the convolution equation. This implies that there is no unique solution for the deconvolution problem (Equation 4.14) and non-linear methods are required to determine the optimal solution. Introducing a priori information, such as the sky being non-negative ($I > 0$) and mostly dark, places constraints on the deconvolution solutions.

Deconvolving with the CLEAN algorithm

While there are a number of deconvolution algorithms available, here I discuss the CLEAN algorithm, which is the most widely used algorithm for deconvolution among radio astronomers. First devised by Högbom (1974), CLEAN provides a solution by representing the radio sky as a collection of point sources on an otherwise empty background. This iterative approach first finds the position and strength of the highest intensity point in the dirty image. The point spread function (dirty beam), multiplied by the peak intensity and modified by a damping factor (the loop gain, which is $\lesssim 1$ and typically $\sim 1 - 5\%$), is then subtracted from the image at the peak position. The position and magnitude of the subtracted point source are recorded in a model. The new highest peak is found and the process repeated. This continues for a specified number of iterations or until any remaining peak is below a user-specified limit. The remaining dirty image is known as the *residual image* (Figure 4.4), which should be noise-like. The collection of CLEAN components is then convolved with an idealised restoring beam, which is usually an elliptical Gaussian with a full width at half maximum (FWHM) equal to that of the central lobe of the dirty beam, and the residual image is added back in to produce the CLEAN image (Figure 4.5).

Clark (1980) developed a more efficient Fast-Fourier transform (FFT)-based CLEAN algorithm that works in the uv-plane. This approach consists of a major and a minor cycle. In a minor cycle, a small fraction of the dirty beam is first

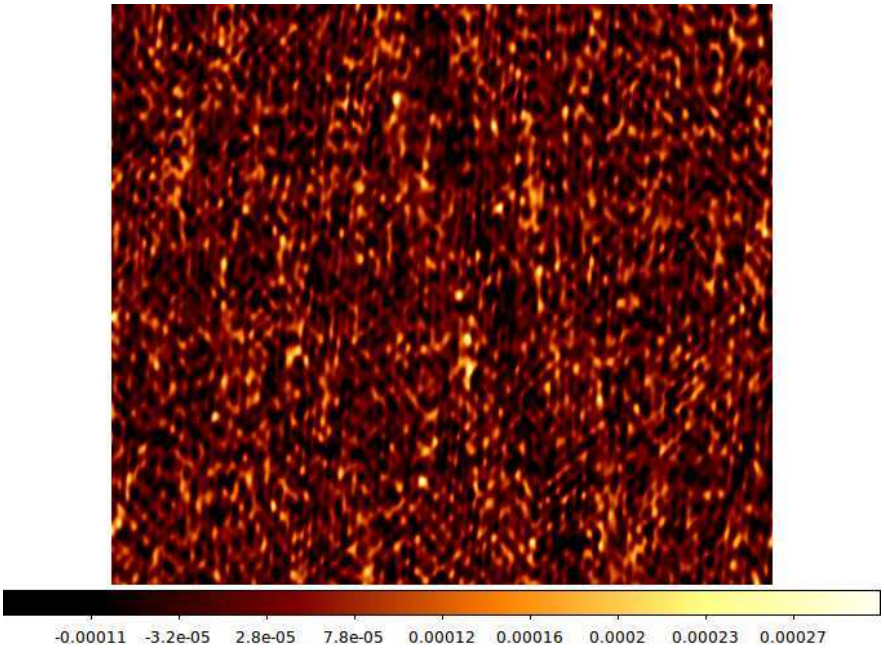

Figure 4.4: The remaining dirty image following CLEAN is known as the residual image. This image should be noise-like. The colour bar indicates the flux density in units of Jy beam^{-1}.

selected to include the highest exterior sidelobe. Points are then selected from the dirty image if they have an intensity that is greater than the highest exterior sidelobe (as a fraction of the image peak). A standard CLEAN is performed using the beam patch and the selected points of the dirty image until there are no more components to be selected in the dirty image. In a major cycle, the CLEAN components are Fourier transformed to the visibility plane, convolved with the sampling function, before being transformed back to the image plane and subtracted from the dirty image. A further variant of the Clark algorithm was developed by Cotton and Schwab (described in Schwab 1984), in which the subtraction of the CLEAN components is performed on the ungridded visibility data, eliminating aliasing noise and gridding errors.

In this thesis, the region of the image searched for peaks was restricted to user-specified areas (called CLEAN boxes) within which emission was either known to be or believed to be real. These boxes minimise the number of degrees-of-freedom in the deconvolution.

Figure 4.5: The CLEAN image, which is produced by convolving the CLEAN components with an idealised restoring beam before adding the residual image. The colour bar indicates the flux density in units of Jy beam^{-1}.

4.1.4 Self-calibration

As described in Section 4.1.2, in most real situations the structure/brightness of the field being observed is not known, and therefore calibrator sources must be observed to determine and transfer the gains onto the target. However, due to temporal and spatial variation in the atmosphere, resolved structure in the calibrator sources or weak calibrators, the gains are unlikely to be correct for the target observations. Self-calibration is based on an iterative scheme where the complex antenna gains are iteratively improved by using a model derived from the initial imaging of the target source.

The aim of the self-calibration procedure is to derive the true gains in the direction of the target source at the time of observation. This process uses a least squares approach to minimise the difference $\mathcal{S}$ between the model visibilities $\hat{V}$ and the observed visibilities $\tilde{V}$ (Cornwell and Fomalont, 1999):

$$\mathcal{S} = \sum_{k} \sum_{\substack{i,j, \\ i \neq j}} w_{ij}(t_k) \left| \tilde{V}_{ij}(t_k) - g_i(t_k) g_j^*(t_k) \hat{V}_{ij}(t_k) \right|^2, \tag{4.16}$$

where $w_{ij}(t_k)$ are weights, which are set to the reciprocal of the variance at time t_k. This process starts with an initial model, usually a point source or an initial

image of the source. The observed visibilities are then divided by this model to solve for the antenna gains $g(t)$ which are then used to correct the visibilities,

$$V_{ij,\mathrm{corr}}(t) = \frac{\tilde{V}_{ij}(t)}{g_i(t)g_j^*(t)}. \tag{4.17}$$

A new model is produced from imaging the corrected visibilities, which can then be used for the next iteration. This process can be repeated until a satisfactory intensity map is produced. For self-calibration to work effectively, the total number of free parameters can not be greater than the number of individual visibility measurements, there must be an adequate signal-to-noise ratio (SNR), and the source structure must not be too complex for the model.

4.1.5 VLBI data reduction and calibration

VLBI uses an array of independent radio telescopes with baseline distances of up to an Earth diameter[4] to achieve milliarcsecond resolution. Differing from other forms of interferometry, VLBI antennas are generally not directly linked and the interferometry of VLBI is not conducted in real-time[5]. The recorded signals from the stations must be transferred to a location where the data can be lined up in time and cross-correlated to produce an interferometric response for each baseline as a function of time, calculating the signals that correspond to the same arriving wavefront. Stations look through independent atmospheres to observe the same target, which can be at vastly different elevations, leading to rapid phase variation between elements. Therefore, stations must use highly accurate atomic clocks (usually hydrogen masers) to maintain temporal coherence. Treating each interferometer pair as a single dish with a diameter equal to the baseline distance, due to the large separation, the filling factor (the fraction of the 'single dish' that is filled by the two antenna) is extremely low and the uv-coverage is generally poor. Therefore, only very bright, compact sources may be observed with high accuracy. The field of view of VLBI observations is limited by the time and frequency averaging that is applied, and is considerably smaller than the primary beam size of the participating antennas. In fact, in a typical observation, a field of view of only a few tens of synthesised beams is possible.

The calibration process in VLBI is more complicated than that of connected interferometers. Amplitude calibration is completed using the system temper-

[4]Even larger baseline distances can be achieved with the use of space-based VLBI stations.

[5]With electronic-VLBI (e-VLBI), the data are transferred over the internet in real time to a central location for correlation.

ature and antenna gains, as sufficiently bright compact sources (such that flux calibration can be carried out) are generally highly variable. For phase calibration there are few unresolved sources (especially at VLBI resolution) that are usable and they are generally far removed on the sky from the target sources. Large slew times between the target and the phase calibrator, as well as the atmospheric differences along the line of sight, may also introduce phase errors. The data from individual stations are recorded prior to correlation using independent clocks, introducing errors that must be incorporated into the antenna phase gain terms. Due to these constraints, while relatively similar, the principles of VLBI and connected interferometers differ. Summarising Walker (1999), this Section highlights the techniques used in VLBI to overcome these observational constraints.

Amplitude calibration

The first step in the calibration process is the amplitude calibration. The correlator outputs raw correlation coefficients ρ, which are converted to correlated flux densities S_{c} such that

$$S_{\mathrm{c}} = f_s \rho \sqrt{\frac{T_{\mathrm{sys},1} T_{\mathrm{sys},2}}{K_1 K_2}}, \tag{4.18}$$

where f_s is a scaling factor that includes both correlator-specific scaling and corrections for digitisation, $T_{\mathrm{sys},i}$ is the system temperature of the ith antenna, and K_i is the antenna gain of the ith antenna at the pointing position of the observation (after the gain curve has been applied). System temperatures are measured at multiple times over the course of the observation for each antenna. The sensitivity of an antenna is dependent on the location of the source in the sky and varies during the observation. The antenna sensitivity (at a variety of elevation angles) is measured at each VLBI station and gain curves are produced regularly for the purpose of calibrating the amplitude of the data.

Fringe fitting

Due to the large antenna separation, a signal will arrive from a source at vastly different times, with different Doppler shifts (due to antennas moving at different speeds relative to the source due to the motion of the Earth). Complex visibilities from the correlation process may still suffer from errors in the atmospheric, geometric and clock models used by the correlator. These errors leave both delay and rate residuals in the data causing phase slopes over frequency and time,

respectively, which must be removed. Removing the phase slopes will allow for data averaging in both time and frequency, improving the SNR and reducing the data volume.

Fringe fitting estimates the residual delay and fringe rate over the course of the observation for each baseline in the array and each source observed. It is a self-calibration process that solves for amplitude and phase gains, as well as the first derivative of the phase gain. Typically, fitting programs first Fourier transform the data from the time-frequency domain to the delay-rate domain. There will be a peak in the Fourier transform modulus, corresponding to the correct values of delay and rate. Several fringe fitting algorithms can be used, including baseline-based methods or antenna-based methods. Global fringe fitting (Schwab and Cotton, 1983) is a widely used antenna-based method where all gain terms are antenna-dependent. Therefore, it is possible to use data from more than one baseline to solve for the derivatives of the phase gains in frequency and time, the residual delay, and the residual fringe rate of each antenna. In this process, the sensitivity of the fitting is improved since data from baselines with a higher response can be used to help determine the delay and rate parameters for the weaker baselines. For further discussion see Schwab and Cotton (1983) and Cotton (1995).

Imaging

At this stage, the phases for the target source remain un-calibrated. Traditional VLBI imaging generally attempts to solve for the phase errors post deconvolution with self-calibration, where the antenna gains are corrected iteratively using trial visibilities calculated from the source model. This process requires sufficiently bright sources[6] and does not preserve the absolute position of the source.

If the correlator model is good (such that the phase errors vary slowly in time and direction in the sky), phase referencing can be used. Phase referencing is the process where all phases, delays and rates are determined from fringe fitting on the calibrator source, and are transferred to the target (as described in Section 4.1.2). This technique can be used to image sources much too weak for self-calibration (ruling out self-calibration to determine the phase errors, as previously described) and provides an accurate source position, that is limited by the accuracy of the phase transfer. However, due to the high resolution of VLBI observations, the

[6]Such that they can be detected in the atmospheric coherence time, which is the maximum time over which self-calibration can be done.

phase calibrator must be imaged (with self-calibration) before being used to derive the calibration phases for the target source.

Imaging and self-calibration are described in detail in Sections 4.1.3 and 4.1.4, respectively.

4.2 Optical/infrared observations and calibration

Optical and IR observations follow very similar reduction and calibration techniques to determine the intrinsic brightness of an astronomical source. This section outlines the basic principles of data reduction in these two wavebands.

Optical image reduction

Raw optical images contain both intrinsic observational and instrumental effects, such as background emission, detector response, internal reflections and dust on the optics. These effects must be accounted for before the true source brightness can be determined.

Firstly, *bias* images are used to account for the charge pattern on the detector for an exposure time of zero. The bias is estimated by taking images with no light falling on the detector, so that the only values present in the pixels are due to the detector bias and noise introduced by thermal events within the detector (*dark current*). Multiple bias images are generally taken, which are combined and averaged to form a master-bias that will be subtracted from all observation frames. These images are taken with the same settings as the science images and are typically produced with the use of a light-proof cover. To minimise differences between the science and the calibration images, it is best to take the dark images directly before and/or after the science images.

Flat-field images are also taken to minimise the effects of differing pixel-to-pixel sensitivity, dust or smudging on the optics, internal reflections and optical vignetting (where the image is darker away from the centre). Flat field images are either exposures of an evenly illuminated screen with the dome closed (dome-flats) or of empty sky (sky-flats). Typically, a set of dome-flats are acquired each night and combined into a master flat-field frame, which is normalised such that its median is equal to unity. Sky-flats are taken by pointing the telescope at an area devoid of bright stars, either at twilight or during the night. At twilight, the changing brightness level is taken into account with template images, and

stars that become visible as the sky darkens are masked. Night-sky flats are produced by taking the median pixel value of slightly offset sky images. With enough images, the median pixel value can be taken as a good representation of the non-source background.

The master bias is subtracted from each single flat-field exposure. The resulting flat-fields are then averaged to form a master flat-field, which is normalised to provide the pixel-by-pixel fractional deviation from a perfectly uniform detector response. Finally, the raw science exposures have the bias subtracted from it, before being divided by the normalised flat field, to produce a calibrated science image.

4.2.1 Photometry

Photometry is the measurement of the brightness of an astronomical source using a standard reference scale. Traditionally, in optical astronomy, the source brightness is measured in magnitudes (mag), which is a logarithmic scale. If we define an arbitrary standard flux density S_0, then the apparent magnitude m_{app} (observed from Earth), of any source with an observed flux density S is defined by:

$$m_{\text{app}} = -2.5 \log \frac{S}{S_0}. \tag{4.19}$$

Therefore, the magnitudes of any two sources with observed flux densities S_1 and S_2 are related such that

$$m_{\text{app},1} - m_{\text{app},2} = -2.5 \log \frac{S_1}{S_2}. \tag{4.20}$$

The observed intensity of an object is then determined either by aperture or point spread function (PSF) photometry. However, the apparent magnitude is reliant on the observed flux density, which is a function of distance and is not the intrinsic brightness of the star. The absolute magnitude m_{abs} normalises this distance and is defined as the apparent magnitude of the star (in the absence of extinction; see Appendix A) at a distance of 10 parsecs. Considering the flux density at 10 parsecs S_{10} and the observed distance to the source D, the ratio of the flux at D to S_{10} is $S_D/S_{10} = (10/D)^2$. Therefore, the relationship between

the apparent and absolute magnitude is

$$m_{\rm app} - m_{\rm abs} = -2.5 \log \frac{F_D}{F_{10}} = -2.5 \log \left(\frac{10}{D}\right)^2 \tag{4.21}$$

$$= 5 \log D - 5 \tag{4.22}$$

$$= 5 \log \frac{D}{10{\rm pc}}. \tag{4.23}$$

Which is a measure of the distance to the object and is referred to as the distance modulus (dm).

Aperture photometry sums the intensity within a given radius (or aperture) from the centre of an object, so that the aperture entirely encloses the image of the star, and the background contribution is accounted for by selecting an area from the image with no stars, which is then subtracted. PSF photometry approximates the PSF by fitting either an analytical or numerical function to bright, isolated objects in the field, and scaling other objects according to their peak brightness. The local PSF background may be estimated in a similar fashion to aperture photometry, or by determining the value at which the profile becomes flat.

Aperture photometry is generally best used for isolated stars where there is less chance of contamination by nearby stars, while PSF photometry is typically used to measure the brightness of objects in crowded star fields. Another feature of PSF photometry is that the point sources in the field may be 'cleaned' from the frame, revealing any underlying structure.

Magnitudes derived from the calibrated images are instrumental and contain atmospheric and detector effects, which will vary both between telescopes and night to night. Therefore, the instrumental magnitudes $m_{\rm inst}$ must be converted to correctly provide the true magnitude $m_{\rm true}$:

$$m_{\rm true} = m_{\rm inst} + Z + kX, \tag{4.24}$$

where Z is a photometric zero-point offset between catalogued standard and instrumental magnitudes, k is the atmospheric extinction coefficient and X is the air mass. X can be calculated and is simply the ratio of the thickness of the atmosphere at the observing altitude to zenith, depending solely on the zenith angle of the observations which is calculated using celestial coordinates of the target, the time of observation, and the location of the observatory. k and Z can be determined by interspersing the target observations with observations of standard stars. Suitable standard stars are generally chosen from a catalogue

of known standard stars and k and Z are then derived by using a least-squares interpolation or similar. For space-based telescopes, no air mass correction is required, only the zero-point offset to the preferred photometric system.

4.2.2 Optical spectroscopy

To obtain the optical spectra of a stellar object, a spectrograph is attached to the telescope. Spectrographs work by observing an object through a slit aperture and diffracting the incoming light with a grating onto the detector. As a consequence of multiple orders of diffraction, filters are used between the diffraction grating and the CCD to remove the higher order diffraction patterns and isolate the wavelength of interest. To ensure that the target is well-centred in the slit, through-slit acquisition images are acquired at the beginning of spectroscopic observations.

In order to have a usable spectrum, the instrumental effects of the detector must first be removed with bias and flat-field images. The spectra are then wavelength calibrated with comparison-lamp spectra observations to convert the pixel scale to a wavelength scale. Comparison lamps are filled with a combination of gases for which the wavelengths of emission lines are well known. With line lists[7] and sample spectra, the wavelength dispersion ($\Delta\lambda$) per pixel and instrumental resolution of the spectrograph ($\delta\lambda$) are calculated. This calibration is temperature dependent and may need to be carried out multiple times throughout the observing night. The spectrum of the target is then extracted, creating a two-dimensional spectrum along the dispersion axis. Following the wavelength calibration and spectrum extraction, the continuum can be normalised by fitting a polynomial function to the spectrum of the target (avoiding spectral lines) and dividing through by this function.

4.2.3 Infrared image reduction

Due to the presence of background emission from the atmosphere (such as airglow) and even the telescope itself, IR photometry can be challenging, requiring an accurate subtraction of the background emission, which can be changing constantly. IR emission also may be affected by atmospheric water vapour, which must also be taken into account.

[7]Such as http://www.eso.org/observing/dfo/quality/FORS2/qc/lsswlc/FORS_CompLines.dat for the Focal Reducer and Low Dispersion Spectrograph 2 (FORS2) detector on the Very Large Telescope (VLT).

IR observation and reduction principles are very similar to those described at optical wavelengths, with a few small additions. In a typical experiment, an IR observation is composed of multiple, short exposure images with slightly offset (*dithered*) fields of view. This offset is created by shifting the internal mirror while maintaining the telescope's pointing. This technique can help correct for bad pixels, cosmic rays, and background saturation, as well as background emission. Raw images also contain significant background emission, which must be subtracted to improve the image quality. The background sky image is created by combining the offset-dithered images and determining the median value for each pixel. The likelihood that a pixel will coincide with a source in the majority of images depends both on the number of offset images and how crowded the field is. Therefore, it may be necessary to observe a much larger field than required to ensure that a reliable background value for each pixel is obtained.

In a typical observation, each dithered science image is divided by a flat-field frame before the background is subtracted. The frames are then aligned, co-added and cropped to produce a single IR image, from which the magnitude of the target star can be determined in the same way that it is for optical observations (Section 4.2.1).

As is the case for optical procedures, IR observation and reduction procedures may differ between detectors. For example, the Very Large Telescope (VLT) Imager and Spectrometer for the mid-Infrared (VISIR) instrument uses a method referred to as chopping and nodding (chop/nod) to suppress the bright IR background. In the chopping part of the technique, two sets of observations are performed. One set of exposures includes the target and background while the second set is offset and doesn't include the target, measuring just the background. The instrument alternates between these two sets at a rate faster than the rate of the background fluctuations (usually $\sim$0.25 Hz) by shifting the secondary mirror. The background is then subtracted away from the target observations. However, some residuals due to the difference in optical path may remain (which vary at a time-scale that is long compared to that of the sky). These residuals are accounted for with the nodding part of the technique, which is where the telescope is pointed off-source (to an area of similar air-mass) and the chopping observations are repeated. This provides an estimate of the optical path residuals which are then subtracted from the target observations.

4.3 X-ray observations

X-ray detectors orbit the Earth to avoid the absorbing effects of the Earth's atmosphere. Raw data from these satellites can be accessed from the National Aeronautics and Space Administration's (NASA) High Energy Astrophysics Science Archive Research Center (HEASARC)[8] public archives. This section outlines the basics of X-ray data reduction as described by Arnaud et al. (2011).

4.3.1 Spectral analysis and modelling

The X-ray spectrum of a source is measured as the number of counts C in each instrumental channel N. For a perfect instrument in a theoretical experiment, each energy would be mapped to a single channel and all observed X-ray photons would be emitted from the target source. However, with a real detector there will be some spread in the response and X-rays of energy E may be smeared across a number of channels, as well as counts from background emission. Therefore, to extract the true spectrum of an X-ray source, the instrumental response and the X-ray background must be taken into consideration.

The instrumental response $R(N, E)$ is proportional to the probability of a photon of energy E being detected in channel N. The response matrix is provided by the observatory and is determined prior to the launching of the telescope with detailed simulations. Following telescope launch, measurements of calibration sources allow the observatory to make any necessary fine corrections.

To obtain the measured spectrum $C(N)$, the background counts $B(N)$ must be subtracted from the raw data. The average X-ray background count rate and statistical uncertainty are calculated by selecting a source-free region of the sky or an annulus centred on a specific astronomical object. The background count rates for the combined bands are simply the sum of the count rates for each component band, and the uncertainty in the combined band count rate is the square root of the sum of the squares of the uncertainties of each component band.

Following the removal of the background, the source spectrum $S_{\rm spec}$ relates to the measured spectrum $C(N)$ and the instrument response such that

$$C(N) = \int_0^\infty S_{\rm spec}\, R(N, E)\, \mathrm{d}E. \tag{4.25}$$

However, $S_{\rm spec}$ cannot be inferred by inverting Equation 4.25 due to non-unique solutions. Therefore, a model spectrum must first be chosen. The model, which is

[8] http://heasarc.nasa.gov/

described by a number of parameters, is convolved with the instrument response, and then fit to the observed data. By comparing the predicted number of counts $C_{\rm p}(N)$ in an energy band (from the model) to the observed number of counts, the model parameters can be adjusted to provide a best fit.

The best estimates of the model parameters are generally inferred through χ^2 minimisation, where the spectral model parameters are adjusted until the minimum χ^2 is reached.

$$\chi^2 = \sum \frac{|C(N) - C_{\rm p}(N)|}{\sigma(N)^2}, \tag{4.26}$$

where $\sigma(N)$ is the uncertainty in the number of counts in channel N, which is estimated as $\sigma(N) = \sqrt{C_{\rm p}(N)}$. The best fit is then determined when the reduced chi-squared (χ^2/dof, where dof is the number of degrees of freedom) is close to unity, i.e. when $\chi^2/dof \approx 1$. A reduced-χ^2 much larger than one indicates that the model is a poor fit, while a reduced-χ^2 much less than one indicates that either the model is over-parameterised or the uncertainties in the data are not constraining (or over-estimated).

Chapter 5

Constraining the system parameters of MAXI J1836−194

Adapted from:
T. D. Russell, R. Soria, C. Motch, M. W. Pakull, M. A. P. Torres, P. A. Curran, P. G. Jonker, and J. C. A. Miller-Jones (2014), 'The face-on disc of MAXI J1836-194' *Monthly Notices of the Royal Astronomical Society*, Volume 439, Issue 2, p.1381-1389, DOI:10.1093/mnras/stt2480

In this chapter we present the results of an optical spectroscopic study of the X-ray transient MAXI J1836−194, expanding on preliminary VLT results presented by Pakull and Motch (2011). We show that the optical/UV signatures of an accretion disk were already present in the first few days after the discovery of the outburst although the optical/Near-IR (NIR) band contained a significant contribution from the jet. We then use these signatures to infer the inclination i of the accretion disk. With *Swift* Ultraviolet/Optical Telescope (UVOT) and European Southern Observatory (ESO) New Technology Telescope (NTT) measurements of the optical luminosity in quiescence, we also constrain the size of the donor star and hence the orbital period of the binary system, as well as place a lower limit on the black hole mass.

5.1 Observations and data reduction

5.1.1 VLT

MAXI J1836−194 was observed during its 2011 outburst with the FOcal Reducer and low dispersion Spectrograph (FORS2) on the VLT as a target of opportunity during the implementation of Program 087.D-0870 (PI: M. Pakull). The target was observed on 2011 August 31, between Modified Julian Date (MJD) 55804.99–55805.05, and 2011 September 1 (MJD 55805.99–55806.02). We used the 1200B grism, covering the wavelength range from 3729 Å to 5200 Å ('blue spectra'), and the 1200R grism, from 5869 Å to 7308 Å ('red spectra'). The first night consisted of four 900 s observations for the blue spectra and four 450 s observations for the red spectra, while the second night consisted of two 900 s observations and two 450 s observations for the blue and red spectra respectively.

Calibration data (bias, flatfield and wavelength calibrators) were acquired following the standard calibration plan, implemented at the beginning or the end of the observing nights. We used the same slit width (1″.0) for all observations, giving a spectral resolution of 2.3 Å for the red spectra and 1.9 Å for the blue spectra on the first night, and 1.6 Å for both the red and the blue spectra on the second night. The orientation of the slit was at a parallactic angle of 112.5° on the first night, and 141.3° on the second night. We took B-band sky and through-slit acquisition images each night before starting our spectroscopic observations to confirm that the target was well centred in the slit. The average FWHM seeing, estimated at 5000 Å, was 1″.18 for the blue spectra and 1″.51 for the red spectra on the first night, and 0″.81 and 0″.68 respectively on the second night.

The data were reduced with ESOREX version 3.9.6 and the FORS2 kit recipes version 4.8.7 (Appenzeller et al., 1998) were used to correct raw frames for bias, apply flat-fields and to apply wavelength calibration. Arc images of He, Hg and Cd, as well as Hg, Cd, Ar and Ne lamps provided wavelength solutions for the 1200B and 1200R grisms respectively, yielding a wavelength accuracy of ~ 0.05Å for both the blue and red spectra (taken from the scatter of the fit to all the arc lines). One-dimensional spectra were extracted from the wavelength calibrated image using a Munich Image Data Analysis System (MIDAS; Banse et al. 1988) procedure optimised for providing the best signal to noise ratio. We then used the Image Reduction and Analysis Facility (IRAF; Tody 1986) tasks `rvcorrect` and `dopcorrect` to correct the spectra for the relative radial velocity of the Earth, shifting the wavelength scale to the heliocentric system. We also used standard

IRAF tasks to combine and/or compare the spectra from the two nights. We then normalised the spectrum to the continuum with an 8$^{\rm th}$ order cubic spline, where we masked the Balmer lines (including their broad absorption components), the interstellar lines, He II λ4686 and the Bowen blend. We then measured the main properties of the lines (central position, full-width at half-maximum, equivalent width) with the IRAF task `SPLOT`, where the errors are taken as the statistical error in the Gaussian fit, and verified the results with the fitting package Quick and Dandy Plotter (QDP; Tennant 1991).

5.1.2 *Swift*/UVOT

Swift/UVOT monitored MAXI J1836−194 every few days during its 2011 outburst and 2012 re-flaring. Observations in six optical/UV filters were made with the UVOT (Roming et al., 2005), of which we use the three optical filters (u, b and v) that provide the strictest constraints on the luminosity of the donor star. UVOT data were pre-processed at the *Swift* Data Centre (Breeveld et al., 2010) and reduced using standard *Swift* pipelines. The FTOOLS[1] (Blackburn, 1995) task `uvotimsum` was used to combine all images from the same filter. We used `uvotsource` and a suitable background region to extract an aperture photometry magnitude from a source region of 2″.5 radius, centred on the UVOT position. Magnitudes are based on the UVOT photometric system, which differs from the Bessell system by $V - v < 0.04$ mag (for all colours) and $B - b < 0.04$ mag (for colours $b - v < 1.5$ mag; Poole et al. 2008). The differences between the UVOT and Bessell photometric magnitudes are small compared to the uncertainty in our photometry (see Section 5.2.1) and we therefore treat the UVOT v and b magnitudes as standard V and B magnitudes.

5.1.3 NTT

We obtained optical images during quiescence using the ESO Faint Object Spectrograph and Camera (EFOSC2; Buzzoni et al. 1984) mounted on the NTT at La Silla Observatory, Chile. On 2013 June 11 three observations were acquired in the Gunn i-band with an exposure time of 300 s and a FWHM seeing of 1″.0–1″.1. On 2013 June 12 and 13 single exposures of 300 s were obtained in the Gunn g, r and i-band filters with a seeing in the i-band of 1″.1 and 0″.7, respectively. Sky conditions were not photometric on all three nights, so additional 10, 30 and 60 s

[1] http://heasarc.gsfc.nasa.gov/ftools/

exposures of the field were obtained on June 12 and 13 to enable absolute flux calibration of the frames relative to data from the American Association of Variable Star Observers (AAVSO) Photometric All-Sky Survey data release 7 (APASS; Henden et al. 2009). We used 2×2 on-chip binning during the observations, providing a scale of approximately $0''.24$ per pixel. Frames were bias subtracted and then flat-fielded using dome flat-field observations. Given the faintness of the optical sources under study (see Figure 5.1, bottom panel), we excluded data with image quality worse than $1''.0$ FWHM seeing.

We applied point-spread function fitting on the images using `daophot` in IRAF to compute the instrumental magnitudes of the detected stars. Flux calibration of the field was performed using APASS objects in the MAXI J1836−194 field, achieving zero-point errors < 0.1 mag. Differential photometry was performed to derive the fluxes of the sources of interest. The atmospheric calibration of the frames was defined by fitting for the reference point position, the scale and the position angle. As a first step, we obtained an astrometric solution on a 10-second *i*-band exposure. By comparing the positions of stars against entries from the fourth U.S. Naval Observatory CCD Astrograph Catalogue (UCAC4; Zacharias et al., 2013), we found nine suitable UCAC4 sources well distributed on the image that were not saturated or blended and appear stellar. We obtained a solution with 0.0788 arcsecond rms residuals. We then used the sources from this 10 s *i*-band image as secondary astrometric calibrators for our 300 s images. Taking into account uncertainties (including the systematic $0''.05$ uncertainty that is inherent to the UCAC4 catalogue) we estimated a positional accuracy of $0''.13$. Additionally a publicly-available 30 s *i*-band image of the field obtained during outburst with the Faulkes telescope on 2011 September 15 was calibrated using the same secondary reference tiers as for the 300 s NTT images. This frame was acquired with a $0''.3$ per pixel scale under a seeing of $1''.2$ FWHM and shows the optical counterpart at a J2000 position of right ascension (R.A.) = 18:35:43.451 and declination (DEC) = −19:19:10.43.

5.2 Results

5.2.1 Optical photometry

During the two nights of VLT observations (2011 August 31, 2011 September 01), MAXI J1836−194 was detected as one of the brightest optical sources in the field (Figure 5.1, top left panel). Quasi-simultaneous *Swift*/UVOT observations on the

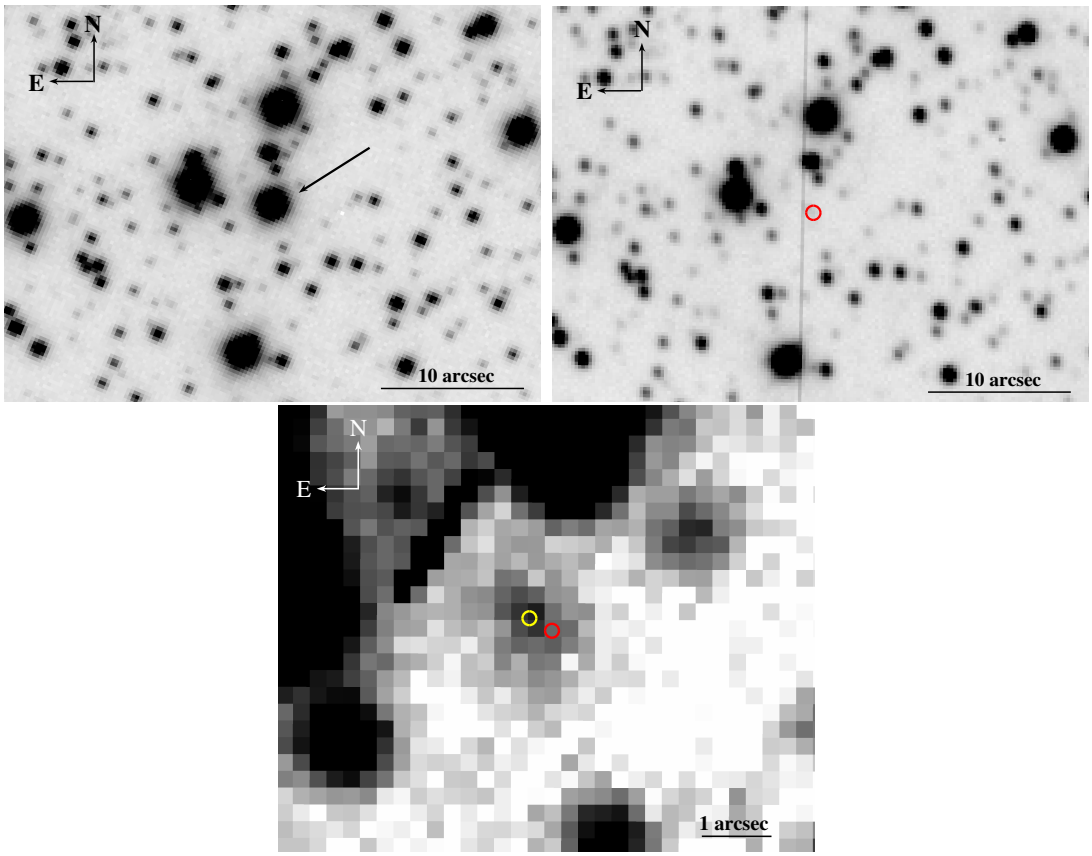

Figure 5.1: Top left panel: B-band image of MAXI J1836−194 (marked by an arrow) and surrounding field, taken with VLT/FORS2 on 2011 August 31 as an acquisition image before our spectral observations. Top right panel: i-band NTT image of the same field taken on 2013 June 13, after the system had returned to quiescence, where the red circle of radius 0″.5 indicates the outburst position of the system. Bottom panel: Another i-band NTT image of the field taken on 2013 June 11 of the system in quiescence. Here the yellow circle of radius 0″.08 shows the unrelated field star at a J2000 position of R.A.= 18:35:43.474 and DEC= −19:19:10.25, while the red circle of radius 0″.08 shows the fitted location of the optical counterpart detected during outburst, at the J2000 position of R.A.= 18:35:43.451 and DEC = −19:19:10.43. The optical counterpart of MAXI J1836−194 is no longer detected.

same nights provided an accurate measurement of its optical/UV brightness and colours: we obtained $u = 16.43 \pm 0.08$ mag, $b = 17.12 \pm 0.08$ mag, $v = 16.37 \pm 0.08$ mag on the first night, and $u = 16.39 \pm 0.07$ mag, $b = 16.97 \pm 0.07$ mag, $v = 16.40 \pm 0.07$ mag on the second night (Figure 5.2).

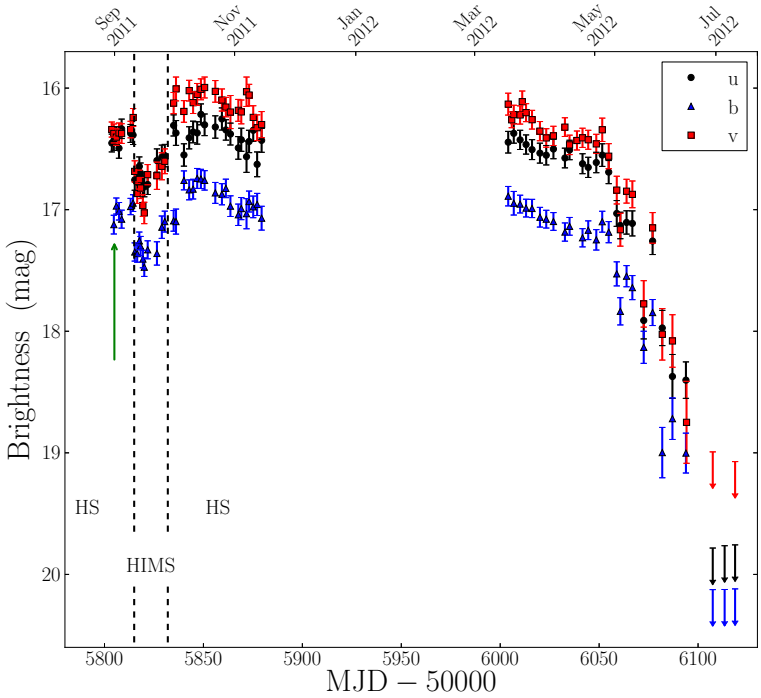

Figure 5.2: *Swift*/UVOT lightcurve, showing the 2011 outburst and decline towards quiescence. The date of the first VLT observation is marked by the green arrow. The state transitions are marked by the vertical dashed lines, HS denotes the hard state and HIMS is the hard intermediate state, where the states are defined by X-ray spectral and timing properties presented by Ferrigno et al. (2012).

Instead of brightening as the source moved into the HIMS, the optical/UV luminosity decreased; on 2011 September 17, we measured $u = 16.79 \pm 0.08$ mag, $b = 17.33 \pm 0.07$ mag, $v = 17.18 \pm 0.07$ mag from *Swift*/UVOT (Figure 5.2). The optical/UV dimming is discussed further in Section 5.3. We used the *Swift*/X-ray Telescope (XRT) data where the soft, disk-like component of the XRT spectra was largest (mid-September; see Chapter 7) to infer the most important disk parameters; in particular, in the context of this work, the outer disk radius and X-ray reprocessing fraction.

MAXI J1836−194 underwent a re-brightening during March 2012, followed by a decline to quiescence (Krimm et al., 2012; Yang et al., 2012). In the last three *Swift*/UVOT observations of 2012 June 29, July 5 and July 10, the optical counterpart was not visible, nor was it found in the stacked image from the three datasets. We take the detection limit for that combined image as the best-

available 3σ upper limit to the quiescent optical flux in the u, b and v bands: $u > 20.5$ mag, $b > 20.8$ mag, $v > 19.5$ mag (Table 5.1).

Table 5.1: Upper limits on the magnitude and magnitude minus the distance modulus (Section 4.2.1) of MAXI J1836−194 during quiescence; u, b and v upper limits are determined from the summed *Swift*/UVOT images of 2012 June 29, July 05 and July 10, while the g, r and i upper limits are from the 2013 June 12 and 13 NTT images of the system in quiescence. The distance ranges presented cover the extent of plausible distances to the source (derived from the temperature and flux of the disk; see Chapter 7) and magnitudes presented are not corrected for extinction.

Filter	Magnitude	Mag−dm			
		4 kpc	6 kpc	8 kpc	10 kpc
u	> 20.5	> 7.5	> 6.6	> 6.0	> 5.5
b	> 20.8	> 7.8	> 6.9	> 6.3	> 5.8
v	> 19.5	> 6.5	> 5.6	> 5.0	> 4.5
g	> 24.0	> 11.0	> 10.1	> 9.5	> 9.0
r	> 23.7	> 10.7	> 9.8	> 9.2	> 8.7
i	> 23.5	> 10.5	> 9.6	> 9.0	> 8.5

Our more recent NTT images of the system in quiescence (Figure 5.1, top right and bottom panels) show a number of blended sources near the location of MAXI J1836−194 (Figure 5.1, bottom panel). The brightest of these sources is a point-like object at a J2000 position of R.A.= 18:35:43.474 DEC= −19:19:10.25. PSF photometry yields $i = 21.4 \pm 0.1$ mag (2013 June 11) and $g = 23.7 \pm 0.2$ mag, $r = 22.4 \pm 0.1$ mag and $i = 21.6 \pm 0.2$ mag (2013 June 13). This source is $0''.37$ away ($0''.32$ in R.A. and $0''.18$ in DEC) from the position derived for the optical counterpart to MAXI J1836−194 during outburst (R.A = 18:35:43.451 and DEC = −19:19:10.43, J2000; Section 5.1.3). Given that the images were astrometrically calibrated using the same reference stars, the uncertainty in the separation between the two objects is dominated by the uncertainty in the determination of the target profile centre. Using different algorithms implemented in IRAF to calculate these positions (centroid, Gaussian and PSF fitting), we derive positional uncertainties of $0''.06$ and $0''.08$ in R.A. and DEC, respectively (from the different fitting algorithms), for the source found in the NTT images. The positional uncertainties are negligible for the bright optical counterpart detected in outburst. Therefore, the separation between the two objects is significant (5σ

in R.A.), showing that the object in the NTT images is a field star unrelated with the transient. South-West from this source there is evidence for unresolved emission overlapping the expected position for the transient. At the position of MAXI J1836−194, we derive 3σ upper limits of $g > 24.0$ mag, $r > 23.7$ mag and $i > 23.5$ mag for the best quality images (Table 5.1), which we take as an upper-limit on the magnitude of the companion star.

5.2.2 Optical spectroscopy

Our early outburst VLT spectra (Figure 5.3) show clear signs of an optically-thick, X-ray irradiated accretion disk; rotationally-broadened He II λ4686, Hα, Hβ and Hγ emission in a broad absorption trough, the Bowen region at $\lambda \sim 4630$–4640 Å, as well as other rotationally-broadened H I absorption lines from the Balmer series (identifiable up to H_{10}) and He I absorption lines, consistent with findings presented by Pakull and Motch (2011).

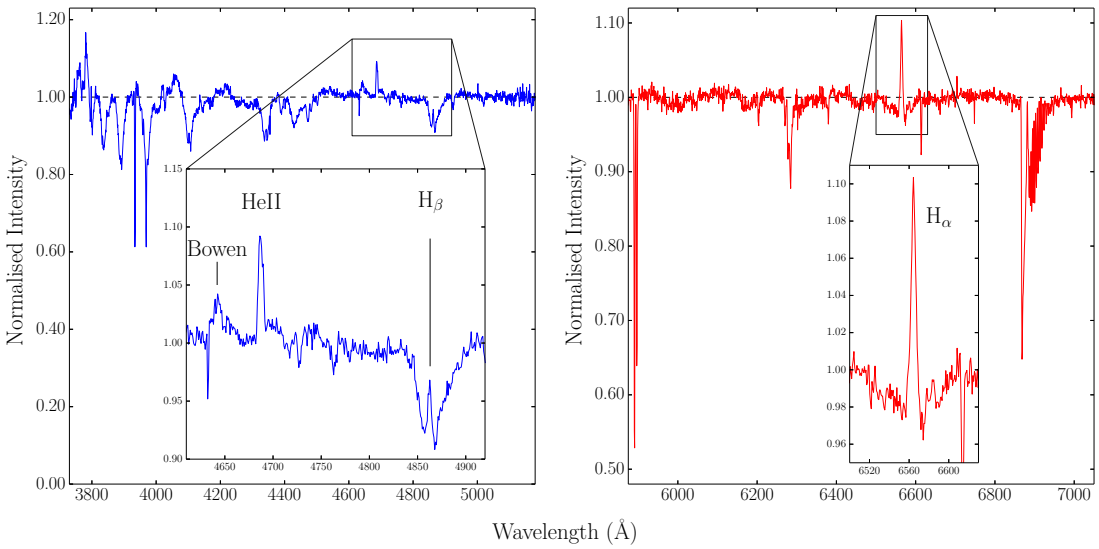

Figure 5.3: Left panel: averaged blue spectrum of MAXI J1836−194 obtained 2011 August 31 and 2011 September 01, with a zoomed portion showing the He II λ4686, Hβ and Bowen region. Right panel: averaged red spectrum from August 31 and September 01, with a zoom of the Hα peak. Continuum intensities have been normalised at one.

We fitted Gaussian profiles to a selection of the de-blended Balmer emission and absorption components (Table 5.2). We found equivalent widths (EW) of the emission components, measured from the two-night combined spectrum, to

Table 5.2: The intrinsic full width at half maximum (FWHM), equivalent width (EW) and the de-reddened flux within the line for some notable lines at the onset of the 2011 outburst, along with their rest wavelengths. Negative values for the EW represent emission and positive represent absorption. Both the emission core and broad absorption of Hα, Hβ, and H$_\gamma$ were recorded.

Line	Rest wavelength (Å)	FWHM (Å)	EW (Å)	Emitted flux $\times 10^{-15}$ (erg s^{-1} cm^{-2})
Hα(emis.)	6562.8	6.0±0.2	−0.83±0.02	3.15±0.09
Hα(abs.)		≈ 50	1.20±0.05	–
Hβ(emis.)	4861.3	4.0±0.4	−0.25±0.03	1.5±0.2
Hβ(abs.)		35.1±0.9	2.54±0.07	–
Hγ(emis.)	4101.7	4.2±0.7	−0.15±0.03	1.0±0.2
Hγ(abs.)		23±2	2.5±0.1	–
He II λ4686	4686	5.5±0.3	−0.52±0.03	3.2±0.2
Bowen blend	∼4640–4650	–	−0.58±0.06	3.9±0.4

be: H$\alpha = -0.83 \pm 0.02$ Å, Hβ emission core $= -0.25 \pm 0.03$ Å and Hγ emission core $= -0.15 \pm 0.03$ Å (where negative EWs represent emission and positive EWs represent absorption). We find EWs for the Hβ and Hγ absorption components of 2.54 ± 0.07 Å and 2.5 ± 0.1 Å, respectively. For the broad and shallow Hα absorption trough, the FWHM is not well constrained due to the strong emission line, but we estimate the FWHM to be ≈ 50 Å and the Full Width at Zero intensity (FWZI) to be ≈ 90 Å. The de-reddened fluxes of the Balmer series and He II λ4686 line are presented in Table 5.2 and will be discussed further in Section 5.3 (see Appendix A, for a full description of extinction and reddening). We determined the reddening, $E(B-V) = 0.53^{+0.03}_{-0.02}$ mag, by fitting an irradiated disk model to the broadband optical/UV/X-ray spectrum with the X-Ray Spectral Fitting Package (XSPEC; Arnaud 1996), see Chapter 7 for full analysis. Diffuse interstellar bands provided an alternative estimate of the extinction. In particular, the λ4430 interstellar band is clearly visible with a central absorption of 6.5% corresponding to $E(B-V) = 0.6^{+0.2}_{-0.1}$ mag (Krelowski et al., 1987). We also get similar results from the λ6284 interstellar band using the calibration from Jenniskens and Desert (1994). Results from Marshall et al. (2006) indicate that there is an absorption layer of $E(B-V) \approx 0.5$ mag located within 2 kpc in the

direction of the source, providing a lower limit on the distance to the source.

Table 5.3: Line positions and calculated systemic velocity for each individual night and for the two-night combined spectrum. The 1σ uncertainties in the stronger lines (Hα, Hβ and He II λ4686) are $\pm$0.2 Å and $\pm$0.3 Å for all other lines. The average recessional velocity was determined by averaging the velocity shifts for each night, as well as that of the combined spectra.

Line (Å)	Night 1 (Å)	Night 2 (Å)	Combined (Å)
Hα 6562.8	6564.1	6563.7	6563.8
Hβ 4861.3	4862.4	4861.9	4862.3
Hγ 4340.5	4341.2	4341.3	4341.3
Hδ 4101.7	4102.0	4102.1	4102.1
H_8 3889.1	3890.3	3889.7	3889.7
H_9 3835.4	3836.4	3836.2	3836.3
H_{10} 3799	3800.1	3799.7	3800.0
He I 4026.2	4027.0	4027.3	4027.0
He I 4143.8	4145.2	4145.1	4145.0
He I 4387.9	4389.0	4388.9	4389.0
He I 4471.5	4472.5	4472.0	4472.5
Mg II 4481.3	4482.1	4482.2	4482.1
He II 4686	4686.9	4686.7	4686.8
Velocity (km/s)	68 ± 20	55 ± 17	61 ± 15

We determined the heliocentric velocity of the disk on both nights by fitting Gaussian profiles to a selection of suitable emission and absorption lines (Table 5.3) and measuring their average velocity shifts. The average recessional velocity is $68 \pm 20\,\mathrm{km\,s^{-1}}$ for the first night of VLT observations, $55 \pm 17\,\mathrm{km\,s^{-1}}$ for the second night and $61 \pm 15\,\mathrm{km\,s^{-1}}$ for the combined two-night spectrum. We also obtain consistent velocity shifts when we use only the sample of emission lines ($59 \pm 9\,\mathrm{km\,s^{-1}}$) or the sample of absorption lines ($60 \pm 16\,\mathrm{km\,s^{-1}}$); we thus conclude that both emission and absorption lines in Table 5.3 come from the disk surface. In principle the recessional velocity may be different on each night due to the orbital phase of the system because the disk follows the orbital motion of the black hole. However, from the derived system parameters (presented in Section 5.3) we verify that the amplitude of the projected radial velocity of the black hole

around the centre of mass is $\sim$9 km s^{-1} for a 5 $M_\odot$ black hole and $\sim$5 km s^{-1} for a 12 $M_\odot$ black hole, so this effect is well within the uncertainties from our averaged velocities.

The Hα and He II λ4686 lines are single-peaked and narrower than typically observed in Galactic LMXBs. Therefore, instead of using the peak-to-peak separation, we use their FWHM to provide an approximation of twice the projected Keplerian velocity of the disk annulus of the emitting region. For Hα we measure a Gaussian FWHM of 6.40±0.20 Å for night one and 5.75±0.20 Å for night two. The He II λ4686 line profile produces FWHM=5.57±0.30 Å on night one and FWHM = 5.43±0.30 Å on night two. We deconvolved the instrumental resolution for both the red and the blue spectra on the second night (seeing limited). Averaging the intrinsic FWHMs from both nights, we obtain a velocity of 260 ± 6 km s^{-1} for Hα and 333 ± 14 km s^{-1} for He II λ4686. We assume that this corresponds to approximately twice the Keplerian velocity of the disk rings that give the highest contribution to those emission lines, and we use these results to determine the disk inclination (Section 5.3.2).

5.3 Analysis and Discussion

During the first few days after the discovery of the outburst, MAXI J1836−194 was in the hard spectral state with a significant contribution to the optical/UV emission from the optically-thin synchrotron emission from the radio jet (a spectral index of $\alpha = -0.6 \pm 0.1$, where flux density $S_\nu \propto \nu^\alpha$), see Section 7.3.2 for further discussion. In addition to this power-law synchrotron component, the optical emission on 2011 August 31 (night 1) and September 1 (night 2) contained a multicolour thermal component from the irradiated accretion disk. From multi-wavelength spectral fitting, we estimate that ≈55% of the B-band flux, and ≈70% of the V-band flux came from the synchrotron component on those dates (see Chapter 7). Two weeks after the VLT observations, the disk became the dominant source of optical emission, not because of a dramatic increase in its flux, but because of the temporary disappearance of the synchrotron component due to jet quenching (Section 7.3.2), resulting in a reduction in the total optical/UV emission (Figure 5.2).

5.3.1 Emission lines

The emission lines or cores of the Balmer series are seen clearly at Hα, Hβ and Hγ, with Hβ and Hγ being dominated by pressure-broadened absorption troughs (Mayo et al., 1980). In particular, the FWHM of the Hα and Hβ absorption troughs are $\approx$50 Å and $\approx$35 Å, respectively, while the FWZI of the Hα and Hβ absorption troughs are $\approx$90 Å and $\approx$75 Å, similar to other Galactic LMXBs (e.g. GRO 1655−40 and XTE J1118+480; Soria et al. 2000; Torres et al. 2002).

While the spectra look remarkably similar, the EW of the Hα emission line (-0.83 ± 0.02 Å) is much smaller (in absolute value) than what is usually found in Galactic black hole transients early in an outburst, when typical magnitudes of the equivalent widths are $\sim$ 3–6 Å (Fender et al., 2009). The reason for this significantly lower EW is the optically-thin synchrotron component from the jet dominating the red part of the optical spectrum, which we shall argue in Section 5.3.2 is due to beaming because of the face-on nature of the system. Accounting for the jet component (full model presented in Chapter 7), we find that the EW of Hα with respect to the disk continuum alone is in fact -4.2 ± 0.1 Å, similar to other Galactic XRBs (Fender et al., 2009). Similarly, the EW of He II λ4686 with respect to the total blue continuum is -0.52 ± 0.03 Å, but with respect to the disk continuum alone is -1.6 ± 0.1 Å. The corrected EWs with respect to the disk component imply that the conditions in the disk in terms of optical depth and irradiation are similar to other LMXBs in the early stages of outburst.

From the de-reddened fluxes we find a Balmer decrement of $f_{\mathrm{H}\alpha}/f_{\mathrm{H}\beta}$=2.1 $\pm$ 0.3, lower than the canonical value of $\approx$ 2.87 valid for Case-B recombination of optically thin gas at $T \approx 10^4$ K (Osterbrock and Ferland, 2006); also, the ratio of $f_{\mathrm{H}\gamma}/f_{\mathrm{H}\beta} = 0.71 \pm 0.2$ is slightly higher than the expected Case-B recombination value of $\approx$ 0.466 (Osterbrock and Ferland, 2006). The most likely explanation of such a discrepancy is that the lines are emitted in a layer with high electron density and optical depth, $\tau_{\mathrm{H}\alpha} > 1$, where the collisional excitation and de-excitation becomes dominant and case-B recombination is no longer valid. From Drake and Ulrich (1980), the measured Balmer ratios from our spectra suggest an electron density of $\sim 10^{12}$–10^{14} cm^{-3}, consistent with their expectations for the upper layers of an optically-thick accretion disk.

For He II λ4686 we assume instead that collisional processes are not significant, at least in the outer disk. In this case the de-reddened flux of this line, $f_{\mathrm{HeII}} = (3.2 \pm 0.2) \times 10^{-15}$ erg cm^{-2} s^{-1} = $(7.5 \pm 0.4) \times 10^{-4}$ λ4686 photons cm^{-2} s^{-1}, can be used to estimate the fraction of X-ray luminosity intercepted by the disk.

Following Pakull and Angebault (1986), for X-ray photoionised gas, the He II λ4686 photon flux is proportional to the illuminating flux of ionising photons above 54 eV; for an optically-thick region, the scaling factor is simply the ratio between the He^+ recombination coefficient (summed over all levels above the ground state) and the effective recombination coefficient for the $n = 4 \rightarrow 3$ transition. This ratio varies between ≈ 4.2 and ≈ 6.3 for temperatures $T \approx 10,000$–$40,000$ K (Osterbrock and Ferland, 2006), and implies that approximately one He II λ4686 photon is emitted for every $\sim$ 4–6 UV/X-ray photons that are intercepted by the disk. The unabsorbed, isotropic photon flux above 54 eV measured from *Swift*/XRT data taken on August 31 is ≈ 3.9 photons $cm^{-2}\,s^{-1}$ (Chapter 7), meaning that we should observe approximately (0.65–0.98) f_{out} λ4686 photons $cm^{-2}\,s^{-1}$, where f_{out} is the disk interception and reprocessing fraction. As $\approx 7.5 \times 10^{-4}$ λ4686 photons $cm^{-2}\,s^{-1}$ are observed this means that the outer accretion disk must be intercepting $\sim 10^{-3}$ of the UV/X-ray photons that are emitted from closer to the black hole; this reprocessing fraction is in good agreement with theoretical models (Vrtilek et al., 1990; de Jong et al., 1996; Hynes et al., 2002; Gierliński et al., 2009), demonstrating that, even at this early stage of the outburst, the accretion disk is already relatively large, bright and optically thick.

5.3.2 Inclination angle of the disk

The profiles and widths of the Hα and He II λ4686 emission lines are good indicators of the Keplerian rotational velocity of the disk annuli responsible for their emission. Instead of the usual flat-topped or double-peaked profile (Paczyński, 1977; Smak, 1981), we observe single-peaked and relatively narrow Hα and He II λ4686 profiles (Figure 5.3), which are indicative of a face-on accretion disk (Smak, 1981). Using the FWHM provides a good approximation of twice the Keplerian velocity of the disk annulus that contributes most to the line emission[2].

First, we determined whether the peak of the Hα emission originates in the outermost disk annulus, that is, whether $R_{H\alpha} \approx R_{out}$. To determine R_{out}, we modelled the broadband optical/UV/X-ray spectrum (see Chapter 7 for full model

[2]In fact, the FWHM is a slight overestimate of the projected rotational velocity (Smak, 1981), but the difference is $\lesssim 10\%$ for the moderately flat radial temperature profile expected in the outer region of an irradiated disk. In the absence of more direct measurements, the FWHM of the disk lines is a robust and conservative approximation to the projected rotational velocity of the emitting gas; if anything, the true projected rotational velocity may be slightly lower, which would further reduce the inclination angle estimated here.

details) with the irradiated disk model *diskir* (Gierliński et al., 2008) within XSPEC; (Arnaud, 1996); the main free parameters of this model are the colour temperature of the inner disk $T_{\rm in}$, the disk-blackbody normalisation constant K, the fraction of X-ray flux intercepted and reprocessed in the outer disk $f_{\rm out}$, and $R_{\rm out}$ expressed as a function of the inner-disk (fitting) radius $r_{\rm in}$. The X-ray data provide strong constraints on $T_{\rm in}$ and K (and therefore also $r_{\rm in}$; Soria 2007), while the optical/UV data constrain $R_{\rm out}/r_{\rm in}$ and the irradiation fraction. In particular, we find typical irradiation fractions $f \approx 10^{-3}$ (in agreement with what we estimated from the X-ray/λ4686 flux ratio, Section 5.3.1), and typical values of $y \equiv \log(R_{\rm out}/r_{\rm in}) \approx 4.1$. Since $r_{\rm in} \approx D_{10\,\rm kpc}\,[K/\cos(i)]^{1/2}$, we obtain $R_{\rm out} = 10^{y} r_{\rm in} \approx 1.4 \times 10^{11}\cos(i)^{-1/2} D_{10\,\rm kpc}\,\rm cm$. The Rayleigh-Jeans tail of the irradiated outer disk spectrum suggests that $T(R_{\rm out}) \approx 15,000\,\rm K$. This characteristic temperature confirms that the outermost disk annulus must be a strong Balmer emitter (Osterbrock and Ferland, 2006). Therefore, we are justified in assuming that the projected rotational velocity of the outer disk $v_{R_{\rm out}} \approx v_{\rm H\alpha} \approx 130 \pm 4\,\rm km\,s^{-1}$.

Using other well-known analytic models of irradiated disks (Vrtilek et al., 1990; King et al., 1997; Dubus et al., 1999), we obtain a temperature range of ≈10,000–20,000 K for an outer disk radius of $\approx 10^{11}$ cm and an X-ray luminosity $\approx 10^{37}\,\rm erg\,s^{-1}$; typical of this system and consistent with the Hα emission. Even if we did not have any X-ray information available, we could still estimate $R_{\rm out}$ and $T(R_{\rm out})$ simply by fitting a blackbody curve to the characteristic spectral peak in the optical/UV region that is typical of irradiated disks. This approximation can be qualitatively understood from the fact that the outer disk annuli dominate the optical emission by virtue of their large emitting area and moderately flat radial temperature gradient. It can also be quantitatively verified by re-fitting a simple blackbody to the optical/UV peak of a full irradiated disk spectrum. With this simpler method, we obtain a characteristic value of $R_{\rm out} \approx 1.4 \times 10^{11}\cos(i)^{-1/2} D_{10\,\rm kpc}\,\rm cm$ at a temperature $T \approx 15,000\,\rm K$, in agreement with what we obtained from our full optical to X-ray model. We can now write:

$$
\begin{aligned}
v_{\rm H\alpha} \approx v_{\rm out} &\approx \sqrt{\frac{G\,M_{\rm blackhole}}{R_{\rm out}}}\,\sin(i) \\
&\approx \frac{(GM_{\rm blackhole})^{1/2}}{(10^{y} D_{\rm 10kpc})^{1/2}\,K^{1/4}}\,\sin(i)[\cos(i)]^{1/4}, \qquad (5.1)
\end{aligned}
$$

where $v_{\rm H\alpha} \approx 130 \pm 4\,\rm km\,s^{-1}$. The rotational broadening of the emission cores

in higher Balmer lines ($v_{\mathrm{H}\beta} \approx 123\,\mathrm{km\,s^{-1}}$; $v_{\mathrm{H}\gamma} \approx 146\,\mathrm{km\,s^{-1}}$; Table 5.2) is comparable to that of Hα; however, the uncertainty is larger because Hβ and Hγ are dominated by the broader absorption troughs. The rotational broadening of He II λ4686 is slightly higher ($v_{\mathrm{HeII}} = 166 \pm 7\,\mathrm{km\,s^{-1}}$), consistent with peak emission at a characteristic radius $R_{\mathrm{HeII}} \approx 0.6 R_{\mathrm{H}\alpha}$, at higher temperatures. We numerically solve Equation 5.1 for i as a function of distance and black hole mass. We find that MAXI J1836−194 has a face-on disk (Table 5.4), with an inclination i of between 4° and 15° at a 90% confidence limit (where the line-of-sight is normal to the disk plane) for a distance of 4–10 kpc and assuming a black hole mass of between 5–12 $\mathrm{M_\odot}$ (the typical range of Galactic black hole masses; Kreidberg et al. 2012).

Table 5.4: Outer disk radii and inclination angles for a range of plausible black hole masses (Kreidberg et al., 2012) and source distances.

black hole mass	Distance to source (kpc)	$\mathrm{R_{out}}$ ($\times 10^{10}$) cm	Inclination angle (i°)
5 $\mathrm{M_\odot}$	4	$5.3^{+1.3}_{-1.6}$	$7.0^{+2.2}_{-1.0}$
	6	$7.9^{+2.0}_{-2.3}$	$8.5^{+2.7}_{-1.2}$
	8	$10.6^{+2.6}_{-3.1}$	$9.8^{+3.1}_{-1.4}$
	10	$13.2^{+3.3}_{-3.9}$	$11.0^{+3.5}_{-1.5}$
8 $\mathrm{M_\odot}$	4	$5.3^{+1.3}_{-1.6}$	$5.5^{+1.8}_{-0.8}$
	6	$7.9^{+2.0}_{-2.3}$	$6.7^{+2.1}_{-1.0}$
	8	$10.5^{+2.6}_{-3.1}$	$7.8^{+2.5}_{-1.1}$
	10	$13.2^{+3.3}_{-3.9}$	$8.7^{+2.8}_{-1.2}$
12 $\mathrm{M_\odot}$	4	$5.3^{+1.3}_{-1.6}$	$4.5^{+1.4}_{-0.6}$
	6	$7.9^{+2.0}_{-2.3}$	$5.5^{+1.7}_{-0.8}$
	8	$10.5^{+2.6}_{-3.1}$	$6.3^{+2.0}_{-0.9}$
	10	$13.2^{+3.3}_{-3.9}$	$7.1^{+2.3}_{-1.0}$

The inclination angle we determined is much lower than the $\sim 20°$ to $\sim 80°$ range seen in other LMXBs (Muñoz-Darias et al., 2013; Narayan and McClintock, 2005) and could be the reason why this system is so suitable for jet and jet break studies (see Chapter 7), as Doppler boosting would make the jet appear much brighter and may shift the jet break to higher frequencies than in similar systems with a less favourable orientation. The lack of phase-dependent modulation in the *Swift*/UVOT lightcurve (Figure 5.2) supports our conclusion of a face-on accretion

disk, and the flat-topped shape of the hardness-intensity diagram (Ferrigno et al. 2012, figure 5) is also consistent with other relatively low-inclination LMXBs (Muñoz-Darias et al., 2013), even though the system never settled into a full soft state. We also note that the widths of the Balmer absorption troughs are similar between this face-on system and other higher-inclination systems suggesting that the broadening is mostly due to pressure effects, rather than Keplerian rotation.

5.3.3 Donor star size and orbital period

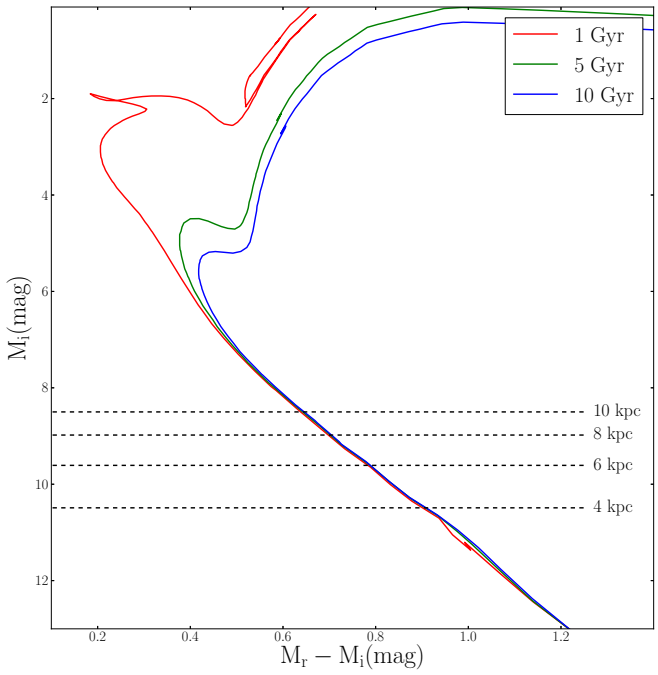

Figure 5.4: Padova stellar evolutionary models for stellar populations of age 1 Gyr, 5 Gyr and 10 Gyr (Bressan et al., 2012), corrected for a reddening of $E(B-V) = 0.53$ mag, to compare with the magnitudes presented in Table 5.1. Coloured lines represent the stellar population of given ages and black dashed lines are the upper limits on the magnitude from quiescent photometric observations.

LMXBs are usually associated with older stellar populations (Zhang et al., 2012). Using solar-abundance isochrones based on the Padova stellar evolutionary models[3] (Bressan et al., 2012) for stellar populations of age 1 Gyr, 5 Gyr and 10 Gyr, we place mass and radius constraints (Figure 5.4) on the companion star from the deepest quiescent luminosity limits of MAXI J1836−194 (Table 5.1).

[3]http://stev.oapd.inaf.it/cgi-bin/cmd

Generating a theoretical stellar population based on the *Swift*/UVOT and NTT photometric systems we find that the donor must be a main sequence star with a mass $<0.65 M_\odot$ and a radius $<0.59\,R_\odot$ (this occurs for a 1 Gyr population at a distance of 10 kpc). The binary period, P, can be determined solely from the mean density ($\bar{\rho}$) of the Roche lobe-filling companion star (Frank et al., 2002),

$$\bar{\rho} = \frac{3M_2}{4\pi R_2^3} \cong \frac{3^5\pi}{8GP^2} \cong 110 P_{\rm hrs}^{-2}\ {\rm g\,cm^{-3}}. \tag{5.2}$$

As the companion is on the lower main sequence, we know that its radius and mass are approximately equal in solar units (Kippenhahn and Weigert, 1990; Frank et al., 2002), hence we place a conservative upper limit on the binary period of <4.9 hours. Table 5.5 presents the maximum allowable companion mass and radius, as well as the binary period for all population ages at distances of 4, 6, 8 and 10 kpc. Our derived mass, radius and orbital period values depend on the extinction. If we consider the lowest plausible reddening of $E(B-V) = 0.5$ mag (see Section 5.2.2) we find that, for all plausible distances, the donor star mass and radius would only reduce by < 0.05 (in $M_\odot$ and $R_\odot$, respectively), and the orbital period would decrease by a maximum of ~ 0.05 hours. If the reddening is increased to $E(B-V) = 0.7$ mag, the limits on the mass and radius increase by < 0.05 (in $M_\odot$ and $R_\odot$, respectively) and the orbital period will only increase by a maximum of 0.5 hours, for all plausible distances. This demonstrates that uncertainty in the extinction does not have a significant effect on our companion star results. The mass and radius limits restrict the donor star to being a K or M type main sequence star with a mass and radius that are consistent with other transient black hole LMXB systems such as GRO J0422+32 and XTE J1118+480 (Remillard and McClintock, 2006).

Table 5.5: Largest possible mass, size and period estimates derived from quiescent *Swift*/UVOT and NTT observations and Padova stellar evolutionary models of different population ages. Presented are the maximum limits for all population ages.

Distance	4 kpc	6 kpc	8 kpc	10 kpc
M_2 ($M_\odot$)	< 0.33	< 0.45	< 0.55	< 0.65
R_2 ($R_\odot$)	< 0.31	< 0.41	< 0.50	< 0.59
Period (hrs)	< 2.7	< 3.4	< 4.1	< 4.9

5.3.4 Black hole mass

From the mass and radius limits we place on the companion star, and the outer disk radius from X-ray analysis (Table 5.4), we are able to infer a lower limit on the black hole mass. The size of the Roche lobe is dependent on the mass ratio ($q = M_2/M_1$) and the binary separation a, approximated by the form (Eggleton, 1983; Frank et al., 2002):

$$\frac{R_{\rm L2}}{a} \approx \frac{0.49q^{2/3}}{0.6q^{2/3} + \ln\left(1 + q^{1/3}\right)}. \tag{5.3}$$

Similarly, we obtain the average Roche lobe radius of the primary by replacing q with q^{-1} in Equation 5.3. The ratio of the two radii is:

$$\frac{R_{\rm L2}}{R_{\rm L1}} \approx \frac{q^{4/3}\left[0.6q^{-2/3} + \ln\left(1 + q^{-1/3}\right)\right]}{0.6q^{2/3} + \ln\left(1 + q^{1/3}\right)} \approx q^{0.45}, \tag{5.4}$$

where the second approximation holds for 0.03<q<1. In Equation 5.4, M_2 and R_2 (= $R_{\rm L2}$) are constrained by the photometric observations in quiescence, and $R_{\rm L1} \approx 1.3\,R_{\rm out}$ (Paczyński, 1977; Whitehurst, 1988) is obtained from the X-ray spectrum of the disk in outburst (as a function of distance). Thus, we can use Equation 5.4 to place a lower limit on the mass of the primary. We find that the compact object must have a mass $M_1 > 1.9\,M_\odot$ if the system is located at 4 kpc, $M_1 > 3.8\,M_\odot$ at 6 kpc, $M_1 > 5.5\,M_\odot$ at 8 kpc, and $M_1 > 7.0\,M_\odot$ at 10 kpc. This confirms that the compact object is a stellar-mass black hole, unless at the lowest projected distance (4 kpc), with a mass comparable to other transient black hole LMXBs (Kreidberg et al., 2012). With this same method, if we could detect and measure the quiescent magnitude of the donor star (rather than just the upper limit) with deeper photometric observations, we could infer the black hole mass without the need for phase-resolved spectroscopic measurements of radial velocity shifts (which are difficult to do in face-on and short-period systems).

5.4 Summary

In this chapter, we have used optical spectroscopic and photometric observations to determine or constrain the binary system parameters of MAXI J1836−194. The main results of this chapter are:

- The inclination angle of the disk is between $\approx 4^\circ$ and $\approx 15^\circ$ for a range of distances suggested by the X-ray luminosity.

- The donor star must be a main sequence K or M star, with a mass of $<0.65\,M_{\odot}$ and a radius of $<0.59\,R_{\odot}$. We also determine that the binary period is <4.9 hr.
- We conclude that the primary is a typical stellar mass black hole with similar mass to other Galactic low-mass X-ray binary transients.

Chapter 6

Radio monitoring of the compact jets of MAXI J1836−194

Adapted from:
T. D. Russell, J. C. A. Miller-Jones, P. A. Curran, R. Soria, D. Altamirano, S. Corbel, M. Coriat, A. Moin, D. M. Russell, G. R. Sivakoff, T. J. Slaven-Blair, T. M. Belloni, R. P. Fender, S. Heinz, P. G. Jonker, H. A. Krimm, E. G. Körding, D. Maitra, S. Markoff, M. Middleton, S. Migliari, R. A. Remillard, M. P. Rupen, C. L. Sarazin, A. J. Tetarenko, M. A. P. Torres, V. Tudose, and A. K. Tzioumis (2015), 'Radio monitoring of the hard state jets in the 2011 outburst of MAXI J1836−194', *Monthly Notices of the Royal Astronomical Society*, Volume 450, Issue 2, p.1745-1759, DOI:10.1093/mnras/stv723

In this chapter we present the full results from an intensive VLA, ATCA and VLBA radio monitoring campaign of MAXI J1836−194, which began during the early phase of the outburst (2011 September 3) and continued until the source became sun-constrained (our last radio observation occurred on 2011 December 3). With these observations we observe the evolution of the radio flux density, morphology and polarisation. With our high-resolution VLBA observations, we determine the orientation of the jet axis and derive the proper motion of the system.

6.1 Observations

6.1.1 Radio observations

VLA

From 2011 September 3 through December 3, we conducted an intensive monitoring campaign on MAXI J1836−194 with the VLA, under project code VLA/10B-218. We report the full 18 epochs of VLA radio observations covering the rise, transition to and from the HIMS, and subsequent decay of the 2011 outburst of MAXI J1836−194. The VLA observations were taken every 2–5 days during the brighter phase of the outburst (September 3 – September 30) and every 1 – 2 weeks as the outburst decayed, until the final observation on 2011 December 3. The array was in its most-extended A configuration until September 12, in the A→D move-configuration until September 18, and thereafter in the most-compact D configuration.

The observations were taken over a wide range of frequencies (between 1 and 43 GHz) with an integration time of 3 seconds for all observations prior to November 11, following which the data were taken with an integration time of 5 seconds. The lowest-frequency 1–2 GHz observations were recorded in two 512-MHz basebands, each containing eight 64-MHz sub-bands made up of sixty-four 1-MHz channels. All other frequencies were recorded in two 1024-MHz basebands comprised of eight 128-MHz sub-bands made up of sixty-four 2-MHz channels. Following standard data reduction procedures within the Common Astronomy Software Application (CASA; McMullin et al. 2007) the data were corrected for shadowing, instrumental issues, and radio frequency interference. 3C286 was used for bandpass and amplitude calibration, J1407+2827 was used as a polarisation leakage calibrator, and phase calibration was performed using the nearby ($\sim 7^\circ$ away) compact source J1820−2528. Calibrated data were then imaged on a per-baseband basis using the multi-frequency synthesis algorithm within CASA and subjected to multiple rounds of self-calibration, down to a typical solution interval of 15 s. To determine the flux density of the source, we fitted a point source to the target in the image plane (Stokes I) and standard VLA systematic errors were added. Stokes Q and U were also measured at the position of the peak source flux density in the lower-frequency (<10 GHz) data (Table 6.1). At no epoch was the source observed to be significantly extended.

Table 6.1: Sample of the VLA flux densities of MAXI J1836−194. Dates are Universal Time (UT). α is the radio spectral index. 1σ errors are uncertainties on the fitted source parameters. Stokes Q and U are given before systematic errors are added. See Appendix C for full radio monitoring results.

Date (UT)	MJD	Frequency (GHz)	Flux density (mJy)	Q (mJy beam^{-1})	U (mJy beam^{-1})	α
2012 Sep 3	55807.1	4.60	27.2±0.3	0.24±0.05	-0.29±0.06	0.64±0.03
		7.90	38.4±0.5	0.67±0.06	-0.49±0.07	
2011 Sep 5	55809.1	5.00	23.2±0.3	0.08±0.02	-0.08±0.02	0.84±0.04
		7.45	32.5±0.4	0.18±0.02	-0.16±0.02	
2011 Sep 7	55811.2	1.50	18.1±0.4	–	–	0.51±0.01
		5.00	28.6±0.7	0.25±0.07	-0.13±0.07	
		7.45	39.3±0.9	0.58±0.09	-0.08±0.08	
		20.80	68±2	–	–	
		25.90	79±2	–	–	
		32.02	88±5	–	–	

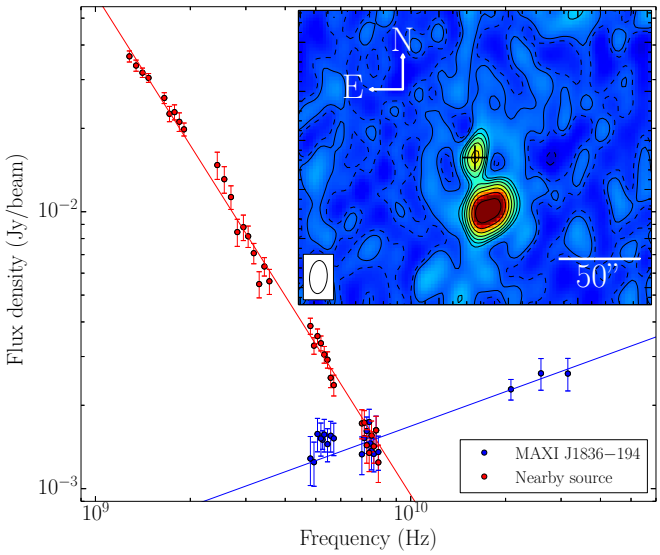

Figure 6.1: VLA spectrum of MAXI J1836−194 (blue points) and the nearby unrelated source (red points) from 2011 November 1. At frequencies where the nearby object could not be resolved from our target (<4 GHz) we subtracted the expected MAXI J1836−194 brightness from the combined flux densities to approximate the emission from the unrelated source. Inset: November 1 VLA 5 GHz image of MAXI J1836−194 (black cross), showing the confusing source to the south west of the target. Contour levels are at $\pm(\sqrt{2})^n$ times the rms noise (0.1 mJy), where $n = -3, 3, 4, 5\ldots$ (dashed contours represent negative values). At low frequencies (<4 GHz) when the VLA was in the compact D configuration, MAXI J1836−194 was unresolved from the nearby unrelated object. Fitting S_ν against ν with a power law, we then estimate the spectral index of the confusing source to be -1.81 ± 0.02.

A nearby source is located to the south-west of MAXI J1836−194 (∼30″away; see Figure 6.1, inset). This unrelated, steep-spectrum source was not aligned with the jet axis (Section 6.2.3) and was not variable over the duration of the outburst. At times when the VLA was in its most compact D-configuration (for all observations after 2011 September 18), our low-frequency (<4 GHz) VLA observations could not resolve the target from the confusing source. In these observations, our measurements of MAXI J1836−194 are contaminated by the nearby source. We must determine the spectrum of the unrelated object to estimate its contribution, which can then be subtracted from the measured flux densities in the affected observations. Using an epoch when MAXI J1836−194 was faint (2011 November 01), we measured the brightness of the confusing source (Figure 6.1).

At frequencies where we were unable to resolve the two sources from each other, we subtracted the expected MAXI J1836−194 brightness (determined by fitting a power law to the higher frequencies) from the total spectrum to give an approximation of the unrelated source. Fitting the measured radio flux densities, S_ν, against frequency, ν, with a power law, we then estimated the spectrum of the nearby source ($\alpha = -1.81 \pm 0.02$) and MAXI J1836−194 (Table 6.1). The spectrum of MAXI J1836−194 was well fit by a single power law at all epochs.

VLBA

MAXI J1836−194 was observed five times with the VLBA during the outburst, for between 4 and 6 hours per epoch, under project code BM339 (Table 6.2). We observed in dual polarisation mode, with 64 MHz of bandwidth per polarisation. In the first four epochs, we made use of the dual 13/4-cm recording mode to split the bandwidth equally between two frequency bands centred at 8.4 and 2.25 GHz. However, since our VLA monitoring indicated the source flux density to be < 1 mJy at the time of the final epoch, we observed at 8.4 GHz only on November 18, using the full 64 MHz of available bandwidth.

The observations were phase-referenced, using the closest available extragalactic calibrator source, J1832-2039, from the VLBA Calibrator Survey (VCS; Beasley et al., 2002), whose assumed position (from the most up-to-date global astrometric solution available at the time of the observations[1]) was $18^{\rm h}32^{\rm m}11^{\rm s}.0465$, $-20°39'48''.202$ (1.6° from the target source). The phase referencing cycle time was 3 minutes, spending 2 minutes on the target source and 1 minute on the phase reference calibrator in each cycle. Every seventh observation of the target was substituted for a 1-minute observation of an astrometric check source. We used two different check sources, alternating between J1845-2200, taken from the Fourth VLBA Calibrator Survey (VCS-4; Petrov et al., 2006), and J1825-1718, from the Second VLBA Calibrator Survey (VCS-2; Fomalont et al., 2003). 30 minutes at the start and end of each observation were used for geodetic blocks, observing several bright extragalactic calibrators over a range of elevations. This improved the accuracy of the phase referencing process by allowing us to solve for unmodelled tropospheric delays and clock errors.

The data were correlated using the VLBA-Distributed FX (DiFX) implementation of the software correlator developed by Deller et al. (2007), and reduced using the Astronomical Image Processing System (AIPS; Greisen, 2003), accord-

[1] http://astrogeo.org/vlbi/solutions/rfc_2011c/

ing to standard procedures. Data with elevations $< 15^{\circ}$ were flagged, to prevent the increased atmospheric phase fluctuations at low elevations from affecting the astrometric accuracy. Scatter-broadening affected the data at 2.25 GHz, reducing the amplitude measured on the longer baselines, and we were unable to calibrate the station at Mauna Kea. Phase solutions for MAXI J1836-194 were derived by fringe-fitting the phase reference calibrator, using as a model the best available image of the calibrator following self-calibration.

For the first four epochs, the data were imaged with robust weighting as a compromise between sensitivity and resolution. For the first three epochs, phase-only self-calibration was performed down to a solution interval of 5 minutes. These phase corrections were applied, before a single round of amplitude and phase calibration was used to adjust the overall amplitude gains of the individual antennas. By the fourth epoch, the source was significantly fainter, and we were only able to perform a single round of phase-only self calibration on a timescale of 1 hour. For the faint, fifth epoch, we imaged the data with natural weighting to maximise the sensitivity, but the source was too faint for self-calibration.

Since the final images showed the source to be marginally resolved in the first four epochs, we exported the self-calibrated data to DIFMAP (Shepherd, 1997), and fit the source with a single elliptical Gaussian in the uv-plane. Since DIFMAP does not provide uncertainties on fitted model parameters, we used the best-fitting values as initial estimates for the AIPS task UVFIT, which was used to determine the final fitted source sizes.

Table 6.2: Elliptical Gaussian fits (in the *uv*-plane) to the 2.3 and 8.4 GHz VLBA images of MAXI J1836−194, showing the flux density, beam size, and the fitted major axis, minor axis and the position angle for each VLBA epoch. The radio flux brightened during the X-ray peak of the outburst and the major axis size remained fairly steady at 8.4 GHz during our observations.

Date 2011 (UT)	MJD	Freq. (GHz)	Flux density (mJy)	Beam size (mas)	Major axis (μas)	Minor axis (μas)	Position Angle (°)
Sep 4	55808.12 ± 0.06	8.42	30.8 ± 0.2	2.5×0.8	584 ± 52	188 ± 27	-17.0 ± 4.6
		2.27	15.9 ± 0.3	16.5×4.8	2950 ± 200	2180 ± 1380	90.0 ± 0.1
Sep 9	55813.08 ± 0.08	8.42	38.5 ± 0.2	2.6×0.8	699 ± 33	140 ± 45	-25.7 ± 3.3
		2.27	24.6 ± 0.3	12.2×3.4	6810 ± 320	2180 ± 170	-17.5 ± 2.5
Sep 19	55823.06 ± 0.08	8.42	29.3 ± 0.1	2.4×0.8	685 ± 32	101 ± 46	-25.6 ± 3.0
		2.27	28.9 ± 0.2	14.3×4.4	4870 ± 310	2830 ± 110	-18.9 ± 5.7
Oct 12	55846.02 ± 0.10	8.42	5.0 ± 0.1	2.3×0.8	833 ± 123	0 ± 395	-11.8 ± 4.5
		2.27	3.4 ± 0.2	19.6×0.8	9850 ± 1750	2 ± 2730	-15.5 ± 5.5
Nov 18	55883.88 ± 0.10	8.42	0.36 ± 0.09	2.8×1.0	–	–	–

ATCA

The Australia Telescope Compact Array (ATCA) observed MAXI J1836−194 four times during its 2011 outburst and five times in 2012. Here we consider only observations taken during the 2011 outburst decay (Table 6.3). See Section 8.1.2 for observations of the system during the 2012 reflare.

All ATCA observations were taken at 5.5 and 9.0 GHz with a bandwidth of 2 GHz at each frequency. The ATCA data were reduced using standard routines in Australia Telescope National Facility's (ATNF) MIRIAD package (Sault et al., 1995). Primary flux calibration for all observations was done using 1934−638. Phase calibration was carried out with 1817−254 during the 2011 September 5, 20, and 21 observations. 1908−201 was used for all other observations, except on 2012 April 8 where 1829−207 was used. Due to a combination of antenna shadowing in the compact H75 configuration and a missing antenna, only one baseline was usable for the 2011 September 20 and 21 observations. Therefore, for these two epochs a point source was fit to the calibrated data in the uv-plane. For all other observations, calibrated data were then exported to DIFMAP for imaging and flux densities were obtained by fitting a point source model to the target in the image plane (Table 6.3). Due to the compact array configuration on 2011 September 20 and 21, our ATCA observations were unable to resolve MAXI J1836−194 from the nearby unrelated object. The estimated flux density of the nearby source was subtracted from our measured flux density to estimate the flux density of MAXI J1836−194 in our ATCA observations (see Section 6.1.1 and Figure 6.1 for further discussion).

The ATCA radio counterpart of MAXI J1836−194 was detected for all 2011 observations at a position coincident with those of the X-ray, optical, VLA and VLBA counterparts. During our 2012 observations, the source was detected only on April 8 (during the minor re-flare). When detected, the source was found to be unresolved within the ATCA beam.

6.1.2 X-ray observations

RXTE

The outburst of MAXI J1836−194 was monitored with the Proportional Counter Array (PCA) on board the *Rossi X-ray Timing Explorer* (RXTE; see Jahoda et al. 1996, 2006). A total of 74 pointed observations sample this outburst, for a period of about 92 days. The RXTE data were reduced using the Heasoft software

Table 6.3: ATCA flux densities of MAXI J1836−194. Due to the presence of a nearby unrelated source (within the ATCA beam, Figure 6.1 inset), for the observations in which the array was in the compact H75 configuration the interpolated flux density of the unrelated source (determined from our VLA observations; Figure 6.1) was subtracted to estimate the flux density of MAXI J1836−194 (see Section 6.1.1). At other epochs, the more extended array configuration meant the two sources were resolved from each other. Upper limits are 3σ.

Date (UT)	MJD	Array config.	Freq. (GHz)	Flux density (mJy)
2011 Sep 05	55809.45	6B	5.5	28±2
			9.0	36±4
2011 Sep 20	55824.22	H75	5.5	45±4[a]
			9.0	50±3[a]
2011 Sep 21	55825.21	H75	5.5	39±4[a]
			9.0	44±3[a]
2011 Dec 01	55897.27	1.5D	5.5	0.4±0.1
			9.0	0.24±0.05
2012 Jan 13	55939.92	6A	5.5	≤0.09
			9.0	0.27±0.07
2012 Feb 03	55960.05	6A	5.5	≤0.11
			9.0	≤0.21

[a]The flux density of the nearby source was subtracted from our measured flux density (see Section 6.1.1).

package v6.8, following the standard steps described in the RXTE cookbook. To estimate the source intensity and a spectral colour, we followed Altamirano et al. (2008): we used the 16 second time-resolution Standard 2 mode of all active Proportional Counter Units (PCUs, all layers) in each observation. The hard colour was defined as the count rate ratio (6–16 keV)/(2–6 keV) and the intensity was defined as the total count rate in the 2.0–20.0 keV band. We subtracted the background and performed deadtime corrections on a per-PCU basis. To take into account response differences between PCUs, we normalised the intensity and hard colour by the Crab before estimating the average intensity and hard colour on a per-observation basis. Due to the low column density along the line-of-sight ($n_{\rm H} = 3.0 \times 10^{21}$ cm^{-2}; Section 7.3.2) and the spectrum being dominated by a power-law component during the hard state decay, the 3–9 keV band during the decay phase of the outburst was unaffected by absorption.

Due to Sun constraints, no simultaneous RXTE data were available to coincide with the 2011 December 3 VLA data (the final RXTE epoch was 2011 November 25). We estimate the X-ray intensity on December 3 by fitting the observed exponential decay of the source following its transition back to the hard state (see Figure 6.2), and extrapolating to the required date (error bars were conservatively estimated from the uncertainty of the exponential fit).

6.2 Results

6.2.1 Source evolution

With our VLA, VLBA, and ATCA monitoring, we observed the brightening and decay of the compact jet of MAXI J1836−194 during its 2011 outburst (Figure 6.2, top panel). The VLA, VLBA and ATCA radio observations (Tables 6.1, 6.2 and 6.3, respectively) show that the flux density of the system increased during the bright, early hard state and HIMS, before the outburst failed. The VLA radio spectrum (which was initially inverted in the hard state) flattened as the system softened and transitioned to the HIMS (Figure 6.2, bottom panel). Never entering the soft state, the source transitioned back to the hard state on September 28 and the radio emission faded by $\sim$2 orders of magnitude and the spectrum became more inverted during the decay towards quiescence.

Visualising the X-ray evolution with a HID shows the variation of X-ray intensity with the X-ray spectral shape (where harder spectra are dominated by the X-ray power-law component and the softer emission by the blackbody disk

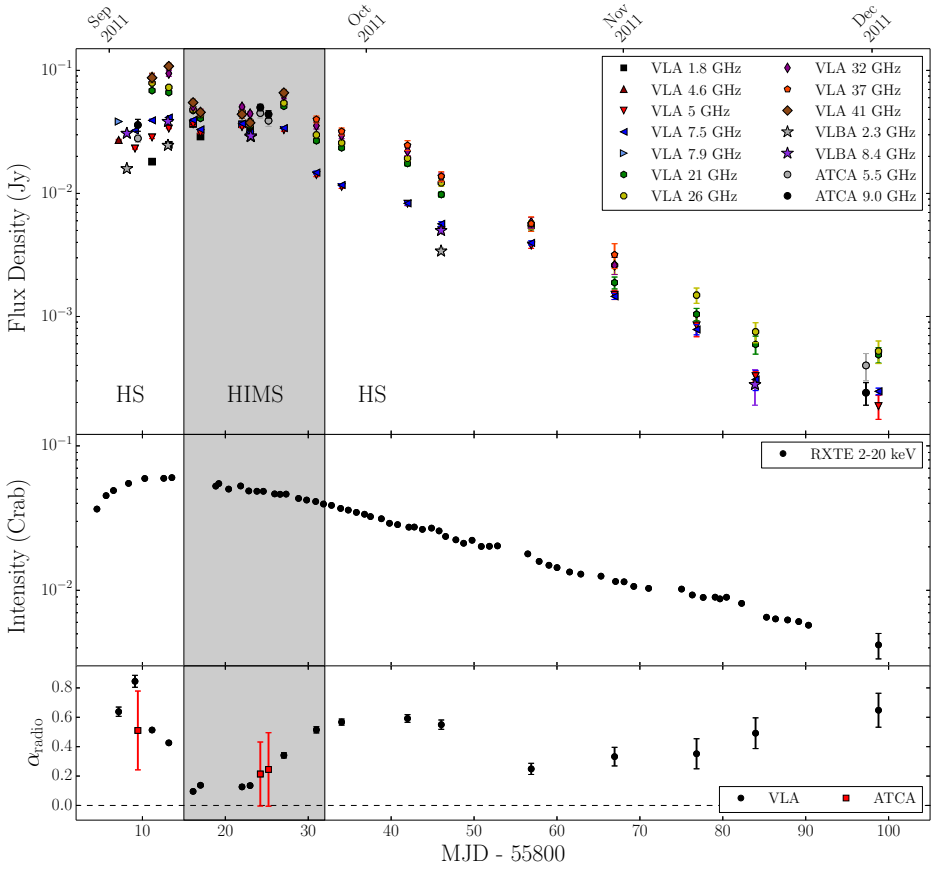

Figure 6.2: Radio and X-ray lightcurves of MAXI J1836−194 during the VLA, VLBA, ATCA and RXTE monitoring. The grey shaded region represents the HIMS and HS is the hard state, as defined by Ferrigno et al. (2012). The top panel shows the flux densities of the VLA, VLBA and ATCA monitoring. The second panel gives the RXTE 2–20 keV lightcurve (normalised to the Crab) and the third panel shows the evolution of the radio spectral index, α, where $S_\nu \propto \nu^\alpha$ (calculated from the ATCA and VLA observations, see Section 6.2.1). The spectral index flattens during the HIMS, and then becomes more inverted during the decay.

emission; e.g. Fender et al. 2004). Figure 6.3 shows how the flux density of the VLA and ATCA observations varied with X-ray intensity and spectral shape, and indicates the timing of the VLA, ATCA and VLBA radio observations.

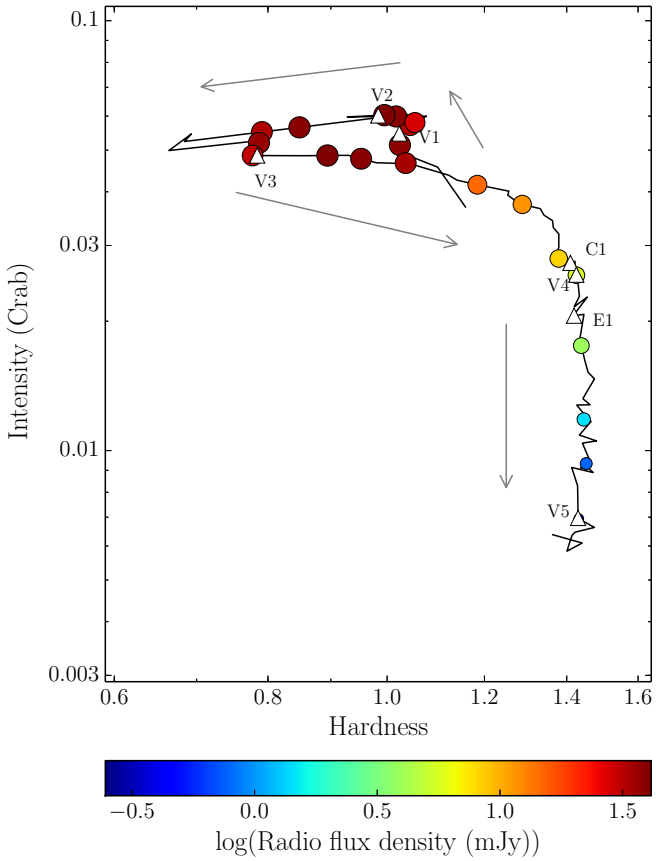

Figure 6.3: Hardness-intensity diagram of MAXI J1836−194. The RXTE X-ray hardness (6–16 keV/2–6 keV) and intensity (2–20 keV) are normalised to the Crab. The 5 GHz VLA and 5.5 GHz ATCA radio observations are shown as filled circles, with the marker size and colour representing the radio flux density. The white triangles represent the timing of the VLBI observations (including the two CVN and EVN observations from Yang et al. 2012, see Section 6.2.4). V1 through V5 refer to the VLBA observational epochs, C1 is the CVN observation and E1 is the EVN observation. Our high-cadence radio observations show the full evolution of the compact jet during the failed outburst.

6.2.2 Polarisation of the radio jet

Linear polarisation was significantly detected ($> 3\sigma$) for the first eight VLA epochs at both 5 and 7.5 GHz (see Figure 6.4, panel b). The linear polarisation (P), fractional polarisation (FP) and polarisation position angle (PA) were derived from the measured flux densities of the Stokes Q and U images, where $P = \sqrt{Q^2 + U^2}$, $FP = 100 \times P/I$ and $PA = 0.5 \arctan(U/Q)$. Following the

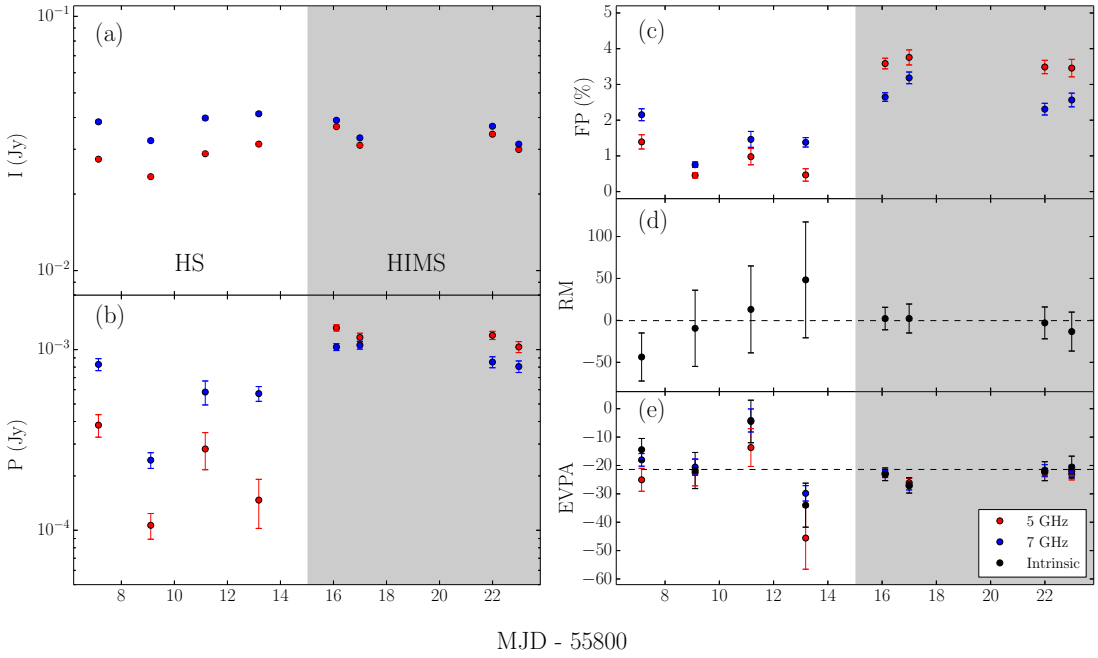

Figure 6.4: Polarisation parameters of MAXI J1836−194 during the early part of the outburst, before the VLA shifted to a more compact configuration and the target could not be resolved from the nearby confusing source. The unshaded region represents the hard state (HS) and the shaded represents the HIMS. Panel (a): Stokes I at 5 and 7.5 GHz (red and blue points respectively). Panel (b): linear polarisation (P) at 5 and 7.5 GHz (red and blue points respectively), where $P = \sqrt{Q^2 + U^2}$. Panel (c): fractional polarisation (FP) at 5 and 7.5 GHz (red and blue points respectively), where $FP = 100 \times P/I$. Panel (d): the rotation measure (RM), the black dashed line is a weighted mean of the RM values. Panel (e): the intrinsic electric vector position angle ($EVPA$; black circles), derived from fitting the observed 5 and 7.5 GHz polarisation angles on a per-subband basis against λ^2. The red and blue points represent the 5 and 7.5 GHz polarisation angles (per-baseband), respectively. We see low levels of fractional polarisation from MAXI J1836−194 during the early hard state and HIMS, a steady RM (of $|RM| \leq 32$ rad m^{-2} to 1σ) and weighted mean $EVPA$ of $-21 \pm 4°$ (fifth panel, black dashed line).

September 18 epoch the target faded and the VLA shifted to a more compact configuration and, due to the presence of the polarised confusing source, we were not able to place any constraints on the source polarisation.

Faraday rotation is the rotation of the plane of polarisation as a function of

wavelength λ, due to birefringence of the interstellar and local medium. The rotation measure, RM, is given by $RM \propto \int_0^D n_{\rm e} B_{||} {\rm d}l$ (where $n_{\rm e}$ is the thermal electron density along the line of sight, $B_{||}$ is the magnetic field parallel to the line of sight, and D is the source distance). The intrinsic electric vector position angle ($EVPA$) of the source is related to the wavelength and polarisation position angle by $EVPA{=}PA{-}RM\lambda^2$. Therefore, the RM and $EVPA$ can be determined from the 5 and 7.5 GHz observations by linearly fitting the PA for all 16 subbands (ensuring we do not suffer from an $n\pi$ ambiguity). Our results show that the RM and $EVPA$ remained constant within errors throughout the outburst and we find that $|RM| \leq 32$ rad m^{-2} (to 1σ) and $EVPA{=}-21 \pm 4^\circ$ (Figure 6.4, panels d and e, respectively).

6.2.3 VLBA radio morphology

Our VLA, ATCA and VLBA radio observations of MAXI J1836−194 during its outburst show similar flux densities. Also, contemporaneous VLBI observations of this system with the Chinese VLBI Network (CVN) on 2011 October 10 and the European VLBI Network (EVN) on 2011 October 17, reported by Yang et al. (2012), show comparable flux densities to our radio observations, suggesting that the high resolution observations do not resolve out any significant extended emission.

The compact jet was not directly resolved in the individual images, except on September 19 at 2.3 GHz. Model fitting in the uv-plane shows the source to be slightly extended at all frequencies, and in all but the last epoch (Table 6.2), as confirmed during the deconvolution process while imaging. As a check on the quality of the fits, the fitted Gaussian was subtracted from the uv-data, and the data were re-imaged. The resulting residual images were noise-like, with the exception of the 2.3 GHz September 19 observation, for which some structure remained at the level of 1.0 mJy beam^{-1}, suggesting that a simple elliptical Gaussian was not a good representation and that the source structure was more complex (Figure 6.5). However, since it can account for >96% of the emission at that epoch, we take the fitted parameters as a good approximation to the source structure in this epoch, together with a faint residual jet component separated by ∼15 mas from the core, along a position angle $-29 \pm 3^\circ$. Excluding the September 4 2.27-GHz observation, which was taken early in the outburst with relatively low resolution, model fitting in the uv-plane gave a consistent position angle, with a weighted mean of $-21 \pm 2^\circ$. Hereafter, we take the weighted mean as indicative

of the observed jet axis. The fitted major axis of the source (which was smaller at higher-frequency, corresponding to smaller scales within the jet; see also Rushton et al. 2012) did not change significantly during the outburst (Table 6.2).

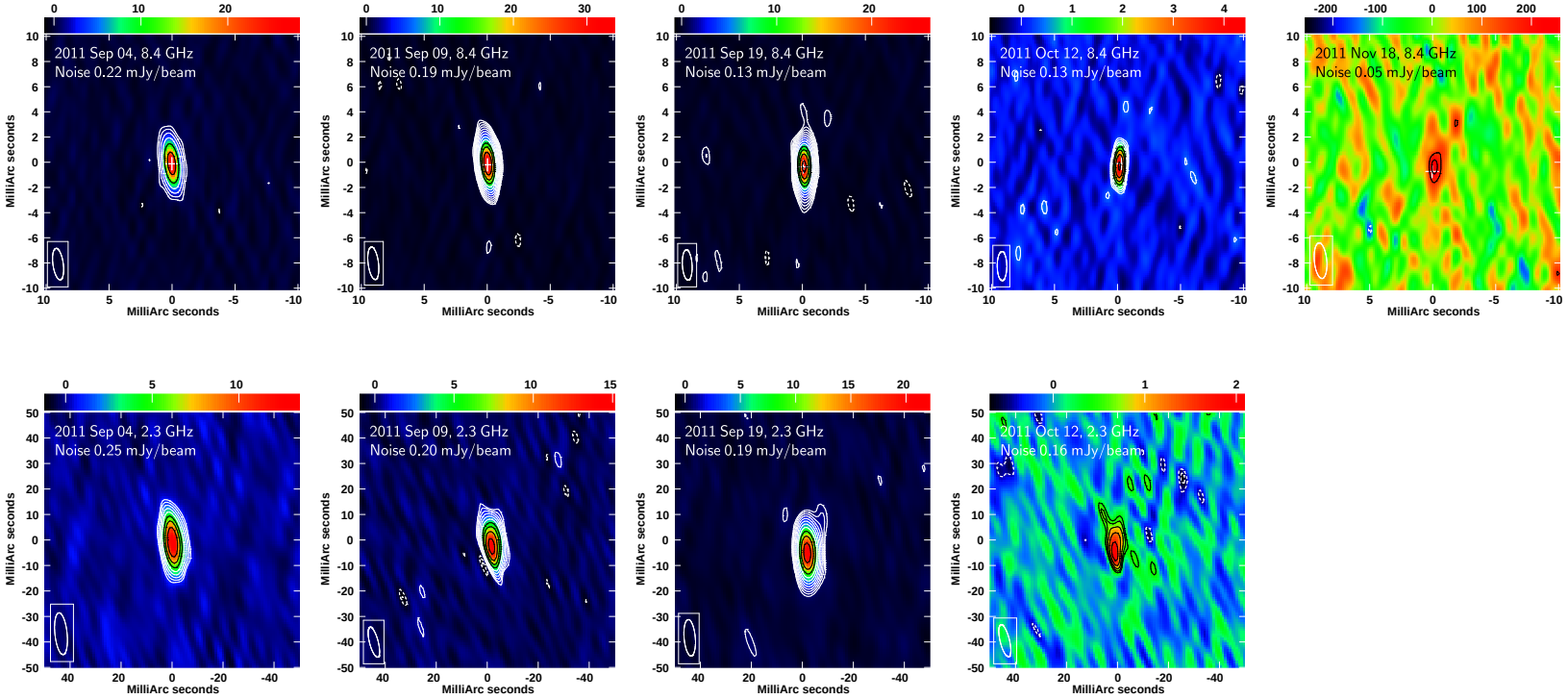

Figure 6.5: VLBA images of MAXI J1836−194. Top panels are at 8.4 GHz, and bottom panels are at 2.3 GHz. Contour levels are $\pm 2^n\sqrt{2}$ times the rms noise level indicated in the top left corner of each image, where $n = -1, 1, 2, 3, 4, ...$ The colour scale shows the image flux density in units of mJy beam^{-1}, except for the final 8.4-GHz image (2011 November 18), for which the units are μJy beam^{-1}. The white crosses in the upper panels mark the predicted core position from the proper motion fit performed in Section 6.2.4. The source is unresolved except in the 2.3-GHz image of 2011 September 19, where a $\sim$15 mas extension is seen along the position angle $-29 \pm 3°$.

6.2.4 Astrometry

To constrain the proper motion of the system, we measured the source position in each of the 8.4 GHz images prior to performing any self-calibration (Table 6.4). In all cases, we fitted the source in the image plane with an elliptical Gaussian, for consistency with the known source structure. We estimated systematics from the scatter on the two check source positions over the five epochs, weighted by their relative distance to the phase calibrator. Over the two months of our observing campaign, the fitted source position changed by 0.76±0.09 mas in R.A. and 0.9±0.2 mas in Dec. To increase the size of our data set, we included the 8.3-GHz position derived by Yang et al. (2012) from their CVN observations. Although the CVN observations used the same phase reference source, J1832-2039, they used a less recent global astrometric solution to determine the assumed position of that calibrator, so we corrected for the shift in calibrator position before adding the CVN point to our astrometric sample.

Table 6.4: VLBA positions of MAXI J1836−194 at 8.4 GHz at each epoch. We see the fitted position change by 0.76±0.09 mas in right ascension (R.A.) and 0.9±0.2 mas in declination (Dec.).

Date 2011 (UT)	MJD	Freq. (GHz)	R.A.	Dec.
Sep 04	55808.12 ± 0.06	8.42	18:35:43.4445732(8)	-19:19:10.48441(3)
Sep 09	55813.08 ± 0.08	8.42	18:35:43.4445671(5)	-19:19:10.48438(2)
Sep 19	55823.06 ± 0.08	8.42	18:35:43.4445587(4)	-19:19:10.48470(2)
Oct 12	55846.02 ± 0.10	8.42	18:35:43.444564(1)	-19:19:10.48520(4)
Nov 18	55883.88 ± 0.10	8.42	18:35:43.444519(6)	-19:19:10.4853(2)

We attempted to correct for the motion of the optical depth $\tau = 1$ surface along the jet axis, by calculating the expected core shift as a fraction of the component of proper motion along the VLBI jet axis. To estimate the expected core shift, we follow the model presented by Heinz (2006), describing the expected core shift in a compact jet. In their model, the jet luminosity L_ν is (Heinz, 2006, equation 5)

$$L_\nu = 5.1 z_0^{17/8} \sin(\theta)^{7/8} \phi^{9/8} C_0 C_1^{-7/8} \delta^{1/4}, \tag{6.1}$$

where z_0 is the position of the radio core, θ is the angle of the jet with respect to the observer, ϕ is the jet opening angle, δ is the Doppler factor, C_0 is related

to the synchrotron emissivity j_ν measured in the observer's frame, such that $j_\nu \equiv C_0 p^{7/4} \delta^2$ (p is the total magnetic and particle pressure), and C_1 is related to the self-absorption coefficient α_ν measured in the observer's frame, such that $C_1 \equiv \alpha_\nu p^2 \delta^2$. Following definitions in Rybicki and Lightman (1979),

$$C_0 = \frac{2.4 \times 10^{-17}\,\mathrm{ergs}}{\mathrm{cm^3\ Hz\ s}} \frac{2\xi_\mathrm{B}^{3/4} f}{1+\xi_\mathrm{p}} \left(\frac{2}{1+\xi_\mathrm{B}}\right)^{7/4} \left(\frac{8.4\,\mathrm{GHz}}{\nu}\right)^{1/2} \tag{6.2}$$

and

$$C_1 = \frac{2.3 \times 10^{-12}\,\mathrm{ergs}}{\mathrm{cm}} \frac{2\xi_\mathrm{B} f}{1+\xi_\mathrm{p}} \left(\frac{2}{1+\xi_\mathrm{B}}\right)^{2} \left(\frac{8.4\,\mathrm{GHz}}{\nu}\right)^{3}, \tag{6.3}$$

where ξ_B is the equipartition fraction between the particles and the magnetic field, ξ_p is the fraction between protons and particles, and f is the volume filling factor of the synchrotron emitting and absorbing plasma. The flux density $S_\nu = 4\pi D^2 L_\nu$, therefore, Equation 6.1 can be rearranged such that

$$z_0^{17/8} = \frac{4\pi D^2}{5.1} S_\nu \sin(\theta)^{-7/8} \phi^{-9/8} C_0^{-1} C_1^{7/8} \delta^{-1/7}. \tag{6.4}$$

Given that D=4–10 kpc (Section 7.4.4) and θ=4–15° (Section 5.3.2), by substituting Equations 6.2 and 6.3 and assuming ϕ=0.3° (Heinz, 2006), $\delta \lesssim 2$ (Fender et al., 2004), and that there is equipartition between the particles and the magnetic field, we calculate the expected shift of the radio core at each epoch due to the change in S_ν. We find that the shift of the radio core relative to the black hole between the brightest and faintest radio epochs is expected to be 0.18±0.02 mas, which is $\lesssim$15% of the total positional shift of the source along the jet axis, which we include (on a point by point basis) in the uncertainties of our proper motion fit.

Using jackknife resampling with a linear function to fit the motion in both co-ordinates (Figure 6.6), we derived proper motions in R.A. and Dec. of

$$\mu_\alpha \cos\delta = -2.3 \pm 0.6 \quad \mathrm{mas} \quad \mathrm{year}^{-1} \tag{6.5}$$

$$\mu_\delta = -6.1 \pm 1.0 \quad \mathrm{mas} \quad \mathrm{year}^{-1}, \tag{6.6}$$

with the reference position

$$\mathrm{R.A.} = 18^\mathrm{h}35^\mathrm{m}43^\mathrm{s}444575 \pm 0.000003 \tag{6.7}$$

$$\mathrm{Dec.} = -19^\circ 19^\mathrm{m} 10^\mathrm{s} 4843 \pm 0.0002 \tag{6.8}$$

at the reference date of MJD 55800.0.

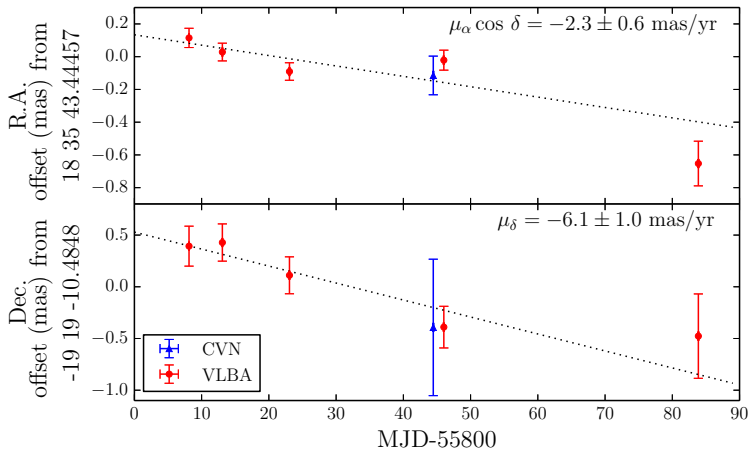

Figure 6.6: The measured positions of MAXI J1836−194 as a function of time (positions given in Table 6.4). Here, the motions in R.A. and Dec. are shown in the upper and lower panels, respectively. VLBA measurements are shown in red, and the 8.3-GHz CVN measurement of Yang et al. (2012) is shown in blue. We include in our error bars the systematic uncertainty determined from the scatter in the check source positions, as well as the uncertainty due to the core shift of the jet (applied on a point by point basis). These high-resolution observations show the proper motion of the system.

6.3 Discussion

6.3.1 The evolving compact jet

During the initial radio observations of MAXI J1836−194, the system was in the hard X-ray spectral state. In this state, the radio spectrum (determined from Stokes I) was very inverted, with a spectral index of $\alpha \sim 0.6 - 0.8$ (Figure 6.2, bottom panel), and linear polarisation was observed at levels of a few percent (Figure 6.4), significantly lower than the maximum expected theoretical levels for a perfectly ordered magnetic field (Section 3.1.4). Synchrotron theory predicts linear polarisation at levels of up to ∼11% for optically-thick synchrotron emission and up to ∼72% for optically-thin synchrotron emission in the presence of an ordered magnetic field (Section 3.1.4; Pacholczyk and Swihart 1967; Scheuer and Williams 1968; Rybicki and Lightman 1979; Longair 2011). However, these levels have rarely been observed in LMXBs (Fender, 2003). For example, like MAXI J1836−194, linear polarisation at levels of a few percent was observed in the hard states of V404 Cyg (Han and Hjellming, 1992) and GX 339−4 (Corbel

et al., 2000). The low polarisation implies either that the magnetic field was intrinsically disordered on large scales (e.g. Brocksopp et al., 2007), possibly due to multiple polarised components (which are polarised differently; Stirling et al. 2004), a rotation of the polarisation position angle within the jet (Blandford and Königl, 1979) or Faraday rotation within the compact jet (see Brocksopp et al. 2013 for further discussion). While X-ray binaries in the hard state typically exhibit flat or slightly inverted radio spectra, where $\alpha \sim 0 - 0.6$ (e.g. Fender, 2001; McClintock et al., 2009; Russell et al., 2013; Brocksopp et al., 2013; van der Horst et al., 2013; Curran et al., 2014), inversions of $\alpha \sim 0.7$ were observed during the decay phase of the 2010–2011 outburst of GX 339−4 (Corbel et al., 2013).

As the system transitioned to the HIMS, the radio emission brightened, the radio spectrum flattened (to $\alpha \sim 0.1 - 0.2$), and the linear polarisation remained at a few percent (although it did increase marginally). During this time, the polarisation spectrum steepened slightly (Figure 6.4, second panel), which the evolution of *FP* shows is not just due to the change in the spectral index of Stokes *I*. While our observations do not allow for a clear interpretation of this result, we speculate that this steepening may have been due to the magnetic field becoming intrinsically more ordered further along the jet (away from the compact object), or less ordered closer to the compact object. The outburst then failed in the HIMS and the radio spectrum became more inverted as the source transitioned back to the hard state.

Our results show that during the transition phases of the outburst, the radio spectrum appeared to track the X-ray hardness (Figure 6.7). However, during the hard state decay the spectrum of the radio jet continued to evolve while the X-ray hardness remained steady. During this time, the jet spectral break was observed to change by an order of magnitude indicating that the jet properties are still changing significantly.

A flattening of the radio spectrum as the source softens has been observed in some (but not all) other systems. The shape of the spectrum is thought to be dependent on the geometry of the compact jet and the flow of material along the jet (e.g. the bulk flow velocity along the jet and shocks and turbulence within the compact jet; Blandford and Königl 1979; Falcke and Biermann 1995; Kaiser 2006; Pe'er and Casella 2009; Jamil et al. 2010; Malzac 2013, 2014). At the beginning of its 2003 outburst, the radio spectrum of H 1743−322 showed a similar evolution to MAXI J1836−194, where the inverted spectrum of the compact jet flattened as the system softened during its transition to the intermediate state (McClintock

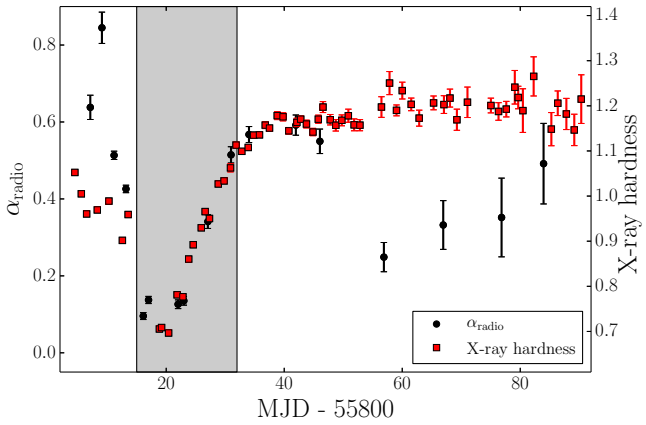

Figure 6.7: The VLA spectral index (α) and RXTE/PCA hardness ratio (6-16 keV/2-6 keV) of MAXI J1836−194 during its 2011 outburst. α (left hand axis) is represented by the black points and X-ray hardness (right axis) is shown as the red squares. The grey shaded region represents the HIMS. During the HIMS and transition back to the HS α appeared to track the X-ray hardness. Following the transition back to the hard state the X-ray hardness remained steady while the jet continued to evolve.

et al., 2009). MAXI J1836−194 reached its softest point in the HIMS, following which the jet spectrum became more inverted as the system transitioned back to the hard state. GX 339-4 (Corbel et al., 2013) showed a similar evolution where the radio spectrum became more inverted following the transition back to the hard state (after the compact jet was re-established). However, a radio spectrum that steepens with a decreasing spectral index as the source softens is not observed in all LMXBs (e.g. van der Horst et al., 2013; Curran et al., 2014). From this small sample, the difference in the evolution of the jet spectrum between systems does not appear to be related to any physical parameter of the system such as inclination angle and black hole mass. While it appears that the evolution of the radio spectrum must be driven by some property of the accretion flow (that may also be driving X-ray hardness, see Section 7.4.1), the surrounding environment, or the magnetic field (that may affect the jet flow and shape), our observations do not allow us to identify what processes may be driving the evolution.

Interestingly, while the flux density of the target changed, the fitted size of the compact jet at 8 GHz remained relatively constant (Table 6.2). According to Heinz (2006), the distance of the radio core along the jet axis, z_0, is expected to scale with the observed flux density, S_ν, where $z_0 \propto S_\nu^{8/17}$. The size of the

compact jet, $d_{\rm core}$, is expected to scale linearly with the distance of the radio core from the origin (Paragi et al., 2013). Therefore, the fitted size of the compact jet should relate to the flux density of the system, where $d_{\rm core} \propto S_{\nu}^{8/17}$. In our VLBA observations we therefore expect to see the jet change size by a factor of $\sim$2.5 at 8 GHz. However, our results show that the jet size remained steady during the outburst (even as the jet faded significantly), which could be due to physical properties of the jet changing as it faded (such as changes to the opening angle, jet confinement region etc.).

The VLA observations show that the RM remained approximately constant throughout the observations (Figure 6.4), where $|RM| \leq 32\,{\rm rad\,m^{-2}}$ (to 1σ). This result is consistent with values found by Taylor et al. (2009) for radio sources along a similar line of sight (where $-100 \lesssim RM \lesssim 100\,{\rm rad\,m^{-2}}$). Faraday rotation of the linearly polarised synchrotron emission is related to the thermal electron density and magnetic field along the line of sight. Therefore, the stable RM suggests that the rotation is not dominated by local material (to the source). The low value of the RM suggests that Faraday rotation is most likely not responsible for the low levels of observed linear polarisation.

6.3.2 Jet axis alignment

We find an agreement between the calculated EVPA ($-21 \pm 4°$; Section 6.2.2) and the observed VLBI jet axis ($-21 \pm 2°$; Section 6.2.3). The total jet spectrum is composed of contributions from both the optically-thick and optically-thin regions of each of the individual synchrotron components (Blandford and Königl, 1979; Hjellming and Johnston, 1988). Fractional polarisation is considerably higher in the optically-thin region of each synchrotron component than the optically-thick region; hence, it is expected that the observed polarisation is dominated by contributions from the optically-thin region of each synchrotron component (Figure 6.8; Zdziarski et al. 2014; Curran et al. 2015) and therefore that the EVPA will be aligned perpendicular to the magnetic field. This implies that the magnetic field is perpendicular to the jet axis in MAXI J1836−194. A perpendicular magnetic field may arise from shock compression of the magnetic field (Laing, 1980), knots or hotspots in the jet (Dreher et al., 1987), or a helical magnetic field structure dominating the observed emission (Marscher et al., 2008), a consequence of the rotation of the accretion disk from which the jets may be launched (Koide et al., 2002; Komissarov et al., 2007; Marscher et al., 2008; Gómez et al., 2008). A similar alignment between jet axis and EVPA has also

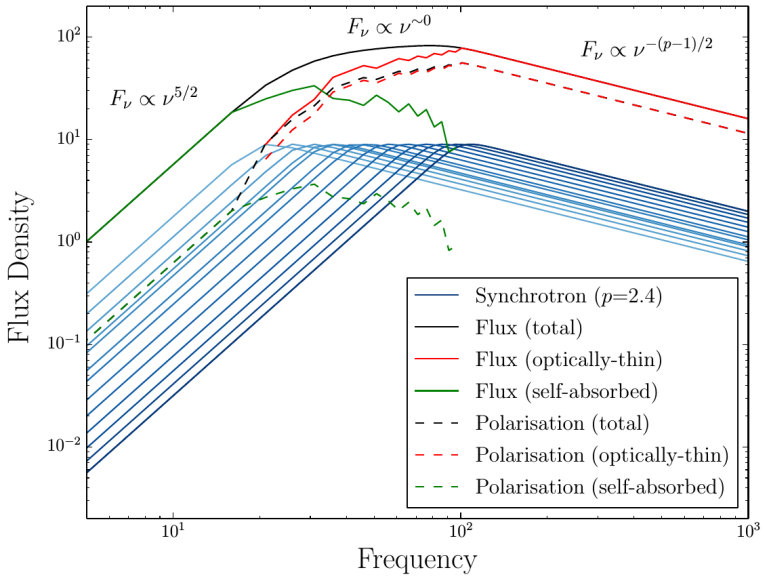

Figure 6.8: Schematic of the flux and polarisation from a compact, partially self-absorbed jet. This demonstrates that the linear polarisation of the flat spectrum is dominated by the polarisation emission from the optically-thin region of the single synchrotron spectra. Flux and frequency units are arbitrary. Figure from Curran et al. (2015).

been observed in the black hole X-ray binaries GX 339−4 (Corbel et al., 2000), GRO J1655-40 (Hannikainen et al., 2000) and Cygnus X−1 (Russell and Shahbaz, 2014, although this measurement is model-dependent). Polarisation studies of BL Lac sources have shown a bimodal distribution of the EVPA relative to the jet axis, where the majority of sources show an alignment between the EVPA and the jet axis (e.g. Cohen et al. 2014 and references therein). If an alignment between the EVPA and jet axis is common to black hole X-ray binaries, high resolution images would not be required to determine the orientation of the jets.

6.3.3 Proper motion

From this single outburst we calculate the proper motion of the system by linearly fitting its VLBI positions in both co-ordinates over time (see Section 6.2.4 and Figure 6.6), which can then be used to constrain the formation mechanism of the black hole. Black holes in LMXB systems are thought to form in two ways (Fryer and Kalogera, 2001): either a massive star collapsing directly into a black hole (e.g. Mirabel and Rodrigues, 2003; Dhawan et al., 2007), or delayed formation

in a supernova, as fallback on to the neutron star of material ejected during the explosion creates the black hole (e.g. Mirabel et al., 2001). Following a supernova, the centre of mass of the ejected material continues moving with the velocity of the progenitor immediately prior to the explosion. The centre of mass of the binary system then recoils in the opposite direction and is constrained to lie in the orbital plane (Blaauw kick; Blaauw 1961). In the presence of asymmetries in the supernova explosion, a further asymmetric kick, which need not be in the orbital plane, may be imparted to the binary (e.g. Brandt and Podsiadlowski, 1995; Portegies Zwart and Yungelson, 1998; Lai et al., 2001; Gualandris et al., 2005; Willems et al., 2005; Fragos et al., 2009). For further discussion on formation see Miller-Jones (2014) and references therein.

With our calculated proper motion, source distance (4–10 kpc; Section 7.4.4), and systemic radial velocity ($61\pm15\,\mathrm{km\,s^{-1}}$; Section 5.2.2), we can determine the peculiar velocity of this system. We calculate the heliocentric Galactic space velocity components using the formalism of Johnson and Soderblom (1987), assuming the standard solar motion measured by Schönrich et al. (2010). We assume circular rotation about the Galactic Centre in the plane of the disk, a flat rotation curve with a tangential velocity of $240\,\mathrm{km\,s^{-1}}$, and a Galactocentric distance for the Sun of 8.34 kpc (Reid et al., 2014). Defining the peculiar velocity as the difference between the measured three-dimensional space velocity and the expected motion of the system due to Galactic rotation (see, e.g. Dhawan et al., 2007), we find that the peculiar velocity is $> 70\,\mathrm{km\,s^{-1}}$ (Figure 6.9). Since stellar velocity dispersion in the disk gives a typical peculiar velocity of $< 45\,\mathrm{km\,s^{-1}}$ even for the oldest M-type stars (Mignard, 2000), and typical Blaauw kicks in LMXBs (while system parameter dependent) have a maximum recoil velocity of $\sim 70\,\mathrm{km\,s^{-1}}$ (e.g. Nelemans et al., 1999), an asymmetric natal kick was most likely required in MAXI J1836−194.

This is just the sixth system in which constraints have been placed on the formation mechanism of the black hole (see Miller-Jones, 2014, and references therein). While measuring the distribution of black hole kick velocities can constrain the formation mechanism of black holes, these astrometric observations must be carried out in a quiescent or hard state due to jet quenching in the soft state and discrete radio knots in the transitional states (which are not connected to the central binary). The quiescent or hard state jets are faint, and hence, high resolution observations of LMXBs are generally taken during full outburst. Therefore, with so few systems having accurate constraints, there is relatively little observational data on black hole kicks, so more observations such as these

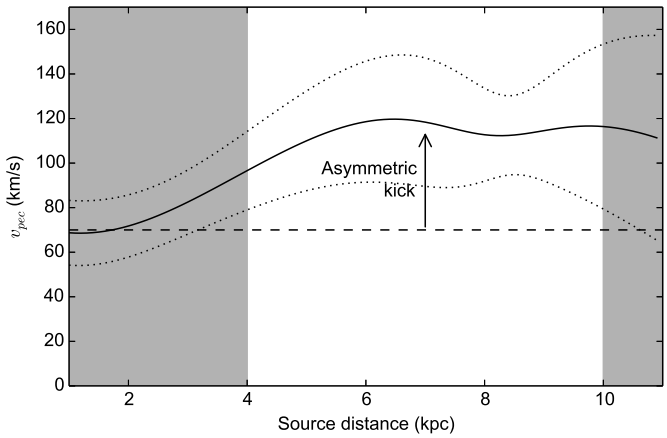

Figure 6.9: Peculiar velocity ($v_{\rm pec}$) of MAXI J1836−194 as a function of source distance (in kpc). The black solid line is $v_{\rm pec}$, the dotted lines are the error bars from uncertainties in proper motion and systemic velocity, and the unshaded regions denote the source distance limit of between 4 and 10 kpc (Section 7.4.4). The area above the horizontal dashed line represents the requirement of an asymmetric supernova kick. Our results suggest that an asymmetric supernova kick is required to explain the peculiar velocity of the system.

are required to make further progress.

6.4 Summary

In this chapter, we have presented VLA, ATCA and VLBA monitoring of the 2011 outburst of MAXI J1836−194. With our intensive radio coverage of the system we have observed the evolution of the polarised compact jet. We find that:

- The compact jet was linearly polarised at a level of a few percent during the early, bright phase of the outburst.
- The VLBI jet axis is aligned with the intrinsic EVPA and hence the magnetic field is perpendicular to the jet axis.
- The black hole likely required an asymmetric natal kick during formation to account for its high peculiar velocity.

Chapter 7

Accretion-ejection coupling in MAXI J1836−194

Adapted from:

T. D. Russell, R. Soria, J. C. A. Miller-Jones, P. A. Curran, S. Markoff, D. M. Russell, and G. R. Sivakoff (2014), 'The accretion-ejection coupling in the black hole candidate X-ray binary MAXI J1836−194', *Monthly Notices of the Royal Astronomical Society*, Volume 439, Issue 2, p.1390-1402, DOI:10.1093/mnras/stt2498

and

D. M. Russell, **T. D. Russell**, J. C. A. Miller-Jones, K. O'Brien, R. Soria, G. R. Sivakoff, T. Slaven-Blair, F. Lewis, S. Markoff, J. Homan, D. Altamirano, P. A. Curran, M. P. Rupen, T. M. Belloni, M. Cadolle Bel, P. Casella, S. Corbel, V. Dhawan, R. P. Fender, E. Gallo, P. Gandhi, S. Heinz, E. G. Körding, H. A. Krimm, D. Maitra, S. Migliari, R. A. Remillard, C. L. Sarazin, T. Shahbaz, and V. Tudose (2013) 'An Evolving Compact Jet in the Black Hole X-Ray Binary MAXI J1836−194', *The Astrophysical Journal Letters*, Volume 768, Issue 2, article id. L35, 6 pp, DOI:10.1088/2041-8205/768/2/L35

In this chapter we present the results of a simultaneous radio, sub-millimeter, IR, optical, UV and X-ray observing campaign of MAXI J1836−194 during its 2011 outburst, as well as quasi-simultaneous radio and X-ray observations of the system during its 2012 reflare. We use our multiwavelength observations to model the evolving broadband spectrum of the source, detailing the evolution of the fit parameters (and therefore the source parameters) over the course of the outburst. In particular, we discuss the evolution of the accretion flow and

the corresponding changes within the jet that occurred during the outburst and compare our observations with expected relations. Using X-ray observations and following standard disk luminosity and temperature relations, we estimate the distance to the source.

7.1 Observations

7.1.1 VLA

In this chapter, we consider only the VLA observations that either had quasi-simultaneous mid/near-infrared, optical and X-ray data for the broadband modelling. See Section 6.1.1, for full details of the observations and data reduction.

7.1.2 Submillimeter Array

MAXI J1836−194 was observed on 2011 September 13 and 2011 September 15 with the Submillimeter Array (SMA). Observations were taken at 256.5 GHz and 266.8 GHz in 2912 MHz basebands. Each of these 2912 MHz basebands was made up of twenty-eight 104 MHz sub-bands. 25 of the 28 sub-bands were comprised of 32 spectral channels of width 3250 kHz, two of the sub-bands were comprised of 512 spectral channels of width 203.125 kHz, and the final sub-band contained 1 channel of width 104 MHz.

Initial data reduction was carried out with MIRIAD (Sault et al., 1995) to apply a required system temperature correction. The data were then calibrated and imaged in CASA; McMullin et al. 2007 following standard procedures. We used 3C454.3 to calibrate the bandpass, Neptune to set the flux scale, and the nearby phase calibrators J1911-201 and J1924-292. Target observations of approximately 30 minutes were interleaved between phase calibrator observations. Amplitude and phase calibration were derived for the calibrator sources and interpolated onto the target. MAXI J1836−194 was detected with high significance at a level of 69.7±6.9 mJy at 256.5 GHz and 66.4±6.3 mJy at 266.8 GHz on 2011 September 13. Phase de-correlation due to poor weather on 2011 September 15 meant that we were unable to place any constraint on the source brightness for this date.

7.1.3 IR/Optical/UV

Mid-IR observations of MAXI J1836−194 were taken by the VLT with the VISIR instrument on four dates during the 2011 outburst. We observed the system in

the *PAH1* (8.2-9.0 μm), *SIV* (10.3-10.7 μm) and *J12.2* (11.7-12.2 μm) filters for all observations, and in the K (2.0-2.3 μm) band on some of the dates. The source was observed for half of the approximately one hour observation time on each date, due to the chop-nod observing mode. Data were then reduced with the VISIR pipeline. Raw images were recombined and sensitivities were estimated based on standard star observations taken on the same night. K band flux calibration was achieved using two nearby ($\sim$6″) $K\sim$12.4 mag stars from the Two Micron All Sky Survey (2MASS; Skrutskie et al., 2006).

Optical images in the Bessel *B, V, R* and Sloan Digital Sky Survey (SDSS) *i'* band were taken with the Faulkes Telescopes (North and South) on six dates spanning September 5–30 that were coincident with the mid-IR and radio data. Images were reduced and calibrated using standard methods for X-ray binaries observed by the Faulkes Telescopes (e.g. Russell et al., 2011). Flux calibration in the B and V bands was carried out using the *Swift*/UVOT calibration described in Section 5.1.2. R and *i'* band images were calibrated with Landolt standard stars and a number of other calibrated fields. The standard transformation to SDSS *i'* band from R and I was used (Jordi et al., 2006).

Swift/UVOT observed MAXI J1836−194 in six optical and UV filters (*v, b, u* and *uvw1, uvm2, uvw2*, respectively; Poole et al. 2008) every few days for the duration of the 2011 outburst (Ferrigno et al., 2012). Here, we consider UVOT observations that are coincident with the multiwavelength monitoring of MAXI J1836−194. For a full description of the observations and data reduction see Section 5.1.2.

7.1.4 X-ray

During its 2011 outburst, *Swift*/XRT monitored MAXI J1836−194 every few days. Observations coincident with simultaneous radio, submillimetre, IR, optical and UV epochs were retrieved from the HEASARC public archives. Light curves and spectra, including the background and ancillary response files were extracted with the online XRT data product generator (Evans et al., 2009). Suitable spectral response files for single and double events in photon-counting (PC) mode and windowed-timing (WT) mode were downloaded from the latest calibration database. The XRT count rates were high enough (>1 count s^{-1}) to create problems due to pile-up in PC mode, but not in WT mode. Based on our experience with other XRT sources (e.g. Soria et al. 2011), we only fit the WT-mode X-ray data between 0.5 and 10 keV. The *Swift*/Burst Alert Telescope

(*Swift*/BAT) observations were downloaded from the HEASARC public archives and processed with the FTOOL `batsurvey` to apply standard corrections. The 8-channel spectra and response files were then extracted and `batphasyserr` was used to correct for a standard spectral systematic error. The *Swift*/XRT and BAT spectra were both re-binned to a minimum of 20 counts per spectral channel with FTOOLS so that chi-squared statistics could be used. *Swift* X-ray light curves were then extracted using standard procedures from the XRT online tool[1] (Evans et al., 2009) and the BAT transient monitor[2] (Krimm et al., 2013).

The outburst was also extensively monitored with *RXTE*/PCA (Jahoda et al., 1996, 2006). *RXTE* data were reduced using the Heasoft software package v6.8, following the standard steps described in the *RXTE* cookbook. For full reduction details, see Section 6.1.2.

7.2 Spectral Modelling

For epochs with simultaneous radio, submillimetre, IR, UV, optical and X-ray observations (Figure 7.1), the complete broadband spectra were modelled with XSPEC version 12.7 (Arnaud, 1996). Compatible XSPEC spectral files of the radio/sub-mm and IR data were created with the FTOOL `flx2xsp`, allowing for the modelling of the complete broadband spectra, from the radio band through to the X-ray band.

7.2.1 Simultaneous multiwavelength observations

We used a composite of a broken power-law (for the optically thick and thin synchrotron emission, see Section 3.1.3) plus irradiated disk model (`diskir`; Gierliński et al. 2008, for the optical, UV and X-ray bands, see Section 3.4.1) to fit the simultaneous broadband spectra. Absorption in the IR/optical/UV and X-ray bands by gas and dust in the interstellar medium was accounted for with the XSPEC models `redden` (for the IR/optical/UV band; Cardelli et al. 1989) and `TBabs` (for the X-ray band; Wilms et al. 2000).

`diskir` is a Comptonisation model that fits the seed photon spectrum as a standard disk-blackbody. This spectrum is modified by thermal Comptonisation in a hot corona, producing a power-law like component above the peak of the disk emission that is separate from the optically thin synchrotron jet emission.

[1] http://www.swift.ac.uk/user_objects/

[2] http://swift.gsfc.nasa.gov/docs/swift/results/transients/

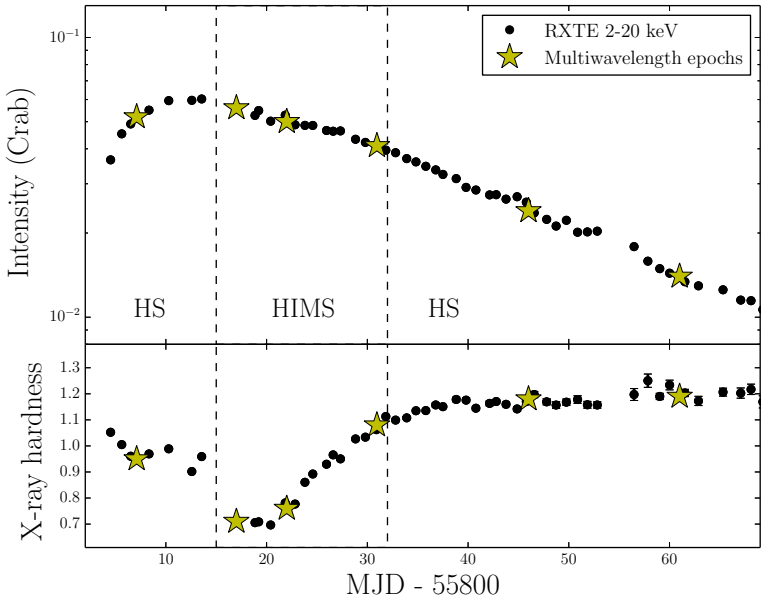

Figure 7.1: Top panel: *RXTE* 2–20 keV lightcurve of MAXI J1836−194 (black points, normalised to the Crab), showing the timing of the multiwavelength epochs (yellow stars). Bottom panel: *RXTE*/PCA hardness ratio (6–16 keV/2–6 keV). The state transitions are marked by the vertical dashed lines, where HS denotes the hard state and HIMS is the hard intermediate state, where states are as defined by Ferrigno et al. (2012).

At low energies, the model accounts for the irradiation and re-processing of the X-ray photons in the outer disk and is responsible for the secondary emission bump in the optical/UV band. `diskir` fits the colour temperature $T_{\rm in}$ of the inner disk, the disk-blackbody normalisation constant K, the fraction of X-ray flux intercepted and reprocessed in the outer disk, the physical inner radius of the accretion disk ($R_{\rm in}$) and the ratio of outer and inner disk radii ($R_{\rm out}/R_{\rm in}$). An apparent inner disk radius is derived from the normalisation parameter, where $r_{\rm in} \approx D_{\rm 10kpc}[K/\cos(i)]^{1/2}$ (where i is the inclination angle of the disk, relative to the line of sight). The physical inner disk radius is related to the apparent inner radius according to $R_{\rm in} \equiv (\xi^{1/2}\kappa)^2 r_{\rm in} \approx 1.19 r_{\rm in}$ (Shimura and Takahara, 1995; Kubota et al., 1998; Soria, 2007), where ξ is a numerical correction factor to correctly normalise the bolometric disk luminosity, reflecting that $T_{\rm in}$ occurs at a radius larger than $R_{\rm in}$ (ξ is ~ 0.412, Kubota et al. 1998) and $\kappa \sim 1.7$ (e.g. Shimura and Takahara 1995) is the ratio of the colour temperature to the effective temperature (the spectral hardening factor). Our composite model does not

require any a priori assumptions on whether the near-IR, optical and UV bands are dominated by the optically-thin synchrotron component or by the reprocessed outer disk emission. Magnetic fields are required to launch jets from an accretion flow. The Compton component from `diskir` can, in principle, contain a contribution from thermal electrons, non-thermal electrons, or synchrotron self-Compton due to the presence of a magnetic field. We do not attempt to distinguish between the different Compton components.

We considered two alternative scenarios for our multiwavelength XSPEC model; one in which the X-ray power-law component is due to inverse-Compton emission and the other in which it has a significant contribution from the optically-thin synchrotron emission. In the first scenario we truncated the optically-thin synchrotron emission in the far-UV band so that the synchrotron power-law does not contribute significantly to the hard X-ray emission. In the second we left the optically-thin synchrotron power-law unbroken, testing the possibility that the X-ray power-law may be synchrotron emission rather than Comptonisation (see Section 7.3.2 for a full discussion).

7.3 Results

7.3.1 Light curves and spectral evolution

MAXI J1836−194 was detected early during its 2011 outburst. During the initial multi-wavelength observation (2011 September 3; Figure 7.2) the system was observed in the hard X-ray spectral state (Ferrigno et al., 2012). The system transitioned to the HIMS on 2011 September 11, reaching its softest state on 2011 September 16 (still within the HIMS) before it underwent spectral hardening, transitioning back to the hard state on 2011 September 28 and fading towards quiescence. Similar to other LMXBs in outburst, the source brightened first in the hard X-ray band (15-50 keV) and then in the soft X-ray (0.5-10 keV) and radio bands as it transitioned from the hard state into the HIMS (Figure 7.2). At IR, optical and UV wavelengths the source faded during the HIMS, which was attributed to the quenching of the synchrotron component, resulting in a reduction of the emission in those bands, which then re-brightened as the system hardened (Figure 7.2; see Chapter 7.4 for further discussion). The outburst did not reach the soft state and the compact jet remained on, hence the continued emission in the radio band.

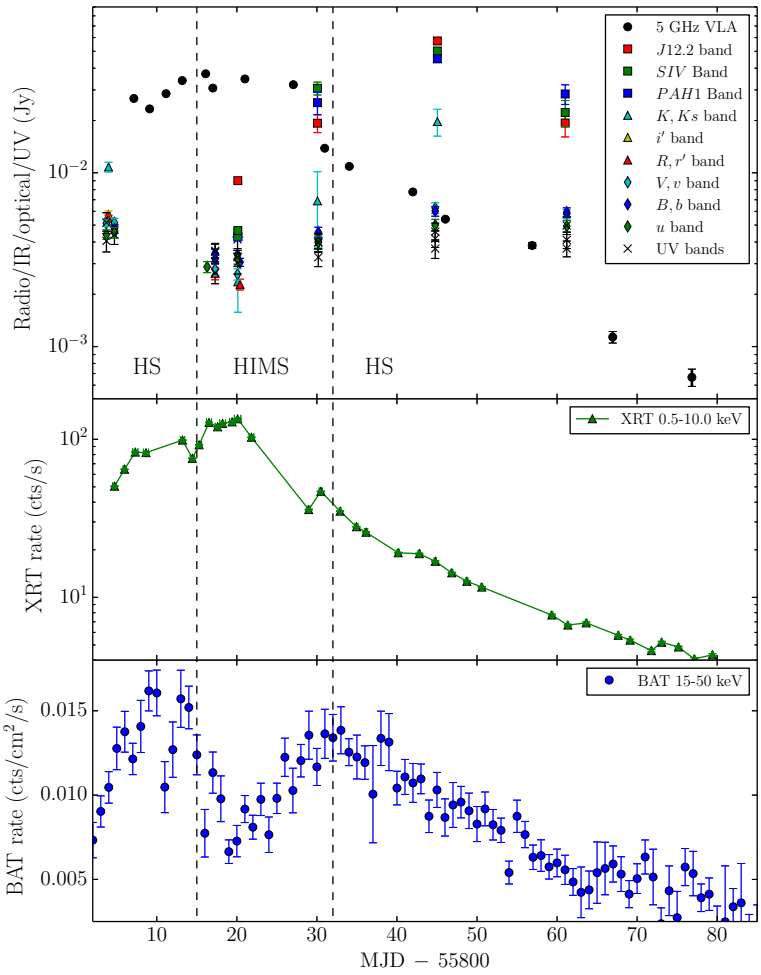

Figure 7.2: Top panel: quasi-simultaneous radio, IR, optical and UV lightcurves of the 2011 outburst of MAXI J1836−194. Middle panel: the *Swift*/XRT (0.5-10.0 keV) light curve. Bottom panel: *Swift*/BAT (15-50 keV) light curve. The state transitions are marked by the vertical dashed lines (Ferrigno et al., 2012).

7.3.2 Source evolution

While each epoch of the broadband data was fit independently in XSPEC, absorption in the optical/UV band due to dust in the interstellar medium (Appendix A) is not expected to change significantly, therefore the reddening, $E(B-V)$, was fit as a global parameter, tied across all six epochs and found to be $E(B-V) = 0.53^{+0.02}_{-0.03}$ mag ($A_V \approx 1.64$ mag). This is in good agreement with estimates from diffuse interstellar bands (from which $E(B-V) \approx 0.6^{+0.2}_{-0.1}$ mag) and results from Marshall et al. (2006) suggesting there is an absorption layer of $E(B-V) \approx 0.5$ mag in the direction of the source (Section 5.2.2). All other parameters were

modelled independently, with the best fitting spectral parameters displayed in Table 7.1 and the broadband models presented in Figure 7.3.

Table 7.1: Best fitting spectral parameters for the broadband radio to X-ray observations. $E(B-V) = 0.53^{+0.03}_{-0.02}$ mag was fit as a tied global parameter. $n_{\rm H}$ refers to the column density along the line of sight. $\alpha_{\rm thick}$ and $\alpha_{\rm thin}$ represent the spectral index of the optically thick and optically thin synchrotron emission, following the convention $S_\nu \propto \nu^\alpha$. $kT_{\rm disk}$ is the disk temperature in keV. $\Gamma_{\rm X}$ is the photon index of the high energy power-law (photon index=1−spectral index) simultaneously fitted over the *Swift*/XRT and BAT energy range. K is the normalisation parameter and gives the fitted radius of the inner accretion disk in terms of distance to the source and inclination angle (Kubota et al., 1998; Soria, 2007). y gives the log of the outer disk radius in terms of the inner disk radius, i.e. $y \equiv \log(R_{\rm out}/R_{\rm in})$, where $R_{\rm in}$ and $R_{\rm out}$ are calculated from K, the inclination angle of the system and the source distance (see Section 7.2). $\nu_{\rm b}$ is the fitted break frequency and $S_{\rm break}$ is the flux density of the break. $\nu_{\rm c}$ is the high energy cooling break of the optically thin synchrotron emission. $R_{\rm in}$ is the calculated inner radius of the accretion disk in $r_{\rm g}$ (assuming a $10\,M_\odot$ black hole and a distance to source of 8 kpc; see Section 7.2 for full details). Errors are 90% confidence limits and the dates presented are those of the VLA observations.

Date (VLA)	2011 Sep 3	2011 Sep 12	2011 Sep 17	2011 Sep 26	2011 Oct 12	2011 Oct 27
MJD	55807.12	55816.97	55821.97	55830.95	55846.01	55861.00
$n_{\rm H}$ ($\times10^{22}$cm^{-2})	0.20 ± 0.02	0.27 ± 0.01	0.29 ± 0.01	0.24 ± 0.03	0.33 ± 0.02	$0.39^{+0.04}_{-0.02}$
$\alpha_{\rm thick}$	$0.70^{+0.08}_{-0.09}$	0.20 ± 0.02	0.19 ± 0.03	$0.60^{+0.05}_{-0.02}$	$0.51^{+0.04}_{-0.03}$	0.26 ± 0.03
$\alpha_{\rm thin}$	-0.61 ± 0.1	≤ -0.51	-0.70 – -0.33	$-0.71^{+0.03}_{-0.02}$	-0.76 ± 0.03	$-0.73^{+0.06}_{-0.03}$
$kT_{\rm disk}$ (keV)	0.23 ± 0.01	0.39 ± 0.01	0.42 ± 0.01	0.23 ± 0.01	$0.12^{+0.02}_{-0.01}$	0.10 ± 0.01
$\Gamma_{\rm X}$	1.72 ± 0.03	1.98 ± 0.05	$2.03^{+0.07}_{-0.06}$	$2.01^{+0.07}_{-0.06}$	$1.77^{+0.03}_{-0.04}$	1.78 ± 0.05
K ($\times10^3$)	$25.59^{+3.90}_{-3.40}$	$10.24^{+0.84}_{-0.76}$	$8.17^{+0.73}_{-0.66}$	$23.64^{+9.38}_{-6.10}$	$114.06^{+31.14}_{-18.61}$	$100.08^{+35.87}_{-20.25}$
y	$3.69^{+0.31}_{-0.32}$	$4.19^{+0.19}_{-0.13}$	$4.09^{+0.19}_{-0.31}$	$3.78^{+0.20}_{-0.33}$	$5.12^{+0.32}_{-0.24}$	$3.71^{+0.98}_{-0.27}$
$\nu_{\rm b}$ (Hz)	$2.35^{+0.70}_{-1.10} \times 10^{11}$	$\geq 2.67 \times 10^{11}$	$(0.41$ – $5.08) \times 10^{11}$	$9.57^{+8.51}_{-3.62} \times 10^{11}$	$5.51^{+1.79}_{-0.20} \times 10^{12}$	$5.09^{+6.80}_{-0.17} \times 10^{13}$
$S_{\rm break}$ (mJy)	415^{+700}_{-190}	≥ 63	48 – 80	260^{+140}_{-45}	185^{+30}_{-15}	27^{+18}_{-5}
$\nu_{\rm c}$ (Hz)	$(3.2$ – $4.5) \times 10^{14}$	–	–	–	–	–
$R_{\rm in}$ ($r_{\rm g}$)	$10.2^{+0.9}_{-0.8}$	6.5 ± 0.3	5.8 ± 0.3	$9.9^{+1.9}_{-1.3}$	$21.6^{+3.0}_{-1.8}$	$20.2^{+3.7}_{-2.1}$
χ^2/d.o.f.	538.48/456	788.03/590	598.93/501	409.01/496	360.95/341	287.86/294

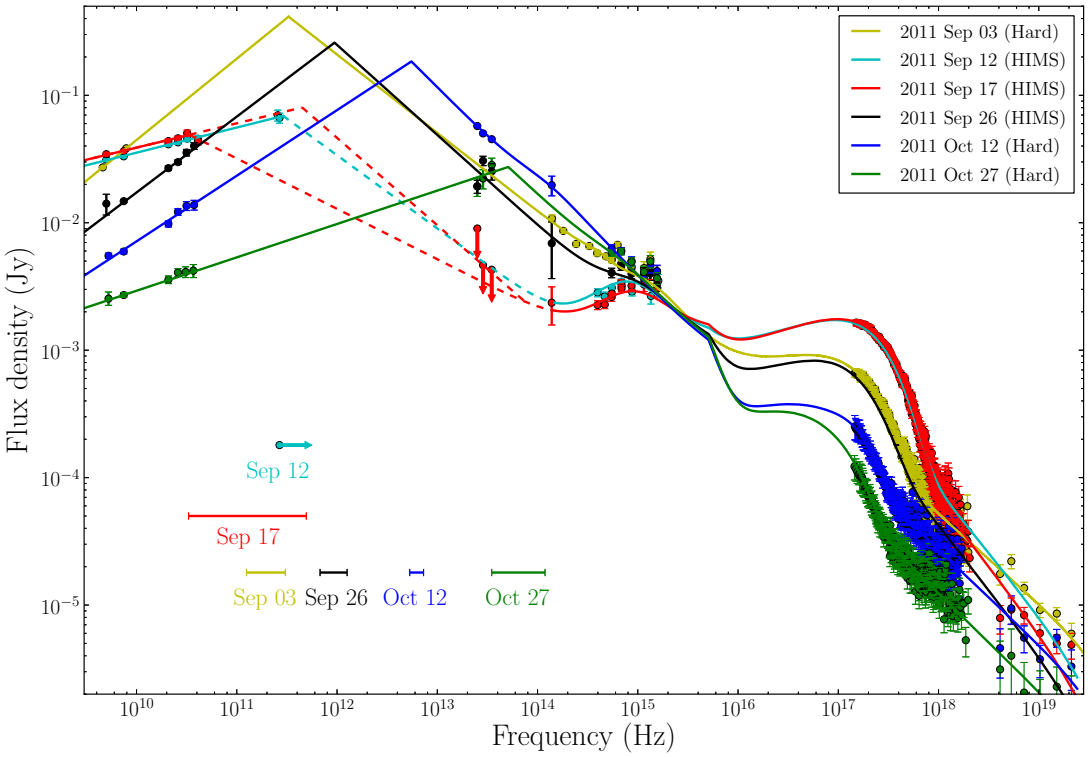

Figure 7.3: Broadband radio to X-ray spectra of MAXI J1836−194 taken during its 2011 outburst. Solid lines represent the XSPEC fits, irradiation of the outer disk causes the slight excess in the IR to UV band. Dashed lines indicate possible ranges of parameters, where the dashed light blue line is the lower limit on the spectral break frequency $\nu_{\rm b}$ for September 12 and the dashed red lines are the lower and upper limits for the September 17 data. Horizontal bars denote the uncertainty range for the spectral break from optically thick to optically thin synchrotron emission. Only four epochs of X-ray observational data (September 3, September 17, October 12 and October 27) are depicted to avoid crowding. The jet spectral break moves to higher (IR) frequencies following the transition back to the hard state during the outburst decay.

During our first multiwavelength epoch (2011 September 3), taken in the hard state, the X-ray spectrum was dominated by a fairly hard X-ray power-law component where $\Gamma_{\rm X} = 1.72\pm0.03$ (Figure 7.4), combined with a relatively cool accretion disk ($kT_{\rm disk}$=0.23±0.01) and the radio spectrum was inverted ($\alpha_{\rm thick} = 0.70^{+0.08}_{-0.09}$). Our model gives a disk temperature of 0.23 ± 0.01 keV and an inner disk radius of $\sim$10±1 $r_{\rm g}$ (assuming a 10M$_{\odot}$ black hole). During this observation, the break from the optically-thick to optically-thin synchrotron emission was at a relatively low frequency ($\sim2.3\times10^{11}$ Hz). Our VLT spectra for this epoch (Section 5.2.2)

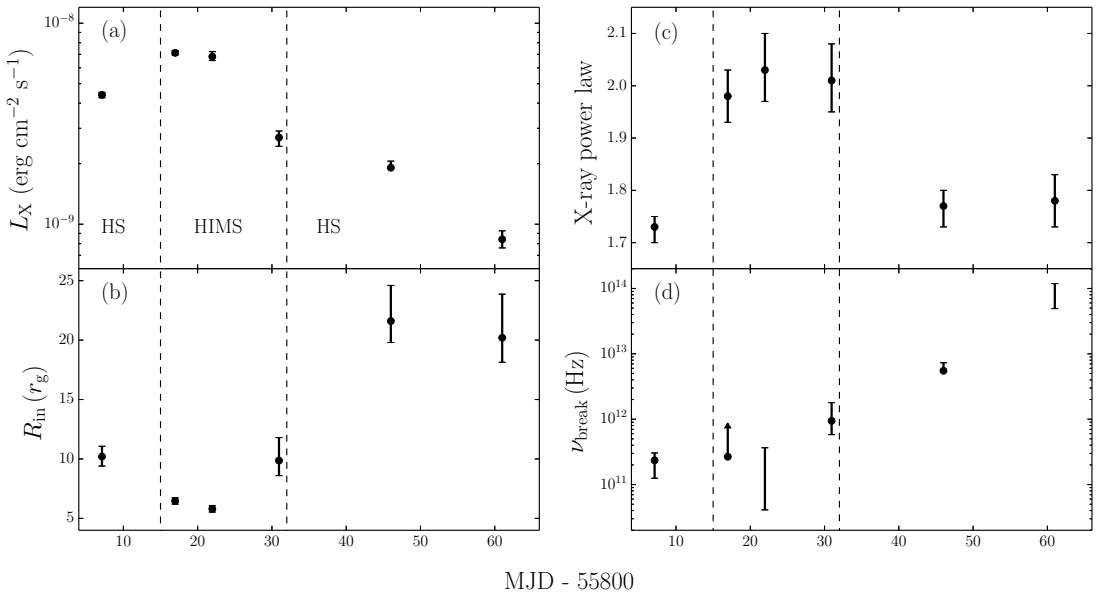

Figure 7.4: Evolution of the system during the outburst, the dashed vertical lines represent the state transitions. Panel (a): Source X-ray luminosity (0.5–100.0 keV). Panel (b): The inner radius of the accretion disk, R_{in}, increases as the system moves from the more disk dominated HIMS to the hard state. Panel (c): The X-ray power law component steepened as the disk component increased before decreasing during the decay. Panel (d): The evolution of jet spectral break, ν_b, during the outburst, shifting by more than two orders of magnitude to higher frequencies as the outburst faded.

show that the synchrotron contribution to the optical/UV continuum must be less than the disk contribution, implying a break in the synchrotron component at lower frequencies. This allows us to constrain the position of the high-energy cooling break to between 3.2×10^{14} Hz and 4.5×10^{14} Hz (see Section 7.3.3 for further discussion). We were unable to place any constraint on the position of the high energy cooling break for any other epoch and therefore sharply truncate the optically thin synchrotron emission with an exponential cut-off at 20 eV ($\sim 4.84 \times 10^{15}$ Hz, in the far-UV band where we do not have any data available) so that it does not contribute to the X-ray emission. We discuss the alternative possibility that the optically-thin synchrotron emission extends unbroken into the hard X-ray band in Section 7.3.4.

MAXI J1836−194 was observed three times during the HIMS (on September 12, September 17 and September 26). As the system evolved towards the softest state, the X-ray power-law component steepened (reaching a maximum of $\Gamma_X =$

$2.03^{+0.07}_{-0.06}$ on September 17) and the disk contribution increased significantly. At this point the disk reached its hottest temperature of 0.42±0.01 keV, close to the peak colour temperature of $\approx 0.45 - 0.50$ keV seen in standard Galactic LMXBs at similar luminosities, and $R_{\rm in}$ reached its minimum value of 5.8 ±0.3 $r_{\rm g}$. During the initial two observations in the HIMS the radio spectrum flattened (to $\alpha_{\rm thick} \sim 0.2$, see Table 7.1 and Figure 7.3) before it became more inverted prior to the transition back to the hard state ($\alpha_{\rm thick}$ was observed to be $0.6^{+0.05}_{-0.02}$ on September 26). Due to sparse IR data during the September 12 and September 17 observations we can only place limits on the position of the break frequency. For September 12 we determined that the break frequency must lie above the sub-mm detection, at $\geq 2.67 \times 10^{11}$ Hz, and for September 17 the jet break occurred between $0.41{\times}10^{11}$ and $5.08{\times}10^{11}$ Hz (with the lower limit set by requiring the break to lie above the maximum observed radio frequency, and the upper limit dictated by the K-band detection and the lower-frequency IR band upper limits, allowing a minimum optically-thin slope of $\alpha > -0.70$).

After September 17, the outburst faded as the source underwent spectral hardening. MAXI J1836−194 transitioned back to the hard state on September 28, following which the X-ray power-law component hardened (to $\Gamma_{\rm X} = 1.78 \pm 0.05$ on October 27) and the disk contribution decreased, consistent with a typical transition from the HIMS to the hard state (the disk temperature decreased to 0.10 ± 0.01 keV and the inner disk radius increased to $R_{\rm in} = 20^{+4}_{-2}\, r_{\rm g}$ on October 27). Following the transition back to the hard state the spectral index of the optically-thick synchrotron spectrum remained fairly constant ($\alpha \approx 0.6$), consistent with an inverted spectrum (Section 6.3.1). As the system settled in the canonical hard state we observed the jet spectral break shift to much higher frequencies (over two orders of magnitude, to $\sim 5 \times 10^{13}$ Hz by October 27) as the radio spectrum flattened to $\alpha_{\rm thick} = 0.26 \pm 0.03$.

Our best fitting spectral parameters are typical of LMXBs transitioning between the hard state and the HIMS (e.g. Homan and Belloni, 2005) and are in good agreement with those presented by Ferrigno et al. (2012). Any discrepancy between our results and those of Ferrigno et al. (2012) is a result of differences between the data modelled, as well as differences between the physical Comptonisation model and a phenomenological model where the X-ray power-law is not truncated at low energies.

7.3.3 High-energy cooling break

If we simply extrapolate the optically-thin power-law from the IR into the optical band, the synchrotron component would account for at least 80% of the optical continuum during our September 3 epoch. However, the VLT spectra taken on 2011 August 31 and September 1 (taken within a day of the NIR and optical data for our September 3 epoch) show prominent higher-order Balmer absorption lines (H_γ, H_δ, H_ϵ, H_8 and H_9) with a relative depth up to 20% of the continuum flux, which is typical of optically-thick accretion-disk spectra (see inset in Figure 7.5); similar absorption lines are often seen for example in Cataclysmic Variable disks at the onset of an outburst, and particularly in low-inclination systems (Warner, 2003). Strong Balmer absorption lines are inconsistent with a continuum dominated by synchrotron emission (the Balmer lines, which increase in depth at shorter wavelengths, would then span the full depth of the disk continuum; Mayo et al. 1980; Wesemael et al. 1993). The only way to reconcile the synchrotron power-law spectrum in the near IR with a disk component large enough to accommodate the depths of the Balmer lines in the blue optical region is if the expected high-energy spectral break of the synchrotron emission (see Section 3.1.2) is located in the red part of the optical band. We tested this by allowing the cooling break to be at lower frequencies and refitting the data.

Specifically, we find good fits when the break is located between $\approx 3.2 \times 10^{14}$ Hz and $\approx 4.5 \times 10^{14}$ Hz, meaning that at this point in the outburst the disk is contributing around 50% of the optical emission (with the depth of the H_ϵ and H_8 Balmer absorption lines now ∼40% of the disk continuum, consistent with low-inclination accretion disks; Mayo et al. 1980).

The high energy synchrotron break, ν_c, results from the rapid radiative cooling (faster than the dynamical timescale) of the electrons when they are no longer being continuously accelerated (Section 3.1.2). The position and evolution of ν_c dictates the total jet radiative power and is important to understand the outflows from LMXBs. For example, it is still debated whether the high energy (hard) X-ray emission in the low/hard state of LMXBs is dominated by the emission from the outer jet, by synchrotron self-Compton from the base of the jet/corona, or by the inverse-Compton scattering of seed disk photons. Recent work discussing the evolution of the X-ray (and jet synchrotron) spectral index (see Pe'er and Markoff 2012; Russell et al. 2013; Shahbaz et al. 2013) suggests that ν_c may occur at high X-ray energies ($\gtrsim$ 10keV) at the high-luminosity end of the low/hard state following an outburst ($\sim 10^{-3} L_{\rm Edd}$), before shifting to the UV band as the system

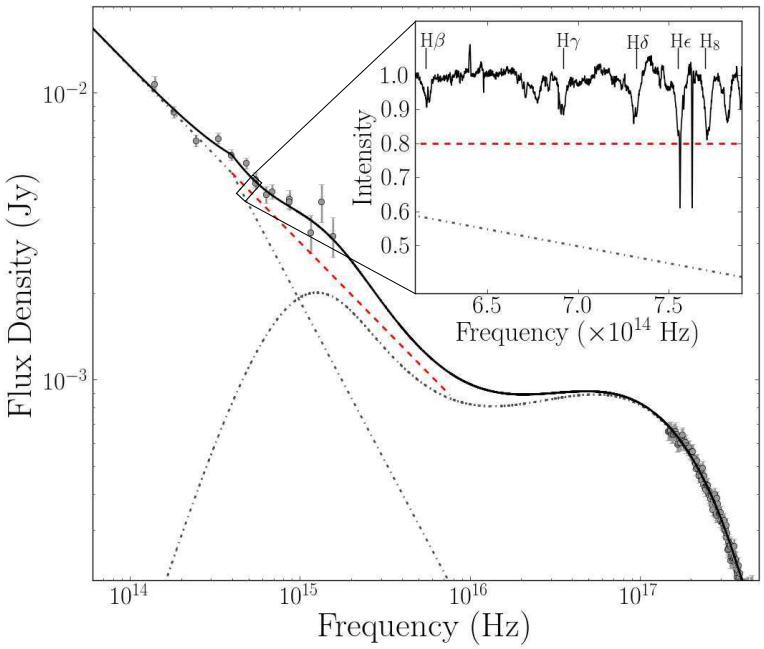

Figure 7.5: Main axes: Unfolded best fit XSPEC model of the September 3 data, showing the contribution of the optically-thin synchrotron emission with the irradiated disk. The high-energy cooling break lies at $\approx 3.2 - 4.5 \times 10^{14}$ Hz. The dash-dotted grey lines represent the separate jet and irradiated disk components, the (red) dashed line represents the extrapolated optically thin power law and the solid line is the total observed spectrum. Inset: The averaged normalised blue spectrum from August 31 and September 1 with a selection of the Balmer lines labelled. The red dashed line is the extrapolated optically thin power law (seen in the main axes), accounting for $\sim 80\%$ of the optical continuum (a similar level as the Balmer absorption lines). The dash-dotted grey line is the optically thin synchrotron emission after the placement of the cooling break. The NIR, optical, UV and X-ray data points are shown as the light grey points. This demonstrates that the cooling break must occur below this frequency band if the Balmer absorption lines are not to span the entire disk continuum.

moves into quiescence ($\sim 10^{-5} L_{\rm Edd}$). It has been suggested that this could imply that the X-rays are always jet dominated, where the X-rays are optically-thin synchrotron emission during the hard state and synchrotron cooled in quiescence (Plotkin et al., 2013). However, it has also been argued that a hardening X-ray spectral index may also be quantitatively explained by a truncated disc with a radiatively inefficient hot inner flow (Gardner and Done, 2013), implying a cooling break below X-ray energies.

Our observations require the synchrotron cooling break to lie at even lower frequencies, in the optical band, in the first few days of the outburst (when the bolometric luminosity is a few $\times 10^{-2} L_{\rm Edd}$). If the cooling break did reside in the X-ray band in the low/hard state, then its evolution to the optical band at the start of the outburst (while still in the hard state) suggests that the jet is already evolving early in the outburst, at the same time as the system is brightening and the disk begins filling in. The apparent similar evolution of $\nu_{\rm b}$ and $\nu_{\rm c}$ to lower frequencies (assuming that $\nu_{\rm c}$ occurs in the X-ray band in the low/hard state; Russell et al. 2013) would suggest that the evolution of $\nu_{\rm c}$ may be coupled with $\nu_{\rm b}$. As $\nu_{\rm b}$ shifts to lower frequencies during spectral softening the electrons are accelerated from much further out (which we discuss in Section 7.4.2) and therefore cannot be accelerated up to X-ray energies. Unfortunately we are unable to place any constraint on $\nu_{\rm c}$ (except that $\nu_{\rm c} > \nu_{\rm b}$) at any other time and therefore cannot speculate further on the evolution as the accretion rate changes.

During our final two observational epochs (October 12 and 27; during the decay phase of the outburst), the measured high-energy (hard) X-ray spectral slope is observed to be very similar to the slope of the optically thin synchrotron emission, and even its normalisation is consistent with an extrapolation of the radio/IR power-law to the X-ray band (in fact, for these two epochs the hard X-ray emission can also be plausibly fit with an extension of the synchrotron power-law; see Section 7.3.4). This would be an intriguing coincidence if the two components had different origins (synchrotron and inverse Compton). Thus, although this does not prove a common origin, it is plausible that the hard X-ray emission is dominated by synchrotron emission from the jet when the system re-enters the low/hard state. A similar result was also observed in the outburst decay of XTE J1550–564, where the slope of the optically-thin synchrotron emission was found to be consistent with that of the hard X-ray power-law, suggesting a single unbroken optically-thin power-law extending from the IR band to the hard X-ray band (Russell et al., 2010), but see Poutanen et al. (2014) for an alternative explanation. Extrapolating the optically-thin power-law to X-ray energies also agrees with the observed X-ray luminosity in a number of other black hole LMXBs at similar Eddington luminosities in the hard state (see figure 5 of Russell et al., 2013). Here, we speculate that $\nu_{\rm c}$ shifts again across the UV band towards the X-ray band as the outburst decays further as the disk cools down or disappears and continuous jet acceleration is re-established.

7.3.4 X-ray synchrotron model

For the epochs where we do not have any constraint on the position of the cooling break, we also considered the possibility that the synchrotron power-law component may have extended unbroken into the hard X-ray band. Due to poor IR data constraints during our September 12 and 17 observations there is a large possible range of slopes for the optically-thin synchrotron power law. As a result the synchrotron component will either not contribute significantly to the X-ray emission (dominated by a Comptonised disk), or may require a break in the X-ray band due to the observed 2–10 keV photon index being steeper than the optically-thin synchrotron slope. Therefore, we did not apply this model to these two epochs.

Table 7.2: Best fitting parameters for the broadband observations with an unbroken optically-thin synchrotron power-law. $L_{\rm synch}/L_{\rm total}$ is the ratio of the synchrotron emission to the total emission. All other parameters are defined as in Table 7.1. Errors are 90% confidence limits and the dates presented are those of the VLA observations.

Date (VLA)	2011 Sep 26	2011 Oct 12	2011 Oct 27
MJD	55830.95	55846.01	55861.00
$\alpha_{\rm thin}$	$-0.70^{+0.02}_{-0.03}$	-0.76 ± 0.03	$(-0.73^{+0.06}_{-0.03})^a$
$kT_{\rm disk}$ (keV)	0.24 ± 0.02	$0.12^{+0.14}_{-0.02}$	0.14 ± 0.05
$\Gamma_{\rm X}$	2.3 ± 0.2	≤ 1.76	$(1.94^{*}_{-0.25})^b$
K ($\times 10^3$)	$19.18^{+18.20}_{-6.28}$	≤ 62.20	$100.08^{+35.87}_{-20.25}$
$R_{\rm in}$ ($r_{\rm g}$)	$8.8^{+4.2}_{-1.4}$	≤ 16.1	$20.2^{+3.7}_{-2.1}$
$L_{\rm synch}/L_{\rm total}$ (0.5–2 keV)	≈ 0.15	≈ 0.59	≈ 0.45
$L_{\rm synch}/L_{\rm total}$ (2–10 keV)	≈ 0.40	≈ 0.70	≈ 0.84
$L_{\rm synch}/L_{\rm total}$ (10–100 keV)	≈ 0.72	≈ 0.66	≈ 0.89
χ^2/d.o.f.	403.47/485	355.64/330	286.91/283

a The error range for this parameter was constrained from the IR to optical data.

b The asterisk represents where this model is unconstrained.

For the final three observational epochs (September 26, October 12 and October 27) we fit the data without truncating the optically-thin synchrotron emission in the UV-band (Table 7.2). For September 26, we cannot rule out the synchrotron power-law extending unbroken into the X-ray band. In that case we find that the synchrotron component can account for $\approx$ 15% of the 0.5–2 keV emission, $\approx$40% of the 2–10 keV emission and $\approx$ 72% of the 10–100 keV emission (the

rest being due to Comptonisation). For the October 12 and 27 epochs, the slope and normalisation of the optically-thin synchrotron emission and the high-energy (hard) X-ray component are very similar. The unbroken synchrotron component would account for the majority of the emission above 2 keV (Table 7.2).

We find that both models (with and without a cooling break) are statistically equivalent[3]. Therefore, we cannot rule out either model with the current data and adopt the conservative scenario in which the hard X-ray emission comes from inverse Compton upscattering in a hot corona (e.g. Done et al., 2007; Malzac et al., 2009; Malzac, 2012). A full investigation of the alternative scenario (where the X-ray emission at energies as high as 100 keV comes from synchrotron emission; e.g. Russell et al. 2010) is beyond the scope of this work.

7.4 Discussion

We have observed the gradual evolution of the compact jet and the accretion disk in MAXI J1836−194 during its 2011 outburst. The spectral break between the optically thick and optically thin synchrotron emission evolved to higher frequencies as the jet recovered and the accretion disk faded following the outburst. In the following section we discuss how the accretion flow may be coupled to the compact jet and compare our observations with expected relations.

7.4.1 Break frequency

A shifting jet spectral break has now been observed during single outbursts in three LMXBs; this source, GX 339-4 (Gandhi et al., 2011; Corbel et al., 2013) and MAXI J1659−152 (van der Horst et al., 2013). In MAXI J1836−194, the break moved to higher frequencies by more than two orders of magnitude as the outburst faded. The radio spectrum of GX 339−4 switched from optically-thin to optically-thick synchrotron emission during the decay phase of its 2010−2011 outburst (Corbel et al., 2013), implying that the jet spectral break transitioned through the radio band to higher frequencies as the outburst faded. For the 2010 outburst of MAXI J1659−152, van der Horst et al. (2013) found that a single power-law did not sufficiently describe the radio spectrum in a number of their observational epochs, which is interpreted as the break being present in the radio

[3]Comparing the χ^2 values with an F-test gives the probability that the two models for September 26, October 12, and October 27 are statistically equivalent to the 83%, 93%, and 99% confidence level, respectively.

band. As a typical LMXB outburst fades, the IR flux is initially seen to increase (e.g. Kalemci et al. 2005; Russell et al. 2007; Coriat et al. 2009; Buxton et al. 2012; Corbel et al. 2013) as ν_b shifts to higher frequencies. This suggests that the movement of ν_b to lower/higher frequency and the IR fading/brightening during an outburst is direct evidence for the quenching and recovery of the compact jet, but the accretion processes that may be responsible for this evolution are yet to be determined.

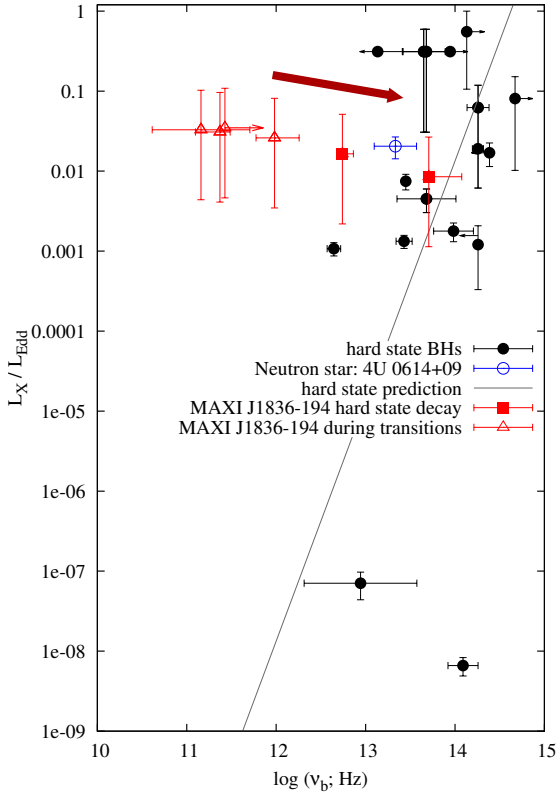

Figure 7.6: Jet break frequency versus X-ray luminosity as a fraction of the Eddington luminosity for hard state and quiescent black hole X-ray binaries (Russell et al., 2013) and the neutron star 4U 0614+09 (Migliari et al., 2010), with the theoretically expected $\nu_b \propto L_X^{1/3}$ relation (grey line). Results from the 2011 outburst of MAXI J1836−194 have been included, where the solid red squares show the position during the hard state and the red triangles for the HIMS and the transitioning September 03 epoch (assuming a distance to the source of 8 kpc and a black hole mass of 10 $M_\odot$). This shows that the jet break frequency in MAXI J1836−194 shifted to much lower than expected frequencies during the HIMS. The break frequency then transitioned back to higher frequencies as the outburst faded (this evolution is outlined by the arrow).

Theoretical relations predict that during the hard state the break frequency should scale with the X-ray luminosity as $\nu_{\rm b} \propto L_{\rm X}^{1/3}$, derived from the mass accretion rate of a radiatively inefficient flow (see Russell et al. 2013, section 3.2.1 for a full review). We observe a clear discrepancy with that relation following the transition back to the hard state; during the decay phase $\nu_{\rm break}$ increased by more than two orders of magnitude as $L_{\rm X}$ decreased (Figure 7.4). In Figure 7.6, we plot the break frequency against X-ray luminosity for MAXI J1836−194 as well as a number of other LMXBs (Russell et al., 2013), illustrating the motion almost perpendicular to the expected $\nu_{\rm b} \propto L_{\rm X}^{1/3}$ relationship. The observed scatter of the jet break frequencies in different sources at similar luminosities rules out a direct global relation between different LMXBs (Russell et al., 2013). This means that other accretion parameters (that are different between sources) such as inner disk radius, disk temperature, magnetic field strength and black hole mass may have a significant effect on $\nu_{\rm b}$. We show that for an individual source (i.e. at constant black hole mass) during spectral state transitions the jet break frequency is being driven primarily by the changing structure of the accretion flow, rather than by luminosity. The spectral break from our final epoch is seen at frequencies comparable to other LMXBs and we speculate that the expected $\nu_{\rm b} \propto L_{\rm X}^{1/3}$ relation may hold once the system has fully settled into a canonical hard state. If the jet has settled into a canonical hard state by our final observational epoch, we can place a minimum timescale of ≈29 days for the jet to settle into the hard state following the X-ray defined state transition.

While the transition to higher frequencies did occur as the inner radius of the accretion disk shifted outwards there does not appear to be a strong relation between $\nu_{\rm b}$ and $R_{\rm in}$ (Figure 7.4). However, the position of the jet break does appear, in part, to be related to the conditions in the X-ray emitting plasma that also drive the source hardness. Performing a Monte Carlo Spearman's rank correlation (Curran, 2014) of the jet break frequency against hardness provides tentative evidence for a positive correlation between the two (Figure 7.7), with a Spearman's rank coefficient of 0.71 ± 0.14 at a significance level of 0.86 ± 0.12. For this test hardness was defined as the ratio of Comptonised flux ($L_{\rm c}$) to disk flux ($L_{\rm disk}$) across the 0.5–100 keV band. Recent results, presented by van der Horst et al. (2013), showed that MAXI J1836−194 reached a full soft state and its $\nu_{\rm b}$ shifted to lower frequencies than we observe here, further suggesting that the source hardness may be correlated with the break frequency in some way. We also observed $\nu_{\rm b}$ shift to lower frequencies as the X-ray photon index steepened; however the change in the photon index only occurred over a very

small range (values range from $\Gamma_{\rm X} \approx 1.73$ to ≈ 2.03, see Figure 7.4) and there was no significant correlation between $\Gamma_{\rm X}$ and $\nu_{\rm b}$ (a Monte Carlo Spearman's rank correlation produces a correlation coefficient of -0.26 ± 0.20 at a significance level of 0.40 ± 0.25).

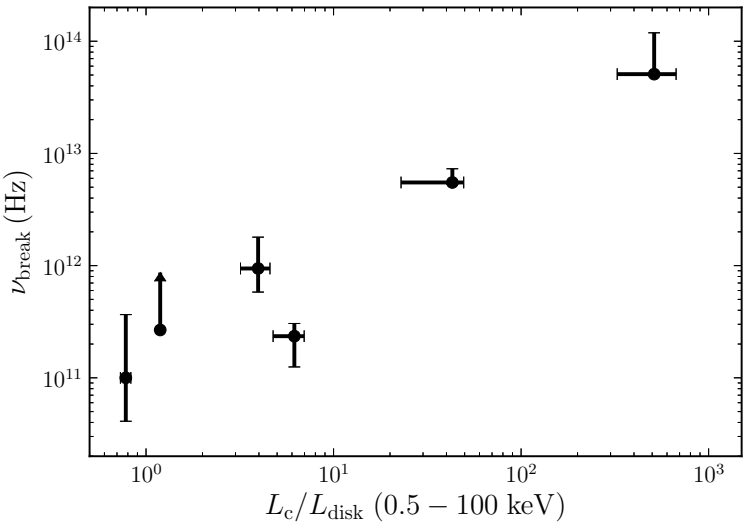

Figure 7.7: Evolution of the spectral break frequency with spectral hardness, parameterised by the ratio of Comptonised flux to disk flux, $L_{\rm c}/L_{\rm disk}$, over the 0.5–100 keV band. Performing a Monte Carlo Spearman's rank correlation test produces a Spearman's rank correlation coefficient of 0.71 ± 0.14 at a significance level of 0.86 ± 0.12.

While the correlation test provides some evidence for source hardness being correlated with $\nu_{\rm b}$, the physical mechanisms that set the position of the first acceleration zone (that is associated with $\nu_{\rm b}$) are likely to involve more complex processes (e.g. set by magnetohydrodynamic and plasma processes; Polko et al., 2010, 2013, 2014).

7.4.2 First acceleration zone

It is thought that the compact jet is launched on scales of a few to 100 $r_{\rm g}$ (comparable to $R_{\rm in}$; Markoff et al. 2005; Pe'er and Markoff 2012). Following the standard single-zone synchrotron theory presented by Chaty et al. (2011), we calculate the evolution of the radius of the region where electrons are first accelerated up into a power law distribution ($R_{\rm F}$, which is defined by the cross-sectional area of this region), as well as an estimate of the equipartition magnetic field ($B_{\rm F}$).

$R_{\rm F}$ is determined by the position and frequency of the spectral break, as well as the spectral index of the optically thin synchrotron emission, according to

$$R_{\rm F} \propto \nu_{\rm b}^{-1} S_{\nu_{\rm b}}^{(p+6)/(2p+13)}, \tag{7.1}$$

where p is the slope of the electron energy spectrum ($p = 1 - 2\alpha$, following the convention $S_\nu \propto \nu^\alpha$) and $S_{\nu_{\rm b}}$ is the flux density at the jet spectral break (see Appendix B for full derivation). Evaluating this expression for each epoch at which we constrain the break frequency, we find that $R_{\rm F}$ was largest during the HIMS ($\sim 10^5 - 10^6 r_{\rm g}$) and moved inwards (to $\sim 10^2 - 10^3 r_{\rm g}$) as the outburst faded in the hard state (Figure 7.8). Our results imply that the particle acceleration occurs at much larger scales than $R_{\rm in}$ and that the jet properties are changing significantly during the outburst. We infer that during outburst the jet luminosity is reduced as the particle acceleration occurs at much larger radii, and then recovers as the acceleration point shifts inwards (demonstrated by $\nu_{\rm b}$ moving to higher frequencies) and reduces in size (demonstrated by the reduction of $R_{\rm F}$). While the particle acceleration is occurring on different scales in the jet, we are unable to say if the jet is thermally dominated at smaller scales. While this model does demonstrate the evolution of the accelerating region, more detailed treatments (e.g. Markoff et al. 2001; Polko et al. 2010, 2013, 2014) are required to accurately determine the jet parameters (although the final results may only be expected to differ by a factor of a few).

The magnetic field in the accelerating region is expected to increase as $R_{\rm F}$ moves inwards. This is due to the magnetic field and density increasing as we probe more compact regions of the jet. An estimate of the equipartition magnetic field can also be calculated from the observed jet break, according to

$$B_{\rm F} \propto \nu_{\rm b} S_{\nu_{\rm b}}^{-2/(2p+13)}, \tag{7.2}$$

(see Appendix B for full derivation). We find that the magnetic field in the acceleration region increased from $\sim 10^2$ G when $R_{\rm F}$ was large to $\sim 5 \times 10^4$ G when the acceleration occurred closer in to the black hole (Figure 7.8).

7.4.3 Radiative jet luminosity

With knowledge of the cooling break frequency, the total radiative jet luminosity for our initial epoch (September 3) can be calculated from the complete jet spectrum. By integrating across the entire jet spectrum (up to infinity) we find

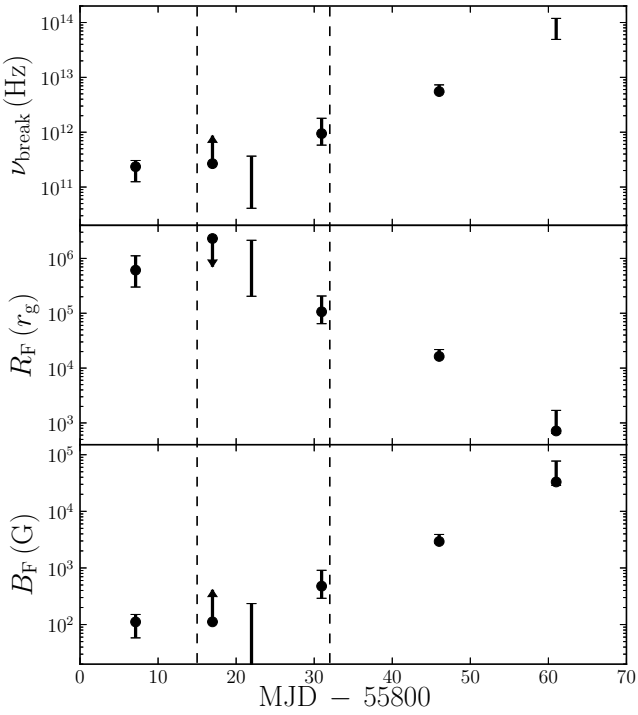

Figure 7.8: Evolution of the jet acceleration region. The dashed vertical lines represent the state transitions. Top panel: The evolution of $\nu_{\rm b}$ during the outburst. Second panel: Radius of the first acceleration zone, $R_{\rm F}$ (in $r_{\rm g}$ and assuming a $10{\rm M}_{\odot}$ black hole), reducing as the outburst progressed. Bottom panel: The magnetic field at the jet base ($B_{\rm F}$) increases as the source transitions from the HIMS to the hard state and decays.

$L_{\rm Jet,rad} \approx 1.8 \times 10^{36}$ erg s^{-1}, assuming a source distance, D, of 8 kpc (for further discussion on assumed distance see Section 7.4.4). Using a canonical radiative to kinetic energy ratio of $\approx 5\%$ (Blandford and Königl, 1979; Fender and Pooley, 2000; Fender, 2001; Gallo et al., 2005; Russell et al., 2007) the total inferred jet power $P_{\rm Jet} \approx 3.6 \times 10^{37}$ erg s^{-1} $(D/8$ kpc$)^2$. However, as the jet is oriented close to the line of sight, it will be significantly Doppler boosted, according to $S = S_0\delta^{3-\alpha}$ (where δ is the relativistic Doppler shift). For example, for a canonical bulk Lorentz factor of 2 (Fender et al., 2004), the intrinsic jet power is reduced (by a factor of ~ 12) to $P_{\rm Jet} \approx 3.1 \times 10^{36}$ erg s^{-1} $(D/8$ kpc$)^2$. From the broadband XSPEC models, the bolometric luminosity at that epoch was $L_{\rm Bol} \approx 4.9 \times 10^{37}$ erg s^{-1} (2×10^{-8}–200 keV), indicating that the jet is $\sim$ 3 % of $L_{\rm Bol}$ if purely radiative. In agreement with findings presented by Fender et al. (2003), this result demonstrates that the system is not jet-dominated at

high luminosities.

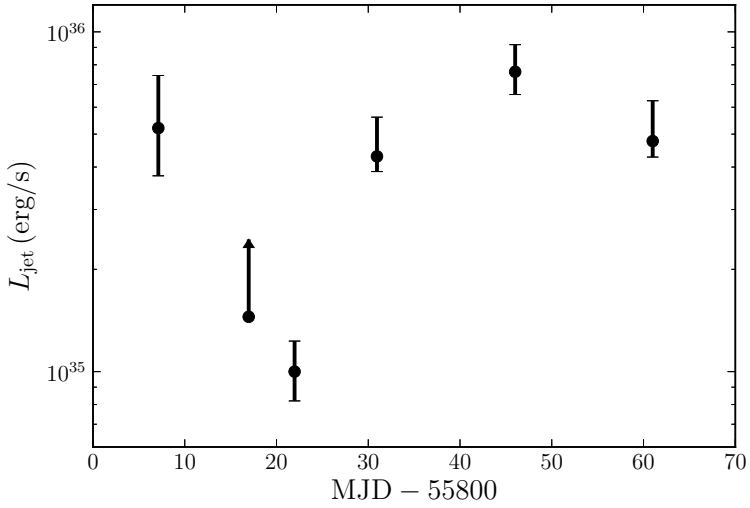

Figure 7.9: The fading and recovery of the compact jet, assuming a distance to source of 8 kpc. Minimum estimate for the total radiative jet luminosity calculated by integrating across the observed jet band (5×10^9 Hz to 7×10^{14} Hz). The minimum radiative luminosity decreases as the system reaches its softest state, and then recovers on spectral hardening.

For all other epochs we are unable to place any observational constraints on $\nu_{\rm c}$ and therefore can only place a lower limit on the jet luminosity. Integrating across the observable jet spectrum (up to 7×10^{14} Hz), we find that the minimum radiative luminosity of the compact jet marginally faded in the HIMS, but did not quench or recover immediately (Figure 7.9). If the jet had switched on or off instantaneously, we would have observed either a decrease or increase of the radio luminosity on short timescales: at least as short as the light travel time over the photosphere or emitting region, and at most, the adiabatic expansion timescale or the synchrotron cooling timescale of the propagating jet matter. For example, assuming a magnetic field strength of 10^4 G, the synchrotron cooling timescale would be on the order of minutes in the IR band and days at radio frequencies (Miller-Jones et al., 2004; Gandhi et al., 2011). However, we observe the jet power vary on timescales of weeks, similar to the accretion flow. The fading and recovery of the compact jet that occurred during the HIMS indicates that this process is coupled with some activity in this state. While we see evidence for a fading of the compact jet, the true radiative jet luminosity will depend on the position of $\nu_{\rm c}$, which will significantly overshadow the observed quenching and

recovery of the minimum radiative jet power in Figure 7.9 (shown by the factor of ∼6 difference between the total jet power and minimum radiative luminosity for September 3).

Assuming that ν_c shifts through the X-ray band by October 27 and lies above XRT energies (at $\sim 2 \times 10^{18}$ Hz), then $L_{\rm Jet,rad} \approx 6 \times 10^{36}\,{\rm erg\,s^{-1}}$ $(D/8\,{\rm kpc})^2$. The bolometric luminosity for Oct 27 is $L_{\rm Bol} \approx 1.1 \times 10^{37}\,{\rm erg\,s^{-1}}$ (2×10^{-8}–200 keV). Therefore, the jet would account for ∼60% of $L_{\rm Bol}$ if purely radiative. Assuming the 5% radiative to kinetic ratio and accounting for Doppler boosting, the total power of the jet would be $P_{\rm Jet} \approx 1 \times 10^{37}\,{\rm erg\,s^{-1}}$ $(D/8\,{\rm kpc})^2$, which is a factor of ∼20 higher than our minimum radiative energy calculation (Figure 7.9). This result demonstrates that the system would become jet dominated should ν_c shift to higher frequencies and the radiative to kinetic ratio remain unchanged.

7.4.4 Distance to the source

From the measured values of inner-disk temperature and the X-ray state evolution we can estimate plausible values of source distance for a range of black hole masses. In a typical outburst only minor spectral softening occurs beyond the HIMS (Belloni, 2010) and there is evidence that, even in the low/hard state, at luminosities ∼0.01 $L_{\rm Edd}$ the inner accretion disk extends close to the ISCO (e.g. Miller et al., 2006; Malzac, 2007; Wilkinson and Uttley, 2009; Reis et al., 2010; Reynolds and Miller, 2010; Uttley et al., 2011; Miller et al., 2012; Reynolds and Miller, 2013). Soria et al. (2011) also observed the inner-disk temperature to remain approximately constant during transitions between the intermediate states and soft states of GRS 1758−258. Therefore, we assume that during our softest spectral observation $R_{\rm in} \approx R_{\rm ISCO}$. At this point in time the disk reached a temperature of 0.42 ± 0.01 keV, close to the peak colour temperature of $\approx 0.45 - 0.50$ keV seen in standard Galactic LMXBs at comparable values of $L_{\rm X}/L_{\rm Edd}$.

For a standard Shakura-Sunyaev disk, the bolometric disk luminosity is related to the inner disk temperature and the apparent inner disk radius by

$$L_{\rm disk} = 4\pi\sigma T_{\rm in}^4 r_{\rm in}^2. \tag{7.3}$$

Following Soria (2007), as $R_{\rm in} \approx R_{\rm ISCO} \approx 6\phi GM/c^2$, where ϕ depends on the black hole spin ($\phi = 1$ for a Schwarzschild black hole and $\phi = 1/6$ for an extreme Kerr black hole) and from the $R_{\rm in}$ to $r_{\rm in}$ relation (see Section 7.2) we find that

the mass of the black hole can be approximated by

$$M \approx 10 \left(\frac{\eta}{0.1}\right) \left(\frac{\xi\kappa^2}{1.19}\right) \left(\frac{L_{\rm disk}}{5 \times 10^{38} {\rm erg\,s^{-1}}}\right)^{1/2} \left(\frac{kT_{\rm in}}{1{\rm keV}}\right)^{-2} M_\odot \qquad (7.4)$$

where σ is the Stefan-Boltzmann constant, η is the radiative efficiency $\approx 1/12\phi$ in a Newtonian approximation, $\xi = 0.412$ which reflects that $T_{\rm max}$ occurs at $R = (49/36)R_{\rm in}$ (Kubota et al., 1998; Frank et al., 2002) and $\kappa \sim 1.7$ (e.g. Shimura and Takahara 1995) is the ratio of the colour temperature to the effective temperature (the spectral hardening factor).

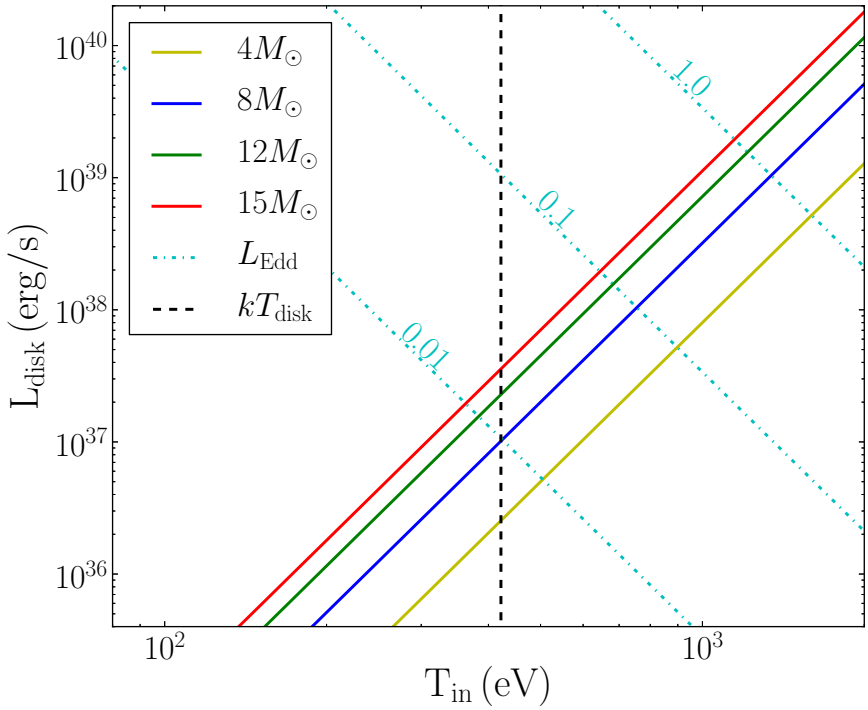

Figure 7.10: Disk luminosity versus disk temperature, allowing an estimate of the source distance. The solid yellow, blue, green and red lines are the expected disk luminosities at each temperature for a range of black hole masses. The dashed cyan lines represent fractions of the Eddington luminosity (where $L_{\rm Edd} = 1.3 \times 10^{38} M/M_\odot$) and the black line is our best fitting disk temperature during the softest state.

For any given black hole mass, $T_{\rm in}$ corresponds to a specific $L_{\rm disk}$. We select a range of representative masses (4–15 $M_\odot$) from Kreidberg et al. (2012), typical of Galactic black holes. Based on our measured value of $T_{\rm in}$, that range of masses corresponds to a range of $L_{\rm disk}$. Comparing the predicted range of $L_{\rm disk}$ with

our measured flux allows us to estimate the source distance (see Figure 7.10). The estimated source distance for a standard LMXB system (with $T_{\rm in} \approx 0.422$) is between 2.75 kpc (calculated for a $4\,M_\odot$ black hole) and 10 kpc (for a $15\,M_\odot$ black hole). We may rule out the lowest distance value as the transition from the hard state to the HIMS is expected at $\geq 0.03\ L_{\rm Edd}$ (Dunn et al., 2010) and the transition back occurs between 0.3% and 3% $L_{\rm Edd}$ (1.2–3.1% for systems with well constrained masses and distances Kalemci et al., 2013) with a mean value of ∼2% (Maccarone, 2003). We can therefore safely assume that the bolometric disk luminosity at the softest point of the outburst is >1% $L_{\rm Edd}$, placing a conservative lower limit of ∼4 kpc to the source.

7.5 Summary

We have modelled the full radio to X-ray spectra of MAXI J1836−194 during its 2011 outburst. We find that:

- $\nu_{\rm b}$ shifts by ∼3 orders of magnitude over the course of the outburst.
- $\nu_{\rm b}$ does not appear to scale with the source luminosity in the hard state, but possibly scales with X-ray hardness ($L_{\rm C}/L_{\rm d}$).
- The radius of the first acceleration zone (derived from $\nu_{\rm b}$) in the compact jet changes by ∼3 orders of magnitude during our observations (from $\sim 10^6\,r_{\rm g}$ during the HIMS to $10^3\,r_{\rm g}$ early in the outburst decay).
- Early in the outburst the high energy synchrotron cooling break occurs in the optical band (between $\approx 3.2 \times 10^{14}$ Hz and $\approx 4.5 \times 10^{14}$ Hz).
- The jet accounts for ∼ 6% of the total energy output of the system early in the outburst.
- The high-energy (hard) X-ray emission may be dominated by the jet during the hard state.
- We estimate that MAXI J1836−194 lies at a distance of 4–10 kpc.

Chapter 8

The radio/X-ray correlation in MAXI J1836−194

Adapted from:
T. D. Russell, J. C. A. Miller-Jones, P. A. Curran, R. Soria, D. Altamirano, S. Corbel, M. Coriat, A. Moin, D. M. Russell, G. R Sivakoff, T. J. Slaven-Blair, T. M. Belloni, R. P. Fender, S. Heinz, P. G. Jonker, H. A. Krimm, E. G. Körding, D. Maitra, S. Markoff, M. Middleton, S. Migliari, R. A. Remillard, M. P. Rupen, C. L. Sarazin, A. J. Tetarenko, M. A. P. Torres, V. Tudose, and A. K. Tzioumis (2015), 'Radio monitoring of the hard state jets in the 2011 outburst of MAXI J1836−194', *Monthly Notices of the Royal Astronomical Society*, Volume 450, Issue 2, p.1745-1759, DOI:10.1093/mnras/stv723, section 4.4

In this chapter we present simultaneous radio and X-ray observations of the LMXB MAXI J1836−194 taken during its 2012 reflare and the hard state decay of its 2011 outburst. We use these observations to investigate the hard state radio/X-ray correlation (Section 2.3.3) of the system as it faded towards quiescence, and attempt to determine what may be driving this correlation.

8.1 Observations

8.1.1 VLA

In this chapter, we consider only the VLA observations taken during the hard state decay (following the transition from the HIMS to the hard state on Septem-

ber 28) that had quasi-simultaneous X-ray data. See Section 6.1.1, for full details of the observations and data reduction.

8.1.2 ATCA

In this chapter, we consider the ATCA observations of MAXI J1836−194 taken during its 2012 minor reflare (Table 8.1). All observations were taken at 5.5 and 9.0 GHz with a bandwidth of 2 GHz at each frequency. The ATCA data were reduced using standard routines in ATNF's MIRIAD package (Sault et al., 1995). Primary flux calibration for all observations was done using 1934−638. Phase calibration was carried out with 1908−201 for all observations, except on 2012 April 8 where 1829−207 was used. Calibrated data were exported to DIFMAP for imaging and flux densities were obtained by fitting a point source model to the target in the image plane (Table 8.1). During our observations of MAXI J1836−194 during its 2012 reflare, the source was detected only on April 8, and we provide 3σ upper limits for all other epochs. When detected, the source was found to be unresolved within the ATCA beam.

Table 8.1: ATCA flux densities of the 2012 reflare of MAXI J1836−194. Upper limits are 3σ.

Date (UT)	MJD	Array config.	Freq. (GHz)	Flux density (mJy)
2012 Apr 8	56024.94	H168	5.5	0.64±0.05
			9.0	0.68±0.04
2012 Jun 24	56102.73	6D	5.5	≤0.23
			9.0	≤0.28
2012 Aug 24	56163.30	6A	5.5	≤0.07
			9.0	≤0.09

8.1.3 RXTE

RXTE (Jahoda et al., 1996, 2006) monitored MAXI J1836−194 throughout the 2011 outburst, for a period of about 92 days (see Section 6.1.2 for full observation and reduction details). In this Chapter, we only examine *RXTE* data taken

with simultaneous radio observations during the hard state decay of the outburst (following the transition from the HIMS back to the hard state).

8.1.4 *Swift*/XRT

Swift/XRT monitored MAXI J1836−194 during its period of renewed activity in 2012. Observations taken on 2012 April 6 and 9, June 15 and 29 (which were closest in time to our April 8 and June 24 ATCA observations) were retrieved from the HEASARC public archives. The 2012 April observations (characterised by a higher count rate) were taken in windowed-timing mode, while those from 2012 June (when the source was fainter) were in photon-counting mode. We extracted the spectral files and their associated background, response and ancillary response files with the online XRT data product generator.

To determine the X-ray flux of the *Swift*/XRT observations of MAXI J1836−194 during its 2012 re-flare, we modelled the spectra in the 0.4–10 keV band with a simple disk-blackbody plus power-law, with fixed line-of-sight Galactic absorption and free intrinsic absorption. For these X-ray data, more complex fits with physical Comptonisation models or irradiated disk models did not improve the fit due to the low signal-to-noise ratio. Moreover, our primary interest was in the flux from the power-law component in the 3–9 keV band (which is the typical band for the radio/X-ray correlation; e.g. Corbel et al. 2013), rather than the details of the soft component. Therefore, an absorbed disk-blackbody plus power-law model was adequate. On 2012 April 6 and 9, a faint disk-blackbody component was significantly detected with a temperature $kT_{\rm in} = 0.16^{+0.04}_{-0.02}$ keV (from the combined spectra), but the 3–9 keV flux was entirely dominated by the power-law component ($\Gamma_{\rm X} = 1.65^{+0.10}_{-0.08}$) and was unaffected by absorption (total $n_{\rm H} \lesssim 4 \times 10^{21}$ cm^{-2}). On 2012 June 15, the spectrum was best fit by a simple power law ($\Gamma_{\rm X} = 1.98^{+0.35}_{-0.32}$). On 2012 June 29, the source was no longer significantly detected. We therefore estimated a 90% confidence limit to its net count rate from the number of counts detected in the source and background regions (using Bayesian statistics; Kraft et al. 1991). We converted this count rate upper limit to a flux upper limit assuming the same power-law spectral model that we fit to the 2012 June 15 spectrum.

8.2 Results and discussion

The decay phase of the outburst allows us to probe the hard-state radio/X-ray correlation of MAXI J1836−194. In Figure 8.1 we plot the observed hard state radio/X-ray correlation of MAXI J1836−194 with representative data from the upper branch (GX 339−4; Corbel et al. 2013) and the lower branch (H1743−322; Coriat et al. 2011). For comparison, we calculate the luminosities of MAXI J1836−194 over the same energies (3–9 keV for the X-rays and 5 GHz in the radio band) as Corbel et al. (2013) and Coriat et al. (2011). During the decay, we find a steeper than usual radio/X-ray correlation, with an index of 1.8±0.2. This correlation index does not appear to be dependent on frequency (e.g. taking any band of our radio data produces a similar index) and therefore cannot be explained by the changing radio spectral index. Comparing this result with expected relations from Plotkin et al. (2012) also shows that the steep correlation cannot be explained by models where the X-ray emission originates either as inverse Compton from a corona, or is dominated by optically thin synchrotron radiation from the jet. We note that our 2011 X-ray observations only span ∼1 order of magnitude in $L_{\rm x}$ and deviations from the expected relationship have been found when the X-ray luminosity range is roughly one order of magnitude (thought to be due to changes in the spectral index, electron cooling, additional X-ray emitting region, etc; Corbel et al. 2013). However, if we include ATCA and *Swift* monitoring of the source during (and following) a re-brightening phase in 2012 we extend the X-ray luminosity range. Our 2012 data show that the source appears to lie on same steep track and at $5{\times}10^{34}\,{\rm erg\,s^{-1}}$ the source is still under radio luminous (Figure 8.1). The relation we observe also holds over ∼2.5 orders of magnitude in radio luminosity and does not appear to be random scatter about the standard correlation. Given the low inclination of this system (between 4° and 15°; Section 5.3.2) it is plausible that variable Doppler boosting affects the correlation. We now investigate this possibility.

Assuming random inclination angles and highly variable boosting, Soleri and Fender (2011) tested a model to determine if variable boosting could account for the scatter of the radio/X-ray correlation for the available sample of black holes. With their model, they were able to qualitatively reproduce both the scatter of the correlation and the 'radio-quiet' lower branch but noted that the model had its limitations. Here, we use a similar approach to test if the steep radio/X-ray correlation in MAXI J1836−194 could be explained by variable relativistic beaming. While recent work has cast doubt over the universality of the two well-defined

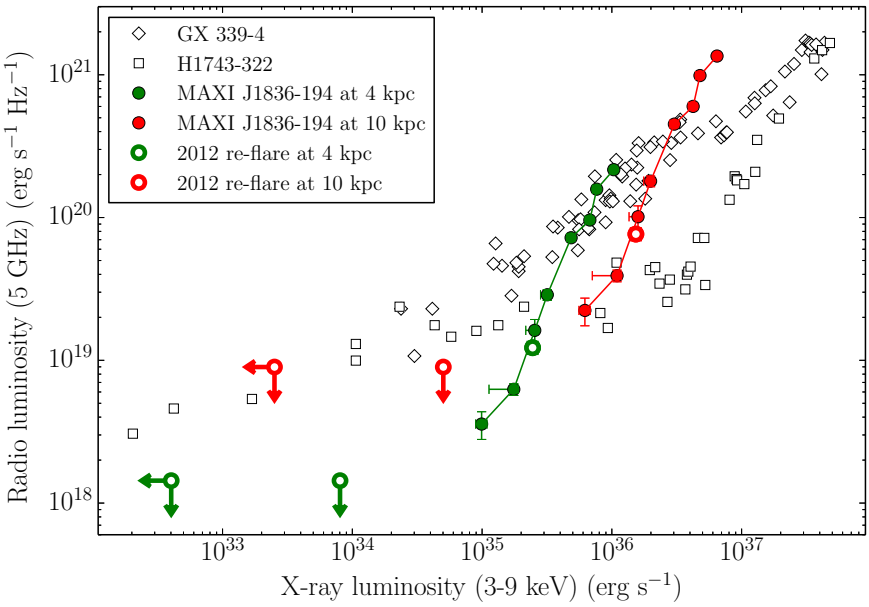

Figure 8.1: The hard-state radio/X-ray correlation of MAXI J1836−194. The open diamonds and squares are representative data from GX 339−4 (Corbel et al., 2013) and H1743−322 (Coriat et al., 2011), respectively. MAXI J1836−194 data from the 2011 outburst decay are shown by the filled green and red circles for the allowable distance limits of 4 and 10 kpc, respectively, while the open red and green circles show the monitoring from its minor re-brightening in 2012. The observed radio/X-ray correlation for this system is significantly steeper than either of the standard tracks shown by the representative data.

tracks for the radio/X-ray correlation (Gallo et al., 2014), we assume that the intrinsic radio luminosity of MAXI J1836−194 lies on the lower canonical hard-state track. We then determine what boosting would be required to account for the observed radio luminosity, testing whether a variable Γ can plausibly account for the steeper than usual correlation. For the system to lie on the upper track, the radio emission at low X-ray luminosities would need to be significantly deboosted (while being boosted at higher X-ray luminosities; Figure 8.1). Deboosted radio emission has been observed in LMXBs (e.g. XTE J1752−223; Yang et al. 2010) but is unlikely to have affected our observations due to the low inclination angle of the system.

We assume that the X-ray emission remains unbeamed (but see Markoff et al. 2005; Russell et al. 2010) and relate the observed beamed radio luminosity, $L_{\rm R,o}$,

to the intrinsic radio luminosity, $L_{\rm R,i}$, by

$$L_{\rm R,o} = L_{\rm R,i}\delta^{n-\alpha}, \tag{8.1}$$

where δ is the Doppler factor, n=2 (for a continuously replenished jet; Fender 2006), and α is the spectral index of the radio emission. The Doppler factor is a function of Γ where $\delta = \Gamma^{-1}(1 - \beta\cos\theta)^{-1}$, β is the velocity of the jet emission as a fraction of the speed of light, and θ is the inclination of the system; because $\Gamma = (1 - \beta^2)^{-1/2}$, we are then able to calculate the Lorentz factor required to shift the modelled intrinsic radio luminosity to that observed.

If we assume an inclination angle of 10° (Section 5.3.2), a source distance of 10 kpc (Section 7.4.4) and a jet axis perpendicular to the plane of the binary, then for $L_{\rm R,i}$ to lie on the lower track of the radio/X-ray correlation Γ must change by a factor of ∼3–4 during the outburst (from $\Gamma \approx$1 at the lowest X-ray luminosity to Γ ∼3–4 at the highest; Figure 8.2). This result is sensitive to the normalisation of the assumed intrinsic radio luminosity, therefore we have tested a range of normalisations that account for the observed scatter about the lower track. The maximum values of Γ are higher than previously thought for both a compact jet (where $\Gamma \leq$2; Fender et al. 2004) and the transient jet of GRS 1915+105 (where 1.6$\leq \Gamma \leq$1.9; Reid et al. 2014). However, due to the low inclination of MAXI J1836−194, the values we estimate are not so high that beaming can be ruled out as an explanation for the steep radio/X-ray correlation. Fitting Γ against X-ray luminosity (as a fraction of the Eddington luminosity for a 10 $M_\odot$ black hole) gives $\log(\Gamma) \propto \kappa l_{\rm x}$, where $l_{\rm x} = L_{\rm x}/L_{\rm Edd}$ and $\kappa \approx$ 100–120. With this result, the bulk Lorentz factor becomes larger than ∼1 above 0.05 percent $L_{\rm Edd}$ (below this luminosity, Γ=1). For comparison, Soleri and Fender (2011) found Γ becomes $\gtrsim$ 1 above 0.1 percent $L_{\rm Edd}$. This level of boosting would be expected to have consequences on the observed radio spectrum, due to the relationship between the opening angle of the forward emission cone and Γ. That is, if the observer remains within the emission cone as Γ increases, the radio spectrum is expected to flatten, whereas if the observer is now outside of the emission cone, then the radio spectrum would appear more inverted (Polko et al., 2014). Therefore, coupling the known inclination angle (assuming that the jet is perpendicular to the disk) and Γ with the observed radio spectral index may provide some insight into physical parameters of the jet (such as the opening angle). However, the spectral index is also expected to change with the bulk flow along the jet (Blandford and Königl, 1979; Falcke and Biermann, 1995; Kaiser, 2006; Pe'er and Casella, 2009) and the injection of energy from, e.g., shocks and

turbulence (Kaiser, 2006; Jamil et al., 2010). Therefore a full modelling analysis would be required to determine the jet parameters, which is beyond the scope of this work.

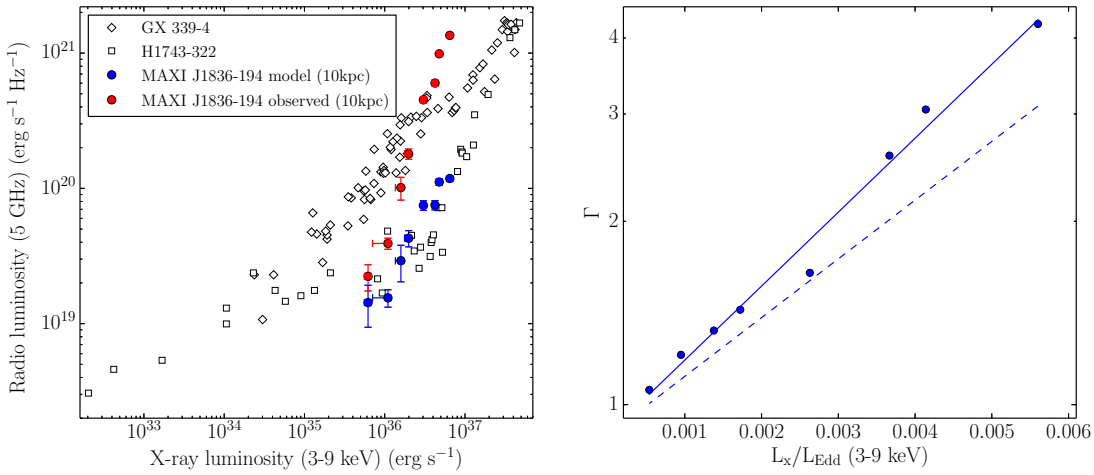

Figure 8.2: Variable boosting of $L_{\rm R}$. Left panel: the observed hard-state radio/X-ray correlation of MAXI J1836−194 (red points), with the de-boosted, modelled intrinsic data (blue points). Right panel: Γ required to shift $L_{\rm R,intrinsic}$ to $L_{\rm R,observed}$, as a function of X-ray luminosity assuming a distance of 10 kpc and an inclination of 10°. Here, $\log(\Gamma) \propto \kappa l_{\rm x}$, where $l_{\rm x} = L_{\rm x}/{\rm L_{Edd}}$ and $\kappa \approx 100$–120 (depending on the normalisation). Here, the blue points and solid blue line show results from the minimum normalisation used to account for the observed scatter about the lower track, while the dashed blue line shows the result for the maximum normalisation. The results show that variable Doppler boosting of the radio emission could in principle account for the unusually steep radio/X-ray correlation in this system.

At a source distance of <8 kpc, the radio emission at low X-ray luminosities falls well below the canonical relation (Figure 8.1) and could not be explained unless it was deboosted. Therefore, if we assume that the steep radio/X-ray correlation is due to a variable Lorentz factor, MAXI J1836−194 must be at a distance greater than 8 kpc.

Our results show that relativistic beaming could in principle account for the observed radio/X-ray correlation in MAXI J1836−194. However, similar to the results of Soleri and Fender (2011), if we applied our boosting argument to the full sample of LMXBs we would see the correlation break down at X-ray luminosities $\gtrsim 0.5$ percent Eddington (Figure 8.3). Following an outburst, black hole

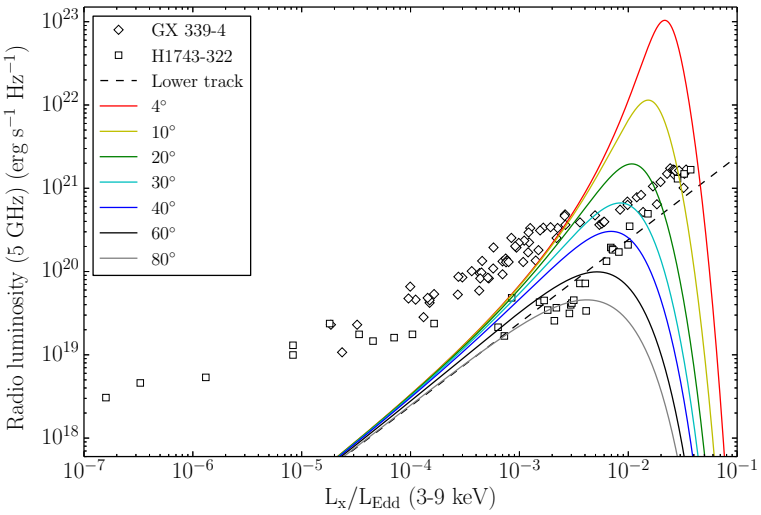

Figure 8.3: Our boosting argument at different inclination angles (coloured solid lines) applied to the lower track of the radio/X-ray correlation (black dashed line). Representative data from GX 339−4 (open diamonds; Corbel et al. 2013) and H1743−322 (open squaresCoriat et al. 2011) are also shown. This shows that, if all black hole LMXBs exhibited the level of boosting required for MAXI J1836−194 to lie on the lower track, the correlation would break down at X-ray luminosities $\gtrsim 0.5\%$ of the Eddington luminosity.

LMXBs generally transition back to the hard state at luminosities between 0.3 and 3 percent Eddington (Kalemci et al., 2013), with a mean value of ∼2 percent (Maccarone, 2003), demonstrating that X-ray luminosities of $\gtrsim 0.5$ percent Eddington are expected during the hard state decay. Heinz and Merloni (2004) analysed the radio/X-ray correlation of GX 339−4 and V404 Cyg and argued that similar Lorentz factors are expected between sources. We therefore conclude that while a variable Lorentz factor can explain the unusually steep radio/X-ray correlation in MAXI J1836−194, it cannot be universally applied to the broad sample of black hole binaries.

It is possible that the steep correlation is a temporary deviation from the standard track (Corbel et al., 2013). However, when we include data from the 2012 re-flare, we see the source appears to lie on the same steep radio/X-ray track and does not immediately rejoin the standard track. This system could simply produce an intrinsically steep correlation ($\sim 2\sigma$ from the steeper track of Coriat et al. 2011, or 4σ from that of Gallo et al. 2012, but see recent results from Gallo et al. 2014). However, this index cannot be explained by models of X-ray

emission originating as inverse Compton from a corona, or being dominated by optically-thin synchrotron emission from the compact jet.

8.3 Summary

With simultaneous radio and X-ray monitoring of MAXI J1836−194, we observed:

- An unusually steep radio/X-ray correlation where $L_{\rm R} \propto L_{\rm x}^{1.8\pm0.2}$.
- The steep correlation could in principle be explained by variable Doppler boosting. However, this argument cannot be applied to the full sample of black hole LMXBs.
- If this model is correct, then MAXI J1836−194 must lie fall on the radio-quiet track, and must be at a distance >8 kpc.

Chapter 9

Conclusions

This thesis has presented the results of an intensive, quasi-simultaneous multi-wavelength observing campaign on the black hole X-ray binary MAXI J1836−194 during its 2011 outburst. This high-cadence campaign has provided the most comprehensive observations to date of a compact jet during X-ray binary spectral state transitions, providing new insights into the evolution of the compact jet and the contemporaneous changes in the accretion flow during the failed outburst.

9.1 Observational results

With optical observations of the system during outburst and in quiescence we place constraints on the physical parameters of the system and find that this system has an inclination angle of 4–15°, which is the lowest currently measured in any transient black hole LMXB. The low inclination means that the jet is pointed towards the observer, appearing brighter than systems with higher inclinations, making this system an ideal candidate for studying the evolution of the jet during the outburst. With the measured X-ray parameters, we find that this system must lie at a distance of 4–10 kpc.

Radio monitoring of the polarised jets has shown a ∼15 mas jet along the same position angle as the intrinsic electric vector position angle. The agreement between the EVPA and compact jet axis implies that the magnetic field was perpendicular to the jet axis, possibly due to helical structure from accretion disk rotation or compression from internal shocks. Interestingly, this is the fourth system where this alignment has been observed (although one is model-dependent). If such an alignment is common to black hole X-ray binaries, high-resolution VLBI images may not be necessary to determine the orientation of the jets. The

peculiar velocity of the system was calculated with astrometric observations. The high space velocity of the system suggests that the black hole required an asymmetric natal kick from a supernova during its formation, making this just the sixth system with accurate constraints on the formation mechanism of the black hole.

The full multiwavelength observations presented have shown the detailed changes in the energetics of the jet over a state transition. For the first time, the observations show the frequency of the jet spectral break shifted by $\sim$3 orders of magnitude during the outburst from $\sim 10^{11}$ Hz to $\sim 10^{14}$ Hz. The evolution of this shift did not scale with X-ray luminosity as expected. Instead the position of the break frequency appears to have been driven by the changing structure of the accretion flow, possibly by the same processes that drive X-ray hardness. The evolution of the break frequency also implies that the radius of the first acceleration zone evolved significantly during the transition, from $\sim 10^6$ gravitational radii during the hard intermediate state, before decreasing to $\sim 10^3$ gravitational radii during the hard state decay, assuming a $10\,M_\odot$ black hole. This result implies that the particle acceleration is occurring on much larger scales than expected during the HIMS. These observations have also resulted in the first observational inference of the high-energy synchrotron cooling break in a LMXB. The cooling break is generally thought to shift from the UV to the X-ray band as the system transitions from quiescence to the bright, hard X-ray states; The observations presented here imply that, just prior to the transition to the HIMS, the cooling break resides in the optical band in the bright hard state (between $\approx 3.2 \times 10^{14}$ and 4.5×10^{14} Hz). This detection implies that the jet is already evolving significantly early in the outburst. With the position of cooling break, by integrating across the entire jet spectrum the total radiative jet luminosity was determined to be $\approx 1.8 \times 10^{36}\,\mathrm{erg\,s^{-1}}$, assuming a source distance of 8 kpc. If purely radiative, the jet will account for $\sim$6% of the bolometric radiative luminosity, indicating that the system was not jet dominated at this time and that the true radiative jet luminosity will depend on the evolution of the cooling break.

The extensive radio and X-ray monitoring have also shown an unusually steep radio/X-ray correlation of $L_\mathrm{R} \propto L_\mathrm{X}^{1.8\pm0.08}$ during this outburst, much steeper than in other black hole LMXB systems. We find that the steep correlation may have been driven by a variable jet Lorentz factor. However, this relation cannot be applied to the full sample of black hole LMXB systems. Interestingly, data from a re-flare in 2012 show that this system appeared to once again lie on the unusually steep track, suggesting that MAXI J1836−194 may have an intrinsically steep

correlation (although it cannot be explained by models of X-ray emission originating as inverse Compton from a corona or optically-thin synchrotron emission from the compact jet).

These detailed measurements of the evolving compact jet and contemporaneous changes in the accretion flow have given an unparalleled view into the physical processes that are occurring within the jet and how they may be driven by the accretion flow. The findings presented here are important given the ubiquity of jets on all scales in the observable universe; understanding the nature of the accretion-ejection coupling is critical to improving our understanding of the processes that occur around a black hole, having implications for accreting sources on all scales. The feedback effect of jets in AGN is thought to heat the surrounding intracluster medium, counteracting cooling flows and affecting the evolution of galaxies and galaxy clusters (e.g. Churazov et al., 2002; McNamara and Nulsen, 2007; Fabian, 2012). The results can also be used to test the universal scaling relations between the accretion inflow and jet outflow, determining the applicability of the accretion-ejection relationship to the more massive black holes in AGN.

9.2 Future work

The state-of-the-art multiwavelength observations presented here have provided ground-breaking details on the evolution of the compact jet during state transitions. However, while the single-zoned synchrotron model used to model jet parameters does clearly demonstrate the evolution of the acceleration region, more detailed treatments (e.g. Markoff et al. 2001; Polko et al. 2010, 2013, 2014), which take into account multiple acceleration regions, internal shocks, and relativistic effects, are required to fully constrain the changing jet parameters. New and next-generation telescopes, such as the Atacama Large Millimeter/submillimeter Array (ALMA) in northern Chile, and the Square Kilometre Array (SKA) in Southern Africa and Australia, will also potentially revolutionise the study and understanding of jets, their emission processes, and how they are coupled to the accretion flow.

This program has pioneered sub-mm observations of black hole LMXB jets with the use of the SMA, bridging the gap between the radio and IR band. When coupled with simultaneous multiwavelength monitoring, millimetre observations are critical to monitoring the evolving jet spectrum, providing crucial information

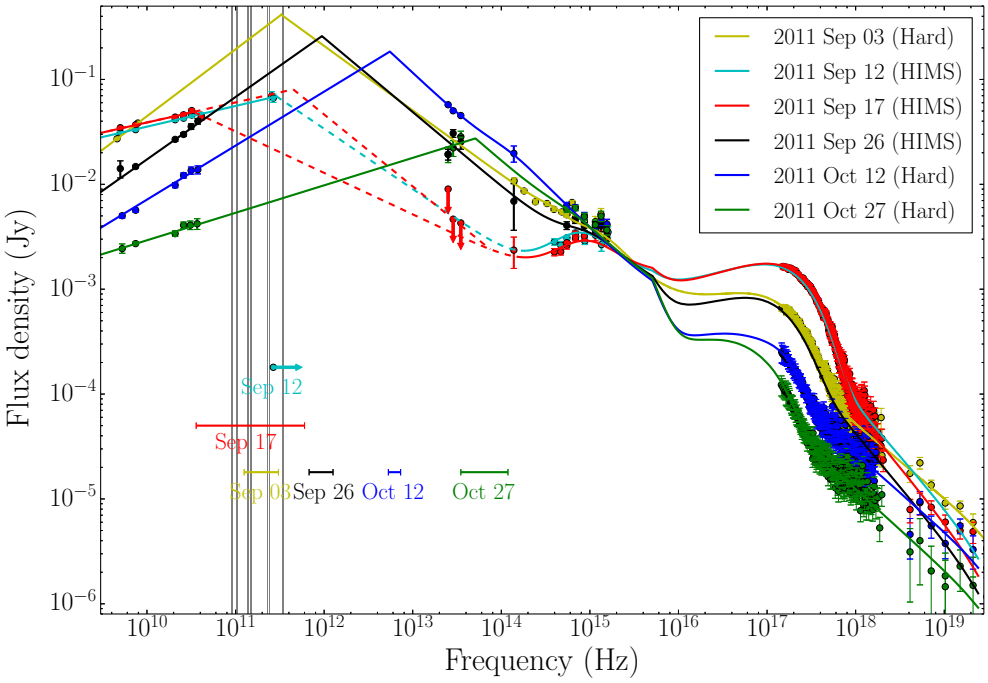

Figure 9.1: The broadband modelling of MAXI J1836−194 during its 2011 outburst, where solid lines indicate fits to the data and dashed lines indicate ranges in which the model is uncertain. The frequency of the ALMA Bands are shown as the grey vertical lines. This coverage shows that ALMA is crucial to accurately probing the mm/sub-mm regime and the evolving jet breaks of LMXBs.

into the underlying jet physics. While the observations presented in this project give new clues as to what parameters of the accretion flow set the jet behaviour, the recent construction of ALMA will further fill the ∼2 orders of magnitude gap in frequency between the radio and IR regime (Figure 9.1). Without such observations the frequency of the jet spectral break must be extrapolated from the radio and IR bands, introducing up to an order of magnitude in uncertainty (as for MAXI J1836−194 on 2011 September 17). The accurate tracking of the jet break as it evolves will then allow for the precise determination of the jet energetics, the radius of the first acceleration zone and the jets magnetic field as they evolve during the outburst. With these better constraints, jet modelling will show how the key physical parameters evolve, which can then be coupled to the accretion properties, such as X-ray hardness, in an attempt to determine what physical processes are driving changes within the compact jet, such as the jet quenching and launching mechanisms. The increased sensitivity provided by ALMA (with an expected SNR>20 for typical 1–5 mJy outbursts), coupled to its

access to the southern skies, will provide detections of X-ray binaries that were previously too faint, increasing the number of systems suitable to jet studies.

The SKA is set to provide orders of magnitude improvements in sensitivity over other radio telescopes, enabling the monitoring of LMXBs from their bright, outburst states, down to their low-luminosity quiescent states, improving our understanding of jet acceleration at all accretion rates. The full SKA is expected to deliver sensitivities $\sim$2 orders of magnitude better than the VLA between 1 and 40 GHz (SKA1 is expected to provide a factor of $\sim$7 improvement). This, coupled with the wide field of view and multibeaming capabilities, will enable for the detection and high-cadence monitoring of all flaring transients within $\sim$10 Mpc, enabling the detailed tracking of the jet parameters at high accretion rates in transient ultra-luminous X-ray sources. The observation of previously undetectable X-ray binaries both in our Galaxy and in the local group will answer questions about the dependence of jet launching on the environment and metallicity of the accreted material. The high angular resolution of the SKA will provide a unprecedented view of the jet, including the evolution of the opacity within individual ejecta. With the many new observable black hole X-ray binaries, accurate astrometric measurements of a large sample of black hole LMXBs can also be used to constrain the formation mechanism of black holes.

This project has shown how multiwavelength observations can be used to probe the relationship between the inflow and outflow around accreting stellar-mass black holes. With new state-of-the-art telescopes, observations of X-ray binaries will provide new information on the accretion and ejection processes, and how they are coupled, helping to determine how accretion powered jets are launched on all physical scales.

Bibliography

Abell, G. O. and B. Margon (1979, June). A kinematic model for SS433. *Nature 279*, 701–703.

Abramowicz, M. A., X. Chen, S. Kato, J.-P. Lasota, and O. Regev (1995, January). Thermal equilibria of accretion disks. *ApJL 438*, L37–L39.

Abramowicz, M. A., B. Czerny, J. P. Lasota, and E. Szuszkiewicz (1988, September). Slim accretion disks. *ApJ 332*, 646–658.

Adams, F. C., D. S. Graff, and D. O. Richstone (2001, April). A Theoretical Model for the M_{BH}-σ Relation for Supermassive Black Holes in Galaxies. *ApJL 551*, L31–L35.

Altamirano, D., M. van der Klis, M. Méndez, P. G. Jonker, M. Klein-Wolt, and W. H. G. Lewin (2008, September). X-Ray Time Variability Across the Atoll Source States of 4U 1636-53. *ApJ 685*, 436–450.

Alvarez, M. A., J. H. Wise, and T. Abel (2009, August). Accretion onto the First Stellar-Mass Black Holes. *ApJL 701*, L133–L137.

Appenzeller, I., K. Fricke, W. Fürtig, W. Gässler, R. Häfner, R. Harke, H.-J. Hess, W. Hummel, P. Jürgens, R.-P. Kudritzki, K.-H. Mantel, W. Meisl, B. Muschielok, H. Nicklas, G. Rupprecht, W. Seifert, O. Stahl, T. Szeifert, and K. Tarantik (1998, December). Successful commissioning of FORS1 - the first optical instrument on the VLT. *The Messenger 94*, 1–6.

Arnaud, K., R. Smith, and A. Siemiginowska (2011, September). *Handbook of X-ray Astronomy*. Cambridge University Press, U.K.

Arnaud, K. A. (1996). XSPEC: The First Ten Years. In G. H. Jacoby and J. Barnes (Eds.), *Astronomical Data Analysis Software and Systems V*, Volume 101 of *Astronomical Society of the Pacific Conference Series*, pp. 17.

Banse, K., D. Ponz, C. Ounnas, P. Grosbol, and R. Warmels (1988). The MIDAS Image Processing System. In L. B. Robinson (Ed.), *Instrumentation for Ground-Based Optical Astronomy*, pp. 431.

Bardeen, J. M., W. H. Press, and S. A. Teukolsky (1972, December). Rotating Black Holes: Locally Nonrotating Frames, Energy Extraction, and Scalar Synchrotron Radiation. *ApJ 178*, 347–370.

Baumgarte, T. W. and S. L. Shapiro (1999, December). Evolution of Rotating Supermassive Stars to the Onset of Collapse. *ApJ 526*, 941–952.

Beasley, A. J., D. Gordon, A. B. Peck, L. Petrov, D. S. MacMillan, E. B. Fomalont, and C. Ma (2002, July). The VLBA Calibrator Survey-VCS1. *ApJS 141*, 13–21.

Begelman, M. C., P. J. Armitage, and C. S. Reynolds (2015, July). Accretion disk dynamo as the trigger for X-ray binary state transitions. *ApJ, in press. ArXiv e-prints: 1507.03996*.

Begelman, M. C. and M. J. Rees (1978, December). The fate of dense stellar systems. *MNRAS 185*, 847–860.

Begelman, M. C., M. Volonteri, and M. J. Rees (2006, July). Formation of supermassive black holes by direct collapse in pre-galactic haloes. *MNRAS 370*, 289–298.

Bell, A. R. (1978, January). The acceleration of cosmic rays in shock fronts. I. *MNRAS 182*, 147–156.

Belloni, T. (2005, October). Black Hole States: Accretion and Jet Ejection. In L. Burderi, L. A. Antonelli, F. D'Antona, T. di Salvo, G. L. Israel, L. Piersanti, A. Tornambè, and O. Straniero (Eds.), *Interacting Binaries: Accretion, Evolution, and Outcomes*, Volume 797 of *American Institute of Physics Conference Series*, pp. 197–204.

Belloni, T. (Ed.) (2010, March). *The Jet Paradigm*, Volume 794 of *Lecture Notes in Physics, Berlin Springer Verlag*.

Belloni, T., J. Homan, P. Casella, M. van der Klis, E. Nespoli, W. H. G. Lewin, J. M. Miller, and M. Méndez (2005, September). The evolution of the timing properties of the black-hole transient GX 339-4 during its 2002/2003 outburst. *A&A 440*, 207–222.

Belloni, T. M., S. E. Motta, and T. Muñoz-Darias (2011, September). Black hole transients. *Bulletin of the Astronomical Society of India 39*, 409–428.

Bildsten, L. and R. E. Rutledge (2000, October). Coronal X-Ray Emission from the Stellar Companions to Transiently Accreting Black Holes. *ApJ 541*, 908–917.

Bisnovatyi-Kogan, G. S. and S. I. Blinnikov (1977, July). Disk accretion onto a black hole at subcritical luminosity. *A&A 59*, 111–125.

Blaauw, A. (1961, May). On the origin of the O- and B-type stars with high velocities (the "run-away" stars), and some related problems. *BAIN 15*, 265.

Blackburn, J. K. (1995). FTOOLS: A FITS Data Processing and Analysis Software Package. In R. A. Shaw, H. E. Payne, and J. J. E. Hayes (Eds.), *Astronomical Data Analysis Software and Systems IV*, Volume 77 of *Astronomical Society of the Pacific Conference Series*, pp. 367.

Blandford, R. D. and M. C. Begelman (1999, February). On the fate of gas accreting at a low rate on to a black hole. *MNRAS 303*, L1–L5.

Blandford, R. D. and A. Königl (1979, August). Relativistic jets as compact radio sources. *ApJ 232*, 34–48.

Blandford, R. D. and D. G. Payne (1982, June). Hydromagnetic flows from accretion discs and the production of radio jets. *MNRAS 199*, 883–903.

Blandford, R. D. and R. L. Znajek (1977, May). Electromagnetic extraction of energy from Kerr black holes. *MNRAS 179*, 433–456.

Brandt, N. and P. Podsiadlowski (1995, May). The effects of high-velocity supernova kicks on the orbital properties and sky distributions of neutron-star binaries. *MNRAS 274*, 461–484.

Breeveld, A. A., P. A. Curran, E. A. Hoversten, S. Koch, W. Landsman, F. E. Marshall, M. J. Page, T. S. Poole, P. Roming, P. J. Smith, M. Still, V. Yershov, A. J. Blustin, P. J. Brown, C. Gronwall, S. T. Holland, N. P. M. Kuin, K. McGowan, S. Rosen, P. Boyd, P. Broos, M. Carter, M. M. Chester, B. Hancock, H. Huckle, S. Immler, M. Ivanushkina, T. Kennedy, K. O. Mason, A. N. Morgan, S. Oates, M. de Pasquale, P. Schady, M. Siegel, and D. vanden Berk (2010, August). Further calibration of the Swift ultraviolet/optical telescope. *MNRAS 406*, 1687–1700.

Bressan, A., P. Marigo, L. Girardi, B. Salasnich, C. Dal Cero, S. Rubele, and A. Nanni (2012, November). PARSEC: stellar tracks and isochrones with the PAdova and TRieste Stellar Evolution Code. *MNRAS 427*, 127–145.

Briggs, D. S. (1995, December). High Fidelity Interferometric Imaging: Robust Weighting and NNLS Deconvolution. In *American Astronomical Society Meeting Abstracts*, Volume 27 of *Bulletin of the American Astronomical Society*, pp. 112.02.

Briggs, D. S., F. R. Schwab, and R. A. Sramek (1999). Imaging. In G. B. Taylor, C. L. Carilli, and R. A. Perley (Eds.), *Synthesis Imaging in Radio Astronomy II*, Volume 180 of *Astronomical Society of the Pacific Conference Series*, pp. 127.

Brocksopp, C., S. Corbel, A. Tzioumis, J. W. Broderick, J. Rodriguez, J. Yang, R. P. Fender, and Z. Paragi (2013, June). XTE J1752-223 in outburst: a persistent radio jet, dramatic flaring, multiple ejections and linear polarization. *MNRAS 432*, 931–943.

Brocksopp, C., R. P. Fender, M. McCollough, G. G. Pooley, M. P. Rupen, R. M. Hjellming, C. J. de la Force, R. E. Spencer, T. W. B. Muxlow, S. T. Garrington, and S. Trushkin (2002, April). Initial low/hard state, multiple jet ejections and X-ray/radio correlations during the outburst of XTE J1859+226. *MNRAS 331*, 765–775.

Brocksopp, C., J. C. A. Miller-Jones, R. P. Fender, and B. W. Stappers (2007, July). A highly polarized radio jet during the 1998 outburst of the black hole transient XTE J1748-288. *MNRAS 378*, 1111–1117.

Buxton, M. M., C. D. Bailyn, H. L. Capelo, R. Chatterjee, T. Dinçer, E. Kalemci, and J. A. Tomsick (2012, June). Optical and Near-infrared Monitoring of the Black Hole X-Ray Binary GX 339-4 during 2002-2010. *AJ 143*, 130.

Buzzoni, B., B. Delabre, H. Dekker, S. Dodorico, D. Enard, P. Focardi, B. Gustafsson, W. Nees, J. Paureau, and R. Reiss (1984, December). The ESO Faint Object Spectrograph and Camera (EFOSC). *The Messenger 38*, 9–13.

Cardelli, J. A., G. C. Clayton, and J. S. Mathis (1989, October). The relationship between infrared, optical, and ultraviolet extinction. *ApJ 345*, 245–256.

Casella, P. and A. Pe'er (2009, September). On the Role of the Magnetic Field on Jet Emission in X-Ray Binaries. *ApJL 703*, L63–L66.

Chandrasekhar, S. (1931, March). The highly collapsed configurations of a stellar mass. *MNRAS 91*, 456–466.

Chaty, S., G. Dubus, and A. Raichoor (2011, May). Near-infrared jet emission in the microquasar XTE J1550-564. *A&A 529*, A3.

Churazov, E., R. Sunyaev, W. Forman, and H. Böhringer (2002, May). Cooling flows as a calorimeter of active galactic nucleus mechanical power. *MNRAS 332*, 729–734.

Clark, B. G. (1980, September). An efficient implementation of the algorithm 'CLEAN'. *A&A 89*, 377.

Clark, B. G. (1999). Coherence in Radio Astronomy. In G. B. Taylor, C. L. Carilli, and R. A. Perley (Eds.), *Synthesis Imaging in Radio Astronomy II*, Volume 180 of *Astronomical Society of the Pacific Conference Series*, pp. 1.

Cohen, M. H., D. L. Meier, T. G. Arshakian, D. C. Homan, T. Hovatta, Y. Y. Kovalev, M. L. Lister, A. B. Pushkarev, J. L. Richards, and T. Savolainen (2014, June). Studies of the Jet in Bl Lacertae. I. Recollimation Shock and Moving Emission Features. *ApJ 787*, 151.

Corbel, S., H. Aussel, J. W. Broderick, P. Chanial, M. Coriat, A. J. Maury, M. M. Buxton, J. A. Tomsick, A. K. Tzioumis, S. Markoff, J. Rodriguez, C. D. Bailyn, C. Brocksopp, R. P. Fender, P. O. Petrucci, M. Cadolle-Bel, D. Calvelo, and L. Harvey-Smith (2013, April). Formation of the compact jets in the black hole GX 339-4. *MNRAS 431*, L107–L111.

Corbel, S., M. Coriat, C. Brocksopp, A. K. Tzioumis, R. P. Fender, J. A. Tomsick, M. M. Buxton, and C. D. Bailyn (2013, January). The 'universal' radio/X-ray flux correlation: the case study of the black hole GX 339-4. *MNRAS 428*, 2500–2515.

Corbel, S. and R. P. Fender (2002, July). Near-Infrared Synchrotron Emission from the Compact Jet of GX 339-4. *ApJL 573*, L35–L39.

Corbel, S., R. P. Fender, J. A. Tomsick, A. K. Tzioumis, and S. Tingay (2004, December). On the Origin of Radio Emission in the X-Ray States of XTE J1650-500 during the 2001-2002 Outburst. *ApJ 617*, 1272–1283.

Corbel, S., R. P. Fender, A. K. Tzioumis, M. Nowak, V. McIntyre, P. Durouchoux, and R. Sood (2000, July). Coupling of the X-ray and radio emission in the black hole candidate and compact jet source GX 339-4. *A&A 359*, 251–268.

Corbel, S., R. P. Fender, A. K. Tzioumis, J. A. Tomsick, J. A. Orosz, J. M. Miller, R. Wijnands, and P. Kaaret (2002, October). Large-Scale, Decelerating, Relativistic X-ray Jets from the Microquasar XTE J1550-564. *Science 298*, 196–199.

Corbel, S., P. Kaaret, R. K. Jain, C. D. Bailyn, R. P. Fender, J. A. Tomsick, E. Kalemci, V. McIntyre, D. Campbell-Wilson, J. M. Miller, and M. L. McCollough (2001, June). X-Ray States and Radio Emission in the Black Hole Candidate XTE J1550-564. *ApJ 554*, 43–48.

Corbel, S., M. A. Nowak, R. P. Fender, A. K. Tzioumis, and S. Markoff (2003, March). Radio/X-ray correlation in the low/hard state of GX 339-4. *A&A 400*, 1007–1012.

Coriat, M., S. Corbel, M. M. Buxton, C. D. Bailyn, J. A. Tomsick, E. Körding, and E. Kalemci (2009, November). The infrared/X-ray correlation of GX 339-4: probing hard X-ray emission in accreting black holes. *MNRAS 400*, 123–133.

Coriat, M., S. Corbel, L. Prat, J. C. A. Miller-Jones, D. Cseh, A. K. Tzioumis, C. Brocksopp, J. Rodriguez, R. P. Fender, and G. R. Sivakoff (2011, June). Radiatively efficient accreting black holes in the hard state: the case study of H1743-322. *MNRAS 414*, 677–690.

Cornwell, T., R. Braun, and D. S. Briggs (1999). Deconvolution. In G. B. Taylor, C. L. Carilli, and R. A. Perley (Eds.), *Synthesis Imaging in Radio Astronomy II*, Volume 180 of *Astronomical Society of the Pacific Conference Series*, pp. 151.

Cornwell, T. and E. B. Fomalont (1999). Self-Calibration. In G. B. Taylor, C. L. Carilli, and R. A. Perley (Eds.), *Synthesis Imaging in Radio Astronomy II*, Volume 180 of *Astronomical Society of the Pacific Conference Series*, pp. 187.

Cotton, W. D. (1995). Fringe Fitting. In J. A. Zensus, P. J. Diamond, and P. J. Napier (Eds.), *Very Long Baseline Interferometry and the VLBA*, Volume 82 of *Astronomical Society of the Pacific Conference Series*, pp. 189.

Cunningham, C. (1976, September). Returning radiation in accretion disks around black holes. *ApJ 208*, 534–549.

Curran, P. A. (2014, November). Monte Carlo error analyses of Spearman's rank test. *ArXiv e-prints 88*, 1–10.

Curran, P. A., M. Coriat, J. C. A. Miller-Jones, R. P. Armstrong, P. G. Edwards, G. R. Sivakoff, P. Woudt, D. Altamirano, T. M. Belloni, S. Corbel, R. P. Fender, E. G. Körding, H. A. Krimm, S. Markoff, S. Migliari, D. M. Russell, J. Stevens, and T. Tzioumis (2014, February). The evolving polarized jet of black hole candidate Swift J1745-26. *MNRAS 437*, 3265–3273.

Curran, P. A., T. J. Maccarone, and P. Casella (2010, December). Swift observations of black hole candidate, XTE J1752-223, during outburst. In *The First Year of MAXI: Monitoring Variable X-ray Sources*, pp. 3.

Curran, P. A., J. C. A. Miller-Jones, A. P. Rushton, D. D. Pawar, G. E. Anderson, D. Altamirano, H. A. Krimm, J. W. Broderick, T. M. Belloni, R. P. Fender, E. G. Körding, D. Maitra, S. Markoff, S. Migliari, C. Rumsey, M. P. Rupen, D. M. Russell, T. D. Russell, C. L. Sarazin, G. R. Sivakoff, R. Soria, A. J. Tetarenko, D. Titterington, and V. Tudose (2015, August). Radio polarimetry as a probe of unresolved jets: the 2013 outburst of XTE J1908+094. *MNRAS 451*, 3975–3985.

Dalton, W. W. and C. L. Sarazin (1995, February). High-mass X-ray binary populations. 1: Galactic modeling. *ApJ 440*, 280–296.

de Jong, J. A., J. van Paradijs, and T. Augusteijn (1996, October). Reprocessing of X rays in low-mass X-ray binaries. *A&A 314*, 484–490.

Del Santo, M., E. Kuulkers, J. Rodriguez, C. Baldovin, E. Bozzo, I. Caballero, M. Cadolle Bel, F. Capitanio, J. Chenevez, I. Kreykenbohm, M. Kuehnel, C. Sanchez-Fernandez, K. Watanabe, and G. Weidenspointner (2011, September). INTEGRAL Observations of MAXI J1836-194. *The Astronomer's Telegram 3652*, 1.

Deller, A. T., S. J. Tingay, M. Bailes, and C. West (2007, March). DiFX: A Software Correlator for Very Long Baseline Interferometry Using Multiprocessor Computing Environments. *PASP 119*, 318–336.

Dhawan, V., I. F. Mirabel, M. Ribó, and I. Rodrigues (2007, October). Kinematics of Black Hole X-Ray Binary GRS 1915+105. *ApJ 668*, 430–434.

Dhawan, V., I. F. Mirabel, and L. F. Rodríguez (2000, November). AU-Scale Synchrotron Jets and Superluminal Ejecta in GRS 1915+105. *ApJ 543*, 373–385.

Díaz Trigo, M., J. C. A. Miller-Jones, S. Migliari, J. W. Broderick, and T. Tzioumis (2013, December). Baryons in the relativistic jets of the stellar-mass black-hole candidate 4U1630-47. *Nature 504*, 260–262.

Done, C., M. Gierliński, and A. Kubota (2007, December). Modelling the behaviour of accretion flows in X-ray binaries. Everything you always wanted to know about accretion but were afraid to ask. *A&AR 15*, 1–66.

Drake, S. A. and R. K. Ulrich (1980, February). The emission-line spectrum from a slab of hydrogen at moderate to high densities. *ApJS 42*, 351–383.

Dreher, J. W., C. L. Carilli, and R. A. Perley (1987, May). The Faraday rotation of Cygnus A - Magnetic fields in cluster gas. *ApJ 316*, 611–625.

Drury, L. O. (1983, August). An introduction to the theory of diffusive shock acceleration of energetic particles in tenuous plasmas. *Reports on Progress in Physics 46*, 973–1027.

Dubus, G., J.-P. Lasota, J.-M. Hameury, and P. Charles (1999, February). X-ray irradiation in low-mass binary systems. *MNRAS 303*, 139–147.

Dunn, R. J. H., R. P. Fender, E. G. Körding, T. Belloni, and C. Cabanac (2010, March). A global spectral study of black hole X-ray binaries. *MNRAS 403*, 61–82.

Eddington, Sir, A. S. (1935a, November). Note on "relativistic degeneracy,". *MNRAS 96*, 20.

Eddington, Sir, A. S. (1935b, January). On "relativistic degeneracy,". *MNRAS 95*, 194–206.

Eggleton, P. P. (1983, May). Approximations to the radii of Roche lobes. *ApJ 268*, 368.

Einstein, A. (1915). Die Feldgleichungen der Gravitation. *Sitzungsberichte der Königlich Preußischen Akademie der Wissenschaften (Berlin), Seite 844-847. 1916*, 844–847.

Esin, A. A., J. E. McClintock, and R. Narayan (1997, November). Advection-Dominated Accretion and the Spectral States of Black Hole X-Ray Binaries: Application to Nova Muscae 1991. *ApJ 489*, 865–889.

Evans, P. A., A. P. Beardmore, K. L. Page, J. P. Osborne, P. T. O'Brien, R. Willingale, R. L. C. Starling, D. N. Burrows, O. Godet, L. Vetere, J. Racusin, M. R. Goad, K. Wiersema, L. Angelini, M. Capalbi, G. Chincarini, N. Gehrels, J. A. Kennea, R. Margutti, D. C. Morris, C. J. Mountford, C. Pagani, M. Perri, P. Romano, and N. Tanvir (2009, August). Methods and results of an automatic analysis of a complete sample of Swift-XRT observations of GRBs. *MNRAS 397*, 1177–1201.

Fabian, A. C. (2012, September). Observational Evidence of Active Galactic Nuclei Feedback. *ARA&A 50*, 455–489.

Fabian, A. C. and M. J. Rees (1979, April). SS 433 - A double jet in action. *MNRAS 187*, 13P–16P.

Falcke, H. and P. L. Biermann (1995, January). The jet-disk symbiosis. I. Radio to X-ray emission models for quasars. *A&A 293*, 665–682.

Falcke, H., E. Körding, and S. Markoff (2004, February). A scheme to unify low-power accreting black holes. Jet-dominated accretion flows and the radio/X-ray correlation. *A&A 414*, 895–903.

Fender, R. (2003, March). Circularly polarised radio emission from GRS 1915+105 and other X-ray binaries. *Ap&SS 288*, 79–95.

Fender, R. (2006, April). *Jets from X-ray binaries*. in Compact stellar X-ray sources, ed. Lewin, W. H. G. and van der Klis, M., Cambridge University Press, Cambridge, U.K.

Fender, R., S. Corbel, T. Tzioumis, V. McIntyre, D. Campbell-Wilson, M. Nowak, R. Sood, R. Hunstead, A. Harmon, P. Durouchoux, and W. Heindl (1999, July). Quenching of the Radio Jet during the X-Ray High State of GX 339-4. *ApJL 519*, L165–L168.

Fender, R. P. (2001, March). Powerful jets from black hole X-ray binaries in low/hard X-ray states. *MNRAS 322*, 31–42.

Fender, R. P., T. M. Belloni, and E. Gallo (2004, December). Towards a unified model for black hole X-ray binary jets. *MNRAS 355*, 1105–1118.

Fender, R. P., E. Gallo, and P. G. Jonker (2003, August). Jet-dominated states: an alternative to advection across black hole event horizons in 'quiescent' X-ray binaries. *MNRAS 343*, L99–L103.

Fender, R. P., S. T. Garrington, D. J. McKay, T. W. B. Muxlow, G. G. Pooley, R. E. Spencer, A. M. Stirling, and E. B. Waltman (1999, April). MERLIN observations of relativistic ejections from GRS 1915+105. *MNRAS 304*, 865–876.

Fender, R. P., J. Homan, and T. M. Belloni (2009, July). Jets from black hole X-ray binaries: testing, refining and extending empirical models for the coupling to X-rays. *MNRAS 396*, 1370–1382.

Fender, R. P. and G. G. Pooley (2000, October). Giant repeated ejections from GRS 1915+105. *MNRAS 318*, L1–L5.

Fender, R. P., D. M. Russell, C. Knigge, R. Soria, R. I. Hynes, and M. Goad (2009, March). An anticorrelation between X-ray luminosity and Hα equivalent width in X-ray binaries. *MNRAS 393*, 1608–1616.

Ferrigno, C., E. Bozzo, M. Del Santo, and F. Capitanio (2012, January). The first outburst of the black-hole candidate MAXI J1836-194 observed by INTEGRAL, Swift, and RXTE. *A&A 537*, L7.

Fomalont, E. B. and B. J. Geldzahler (1991, December). The radio 'lobes' of Scorpius X-1 are unrelated background sources. *ApJ 383*, 289–294.

Fomalont, E. B. and R. A. Perley (1999). Calibration and Editing. In G. B. Taylor, C. L. Carilli, and R. A. Perley (Eds.), *Synthesis Imaging in Radio Astronomy II*, Volume 180 of *Astronomical Society of the Pacific Conference Series*, pp. 79.

Fomalont, E. B., L. Petrov, D. S. MacMillan, D. Gordon, and C. Ma (2003, November). The Second VLBA Calibrator Survey: VCS2. *AJ 126*, 2562–2566.

Fragos, T., B. Willems, V. Kalogera, N. Ivanova, G. Rockefeller, C. L. Fryer, and P. A. Young (2009, June). Understanding Compact Object Formation and Natal Kicks. II. The Case of XTE J1118 + 480. *ApJ 697*, 1057–1070.

Frank, J., A. King, and D. J. Raine (2002, January). *Accretion Power in Astrophysics: Third Edition*. Cambridge University Press, Cambridge, U.K.

Froning, C. S., A. G. Cantrell, T. J. Maccarone, K. France, J. Khargharia, L. M. Winter, E. L. Robinson, R. I. Hynes, J. W. Broderick, S. Markoff, M. A. P. Torres, M. Garcia, C. D. Bailyn, J. X. Prochaska, J. Werk, C. Thom, S. Béland, C. W. Danforth, B. Keeney, and J. C. Green (2011, December). Multiwavelength Observations of A0620-00 in Quiescence. *ApJ 743*, 26.

Fryer, C. L. and V. Kalogera (2001, June). Theoretical Black Hole Mass Distributions. *ApJ 554*, 548–560.

Galama, T. J., R. A. M. J. Wijers, M. Bremer, P. J. Groot, R. G. Strom, C. Kouveliotou, and J. van Paradijs (1998, June). The Radio-to-X-Ray Spectrum of GRB 970508 on 1997 May 21.0 UT. *ApJL 500*, L97.

Galeev, A. A., R. Rosner, and G. S. Vaiana (1979, April). Structured coronae of accretion disks. *ApJ 229*, 318–326.

Gallo, E., R. Fender, C. Kaiser, D. Russell, R. Morganti, T. Oosterloo, and S. Heinz (2005, August). A dark jet dominates the power output of the stellar black hole Cygnus X-1. *Nature 436*, 819–821.

Gallo, E., R. P. Fender, and G. G. Pooley (2003, September). A universal radio-X-ray correlation in low/hard state black hole binaries. *MNRAS 344*, 60–72.

Gallo, E., S. Migliari, S. Markoff, J. A. Tomsick, C. D. Bailyn, S. Berta, R. Fender, and J. C. A. Miller-Jones (2007, November). The Spectral Energy Distribution of Quiescent Black Hole X-Ray Binaries: New Constraints from Spitzer. *ApJ 670*, 600–609.

Gallo, E., B. P. Miller, and R. Fender (2012, June). Assessing luminosity correlations via cluster analysis: evidence for dual tracks in the radio/X-ray domain of black hole X-ray binaries. *MNRAS 423*, 590–599.

Gallo, E., J. C. A. Miller-Jones, D. M. Russell, P. G. Jonker, J. Homan, R. M. Plotkin, S. Markoff, B. P. Miller, S. Corbel, and R. P. Fender (2014, November). The radio/X-ray domain of black hole X-ray binaries at the lowest radio luminosities. *MNRAS 445*, 290–300.

Gandhi, P., A. W. Blain, D. M. Russell, P. Casella, J. Malzac, S. Corbel, P. D'Avanzo, F. W. Lewis, S. Markoff, M. Cadolle Bel, P. Goldoni, S. Wachter, D. Khangulyan, and A. Mainzer (2011, October). A Variable Mid-infrared Synchrotron Break Associated with the Compact Jet in GX 339-4. *ApJL 740*, L13.

Garcia, M. R., J. E. McClintock, R. Narayan, P. Callanan, D. Barret, and S. S. Murray (2001, May). New Evidence for Black Hole Event Horizons from Chandra. *ApJL 553*, L47–L50.

Gardner, E. and C. Done (2013, October). Jets and the accretion flow in low-luminosity black holes. *MNRAS 434*, 3454–3462.

Giacconi, R., H. Gursky, F. R. Paolini, and B. B. Rossi (1962, December). Evidence for x Rays From Sources Outside the Solar System. *Physical Review Letters 9*, 439–443.

Gierliński, M., C. Done, and K. Page (2008, August). X-ray irradiation in XTE J1817-330 and the inner radius of the truncated disc in the hard state. *Monthly Notices in Radio Astronomy 388*, 753–760.

Gierliński, M., C. Done, and K. Page (2009, January). Reprocessing of X-rays in the outer accretion disc of the black hole binary XTE J1817-330. *MNRAS 392*, 1106–1114.

Gies, D. R. and C. T. Bolton (1986, May). The optical spectrum of HDE 226868 = Cygnus X-1. II Spectrophotometry and mass estimates. *ApJ 304*, 371–393.

Gilfanov, M. (2010, March). X-Ray Emission from Black-Hole Binaries. In T. Belloni (Ed.), *Lecture Notes in Physics, Berlin Springer Verlag*, Volume 794 of *Lecture Notes in Physics, Berlin Springer Verlag*, pp. 17.

Gómez, L., L. F. Rodríguez, L. Loinard, S. Lizano, C. Allen, A. Poveda, and K. M. Menten (2008, September). Monitoring the Large Proper Motions of Radio Sources in the Orion BN/KL Region. *ApJ 685*, 333–343.

Grebenev, S. A., A. V. Prosvetov, and R. A. Sunyaev (2013, June). Second outburst of the black hole candidate MAXI J1836-194 from SWIFT and INTEGRAL observations. *Astronomy Letters 39*, 367–374.

Greisen, E. W. (2003, March). AIPS, the VLA, and the VLBA. *Information Handling in Astronomy - Historical Vistas 285*, 109.

Gualandris, A., M. Colpi, S. Portegies Zwart, and A. Possenti (2005, January). Has the Black Hole in XTE J1118+480 Experienced an Asymmetric Natal Kick? *ApJ 618*, 845–851.

Haardt, F. and L. Maraschi (1991, October). A two-phase model for the X-ray emission from Seyfert galaxies. *ApJL 380*, L51–L54.

Haardt, F. and L. Maraschi (1993, August). X-ray spectra from two-phase accretion disks. *ApJ 413*, 507–517.

Haardt, F., L. Maraschi, and G. Ghisellini (1994, September). A model for the X-ray and ultraviolet emission from Seyfert galaxies and galactic black holes. *ApJL 432*, L95–L99.

Haehnelt, M. G. and M. J. Rees (1993, July). The formation of nuclei in newly formed galaxies and the evolution of the quasar population. *MNRAS 263*, 168–178.

Han, X. and R. M. Hjellming (1992, November). Radio observations of the 1989 transient event in V404 Cygni (=GS 2023+338). *ApJ 400*, 304–314.

Hannikainen, D. C., R. W. Hunstead, D. Campbell-Wilson, and R. K. Sood (1998, September). MOST radio monitoring of GX 339-4. *A&A 337*, 460–464.

Hannikainen, D. C., R. W. Hunstead, D. Campbell-Wilson, K. Wu, D. J. McKay, D. P. Smits, and R. J. Sault (2000, September). Radio Emission from GRO J1655-40 during the 1994 Jet Ejection Episodes. *ApJ 540*, 521–534.

Haslam, C. G. T., U. Klein, C. J. Salter, H. Stoffel, W. E. Wilson, M. N. Cleary, D. J. Cooke, and P. Thomasson (1981, July). A 408 MHz all-sky continuum survey. I - Observations at southern declinations and for the North Polar region. *A&A 100*, 209–219.

Haslam, C. G. T., C. J. Salter, H. Stoffel, and W. E. Wilson (1982, January). A 408 MHz all-sky continuum survey. II - The atlas of contour maps. *A&AS 47*, 1.

Heger, A., C. L. Fryer, S. E. Woosley, N. Langer, and D. H. Hartmann (2003, July). How Massive Single Stars End Their Life. *ApJ 591*, 288–300.

Heindl, W. A., T. A. Prince, and J. M. Grunsfeld (1994, August). Observations of 1E 1740.7-2942 with ROSAT and the VLA. *ApJ 430*, 829–833.

Heinz, S. (2006, January). Composition, Collimation, Contamination: The Jet of Cygnus X-1. *ApJ 636*, 316–322.

Heinz, S., H. J. Grimm, R. A. Sunyaev, and R. P. Fender (2008, October). Blazing Trails: Microquasars as Head-Tail Sources and the Seeding of Magnetized Plasma into the ISM. *ApJ 686*, 1145–1154.

Heinz, S. and A. Merloni (2004, November). Constraints on relativistic beaming from estimators of the unbeamed flux. *MNRAS 355*, L1–L5.

Heinz, S. and R. A. Sunyaev (2003, August). The non-linear dependence of flux on black hole mass and accretion rate in core-dominated jets. *MNRAS 343*, L59–L64.

Henden, A. A., D. L. Welch, D. Terrell, and S. E. Levine (2009, May). The AAVSO Photometric All-Sky Survey (APASS). In *American Astronomical Society Meeting Abstracts 214*, Volume 214 of *American Astronomical Society Meeting Abstracts*, pp. 407.02.

Hewish, A., S. J. Bell, J. D. H. Pilkington, P. F. Scott, and R. A. Collins (1968, February). Observation of a Rapidly Pulsating Radio Source. *Nature 217*, 709–713.

Hjellming, R. M. and K. J. Johnston (1981, March). Structure, strength, and polarization changes in radio source SS433. *Nature 290*, 100–107.

Hjellming, R. M. and K. J. Johnston (1988, May). Radio emission from conical jets associated with X-ray binaries. *ApJ 328*, 600–609.

Hjellming, R. M. and M. P. Rupen (1995, June). Episodic ejection of relativistic jets by the X-ray transient GRO J1655 - 40. *Nature 375*, 464–468.

Ho, L. C. (1999, May). The Spectral Energy Distributions of Low-Luminosity Active Galactic Nuclei. *ApJ 516*, 672–682.

Högbom, J. A. (1974, June). Aperture Synthesis with a Non-Regular Distribution of Interferometer Baselines. *A&AS 15*, 417.

Homan, J. and T. Belloni (2005, November). The Evolution of Black Hole States. *Ap&SS 300*, 107–117.

Hynes, R. I., C. A. Haswell, S. Chaty, C. R. Shrader, and W. Cui (2002, March). The evolving accretion disc in the black hole X-ray transient XTE J1859+226. *MNRAS 331*, 169–179.

Iben, Jr., I., A. V. Tutukov, and L. R. Yungelson (1995a, September). A Model of the Galactic X-Ray Binary Population. I. High-Mass X-Ray Binaries. *ApJS 100*, 217.

Iben, Jr., I., A. V. Tutukov, and L. R. Yungelson (1995b, September). A Model of the Galactic X-Ray Binary Population. II. Low-Mass X-Ray Binaries in the Galactic Disk. *ApJS 100*, 233.

Ichimaru, S. (1977, June). Bimodal behavior of accretion disks - Theory and application to Cygnus X-1 transitions. *ApJ 214*, 840–855.

Illarionov, A. F. and R. A. Sunyaev (1975, February). Why the Number of Galactic X-ray Stars Is so Small? *A&A 39*, 185.

Jahoda, K., C. B. Markwardt, Y. Radeva, A. H. Rots, M. J. Stark, J. H. Swank, T. E. Strohmayer, and W. Zhang (2006, April). Calibration of the Rossi X-Ray Timing Explorer Proportional Counter Array. *ApJS 163*, 401–423.

Jahoda, K., J. H. Swank, A. B. Giles, M. J. Stark, T. Strohmayer, W. Zhang, and E. H. Morgan (1996, October). In-orbit performance and calibration of the Rossi X-ray Timing Explorer (RXTE) Proportional Counter Array (PCA). In O. H. Siegmund and M. A. Gummin (Eds.), *EUV, X-Ray, and Gamma-Ray Instrumentation for Astronomy VII*, Volume 2808 of *Society of Photo-Optical Instrumentation Engineers (SPIE) Conference Series*, pp. 59–70.

Jamil, O., R. P. Fender, and C. R. Kaiser (2010, January). iShocks: X-ray binary jets with an internal shocks model. *MNRAS 401*, 394–404.

Jenniskens, P. and F.-X. Desert (1994, July). A survey of diffuse interstellar bands (3800-8680 A). *A&AS 106*, 39–78.

Johnson, D. R. H. and D. R. Soderblom (1987, April). Calculating galactic space velocities and their uncertainties, with an application to the Ursa Major group. *AJ 93*, 864–867.

Jonker, P. G., J. C. A. Miller-Jones, J. Homan, J. Tomsick, R. P. Fender, P. Kaaret, S. Markoff, and E. Gallo (2012, July). The black hole candidate MAXI J1659-152 in and towards quiescence in X-ray and radio. *MNRAS 423*, 3308–3315.

Jordi, K., E. K. Grebel, and K. Ammon (2006, December). Empirical color transformations between SDSS photometry and other photometric systems. *A&A 460*, 339–347.

Kaiser, C. R. (2006, April). The flat synchrotron spectra of partially self-absorbed jets revisited. *MNRAS 367*, 1083–1094.

Kalemci, E., T. Dinçer, J. A. Tomsick, M. M. Buxton, C. D. Bailyn, and Y. Y. Chun (2013, December). Complete Multiwavelength Evolution of Galactic Black Hole Transients during Outburst Decay. I. Conditions for "Compact" Jet Formation. *ApJ 779*, 95.

Kalemci, E., J. A. Tomsick, M. M. Buxton, R. E. Rothschild, K. Pottschmidt, S. Corbel, C. Brocksopp, and P. Kaaret (2005, March). Multiwavelength Observations of the Galactic Black Hole Transient 4U 1543-47 during Outburst Decay: State Transitions and Jet Contribution. *ApJ 622*, 508–519.

Kanbach, G., C. Straubmeier, H. C. Spruit, and T. Belloni (2001, November). Correlated fast X-ray and optical variability in the black-hole candidate XTE J1118+480. *Nature 414*, 180–182.

King, A. L., J. M. Miller, M. T. Reynolds, K. Gültekin, E. Gallo, and D. Maitra (2013, September). A Distinctive Disk-Jet Coupling in the Lowest-mass Seyfert, NGC 4395. *ApJL 774*, L25.

King, A. R., U. Kolb, and E. Szuszkiewicz (1997, October). Why Low-Mass Black Hole Binaries Are Transient. *ApJ 488*, 89.

Kippenhahn, R. and A. Weigert (1990). *Stellar Structure and Evolution*. Springer-Verlag Berlin Heidelberg New York.

Koide, S., K. Shibata, T. Kudoh, and D. L. Meier (2002, March). Extraction of Black Hole Rotational Energy by a Magnetic Field and the Formation of Relativistic Jets. *Science 295*, 1688–1691.

Komissarov, S. S., M. V. Barkov, N. Vlahakis, and A. Königl (2007, September). Magnetic acceleration of relativistic active galactic nucleus jets. *MNRAS 380*, 51–70.

Kotani, T., N. Kawai, T. Aoki, J. Doty, M. Matsuoka, K. Mitsuda, F. Nagase, G. Ricker, and N. E. White (1994, August). Discovery of the double Doppler-shifted emission-line systems in the X-ray spectrum of SS 433. *PASJ 46*, L147–L150.

Kraft, R. P., D. N. Burrows, and J. A. Nousek (1991, June). Determination of confidence limits for experiments with low numbers of counts. *ApJ 374*, 344–355.

Kreidberg, L., C. D. Bailyn, W. M. Farr, and V. Kalogera (2012, September). Mass Measurements of Black Holes in X-Ray Transients: Is There a Mass Gap? *ApJ 757*, 36.

Krelowski, J., G. A. H. Walker, G. R. Grieve, and G. M. Hill (1987, May). Interdependence of the 4430 A diffuse interstellar band, polarization, and ultraviolet extinction. *ApJ 316*, 449–457.

Krimm, H. A., S. D. Barthelmy, W. Baumgartner, J. Cummings, E. Fenimore, N. Gehrels, C. B. Markwardt, D. Palmer, T. Sakamoto, G. Skinner, M. Stamatikos, J. Tueller, and T. Ukwatta (2012, March). Swift/BAT reports an increase in flux from MAXI J1836-194. *The Astronomer's Telegram 3966*, 1.

Krimm, H. A., S. T. Holland, R. H. D. Corbet, A. B. Pearlman, P. Romano, J. A. Kennea, J. S. Bloom, S. D. Barthelmy, W. H. Baumgartner, J. R. Cummings, N. Gehrels, A. Y. Lien, C. B. Markwardt, D. M. Palmer, T. Sakamoto, M. Stamatikos, and T. N. Ukwatta (2013, November). The Swift/BAT Hard X-Ray Transient Monitor. *ApJS 209*, 14.

Kubota, A., Y. Tanaka, K. Makishima, Y. Ueda, T. Dotani, H. Inoue, and K. Yamaoka (1998, December). Evidence for a Black Hole in the X-Ray Transient GRS 1009-45. *PASJ 50*, 667–673.

Lai, D., D. F. Chernoff, and J. M. Cordes (2001, March). Pulsar Jets: Implications for Neutron Star Kicks and Initial Spins. *ApJ 549*, 1111–1118.

Laing, R. A. (1980, November). A model for the magnetic-field structure in extended radio sources. *MNRAS 193*, 439–449.

Laplace, P. S. (1795). Le Système du Monde, Vol. II, Paris (English edition: The System of the World, W. Flint, London, 1809).

Lee, H. M. (1987, August). Dynamical effects of successive mergers on the evolution of spherical stellar systems. *ApJ 319*, 801–818.

Lee, H. M. (1995, February). Evolution of galactic nuclei with 10-M_ black holes. *MNRAS 272*, 605–617.

Li, Y., L. Hernquist, B. Robertson, T. J. Cox, P. F. Hopkins, V. Springel, L. Gao, T. Di Matteo, A. R. Zentner, A. Jenkins, and N. Yoshida (2007, August). Formation of z˜6 Quasars from Hierarchical Galaxy Mergers. *ApJ 665*, 187–208.

Livio, M., G. I. Ogilvie, and J. E. Pringle (1999, February). Extracting Energy from Black Holes: The Relative Importance of the Blandford-Znajek Mechanism. *ApJ 512*, 100–104.

Longair, M. S. (2011, February). *High Energy Astrophysics*. Cambridge University Press, U.K.

Lynden-Bell, D. and J. E. Pringle (1974, September). The evolution of viscous discs and the origin of the nebular variables. *MNRAS 168*, 603–637.

Maccarone, T. J. (2003, October). Do X-ray binary spectral state transition luminosities vary? *A&A 409*, 697–706.

Maitra, D., S. Markoff, C. Brocksopp, M. Noble, M. Nowak, and J. Wilms (2009, October). Constraining jet/disc geometry and radiative processes in stellar black holes XTE J1118+480 and GX 339-4. *MNRAS 398*, 1638–1650.

Malzac, J. (2007, October). Jet disc coupling in black hole binaries. *Ap&SS 311*, 149–159.

Malzac, J. (2012). On the Nature of the X-Ray Corona of Black Hole Binaries. *International Journal of Modern Physics Conference Series 8*, 73–83.

Malzac, J. (2013, February). Internal shocks at the origin of the flat spectral energy distribution of compact jets. *MNRAS 429*, L20–L24.

Malzac, J. (2014, September). The spectral energy distribution of compact jets powered by internal shocks. *MNRAS 443*, 299–317.

Malzac, J., R. Belmont, and A. C. Fabian (2009, December). Energetics of a black hole: constraints on the jet velocity and the nature of the X-ray emitting region in Cyg X-1. *MNRAS 400*, 1512–1520.

Margon, B., S. A. Grandi, R. P. S. Stone, and H. C. Ford (1979, October). Enormous periodic Doppler shifts in SS 433. *ApJL 233*, L63–L68.

Markoff, S., H. Falcke, and R. Fender (2001, June). A jet model for the broadband spectrum of XTE J1118+480. Synchrotron emission from radio to X-rays in the Low/Hard spectral state. *A&A 372*, L25–L28.

Markoff, S., M. Nowak, S. Corbel, R. Fender, and H. Falcke (2003, January). Exploring the role of jets in the radio/X-ray correlations of GX 339-4. *A&A 397*, 645–658.

Markoff, S., M. Nowak, A. Young, H. L. Marshall, C. R. Canizares, A. Peck, M. Krips, G. Petitpas, R. Schödel, G. C. Bower, P. Chandra, A. Ray, M. Muno, S. Gallagher, S. Hornstein, and C. C. Cheung (2008, July). Results from an Extensive Simultaneous Broadband Campaign on the Underluminous Active Nucleus M81*: Further Evidence for Mass-scaling Accretion in Black Holes. *ApJ 681*, 905–924.

Markoff, S., M. A. Nowak, and J. Wilms (2005, December). Going with the Flow: Can the Base of Jets Subsume the Role of Compact Accretion Disk Coronae? *ApJ 635*, 1203–1216.

Marscher, A. P., S. G. Jorstad, F. D. D'Arcangelo, P. S. Smith, G. G. Williams, V. M. Larionov, H. Oh, A. R. Olmstead, M. F. Aller, H. D. Aller, I. M. McHardy, A. Lähteenmäki, M. Tornikoski, E. Valtaoja, V. A. Hagen-Thorn, E. N. Kopatskaya, W. K. Gear, G. Tosti, O. Kurtanidze, M. Nikolashvili, L. Sigua, H. R. Miller, and W. T. Ryle (2008, April). The inner jet of an active galactic nucleus as revealed by a radio-to-γ-ray outburst. *Nature 452*, 966–969.

Marshall, D. J., A. C. Robin, C. Reylé, M. Schultheis, and S. Picaud (2006, July). Modelling the Galactic interstellar extinction distribution in three dimensions. *A&A 453*, 635–651.

Matsuoka, M., K. Kawasaki, S. Ueno, H. Tomida, M. Kohama, M. Suzuki, Y. Adachi, M. Ishikawa, T. Mihara, M. Sugizaki, N. Isobe, Y. Nakagawa, H. Tsunemi, E. Miyata, N. Kawai, J. Kataoka, M. Morii, A. Yoshida, H. Negoro, M. Nakajima, Y. Ueda, H. Chujo, K. Yamaoka, O. Yamazaki, S. Nakahira, T. You, R. Ishiwata, S. Miyoshi, S. Eguchi, K. Hiroi, H. Katayama, and K. Ebisawa (2009, October). The MAXI Mission on the ISS: Science and Instruments for Monitoring All-Sky X-Ray Images. *PASJ 61*, 999–.

Mayo, S. K., D. T. Wickramasinghe, and J. A. J. Whelan (1980, December). Theory and observations of the optical continuum and line spectra of accretion discs around white dwarfs. *MNRAS 193*, 793–824.

McClintock, J. E., R. Narayan, and J. F. Steiner (2014, September). Black Hole Spin via Continuum Fitting and the Role of Spin in Powering Transient Jets. *SSRv 183*, 295–322.

McClintock, J. E. and R. A. Remillard (2006, April). *Black hole binaries*, pp. 157–213. in Compact stellar X-ray sources, ed. Lewin, W. H. G. and van der Klis, M., Cambridge University Press, Cambridge, UK.

McClintock, J. E., R. A. Remillard, M. P. Rupen, M. A. P. Torres, D. Steeghs, A. M. Levine, and J. A. Orosz (2009, June). The 2003 Outburst of the X-Ray Transient H1743-322: Comparisons with the Black Hole Microquasar XTE J1550-564. *ApJ 698*, 1398–1421.

McMullin, J. P., B. Waters, D. Schiebel, W. Young, and K. Golap (2007, October). CASA Architecture and Applications. In R. A. Shaw, F. Hill, and D. J. Bell (Eds.), *Astronomical Data Analysis Software and Systems XVI*, Volume 376 of *Astronomical Society of the Pacific Conference Series*, pp. 127.

McNamara, B. R. and P. E. J. Nulsen (2007, September). Heating Hot Atmospheres with Active Galactic Nuclei. *ARA&A 45*, 117–175.

Meier, D. L. (2005, November). Magnetically Dominated Accretion Flows (MDAFS) and Jet Production in the Lowhard State. *Ap&SS 300*, 55–65.

Menou, K., A. A. Esin, R. Narayan, M. R. Garcia, J.-P. Lasota, and J. E. McClintock (1999, July). Black Hole and Neutron Star Transients in Quiescence. *ApJ 520*, 276–291.

Merloni, A., S. Heinz, and T. di Matteo (2003, November). A Fundamental Plane of black hole activity. *MNRAS 345*, 1057–1076.

Michell, J. (1784). On the Means of Discovering the Distance, Magnitude, &c. of the Fixed Stars, in Consequence of the Diminution of the Velocity of Their Light, in Case Such a Diminution Should be Found to Take Place in any of Them, and Such Other Data Should be Procured from Observations, as Would be Farther Necessary for That Purpose. By the Rev. John Michell, B. D. F. R. S. In a Letter to Henry Cavendish, Esq. F. R. S. and A. S. *Royal Society of London Philosophical Transactions Series I 74*, 35–57.

Migliari, S. and R. P. Fender (2006, February). Jets in neutron star X-ray binaries: a comparison with black holes. *MNRAS 366*, 79–91.

Migliari, S., J. A. Tomsick, S. Markoff, E. Kalemci, C. D. Bailyn, M. Buxton, S. Corbel, R. P. Fender, and P. Kaaret (2007, November). Tracing the Jet Contribution to the Mid-IR over the 2005 Outburst of GRO J1655-40 via Broadband Spectral Modeling. *ApJ 670*, 610–623.

Migliari, S., J. A. Tomsick, J. C. A. Miller-Jones, S. Heinz, R. I. Hynes, R. P. Fender, E. Gallo, P. G. Jonker, and T. J. Maccarone (2010, February). The Complete Spectrum of the Neutron Star X-ray Binary 4U 0614+091. *ApJ 710*, 117–124.

Mignard, F. (2000, February). Local galactic kinematics from Hipparcos proper motions. *A&A 354*, 522–536.

Milgrom, M. (1979, June). On the interpretation of the large variations in the line positions in SS433. *A&A 76*, L3–L6.

Miller, J. M., J. Homan, D. Steeghs, M. Rupen, R. W. Hunstead, R. Wijnands, P. A. Charles, and A. C. Fabian (2006, December). A Long, Hard Look at the Low/Hard State in Accreting Black Holes. *ApJ 653*, 525–535.

Miller, J. M., G. G. Pooley, A. C. Fabian, M. A. Nowak, R. C. Reis, E. M. Cackett, K. Pottschmidt, and J. Wilms (2012, September). On the Role of the Accretion Disk in Black Hole Disk-Jet Connections. *ApJ 757*, 11.

Miller-Jones, J. C. A. (2014, March). Astrometric Observations of X-ray Binaries Using Very Long Baseline Interferometry. *PASA 31*, 16.

Miller-Jones, J. C. A., K. M. Blundell, M. P. Rupen, A. J. Mioduszewski, P. Duffy, and A. J. Beasley (2004, January). Time-sequenced Multi-Radio Frequency Observations of Cygnus X-3 in Flare. *ApJ 600*, 368–389.

Miller-Jones, J. C. A., G. R. Sivakoff, D. Altamirano, M. Coriat, S. Corbel, V. Dhawan, H. A. Krimm, R. A. Remillard, M. P. Rupen, D. M. Russell, R. P. Fender, S. Heinz, E. G. Körding, D. Maitra, S. Markoff, S. Migliari, C. L. Sarazin, and V. Tudose (2012, March). Disc-jet coupling in the 2009 outburst of the black hole candidate H1743-322. *MNRAS 421*, 468–485.

Miller-Jones, J. C. A., G. R. Sivakoff, M. Rupen, and D. Altamirano (2011, September). EVLA radio detections of MAXI J1836-194 suggest it is a black hole X-ray binary. *The Astronomer's Telegram 3628*, 1.

Mirabel, I. F., V. Dhawan, R. P. Mignani, I. Rodrigues, and F. Guglielmetti (2001, September). A high-velocity black hole on a Galactic-halo orbit in the solar neighbourhood. *Nature 413*, 139–141.

Mirabel, I. F. and I. Rodrigues (2003, May). Formation of a Black Hole in the Dark. *Science 300*, 1119–1121.

Mirabel, I. F. and L. F. Rodríguez (1994, September). A superluminal source in the Galaxy. *Nature 371*, 46–48.

Mirabel, I. F. and L. F. Rodríguez (1998, April). Microquasars in our Galaxy. *Nature 392*, 673–676.

Mirabel, I. F. and L. F. Rodríguez (1999). Sources of Relativistic Jets in the Galaxy. *ARA&A 37*, 409–443.

Mirabel, I. F., L. F. Rodriguez, B. Cordier, J. Paul, and F. Lebrun (1992, July). A double-sided radio jet from the compact Galactic Centre annihilator 1E1740.7-2942. *Nature 358*, 215–217.

Mouri, H. and Y. Taniguchi (2002, February). Runaway Merging of Black Holes: Analytical Constraint on the Timescale. *ApJL 566*, L17–L20.

Muñoz-Darias, T., M. Coriat, D. S. Plant, G. Ponti, R. P. Fender, and R. J. H. Dunn (2013, June). Inclination and relativistic effects in the outburst evolution of black hole transients. *MNRAS 432*, 1330–1337.

Nakahira, S., H. Negoro, R. Usui, T. Mihara, M. Sugizaki, M. Serino, T. Yamamoto, T. Sootome, M. Matsuoka, S. Ueno, H. Tomida, M. Kohama, M. Ishikawa, N. Kawai, M. Morii, K. Sugimori, T. Toizumi, A. Yoshida, K. Yamaoka, H. Tsunemi, M. Kimura, H. Kitayama, M. Nakajima, F. Suwa, M. Asada, H. Sakakibara, Y. Ueda, K. Hiroi, M. Shidatsu, Y. Tsuboi, T. Matsumura, and K. Yamazaki (2011, September). MAXI/GSC detects a spectral softening of MAXI J1836-194. *The Astronomer's Telegram 3626*, 1.

Narayan, R., D. Barret, and J. E. McClintock (1997, June). Advection-dominated Accretion Model of the Black Hole V404 Cygni in Quiescence. *ApJ 482*, 448–464.

Narayan, R., M. R. Garcia, and J. E. McClintock (1997, April). Advection-dominated Accretion and Black Hole Event Horizons. *ApJL 478*, L79–L82.

Narayan, R. and J. E. McClintock (2005, April). Inclination Effects and Beaming in Black Hole X-Ray Binaries. *ApJ 623*, 1017–1025.

Narayan, R., J. E. McClintock, and I. Yi (1996, February). A New Model for Black Hole Soft X-Ray Transients in Quiescence. *ApJ 457*, 821.

Narayan, R. and I. Yi (1994, June). Advection-dominated accretion: A self-similar solution. *ApJL 428*, L13–L16.

Narayan, R. and I. Yi (1995, October). Advection-dominated Accretion: Underfed Black Holes and Neutron Stars. *ApJ 452*, 710.

Negoro, H., M. Nakajima, S. Nakahira, M. Morii, H. A. Krimm, D. M. Palmer, J. A. Kennea, T. Mihara, M. Sugizaki, M. Serino, T. Yamamoto, T. Sootome, M. Matsuoka, S. Ueno, H. Tomida, M. Kohama, M. Ishikawa, N. Kawai, K. Sugimori, R. Usui, T. Toizumi, A. Yoshida, K. Yamaoka, H. Tsunemi, M. Kimura, H. Kitayama, F. Suwa, M. Asada, H. Sakakibara, Y. Ueda, K. Hiroi, M. Shidatsu, Y. Tsuboi, T. Matsumura, and K. Yamazaki (2011, August). MAXI/GSC and Swift/BAT detect a new hard X-ray transient MAXI J1836-194. *The Astronomer's Telegram 3611*, 1.

Neilsen, J. and J. C. Lee (2009, March). Accretion disk winds as the jet suppression mechanism in the microquasar GRS 1915+105. *Nature 458*, 481–484.

Nelemans, G., T. M. Tauris, and E. P. J. van den Heuvel (1999, December). Constraints on mass ejection in black hole formation derived from black hole X-ray binaries. *A&A 352*, L87–L90.

Newton, I. (1704). Opticks, or, a Treatise of the Reflections, Refractions, Inflections, and Colours of Light, London.

Novikov, I. D. and K. S. Thorne (1973). Astrophysics of black holes. In C. Dewitt and B. S. Dewitt (Eds.), *Black Holes (Les Astres Occlus)*, pp. 343–450.

Oppenheimer, J. R. and H. Snyder (1939, September). On Continued Gravitational Contraction. *Physical Review 56*, 455–459.

Orosz, J. A., J. E. McClintock, J. P. Aufdenberg, R. A. Remillard, M. J. Reid, R. Narayan, and L. Gou (2011, December). The Mass of the Black Hole in Cygnus X-1. *ApJ 742*, 84.

Osterbrock, D. E. and G. J. Ferland (2006). *Astrophysics of gaseous nebulae and active galactic nuclei*. University Science Books, 2006.

Owen, F. N., T. J. Balonek, J. Dickey, Y. Terzian, and S. T. Gottesman (1976, January). Radio emission from the X-ray source A0620-00. *ApJL 203*, L15–L16.

Pacholczyk, A. G. and T. L. Swihart (1967, November). Polarization of Radio Sources. I. Homogeneous Source of Arbitrary Optical Thickness. *ApJ 150*, 647.

Paczyński, B. (1977, September). A model of accretion disks in close binaries. *ApJ 216*, 822–826.

Page, D. N. and K. S. Thorne (1974, July). Disk-Accretion onto a Black Hole. Time-Averaged Structure of Accretion Disk. *ApJ 191*, 499–506.

Pakull, M. W. and L. P. Angebault (1986, August). Detection of an X-ray-ionized nebula around the black hole candidate binary LMC X-1. *Nature 322*, 511–517.

Pakull, M. W. and C. Motch (2011, September). ESO VLT observations of MAXI J1836-194. *The Astronomer's Telegram 3640*, 1.

Paragi, Z., A. J. van der Horst, T. Belloni, J. C. A. Miller-Jones, J. Linford, G. Taylor, J. Yang, M. A. Garrett, J. Granot, C. Kouveliotou, E. Kuulkers, and R. A. M. J. Wijers (2013, June). VLBI observations of the shortest orbital period black hole binary, MAXI J1659-152. *MNRAS 432*, 1319–1329.

Pe'er, A. and P. Casella (2009, July). A Model for Emission from Jets in X-Ray Binaries: Consequences of a Single Acceleration Episode. *ApJ 699*, 1919–1937.

Pe'er, A. and S. Markoff (2012, July). X-Ray Emission from Transient Jet Model in Black Hole Binaries. *ApJ 753*, 177.

Petrov, L., Y. Y. Kovalev, E. B. Fomalont, and D. Gordon (2006, March). The Fourth VLBA Calibrator Survey: VCS4. *AJ 131*, 1872–1879.

Plotkin, R. M., E. Gallo, and P. G. Jonker (2013, August). The X-Ray Spectral Evolution of Galactic Black Hole X-Ray Binaries toward Quiescence. *ApJ 773*, 59.

Plotkin, R. M., S. Markoff, B. C. Kelly, E. Körding, and S. F. Anderson (2012, January). Using the Fundamental Plane of black hole activity to distinguish X-ray processes from weakly accreting black holes. *MNRAS 419*, 267–286.

Podsiadlowski, P. and S. Rappaport (2000, February). Cygnus X-2: The Descendant of an Intermediate-Mass X-Ray Binary. *ApJ 529*, 946–951.

Podsiadlowski, P., S. Rappaport, and E. D. Pfahl (2002, February). Evolutionary Sequences for Low- and Intermediate-Mass X-Ray Binaries. *ApJ 565*, 1107–1133.

Polko, P., D. L. Meier, and S. Markoff (2010, November). Determining the Optimal Locations for Shock Acceleration in Magnetohydrodynamical Jets. *ApJ 723*, 1343–1350.

Polko, P., D. L. Meier, and S. Markoff (2013, January). Linking accretion flow and particle acceleration in jets - I. New relativistic magnetohydrodynamical jet solutions including gravity. *MNRAS 428*, 587–598.

Polko, P., D. L. Meier, and S. Markoff (2014, February). Linking accretion flow and particle acceleration in jets - II. Self-similar jet models with full relativistic MHD gravitational mass. *MNRAS 438*, 959–970.

Ponti, G., R. P. Fender, M. C. Begelman, R. J. H. Dunn, J. Neilsen, and M. Coriat (2012, May). Ubiquitous equatorial accretion disc winds in black hole soft states. *MNRAS 422*, L11.

Poole, T. S., A. A. Breeveld, M. J. Page, W. Landsman, S. T. Holland, P. Roming, N. P. M. Kuin, P. J. Brown, C. Gronwall, S. Hunsberger, S. Koch, K. O. Mason, P. Schady, D. vanden Berk, A. J. Blustin, P. Boyd, P. Broos, M. Carter, M. M. Chester, A. Cucchiara, B. Hancock, H. Huckle, S. Immler, M. Ivanushkina, T. Kennedy, F. Marshall, A. Morgan, S. B. Pandey, M. de Pasquale, P. J. Smith, and M. Still (2008, January). Photometric calibration of the Swift ultraviolet/optical telescope. *MNRAS 383*, 627–645.

Portegies Zwart, S. F., H. Baumgardt, P. Hut, J. Makino, and S. L. W. McMillan (2004, April). Formation of massive black holes through runaway collisions in dense young star clusters. *Nature 428*, 724–726.

Portegies Zwart, S. F. and L. R. Yungelson (1998, April). Formation and evolution of binary neutron stars. *A&A 332*, 173–188.

Poutanen, J. (1998). Accretion disc-corona models and X/γ-ray spectra of accreting black holes. In M. A. Abramowicz, G. Björnsson, and J. E. Pringle (Eds.), *Theory of Black Hole Accretion Disks*, pp. 100–122.

Poutanen, J., J. H. Krolik, and F. Ryde (1997, November). The nature of spectral transitions in accreting black holes - The case of CYG X-1. *MNRAS 292*, L21–L25.

Poutanen, J., A. Veledina, and M. G. Revnivtsev (2014, December). Colours of black holes: infrared flares from the hot accretion disc in XTE J1550-564. *MNRAS 445*, 3987–3998.

Pringle, J. E. (1981). Accretion discs in astrophysics. *ARA&A 19*, 137–162.

Pringle, J. E. and M. J. Rees (1972, October). Accretion Disc Models for Compact X-Ray Sources. *A&A 21*, 1.

Quataert, E. and A. Gruzinov (2000, August). Convection-dominated Accretion Flows. *ApJ 539*, 809–814.

Quinlan, G. D. and S. L. Shapiro (1990, June). The dynamical evolution of dense star clusters in galactic nuclei. *ApJ 356*, 483–500.

Rahoui, F., J. C. Lee, S. Heinz, D. C. Hines, K. Pottschmidt, J. Wilms, and V. Grinberg (2011, July). A Multiwavelength Study of Cygnus X-1: The First Mid-infrared Spectroscopic Detection of Compact Jets. *ApJ 736*, 63.

Ratti, E. M., P. G. Jonker, J. C. A. Miller-Jones, M. A. P. Torres, J. Homan, S. Markoff, J. A. Tomsick, P. Kaaret, R. Wijnands, E. Gallo, F. Özel, D. T. H. Steeghs, and R. P. Fender (2012, July). The black hole candidate XTE J1752-223 towards and in quiescence: optical and simultaneous X-ray-radio observations. *MNRAS 423*, 2656–2667.

Reid, M. J., J. E. McClintock, R. Narayan, L. Gou, R. A. Remillard, and J. A. Orosz (2011, December). The Trigonometric Parallax of Cygnus X-1. *ApJ 742*, 83.

Reid, M. J., J. E. McClintock, J. F. Steiner, D. Steeghs, R. A. Remillard, V. Dhawan, and R. Narayan (2014, November). A Parallax Distance to the Microquasar GRS 1915+105 and a Revised Estimate of its Black Hole Mass. *ApJ 796*, 2.

Reid, M. J., K. M. Menten, A. Brunthaler, X. W. Zheng, T. M. Dame, Y. Xu, Y. Wu, B. Zhang, A. Sanna, M. Sato, K. Hachisuka, Y. K. Choi, K. Immer, L. Moscadelli, K. L. J. Rygl, and A. Bartkiewicz (2014, March). Trigonometric Parallaxes of High Mass Star Forming Regions: The Structure and Kinematics of the Milky Way. *ApJ 783*, 130.

Reis, R. C., A. C. Fabian, and J. M. Miller (2010, February). Black hole accretion discs in the canonical low-hard state. *MNRAS 402*, 836–854.

Reis, R. C., J. M. Miller, M. T. Reynolds, A. C. Fabian, and D. J. Walton (2012, May). Suzaku Observation of the Black Hole Candidate Maxi J1836-194 in a Hard/Intermediate Spectral State. *ApJ 751*, 34.

Remillard, R. A. and J. E. McClintock (2006, September). X-Ray Properties of Black-Hole Binaries. *ARA&A 44*, 49–92.

Reynolds, M. T. and J. M. Miller (2010, June). Suzaku Observations of the Galactic Center Microquasar 1E 1740.7-2942. *ApJ 716*, 1431–1437.

Reynolds, M. T. and J. M. Miller (2013, May). A Swift Survey of Accretion onto Stellar-mass Black Holes. *ApJ 769*, 16.

Rodriguez, L. F., I. F. Mirabel, and J. Marti (1992, December). The radio counterpart of the hard X-ray source GRS 1758-258. *ApJL 401*, L15–L18.

Roming, P. W. A., T. E. Kennedy, K. O. Mason, J. A. Nousek, L. Ahr, R. E. Bingham, P. S. Broos, M. J. Carter, B. K. Hancock, H. E. Huckle, S. D. Hunsberger, H. Kawakami, R. Killough, T. S. Koch, M. K. McLelland, K. Smith, P. J. Smith, J. C. Soto, P. T. Boyd, A. A. Breeveld, S. T. Holland, M. Ivanushkina, M. S. Pryzby, M. D. Still, and J. Stock (2005, October). The Swift Ultra-Violet/Optical Telescope. *SSRv 120*, 95–142.

Rushton, A., J. C. A. Miller-Jones, R. Campana, Y. Evangelista, Z. Paragi, T. J. Maccarone, G. G. Pooley, V. Tudose, R. P. Fender, R. E. Spencer, and V. Dhawan (2012, February). A weak compact jet in a soft state of Cygnus X-1. *MNRAS 419*, 3194–3199.

Russell, D. M. and R. P. Fender (2010, January). Powerful jets from accreting black holes: evidence from the optical and infrared. *ArXiv e-prints: 1001.1244*.

Russell, D. M., R. P. Fender, E. Gallo, and C. R. Kaiser (2007, April). The jet-powered optical nebula of Cygnus X-1. *MNRAS 376*, 1341–1349.

Russell, D. M., T. J. Maccarone, E. G. Körding, and J. Homan (2007, August). Parallel tracks in infrared versus X-ray emission in black hole X-ray transient outbursts: a hysteresis effect? *MNRAS 379*, 1401–1408.

Russell, D. M., D. Maitra, R. J. H. Dunn, and S. Markoff (2010, July). Evidence for a compact jet dominating the broad-band spectrum of the black hole accretor XTE J1550-564. *MNRAS 405*, 1759–1769.

Russell, D. M., S. Markoff, P. Casella, A. G. Cantrell, R. Chatterjee, R. P. Fender, E. Gallo, P. Gandhi, J. Homan, D. Maitra, J. C. A. Miller-Jones, K. O'Brien, and T. Shahbaz (2013, February). Jet spectral breaks in black hole X-ray binaries. *MNRAS 429*, 815–832.

Russell, D. M., J. C. A. Miller-Jones, T. J. Maccarone, Y. J. Yang, R. P. Fender, and F. Lewis (2011, September). Testing the Jet Quenching Paradigm with an Ultradeep Observation of a Steadily Soft State Black Hole. *ApJL 739*, L19.

Russell, D. M. and T. Shahbaz (2014, March). The multiwavelength polarization of Cygnus X-1. *MNRAS 438*, 2083–2096.

Rybicki, G. B. and A. P. Lightman (1979). *Radiative processes in astrophysics*. WILEY-VCH Verlag GmbH & Co. KGaA, Weinheim.

Salpeter, E. E. (1964, August). Accretion of Interstellar Matter by Massive Objects. *ApJ 140*, 796–800.

Sari, R., T. Piran, and R. Narayan (1998, April). Spectra and Light Curves of Gamma-Ray Burst Afterglows. *ApJL 497*, L17.

Sault, R. J., P. J. Teuben, and M. C. H. Wright (1995). A Retrospective View of MIRIAD. In R. A. Shaw, H. E. Payne, and J. J. E. Hayes (Eds.), *Astronomical Data Analysis Software and Systems IV*, Volume 77 of *Astronomical Society of the Pacific Conference Series*, pp. 433.

Scheuer, P. A. G. and P. J. S. Williams (1968). Radio Spectra. *ARA&A 6*, 321.

Schmidt, M. (1963, March). 3C 273 : A Star-Like Object with Large Red-Shift. *Nature 197*, 1040.

Schönrich, R., J. Binney, and W. Dehnen (2010, April). Local kinematics and the local standard of rest. *MNRAS 403*, 1829–1833.

Schwab, F. R. (1984, July). Relaxing the isoplanatism assumption in self-calibration; applications to low-frequency radio interferometry. *AJ 89*, 1076–1081.

Schwab, F. R. and W. D. Cotton (1983, May). Global fringe search techniques for VLBI. *AJ 88*, 688–694.

Schwarzschild, K. (1916). On the Gravitational Field of a Mass Point According to Einstein's Theory. *Abh. Konigl. Preuss. Akad. Wissenschaften Jahre 1906,92, Berlin,1907 1916*, 189–196.

Shahbaz, T., D. M. Russell, C. Zurita, J. Casares, J. M. Corral-Santana, V. S. Dhillon, and T. R. Marsh (2013, September). Evidence for quiescent synchrotron emission in the black hole X-ray transient Swift J1357.2-0933. *MNRAS 434*, 2696–2706.

Shakura, N. I. and R. A. Sunyaev (1973). Black holes in binary systems. Observational appearance. *A&A 24*, 337–355.

Shapiro, S. L. and A. P. Lightman (1976, March). Black holes in X-ray binaries - Marginal existence and rotation reversals of accretion disks. *ApJ 204*, 555–560.

Shapiro, S. L. and S. A. Teukolsky (1983). *Black holes, white dwarfs, and neutron stars: The physics of compact objects*. WILEY-VCH Verlag GmbH & Co. KGaA, Weinheim.

Shapiro, S. L. and S. A. Teukolsky (1985, May). The collapse of dense star clusters to supermassive black holes - The origin of quasars and AGNs. *ApJL 292*, L41–L44.

Shepherd, M. C. (1997). Difmap: an Interactive Program for Synthesis Imaging. In G. Hunt and H. Payne (Eds.), *Astronomical Data Analysis Software and Systems VI*, Volume 125 of *Astronomical Society of the Pacific Conference Series*, pp. 77.

Shibata, M. and S. L. Shapiro (2002, June). Collapse of a Rotating Supermassive Star to a Supermassive Black Hole: Fully Relativistic Simulations. *ApJL 572*, L39–L43.

Shimura, T. and F. Takahara (1995, June). On the spectral hardening factor of the X-ray emission from accretion disks in black hole candidates. *ApJ 445*, 780–788.

Shklovsky, I. S. (1967, April). On the Nature of the Source of X-Ray Emission of SCO XR-1. *ApJL 148*, L1.

Skrutskie, M. F., R. M. Cutri, R. Stiening, M. D. Weinberg, S. Schneider, J. M. Carpenter, C. Beichman, R. Capps, T. Chester, J. Elias, J. Huchra, J. Liebert, C. Lonsdale, D. G. Monet, S. Price, P. Seitzer, T. Jarrett, J. D. Kirkpatrick, J. E. Gizis, E. Howard, T. Evans, J. Fowler, L. Fullmer, R. Hurt, R. Light, E. L. Kopan, K. A. Marsh, H. L. McCallon, R. Tam, S. Van Dyk, and S. Wheelock (2006, February). The Two Micron All Sky Survey (2MASS). *AJ 131*, 1163–1183.

Smak, J. (1981). On the Emission Lines from Rotating Gaseous Disks. *AcA 31*, 395.

Soleri, P. and R. Fender (2011, May). On the nature of the 'radio-quiet' black hole binaries. *MNRAS 413*, 2269–2280.

Soria, R. (2007, October). Bridging the gap between stellar-mass black holes and ultraluminous X-ray sources. *Ap&SS 311*, 213–222.

Soria, R., J. W. Broderick, J. Hao, D. C. Hannikainen, M. Mehdipour, K. Pottschmidt, and S.-N. Zhang (2011, July). Accretion states of the Galactic microquasar GRS 1758-258. *MNRAS 415*, 410–424.

Soria, R., K. Wu, and R. W. Hunstead (2000, August). Optical Spectroscopy of GRO J1655-40. *ApJ 539*, 445–462.

Spencer, R. E. (1979, November). A radio jet in SS433. *Nature 282*, 483.

Stirling, A. M., R. E. Spencer, T. V. Cawthorne, and Z. Paragi (2004, November). Polarization and kinematic studies of SS 433 indicate a continuous and decelerating jet. *MNRAS 354*, 1239–1254.

Stirling, A. M., R. E. Spencer, C. J. de la Force, M. A. Garrett, R. P. Fender, and R. N. Ogley (2001, November). A relativistic jet from Cygnus X-1 in the low/hard X-ray state. *MNRAS 327*, 1273–1278.

Strohmayer, T. E. and E. A. Smith (2011, August). RXTE Observations of MAXI J1836-194. *The Astronomer's Telegram 3618*, 1.

Sunyaev, R. A. and L. G. Titarchuk (1980, June). Comptonization of X-rays in plasma clouds - Typical radiation spectra. *A&A 86*, 121–138.

Taniguchi, Y., Y. Shioya, T. G. Tsuru, and S. Ikeuchi (2000, June). Formation of Intermediate-Mass Black Holes in Circumnuclear Regions of Galaxies. *PASJ 52*, 533–537.

Taylor, A. R., J. M. Stil, and C. Sunstrum (2009, September). A Rotation Measure Image of the Sky. *ApJ 702*, 1230–1236.

Taylor, G. B., C. L. Carilli, and R. A. Perley (Eds.) (1999). *Synthesis Imaging in Radio Astronomy II*, Volume 180 of *Astronomical Society of the Pacific Conference Series*.

Tennant, A. F. (1991). The QDP/PLT User's Guide. *NASA Technical Memorandum 4301*.

Thompson, A. R., J. M. Moran, and G. W. Swenson, Jr. (2001). *Interferometry and Synthesis in Radio Astronomy, 2nd Edition*. Wiley, New York, U.S.

Tielens, A. G. G. M. (2005, August). *The Physics and Chemistry of the Interstellar Medium*. Cambridge University Press, Cambridge, UK.

Tingay, S. J., D. L. Jauncey, R. A. Preston, J. E. Reynolds, D. L. Meier, D. W. Murphy, A. K. Tzioumis, D. J. McKay, M. J. Kesteven, J. E. J. Lovell, D. Campbell-Wilson, S. P. Ellingsen, R. Gough, R. W. Hunstead, D. L. Jonos, P. M. McCulloch, V. Migenes, J. Quick, M. W. Sinclair, and D. Smits (1995, March). Relativistic motion in a nearby bright X-ray source. *Nature 374*, 141–143.

Tody, D. (1986, January). The IRAF Data Reduction and Analysis System. In D. L. Crawford (Ed.), *Society of Photo-Optical Instrumentation Engineers (SPIE) Conference Series*, Volume 627 of *Society of Photo-Optical Instrumentation Engineers (SPIE) Conference Series*, pp. 733.

Torres, M. A. P., P. J. Callanan, M. R. Garcia, J. E. McClintock, P. Garnavich, Z. Balog, P. Berlind, W. R. Brown, M. Calkins, and A. Mahdavi (2002, April). Optical Spectral Monitoring of XTE J1118+480 in Outburst: Evidence for a Precessing Accretion Disk? *ApJ 569*, 423–431.

Uemura, M., T. Kato, R. Ishioka, A. Imada, D. Nogami, B. Monard, L. M. Cook, R. Stubbings, S. Kiyota, P. Nelson, J.-Y. Beninger, G. Bolt, and B. Heathcote (2004, October). Optical Observation of the 2003 Outburst of a Black Hole X-Ray Binary, V4641 Sagittarii. *PASJ 56*, 823–829.

Uttley, P., T. Wilkinson, P. Cassatella, J. Wilms, K. Pottschmidt, M. Hanke, and M. Böck (2011, June). The causal connection between disc and power-law variability in hard state black hole X-ray binaries. *MNRAS 414*, L60–L64.

van der Horst, A. J., P. A. Curran, J. C. A. Miller-Jones, J. D. Linford, J. Gorosabel, D. M. Russell, A. de Ugarte Postigo, A. A. Lundgren, G. B. Taylor, D. Maitra, S. Guziy, T. M. Belloni, C. Kouveliotou, P. G. Jonker, A. Kamble, Z. Paragi, J. Homan, E. Kuulkers, J. Granot, D. Altamirano, M. M. Buxton, A. Castro-Tirado, R. P. Fender, M. A. Garrett, N. Gehrels, D. H. Hartmann, J. A. Kennea, H. A. Krimm, V. Mangano, E. Ramirez-Ruiz, P. Romano, R. A. M. J. Wijers, R. Wijnands, and Y. J. Yang (2013, December). Broadband monitoring tracing the evolution of the jet and disc in the black hole candidate X-ray binary MAXI J1659-152. *MNRAS 436*, 2625–2638.

van Paradijs, J. and J. E. McClintock (1995). Optical and ultraviolet observations of X-ray binaries. *X-ray Binaries*, 58–125.

Volonteri, M., F. Haardt, and P. Madau (2003, January). The Assembly and Merging History of Supermassive Black Holes in Hierarchical Models of Galaxy Formation. *ApJ 582*, 559–573.

Vrtilek, S. D., J. C. Raymond, M. R. Garcia, F. Verbunt, G. Hasinger, and M. Kurster (1990, August). Observations of Cygnus X-2 with IUE - Ultraviolet results from a multiwavelength campaign. *A&A 235*, 162–173.

Walker, R. C. (1999). Very Long Baseline Interferometry. In G. B. Taylor, C. L. Carilli, and R. A. Perley (Eds.), *Synthesis Imaging in Radio Astronomy II*, Volume 180 of *Astronomical Society of the Pacific Conference Series*, pp. 433.

Walter, R. and T. J.-L. Courvoisier (1992, May). The origin of the X-ray emission in 3C 273 and 3C 120. *A&A 258*, 255–264.

Warner, B. (2003, September). *Cataclysmic Variable Stars*. Cambridge University Press, Cambridge, UK.

Wesemael, F., J. L. Greenstein, J. Liebert, R. Lamontagne, G. Fontaine, P. Bergeron, and J. W. Glaspey (1993, July). An atlas of optical spectra of white-dwarf stars. *PASP 105*, 761–778.

Wheeler, J. A. (1968). Our universe: the known and the unknown. *American Scientist 56*, 1–20.

White, N. E. and S. S. Holt (1982, June). Accretion disk coronae. *ApJ 257*, 318–337.

White, N. E., F. Nagase, and A. N. Parmar (1995). The properties of X-ray binaries. *X-ray Binaries*, 1–57.

Whitehurst, R. (1988, May). Numerical simulations of accretion disks. I - Superhumps - A tidal phenomenon of accretion disks. *MNRAS 232*, 35–51.

Wilkinson, T. and P. Uttley (2009, August). Accretion disc variability in the hard state of black hole X-ray binaries. *MNRAS 397*, 666–676.

Willems, B., M. Henninger, T. Levin, N. Ivanova, V. Kalogera, K. McGhee, F. X. Timmes, and C. L. Fryer (2005, May). Understanding Compact Object

Formation and Natal Kicks. I. Calculation Methods and the Case of GRO J1655-40. *ApJ 625*, 324–346.

Wilms, J., A. Allen, and R. McCray (2000, October). On the Absorption of X-Rays in the Interstellar Medium. *ApJ 542*, 914–924.

Yang, J., C. Brocksopp, S. Corbel, Z. Paragi, T. Tzioumis, and R. P. Fender (2010, November). A decelerating jet observed by the EVN and VLBA in the X-ray transient XTE J1752-223. *MNRAS 409*, L64–L68.

Yang, J., Y. Xu, Z. Li, Z. Paragi, R. M. Campbell, L. I. Gurvits, Z. Shen, X. Hong, B. Xia, and F. Shu (2012, October). Very long baseline interferometry detection of the Galactic black hole binary candidate MAXI J1836-194. *MNRAS 426*, L66–L70.

Yang, Y. J., P. Curran, J. A. Kennea, and A. K. H. Kong (2012, July). MAXI J1836-194 has returned to quiescence. *The Astronomer's Telegram 4255*, 1.

Yang, Y. J., R. Wijnands, and J. A. Kennea (2012, March). Swift XRT and UVOT observations of renewed activity from MAXI J1836-194. *The Astronomer's Telegram 3975*, 1.

Zacharias, N., C. T. Finch, T. M. Girard, A. Henden, J. L. Bartlett, D. G. Monet, and M. I. Zacharias (2013, February). The Fourth US Naval Observatory CCD Astrograph Catalog (UCAC4). *AJ 145*, 44.

Zdziarski, A. A., P. Pjanka, M. Sikora, and Ł. Stawarz (2014, August). Jet contributions to the broad-band spectrum of Cyg X-1 in the hard state. *MNRAS 442*, 3243–3255.

Zhang, Z., M. Gilfanov, and Á. Bogdán (2012, October). Dependence of the low-mass X-ray binary population on stellar age. *A&A 546*, A36.

Appendix A

Interstellar extinction and reddening

The observed emission from astronomical objects will also be affected by turbulent gas, shocks, and magnetic fields that permeate the interstellar medium (ISM). Therefore, the effects of the ISM must be accounted for if the intrinsic source properties are to be correctly determined.

The ISM is mainly composed of gas and dust, where the gas tends to absorb the emission (where often the emission is re-radiated in a different waveband) and the dust will scatter the emission. Collectively, the absorption and scattering processes are generally referred to as extinction. Extinction is not uniform across the spectrum and will have an effect on the apparent magnitude of an object, which is a function of wavelength, line of sight direction and distance to the object. The extinction along the line of sight $A(\lambda)$ is related to the optical depth τ of the material that the radiation must travel through. The fractional change in the intensity of the emission is $I_{\rm obs}(\lambda)/I_{\rm int}(\lambda) = e^{-\tau(\lambda)}$, where $I_{\rm obs}(\lambda)$ is the observed intensity and $I_{\rm int}(\lambda)$ is the intensity without interstellar extinction. Relating the optical depth to the change in observed magnitude (Equation 4.20) gives

$$m_{\rm obs}(\lambda) - m_{\rm int}(\lambda) = -2.5 \log \left(e^{-\tau(\lambda)}\right) \tag{A.1}$$

$$= 1.086\ \tau(\lambda). \tag{A.2}$$

Because the change in the apparent magnitude is just the extinction along the line of sight, $A(\lambda) = 1.086\ \tau(\lambda)$. The optical depth through a cloud is given by

$$\tau(\lambda) = \int_0^s n_d(s')\ \sigma(\lambda)\ {\rm d}s', \tag{A.3}$$

where s is the path distance of the photon, $n_d(s')$ is the number density of the scattering grains, and $\sigma(\lambda)$ is the scattering cross-section. If $\sigma(\lambda)$ is constant along the line of sight

$$\tau(\lambda) = \sigma(\lambda) \int_0^s n_d(s')\ \mathrm{d}s' \tag{A.4}$$

$$= \sigma(\lambda)\ N_d, \tag{A.5}$$

where N_d is the scattering particle column density from the observer to the stellar object. Therefore, the extinction depends on the distance to the source. $A(\lambda)$ is wavelength dependent as red light does not scatter as strongly as blue light. Therefore, emission travelling through the ISM is reddened as the bluer wavelengths are removed. Called interstellar reddening, this process causes objects to appear redder than their effective temperatures imply. The level of reddening can be determined by analysing the observed spectrum of the source.

Interstellar extinction and reddening is typically described as a colour excess which is the difference in extinction between two different photometric bands, such that colour excess is written (Tielens, 2005)

$$E(\lambda_1 - \lambda_2) = A_{\lambda_1} - A_{\lambda_2}. \tag{A.6}$$

This is often represented as the difference between the B and V photometric bands:

$$E(B - V) = A_B - A_V. \tag{A.7}$$

Alternatively, it can be presented as $A(\lambda)/A_{\mathrm{ref}}$, which is the ratio of extinction in a wavelength band centred at wavelength λ to the extinction in some reference waveband such as A_V (see e.g. Cardelli et al., 1989, for further discussion).

Appendix B

Parameters of the first acceleration zone

This section shows the full derivation of the radius $R_{\rm F}$ and magnetic field $B_{\rm F}$ of the region where electrons are first accelerated into a power law distribution described in Section 7.4.2. Here, $R_{\rm F}$ is defined by the cross-sectional area of the accelerating region, while $B_{\rm F}$ the equipartition magnetic field in this region.

B.0.1 Magnetic field $B_{\rm F}$

Following Rybicki and Lightman (1979) and Longair (2011), as described in Equation 3.9, for a synchrotron-emitting source with a power law distribution of electrons (with energy spectrum $N(E)\,dE = \kappa E^{-p}\,dE$, where p is the spectral index of the particle energies) the emissivity per unit volume at frequency ν is (Longair, 2011, equation 8.86)

$$J(\nu) = A\kappa(B\sin a)^{(p+1)/2}\nu^{-(p-1)/2}, \tag{B.1}$$

where

$$A = \frac{\sqrt{3}e^3}{8\pi^2\epsilon_0 c m_e(p+1)}\left(\frac{m_e^3c^4}{3e}\right)^{-(p-1)/2}\Gamma_{\rm f}\left(\frac{p}{4}+\frac{19}{12}\right)\Gamma_{\rm f}\left(\frac{p}{4}-\frac{1}{12}\right), \tag{B.2}$$

e and m_e are the charge and mass of an electron, respectively, B is the magnetic field strength, κ is the normalisation, a is the pitch angle of the electron, ϵ_0 is the permittivity of free space, c is the speed of light and $\Gamma_{\rm f}$ is the gamma function. Assuming that the synchrotron emitting accelerating region is a homogeneous cylinder of radius $R_{\rm F}$ and height $H_{\rm F}$, the flux from the emission region can be

written (Chaty et al., 2011)

$$S_\nu = \frac{1}{2}\left(\frac{R_\mathrm{F}}{D}\right)^2 H_\mathrm{F} j(\nu), \tag{B.3}$$

where D is the source distance. Given that H_F is related to R_F by a factor h, such that $H_\mathrm{F} = hR_\mathrm{F}$, solving Equation B.3 for $j(\nu)$ and substituting into Equation B.1 gives

$$(B_\mathrm{F} \sin a)^{\frac{p+1}{2}} = \frac{2D^2 R_\mathrm{F}^{-3} S_\nu \nu^{(p-1)/2}}{A\kappa h}. \tag{B.4}$$

For a power-law distribution, the absorption coefficient (Equation 3.13) is (Longair, 2011, equation 8.112)

$$\chi_\nu = T\kappa (B \sin a)^{(p+2)/2} \nu^{-(p+4)/2}, \tag{B.5}$$

where

$$T = \frac{\sqrt{3} e^3 c}{32\pi^2 \epsilon_0 m_e}\left(\frac{3e}{2\pi m_e^3 c^4}\right)^{p/2} \Gamma_f\left(\frac{3p+22}{12}\right)\Gamma_f\left(\frac{3p+2}{12}\right). \tag{B.6}$$

Assuming the innermost region with cross-section radius R_F and length H_F is seen side-on, the transition from thick to thin synchrotron emission occurs at $\tau_\nu = \chi_\nu \mathrm{R_F} \approx 1$ and Equation B.5 becomes

$$\chi_\nu R_\mathrm{F} = R_\mathrm{F} T\kappa (B_\mathrm{F} \sin a)^{(p+2)/2} \nu^{-(p+4)/2} \approx 1. \tag{B.7}$$

Therefore,

$$R_\mathrm{F} = \frac{(B_\mathrm{F} \sin a)^{-(p+2)/2} \nu^{(p+4)/2}}{T\kappa}. \tag{B.8}$$

Substituting this into Equation B.4 gives

$$(B_\mathrm{F} \sin a)^{\frac{2p+5}{2}} = \frac{Ah}{2\kappa^2 D^2 T^3} S_\nu^{-1} \nu^{(2p+13)/2}. \tag{B.9}$$

If we assume that the energy in the non-thermal electrons ϵ_e is a fraction ξ of the magnetic field energy density, such that

$$\epsilon_e \equiv \int_{\gamma_\mathrm{min}}^{\gamma_\mathrm{max}} \kappa \gamma^{1-p} m_e c^2 D \Gamma_\mathrm{f} = \xi \frac{B_\mathrm{F}^2}{2\mu_0}, \tag{B.10}$$

where γ_min and γ_max are the minimum and maximum Lorentz factors of the electrons and μ_0 is the permeability of free space. Solving for κ gives

$$\kappa = \xi \frac{B_\mathrm{F}^2}{2\mu_0 m_e c^2 Y}, \tag{B.11}$$

where

$$Y = \frac{\gamma_{\max}^{(2-p)} - \gamma_{\min}^{(2-p)}}{(2-p)}. \tag{B.12}$$

Substituting κ into Equation B.9 and solving for the magnetic field gives

$$B_{\mathrm{F}} = \left(\frac{2\mu_0^2 c^4 A h Y^2}{T^3}\right)^{2/(2p+13)} (D\xi)^{2/(2p+13)} S_\nu^{-2/(2p+13)} \sin a^{(2p+5)/(2p+13)} \nu. \tag{B.13}$$

Therefore, the equipartition magnetic field in region where the particles are accelerated up to a power-law distribution is related to the jet break ν_{b}, such that

$$B_{\mathrm{F}} \propto S_\nu^{-2/(2p+13)} \nu_{\mathrm{b}}. \tag{B.14}$$

B.0.2 Radius R_{F}

The radius of this region R_{F} can now be easily determined with Equations B.8 and B.13, such that

$$R_{\mathrm{F}} = \frac{2\mu_0 c^2 m_e Y}{T\xi} \sin a^{-(p+2)/2} \nu^{(p+4)/2} B_{\mathrm{F}}^{(p+6)/2}. \tag{B.15}$$

Substituting B_{F} gives

$$R_{\mathrm{F}} = 2\mu_0 c^2 \left(2\mu_0^2 c^4 m_e^2 A h\right)^{-(p+6)/(2p+13)} T^{(p+5)/(2p+13)} (\xi Y)^{-1/(2p+13)} \times \sin a^{2/(2p+13)} D^{(2p+12)/(2p+13)} S_\nu^{(p+6)/(2p+13)} \nu^{-1}. \tag{B.16}$$

Therefore, the cross-sectional radius of the region where the electrons are first accelerated up to a power-law distribution can be given as

$$R_{\mathrm{F}} \propto S_\nu^{(p+6)/(2p+13)} \nu^{-1}. \tag{B.17}$$

Appendix C

VLA flux densities of MAXI J1836−194

Table C.1: VLA flux densities of MAXI J1836−194. α is the radio spectral index. Quoted 1σ errors are uncertainties to the measured flux density.

Date (UT)	MJD	Frequency (GHz)	Flux density (mJy)	Q (mJy beam^{-1})	U (mJy beam^{-1})	α
2012 Sep 03	55807.1	4.60	27.2±0.3	0.24±0.05	-0.29±0.06	0.64±0.03
		7.90	38.4±0.5	0.67±0.06	-0.49±0.07	
2011 Sep 05	55809.1	5.00	23.2±0.3	0.08±0.02	-0.08±0.02	0.84±0.04
		7.45	32.5±0.4	0.18±0.02	-0.16±0.02	
2011 Sep 07	55811.2	1.50	18.1±0.4	–	–	0.51±0.01
		5.00	28.6±0.7	0.25±0.07	-0.13±0.07	
		7.45	39.3±0.9	0.58±0.09	-0.08±0.08	
		20.80	68±2	–	–	
		25.90	79±2	–	–	
		32.02	88±5	–	–	
		41.00	87±8	–	–	
2011 Sep 09	55813.2	1.60	24.9±0.5	–	–	0.43±0.01
		5.00	33.7±0.6	-0.00±0.06	-0.15±0.05	
		7.45	41.4±0.9	0.29±0.05	-0.49±0.05	
		20.80	66±2	–	–	
		25.90	73±2	–	–	
		32.02	95±5	–	–	

Date (UT)	MJD	Frequency (GHz)	Flux density (mJy)	Q (mJy beam^{-1})	U (mJy beam^{-1})	α
		41.00	108±6	–	–	
2011 Sep 12	55816.1	1.60	36.7±0.6	–	–	0.10±0.01
		5.00	36.6±0.8	0.93±0.05	-0.94±0.05	
		7.45	39.5±0.8	0.72±0.05	-0.74±0.04	
		20.80	47±2	–	–	
		25.90	48±2	–	–	
		32.02	51±3	–	–	
		41.00	55±3	–	–	
2011 Sep 13	55817.0	1.60	29.0±0.5	–	–	0.14±0.01
		5.00	31.0±0.4	0.72±0.06	-0.92±0.06	
		7.45	33.1±0.4	0.62±0.05	-0.86±0.05	
		20.80	40.7±1	–	–	
		25.90	44±2	–	–	
		32.02	46±3	–	–	
		41.00	46±3	–	–	
2011 Sep 18	55822.0	1.50	37±1	–	–	0.13±0.01
		5.00	34.7±0.4	0.85±0.06	-0.85±0.06	
		7.45	36.9±0.9	0.62±0.06	-0.59±0.06	
		20.80	44±1	–	–	
		25.90	46±2	–	–	
		32.02	50±2	–	–	

Date (UT)	MJD	Frequency (GHz)	Flux density (mJy)	Q (mJy beam^{-1})	U (mJy beam^{-1})	α
		41.00	441±3	–	–	
2011 Sep 18	55822.9	1.56	33±2	–	–	0.14±0.01
		5.00	29.7±0.4	0.72±0.07	-0.75±0.07	
		7.45	31.3±0.4	0.58±0.06	-0.56±0.06	
		20.80	35.5±0.7	–	–	
		25.90	38±2	–	–	
		32.02	44±2	–	–	
		41.00	37±2	–	–	
2011 Sep 23	55827.061	5.00	32.7±0.8	–	–	0.34±0.02
		7.45	34.0±0.8	–	–	
		20.80	51±2	–	–	
		25.90	54±2	–	–	
		32.02	62±3	–	–	
		41.00	66±4	–	–	
2011 Sep 26	55830.9	5.00	14.1±0.4	–	–	0.51±0.02
		7.45	14.8±0.4	–	–	
2011 Sep 26	55830.9	20.80	27±1	–	–	
		25.90	30±1	–	–	0.51±0.02
		31.52	36±2	–	–	
		37.52	40±2	–	–	
2011 Sep 30	55834.0	5.26	11.3±0.3	–	–	0.57±0.02

Date (UT)	MJD	Frequency (GHz)	Flux density (mJy)	Q (mJy beam^{-1})	U (mJy beam^{-1})	α
		7.45	11.7±0.3	–	–	
		20.80	23.5±0.9	–	–	
		25.90	26±1	–	–	
		31.52	30±2	–	–	
		37.52	32±2	–	–	
2011 Oct 07	55841.9	5.26	8±0.3	–	–	0.59±0.03
		7.45	8±0.3	–	–	
		20.80	17.5±0.9	–	–	
		25.90	19.3±0.9	–	–	
		31.52	22±2	–	–	
		37.52	25±2	–	–	
2011 Oct 12	55846.0	5.26	5.0±0.3	–	–	0.55±0.03
		7.45	5.7±0.2	–	–	
		20.80	9.8±0.5	–	–	
		25.90	12.2±0.7	–	–	
		31.52	14±1	–	–	
		37.52	14±1	–	–	
2011 Oct 22	55856.9	5.26	3.8±0.2	–	–	0.25±0.04
		7.45	4.0±0.2	–	–	
		20.80	5.3±0.4	–	–	
		25.90	5.6±0.4	–	–	

Date (UT)	MJD	Frequency (GHz)	Flux density (mJy)	Q (mJy beam^{-1})	U (mJy beam^{-1})	α
		31.52	5.8±0.6	–	–	
		37.52	5.7±0.8	–	–	
2011 Nov 01	55866.9	5.26	1.5±0.1	–	–	0.33±0.06
		7.45	1.46±0.08	–	–	
		20.80	1.9±0.2	–	–	
		25.90	2.6±0.4	–	–	
		31.52	2.6±0.4	–	–	
		37.52	3.2±0.7	–	–	
2011 Nov 11	55876.8	5.26	0.8±0.2	–	–	0.4±0.1
		7.45	0.8±0.1	–	–	
		20.80	1.0±0.1	–	–	
		25.90	1.5±0.2	–	–	
2011 Nov 18	55883.9	5.26	0.33±0.03	–	–	0.5±0.1
		7.45	0.31±0.06	–	–	
		20.80	0.6±0.1	–	–	
		25.90	0.8±0.1	–	–	
2011 Dec 03	55898.8	5.26	0.19±0.04	–	–	0.7±0.1
		7.45	0.25±0.02	–	–	
		20.80	0.49±0.07	–	–	
		25.90	0.5±0.1	–	–	

Appendix D

Publications

Publications directly resulting from work done for this thesis include:

- D. M. Russell, **T. D. Russell**, J. C. A. Miller-Jones, K. O'Brien, R. Soria, G. R. Sivakoff, T. Slaven-Blair, F. Lewis, S. Markoff, J. Homan, D. Altamirano, P. A. Curran, M. P. Rupen, T. M. Belloni, M. Cadolle Bel, P. Casella, S. Corbel, V. Dhawan, R. P. Fender, E. Gallo, P. Gandhi, S. Heinz, E. G. Körding, H. A. Krimm, D. Maitra, S. Migliari, R. A. Remillard, C. L. Sarazin, T. Shahbaz, and V. Tudose (2013) 'An Evolving Compact Jet in the Black Hole X-Ray Binary MAXI J1836−194' (2013), *The Astrophysical Journal Letters*, 768, L35.

- **T. D. Russell**, T. D., R. Soria, C. Motch, M. W. Pakull, M. A. P. Torres, P. A. Curran, P. G. Jonker, and J. C. A. Miller-Jones (2014), 'The face-on disc of MAXI J1836-194' *Monthly Notices of the Royal Astronomical Society*, 439, 1381–1389.

- **T. D. Russell**, R. Soria, J. C. A. Miller-Jones, P. A. Curran, S. Markoff, D. M. Russell, and G. R. Sivakoff (2014), 'The accretion-ejection coupling in the black hole candidate X-ray binary MAXI J1836−194', *Monthly Notices of the Royal Astronomical Society*, 439, 1390–1402.

- **T. D. Russell**, J. C. A. Miller-Jones, P. A. Curran, R. Soria, D. Altamirano, S. Corbel, M. Coriat, A. Moin, D. M. Russell, G. R. Sivakoff, T. J. Slaven-Blair, T. M. Belloni, R. P. Fender, S. Heinz, P. G. Jonker, H. A. Krimm, E. G. Körding, D. Maitra, S. Markoff, M. Middleton, S. Migliari, R. A. Remillard, M. P. Rupen, C. L. Sarazin, A. J. Tetarenko, M. A. P. Torres, V. Tudose, and A. K. Tzioumis (2015), 'Radio monitoring of the

hard state jets in the 2011 outburst of MAXI J1836−194', *Monthly Notices of the Royal Astronomical Society*, 450, 1745–1759.

Other publications not associated with this thesis:

- A. E. Reines, R. M. Plotkin, **T. D. Russell**, M. Mezcua, J. J. Condon, G. R. Sivakoff and K. E. Johnson (2014), 'A Candidate Massive Black Hole in the Low-metallicity Dwarf Galaxy Pair Mrk 709', *The Astrophysical Journal Letters*, 787, L30.

- A. J. Tetarenko, G. R. Sivakoff, J. C. A. Miller-Jones, P. A. Curran, **T. D. Russell**, I. M. Coulson, S. Heinz, D. Maitra, S. B. Markoff, S. Migliari, G. R. Petitpas, M. P. Rupen, A. P. Rushton, D. M. Russell and C. L. Sarazin (2015), 'Sub-mm Jet Properties of the X-Ray Binary Swift J1745−26', *The Astrophysical Journal Letters*, 805, Issue 1, article id. 30, 10 pp.

- P. A. Curran, J. C. A. Miller-Jones, A. P. Rushton, D. D. Pawar, G. E. Anderson, D. Altamirano, H. A. Krimm, J. W. Broderick, T. M. Belloni, R. P. Fender, E. G. Kording, D. Maitra, S. Markoff, S. Migliari, C. Rumsey, M. P. Rupen, D. M. Russell, **T. D. Russell**, C. L. Sarazin, G. R. Sivakoff, R. Soria, A. J. Tetarenko, D. Titterington, V. Tudose (2015), 'Radio polarimetry as a probe of unresolved jets: the 2013 outburst of XTE J1908+094', *Monthly Notices of the Royal Astronomical Society*, 451, 3975–3985.

Astronomer's Telegram alerts:

- James C. A. Miller-Jones, **Thomas D. Russell**, Gregory R. Sivakoff and Peter A. Curran. 2013. 'Radio non-detection of MAXI J1828−249', *The Astronomer's Telegram*, Number 5484.

- Christian Motch, **Thomas Russell**, Roberto Soria, Fabien Grisé, Manfred Pakull, James Miller-Jones. 2014. 'New transient ULX in NGC 7793: upper limits on its radio flux', *The Astronomer's Telegram*, Number 6828.

Appendix E

Copyright permission

Universal Uclick
An Andrews McMeel Universal Company

Gratis # 13490
June 3, 2015

Thomas D. Russell

Dear Thomas D.:

Thank you for your letter requesting permission to reprint:

- (1) CALVIN & HOBBES cartoon in a dissertation.

We extend to you our gratis permission to reprint this cartoon/text feature on a one-time only basis.

We do require that you use this copyright line with each cartoon/text feature:

• CALVIN AND HOBBES © 1992 Watterson. Reprinted with permission of UNIVERSAL UCLICK. All rights reserved.

There can be no additions, deletions or substitutions of any kind to the cartoon or text. All cartoons must be reprinted in their entirety. Portions of cartoons or characters cannot be used.

We appreciate your interest in Universal Uclick and our features.

Sincerely,

Diana Neuwirth
Administrator

1130 Walnut Street, Kansas City, MO 64106-2109 Tel 816-581-7500
http://www.amureprints.com